Petrogenesis of Mesoarchean high-K rocks in the Kaapvaal Craton: Investigating the Boesmanskop Alkaline Complex and Salisbury Kop batholith

by
Marcel Vinicius Santos Leandro

Dissertation presented for the degree of Doctor of Philosophy in the Faculty of Science at Stellenbosch University. The financial assistance of the National Research Foundation (NRF) towards this research is hereby acknowledged. Opinions expressed and conclusions arrived at, are those of the author and are not necessarily to be attributed to the NRF

Supervisor: Professor Gary Stevens, Stellenbosch University (South Africa)
Co-supervisors: Professor Alex Kisters, Stellenbosch University (South Africa)
Professor Jean-François Moyen, Université de Saint-Etienne (France)

March 2025

DECLARATION

By submitting this dissertation electronically, I declare that the entirety of the work contained therein is my own, original work, that I am the sole author thereof (save to the extent explicitly otherwise stated), that reproduction and publication thereof by Stellenbosch University will not infringe any third party rights and that I have not previously in its entirety or in part submitted it for obtaining any qualification. This dissertation includes one original paper submitted for publication in a peer-reviewed journal and two unpublished publications. The development and writing of the papers (published and unpublished) were the principal responsibility of myself and, for each of the cases where this is not the case, a declaration is included in the dissertation indicating the nature and extent of the contributions of co-authors.

Date: March 2025

ABSTRACT

The Boesmanskop Alkaline Complex (BAC) and Salisbury Kop batholith (SB) are two contrasting units of the large ca. 3105 Ma Granodiorite-Monzogranite-Syenogranite (GMS) suite, situated on the eastern margin of the Kaapvaal Craton. The BAC consists of small intrusions at the southern end of the Barberton greenstone belt, recording shear deformation and containing the most potassic and REE-rich rocks of the GMS suite. In contrast, the SB is a homogeneous batholith at the north of the belt with a more sodic character. This study examines the BAC and SB through field observations, petrography, mineral chemistry, whole-rock compositions, and U-Pb zircon geochronology, alongside Rb-Sr and Sm-Nd isotopic data and phase equilibrium modeling for the BAC rocks. The BAC includes coarse-grained syenite, quartz monzonite and leucogranite. Some syenites display porphyritic textures that indicate K-feldspar phenocryst accumulation, with clinopyroxene and Ca-amphibole as intercumulus phases. Field observations indicate that the BAC magmas were emplaced at shallow levels along active shear zones. New U-Pb zircon dating of a quartz monzonite yielded a crystallization age of 3118 ± 9 Ma and inherited cores of ca. 3220 Ma. Zircon, apatite, and titanite compositions reflect high-temperature crystallization from REE-rich felsic magmas, with Ti-in-zircon thermometry recording temperatures up to 915 °C. Additionally, the high K_2O+Na_2O, low MgO and CaO contents of all the rocks, the presence of inherited zircon cores, and crustal isotopic signatures of the cumulus rocks suggest that they derive from magmas produced by low-degrees of fluid-absent anatexis of the lower crust (including recycled sediments). Phase equilibrium modeling conducted at pressure of 1.5 kbar and temperature range from 800 to 950 °C, consistent with intrusion at shallow depths, demonstrated that a subset of high-alkali content GMS granitic compositions is capable of crystallizing K-feldspar as the first tectosilicate. These experiments support the hypothesis that the syenites and quartz monzonites originated from hot granitic melts that underwent significant crystal accumulation of alkali feldspar. These textural and geochemical features and zircon U-Pb ages advocate that the BAC quartz monzonites and syenites formed earlier than the surrounding granitic bodies, representing the onset of the K-high magmatism responsible for transferring incompatible and heat-producing elements to shallow levels, thereby contributing to the stabilization of the Kaapvaal Craton. Conversely, the leucogranites and granodiorites of the SB lack cumulus textures. U-Pb zircon dating of granodiorites yields a crystallization age of 3094 ± 10 Ma and the titanite dating yields a within

error identical age of 3100 ± 11 Ma. The idiomorphic biotite as the only mafic phase suggests that these rocks originated from more evolved and colder magma than the syenites and quartz monzonites. Taken together, the BAC and SB represent two key magmatic complexes that record high-K magmatism associated with the partial melting of the lower crust. The features reported highlight the importance of crustal reworking and lower crustal melting in stabilizing the early cratons, such as the Kaapvaal Craton. The BAC represents the initiation of the magmatic event.

Keywords: Archean syenites; Crustal evolution; Granitogenesis

RESUMO

O Complexo Alcalino Boesmanskop (BAC) e o batólito Salisbury Kop (SB) são duas unidades contrastantes da grande ca. 3105 Ma Granodiorito-Monzogranito-Sienogranito (GMS) suíte, situadas na margem leste do Cráton do Kaapvaal. O BAC consiste em pequenas intrusões ao sul da suíte, registra a ação de deformação cisalhante e contém as rochas mais potássicas e ricas em ETR da suíte GMS. Em contraste, o SB é um batólito majoritariamente homogêneo ao norte da suíte, com afinidade sódica. Este estudo examina o BAC e o SB por meio de observações de campo, petrografia, química mineral, composições de rocha-total e geocronologia U-Pb em zircão, juntamente com dados isotópicos de Rb-Sr, Sm-Nd e modelagem de fases em equilíbrio para o BAC. O BAC inclui sienitos, quartzo monzonitos e leucogranitos de granulação grossa. Alguns sienitos exibem texturas porfiríticas, indicativas do acúmulo de fenocristais de K-feldspato, com clinopiroxênio e Ca-anfibólio como fases intercumulativas. Observações de campo indicam que os magmas do BAC foram colocados em níveis rasos através de zonas de cisalhamento ativas. A nova datação U-Pb em zircão de um quartzo monzonito revelou uma idade de cristalização de 3118 ± 9 Ma, com núcleos herdados de aproximadamente 3220 Ma. As composições de zircão, apatita e titanita refletem cristalização em altas temperaturas a partir de magmas félsicos ricos em ETR, registrando temperaturas de até 915 °C, baseada no geotermômetro de Ti em zircão. Além disso, os altos teores de K_2O + Na_2O, baixos teores de MgO e CaO observado em todas as amostras, a presença de núcleos de zircão herdados e assinaturas isotópicas crustais das rochas cumulativas sugerem que os magmas iniciais derivam de braixos graus de anatexia na ausência de fluido da crosta inferior (incluindo sedimentos reciclados). A modelagem de fases em equilíbrio realizada a uma pressão de 1,5 kbar e intervalo de temperatura entre 800 e 950 °C, consistente com intrusões colocadas a profundidades rasas, demonstrou que um subconjunto de composições graníticas da GMS suíte, ricas em álcalis é capaz de cristalizar K-feldspato como o primeiro tectossilicato. Esses experimentos apoiam a hipótese de que os sienitos e quartzo monzonitos se originaram de *melts* graníticos quentes que passaram por acúmulo significativo de cristais de feldspato alcalino. Essas características texturais e geoquímicas e as idades U-Pb em zircão indicam que os sienitos e quartzo monzonitos do BAC se formaram antes dos corpos graníticos ao redor, representando o início do magmatismo de alto K_2O responsável pela transferência de elementos incompatíveis e produtores de calor para níveis superficiais, contribuindo assim para a estabilização do Cráton de Kaapvaal. Por outro lado, os leucogranitos e granodioritos que

compõem o SB não apresentam texturas cumulativas. A datação U-Pb em zircão de granodioritos revela uma idade de cristalização de 3094 ± 10 Ma e os cristais de titanita registram uma idade de 3100 ± 11 Ma. A biotita idiomórfica como a única fase máfica sugere que essas rochas se originaram de magmas mais evoluídos e frios do que os sienitos e quartzo monzonitos. Juntos, o BAC e o SB representam dois complexos magmáticos fundamentais que registram o magmatismo de alto potássio associado à fusão parcial da crosta inferior. As características relatadas destacam a importância do retrabalho crustal e da fusão da crosta inferior para a estabilidade da crosta continental primitiva. Enquanto o BAC representa o início do evento magmático, o SB marca seus estágios finais.

Palavras-chave: Sienitos Arqueanos; Evolução crustal; Granitogenese

ACKNOWLEDGMENTS

Firstly, greetings to Exu, the great guardian of the crossroads and messenger between worlds. Thank you for opening my paths and facilitating communication and the flow of energies across the Atlantic. May your strength and wisdom always guide us. *Laroyê Exu!*

I would like to express my deepest gratitude to my supervisors, Gary Stevens, Jean-François Moyen, and Alex Kisters, for providing me with the opportunity to *develop this* research project. Thank you, Professor Gary Stevens, for your invaluable time, patience, support, and guidance throughout this research, which allowed me to grasp scientific production with global relevance. A big thank you to Alex and Jeff for our discussions about the Barberton and for willingly sharing their knowledge (and data) with me.

Thank you to the staff of the Earth Science Department at Stellenbosch University, namely Madelaine Frazenberg, Casey Christoffels, Mareli Grobbelaar-Moolman, and Riana Rossouw, for all the analyses done, for help conducting the analytical techniques, and for facilitating my access to the CAF laboratories.

To my mother, Luciane Silva Santos, my father, Antonio Elcio Leandro dos Santos, and my brother, Hebert Matheus Santos Leandro, I express my deepest gratitude for your undying support. All my success reflects the huge love and support you provided. I love you all.

I am also immensely thankful for the good friends made during my journey. I acknowledge all the help given by Alan, Ariela, and Cris, the best compatriot friends I could ever meet, and to my dear friend Jean-Baptiste who taught me the great value of the global citizen brotherhood. I'm grateful for the good moments shared with my colleagues and friends Tahnee, Anna, Daniel, Steve, Katrien, Helena, Isaac, Hope and Jaco. Thank you, Lulutho, Keenan, and Timara, for the academic encouragement and for making my life much easier and more pleasant at *Stellies*.

I also acknowledge the South African National Research Foundation (NRF) and BuCoMO International Research Project (IRP), funded by the French Centre for Scientific Research (CNRS), for their financial assistance. This project was also made possible by the financial support provided by the NRF funding to Gary Stevens via the SARChI program and departmental bursaries granted by the Stellenbosch University Department of Earth Sciences. Thank you to all the Stellenbosch University community for welcoming me.

TABLE OF CONTENTS

Page

DECLARATION ..... **i**

ABSTRACT ..... **ii**

RESUMO ..... **iv**

ACKNOWLEDGMENTS ..... **vi**

TABLE OF CONTENTS ..... **vii**

LIST OF TABLES ..... **xi**

LIST OF FIGURES ..... **xii**

Chapter 1. introduction **21**

1.1. Alkaline rocks definition **21**

1.2. Geodynamic settings of alkaline magmatism **22**

1.3. The Onset of High-K Magmatism **23**

1.4. Archean alkaline rocks **23**

1.5. Alkaline complexes in the Kaapvaal Craton **24**

1.6. Local Geology Overview **26**

1.6.1. Basement **26**

1.6.2. TTG suite **27**

1.6.3. GMS suite **27**

1.7. Objectives **28**

1.8. Structure of the Thesis **29**

1.9. References - Chapter 1 ..... **29**

Chapter 2. PRESENTATION OF RESEARCH PAPER 1 - ARCHEAN SYENITES BY INTRACRUSTAL PROCESSES: THE BOESMANSKOP ALKALINE COMPLEX, EASTERN KAAPVAAL CRATON ..... Error! Bookmark not defined.

2.1. Introduction ..... Error! Bookmark not defined.

2.2. Geological Background ..... Error! Bookmark not defined.

2.2.1. Barberton Granite-Greenstone Terrane overview .. Error! Bookmark not defined.

2.2.2. Granodiorite-Monzogranite-Syenogranite suite overview... Error! Bookmark not defined.

2.2.3. Study area ..... Error! Bookmark not defined.

2.3. Materials and Methods ..... Error! Bookmark not defined.
2.3.1. Sample preparation ..... Error! Bookmark not defined.
2.3.2. Petrography and mineral chemistry ..... Error! Bookmark not defined.
2.3.3. Whole-rock compositions ..... Error! Bookmark not defined.
2.3.4. Isotopic analysis ..... Error! Bookmark not defined.
2.3.5. Phase equilibrium modeling ..... Error! Bookmark not defined.
2.4. Results ..... Error! Bookmark not defined.
2.4.1. Field relationships ..... Error! Bookmark not defined.
2.4.1.1. Boesmanskop Head pluton ..... **Error! Bookmark not defined.**
2.4.1.2. Kees Zyn Doorns pluton ..... **Error! Bookmark not defined.**
2.4.1.3. Boesmanskop Tail pluton ..... **Error! Bookmark not defined.**
2.4.2. Petrography ..... Error! Bookmark not defined.
2.4.2.1. Quartz monzonite ..... **Error! Bookmark not defined.**
2.4.2.2. Syenites ..... **Error! Bookmark not defined.**
2.4.2.3. Granite ..... **Error! Bookmark not defined.**
2.4.3. Whole-rock major and trace element geochemistry ..... Error! Bookmark not defined.
2.4.3.1. Major elements ..... **Error! Bookmark not defined.**
2.4.3.2. Trace elements ..... **Error! Bookmark not defined.**
2.4.4. Mineral compositions ..... Error! Bookmark not defined.
2.4.4.1. Mafic minerals ..... **Error! Bookmark not defined.**
2.4.4.2. Feldspar ..... **Error! Bookmark not defined.**
2.4.5. Sr and Nd isotopic ratios ..... Error! Bookmark not defined.
2.4.6. Modeling fractional crystallization processes ..... Error! Bookmark not defined.
2.4.6.1. Input parameters ..... **Error! Bookmark not defined.**
2.4.6.2. Crystal cumulates modeled ..... **Error! Bookmark not defined.**
2.4.6.3. Trace element modeling ..... **Error! Bookmark not defined.**
2.5. Discussion ..... Error! Bookmark not defined.
2.5.1. Constraints on the origin of the feldspar phenocrysts ..... Error! Bookmark not defined.
2.5.2. Tectonic setting and emplacement mechanisms ..... Error! Bookmark not defined.
2.5.3. Chemical and isotopic assessment ..... Error! Bookmark not defined.
2.6. Conclusion ..... Error! Bookmark not defined.

2.7. Acknowledgment ..... Error! Bookmark not defined.
2.8. References – Chapter 2 ..... Error! Bookmark not defined.
Chapter 3. PRESENTATION OF RESEARCH PAPER 2 - ACCESSORY MINERAL CHEMISTRY OF CA. 3.1 GA SYENITES AND QUARTZ MONZONITES OF THE BOESMANSKOP ALKALINE COMPLEX, KAAPVAAL CRATON: INSIGHTS INTO MAGMATIC PROCESSES DURING CRATON STABILIZATION .... Error! Bookmark not defined.
3.1. Introduction ..... Error! Bookmark not defined.
3.2. Analytical Methods ..... Error! Bookmark not defined.
3.2.1. Sample preparation ..... Error! Bookmark not defined.
3.2.2. Imaging acquisition ..... Error! Bookmark not defined.
3.2.3. Mineral compositions and U-Pb zircon dating ..... Error! Bookmark not defined.
3.2.4. Thermometry ..... Error! Bookmark not defined.
3.3. Local Geology ..... Error! Bookmark not defined.
3.4. Whole-rock Chemistry ..... Error! Bookmark not defined.
3.5. Results ..... Error! Bookmark not defined.
3.5.1. Petrography ..... Error! Bookmark not defined.
3.5.2. Zircon chemistry ..... Error! Bookmark not defined.
3.5.3. Apatite chemistry ..... Error! Bookmark not defined.
3.5.4. Titanite chemistry ..... Error! Bookmark not defined.
3.5.5. Geochronology ..... Error! Bookmark not defined.
3.6. Discussion ..... Error! Bookmark not defined.
3.6.1. Zircon chemistry ..... Error! Bookmark not defined.
3.6.2. Apatite chemistry ..... Error! Bookmark not defined.
3.6.3. Titanite chemistry ..... Error! Bookmark not defined.
3.6.4. Source inferences ..... Error! Bookmark not defined.
3.7. Conclusion ..... Error! Bookmark not defined.
3.8. Acknowledgment ..... Error! Bookmark not defined.
3.9. Data Availability ..... Error! Bookmark not defined.
3.10. References – Chapter 3 ..... Error! Bookmark not defined.

Chapter 4. PRESENTATION OF RESEARCH PAPER 3 – U-Pb zircon geochronology and chemical characterization of the Mesoarchean Salisbury Kop batholith, Kaapvaal Craton ..... Error! Bookmark not defined.

4.1. Introduction ..... Error! Bookmark not defined.

4.2. Analytical Methods ..... Error! Bookmark not defined.

4.2.1. Sample preparation ..... Error! Bookmark not defined.

4.2.2. Petrographic analysis and imagining ..... Error! Bookmark not defined.

4.2.3. Whole-rock compositions ..... Error! Bookmark not defined.

4.2.4. U-Pb dating ..... Error! Bookmark not defined.

4.2.4.1. Zircon ..... **Error! Bookmark not defined.**

4.2.4.2. Titanite ..... **Error! Bookmark not defined.**

4.3. Local Geology ..... Error! Bookmark not defined.

4.3.1. The Barberton Granite-Greenstone Terrane ..... Error! Bookmark not defined.

4.3.2. The GMS suite ..... Error! Bookmark not defined.

4.3.3. The Salisbury Kop batholith ..... Error! Bookmark not defined.

4.4. Results ..... Error! Bookmark not defined.

4.4.1. Petrography ..... Error! Bookmark not defined.

4.4.2. Whole-rock chemistry ..... Error! Bookmark not defined.

4.4.3. U-Pb dating ..... Error! Bookmark not defined.

4.4.3.1. Zircon age ..... **Error! Bookmark not defined.**

4.4.3.2. Titanite age ..... **Error! Bookmark not defined.**

4.5. Discussion ..... Error! Bookmark not defined.

4.6. Conclusion ..... Error! Bookmark not defined.

4.7. Acknowledgment ..... Error! Bookmark not defined.

4.8. References – Chapter 4 ..... Error! Bookmark not defined.

Chapter 5. CONCLUSION ..... Error! Bookmark not defined.

5.1. U-Pb geochronology ..... Error! Bookmark not defined.

5.2. Origins of Heterogeneity in the GMS suite ..... Error! Bookmark not defined.

5.3. Source inference ..... Error! Bookmark not defined.

5.4. References – Chapter 5 ..... Error! Bookmark not defined.

Chapter 6. APPENDIX ..... Error! Bookmark not defined.

6.1. Supplementary material of research paper 1 ..... Error! Bookmark not defined.

6.2. Supplementary material of research paper 2..... Error! Bookmark not defined.
6.3. Supplementary material of research paper 3..... Error! Bookmark not defined.
6.4. Supplementary material of the thesis..... Error! Bookmark not defined.

LIST OF TABLES

Table 2-1. Sample coordinates and facies of the Boesmanskop Alkaline Complex and correlated potassic samples of the Heerenveen batholith. ..... **Error! Bookmark not defined.**

Table 2-2. Whole-rock major element compositions (wt%) of the Boesmanskop Alkaline Complex and associated high-K rocks of the Heerenveen batholith. **Error! Bookmark not defined.**

Table 2-3. Whole-rock relevant trace element contents (ppm). .... **Error! Bookmark not defined.**

Table 2-4. Rb/Sr and Sm/Nd isotopic data of representative rocks, for 3107 Ma crystallization age. ..... **Error! Bookmark not defined.**

Table 2-5. Whole-rock composition of representative initial melts modeled that can crystalize K-feldspar prior plagioclase and compositions of theoretical cumulus rocks produced by the FC with three initial H_2O contents. ..... **Error! Bookmark not defined.**

Table 3-1. Representative trace and rare earth element analyses (ppm) of zircon hosted in the BAC quartz monzonites and syenites. ..... **Error! Bookmark not defined.**

Table 3-2. Representative trace and rare earth element analyses (ppm) of apatite hosted in the BAC quartz monzonites and syenites. ..... **Error! Bookmark not defined.**

Table 3-3. Representative trace and rare earth element analyses (ppm) of titanite hosted in the BAC quartz monzonites and syenites. ..... **Error! Bookmark not defined.**

Table 3-4. U-Pb isotopic data of zircon hosted in the coarse-grained quartz monzonite yielding crystallization ages. The inherited ages are presented in the supplementary materials. ..... **Error! Bookmark not defined.**

Table 4-1. Coordinates of the sampled rocks from the Salisbury Kop batholith and rock type. ..... **Error! Bookmark not defined.**

Table 4-2. Major oxides (wt%), trace elements and REE contents (ppm) of granites and granodiorites of the SB. ..... **Error! Bookmark not defined.**

Table 4-3. U-Pb isotopic data of zircon hosted in the coarse-grained granodiorite. ..... **Error! Bookmark not defined.**

LIST OF FIGURES

Figure 1-1. Evolution of syenitic magmatism. The averaging step is 20 Ma and N is the number of dates in the compilation (Balashov and Glaznev, 2006). GMS: Granodiorite-Monzogranite-Syenogranite suite. 24

Figure 1-2. Geological setting of the Kaapvaal craton, South Africa and adjacent Limpopo Belt (after Eglington and Armstrong, 2004 and Laurent et al., 2014), showing the major structures and the location of relevant alkaline complexes. AGC: Ancient Gneiss Complex; BAC: Boesmanskop Alkaline Complex; BGB: Barberton Greenstone Belt; PAC: Phalaborwa Complex; PIC: Pilanesberg Complex; SAC: Schiel Alkaline Complex; SZ: Shear zone. 26

Figure 2-1. Simplified geological map of the Barberton Granite-Greenstone Terrane showing the GMS suite and surrounding units (after de Ronde and de Wit, 1994; Clemens et al., 2010; Schoene and Bowring, 2010). Insert: location of the Kaapvaal Craton. AGC: Ancient Gneiss Complex; SIFS: Saddleback-Inyoka Fault System; WSZ: Welverdiend Shear Zone. ..... **Error! Bookmark not defined.**

Figure 2-2. Simplified geological map of the Boesmanskop Alkaline Complex illustrating the spatial distribution of main rock types and sample locations. A) Kees Zyn Doorns pluton. B) Boesmanskop Head and Boesmanskop Tail plutons (after Anhaeusser and Robb, 1983; Westraat et al., 2005). BGB: Barberton Greenstone Belt. ..... **Error! Bookmark not defined.**

Figure 2-3. Field features of the BAC. A-B) Syenitic dykes intruding the TTG suite with sharp contacts. C) SC fabric in cumulus syenite. D) Magmatic layering on the quartz monzonite. E) fine-grained quartz monzonite dyke intruding the coarse-grained quartz monzonite. F) Porphyritic syenite with angular euhedral K-feldspar (Kfs) phenocrysts surrounded by smaller K-feldspar, plagioclase (Pl), quartz (Qz) and amphibole (Ca-amph). ..... **Error! Bookmark not defined.**

Figure 2-4. Photomicrographs of representative textures of the quartz monzonite from BAC. A-B) Illustration of the intercumulus anhedral crystals filling gaps between the K-feldspar and plagioclase in a medium-grained rock, under plane- and cross-polarized light, respectively. C-D) Quartz monzonite with a fine-grained matrix showing K-feldspar phenocrysts with variable alteration degree, under cross-polarized light. The fine-grained matrix is predominantly composed of anhedral

plagioclase, K-feldspar, and quartz. E-F) Mylonitized quartz monzonite, with the generation of mineral alignment, augen crystals, quartz ribbon, and a matrix composed of recrystallized crystals, under plane- and cross-polarized light. Ap: Apatite; Bt: Biotite; Ep: Epidote; Ilm: Ilmenite; Mt: Magnetite; Ser: Sericite; Ttn: Titanite..... **Error! Bookmark not defined.**

Figure 2-5. Photomicrography of representative textures of the porphyritic syenites. A-B) Angular euhedral K-feldspar phenocryst with perthite exsolution, apatite, and clinopyroxene inclusions under plane- and cross-polarized light, respectively. C) Homogeneous K-feldspar phenocrysts with interlocked contacts and mafic minerals as intercumulus phases under cross-polarized light. The clinopyroxene is partially replaced by amphibole. D). Titanite, epidote, and magnetite filling the feldspar interstices, under cross-polarized light. ..... **Error! Bookmark not defined.**

Figure 2-6. Chemical classification diagrams of BAC rocks. A) Plot of total alkalis vs silica (TAS) diagram (Middlemost, 1994) showing BAC and GMS suite compositions. B) K_2O vs Na_2O (wt%) diagram with the potassic and sodic series fields of Middlemost (1975). C) Peralkalinity vs Alumina Saturation Index diagram of Shand (1943); A/CNK = molar Al/(2*Ca+Na+K); A/NK = molar Al/(Na+K). The GMS data are from Anhaeusser and Robb, 1983; Westraat et al., 2005; Moyen et al., 2021. The shapes of the symbols correspond to the chemical classification of the rocks. ..... **Error! Bookmark not defined.**

Figure 2-7. The data from Fig. 2-6 plotted on Harker diagrams for relevant major (wt%), trace element (ppm) and REE (ppm) vs SiO_2 (wt%). The graphs illustrate that the BAC rocks do have the highest contents of trace element except for Rb, and high REE relative to the GMS rocks. A) MgO vs SiO_2; B) K_2O vs SiO_2; C) Na_2O vs SiO_2; D) CaO vs SiO_2; E) FeO_T vs SiO_2; F) Mg# vs SiO_2; G) Ba vs SiO_2; H) Rb vs SiO_2; I) Sr vs SiO_2; J) Ce vs SiO_2; K) Sm vs SiO_2; L) Yb vs SiO_2. Mg# = cationic Mg/(Mg+Fe). ... **Error! Bookmark not defined.**

Figure 2-8. Spider diagram for trace elements and REE normalized to the Primitive Mantle (McDonough and Sun, 1995) and chondrite (Nakamura, 1974), respectively. A-B) Plot of the syenite compositions. C-D) Plot of the quartz monzonite compositions. E-F) Plot of the BAC granite compositions. The BAC rocks are subdivided according to their K_2O content. ..... **Error! Bookmark not defined.**

Figure 2-9. A) BAC pyroxene compositions plotted on a Wollastonite-Enstatite-Ferrosillite (Wo-En-Fs) ternary diagram for pyroxene classification (Morimoto, 1988). B) Amphibole compositions plotted on the classification diagram (Hawthorne et al., 2012). C) Biotite compositions plotted on a ternary biotite classification diagram of Nachit et al. (2005). D) BAC feldspar compositions plotted on an Albite-Anorthite-Orthoclase (Ab-An-Or) ternary diagram illustrating the low calcium content of the plagioclase in the syenitic rocks relative to the granites. Apfu: atoms per formula unit. ..... **Error! Bookmark not defined.**

Figure 2-10. REE spider diagram for titanite, clinopyroxene, and amphibole in the A) syenite and B) quartz monzonite Chondrite normalized (Nakamura, 1974). **Error! Bookmark not defined.**

Figure 2-11. Binary diagrams depicting the relevant radiogenic isotope compositions of the BAC and spatially related TTG and GMS suite. A) εNd(t) vs U-Pb age. B) $^{143}Nd/^{144}Nd_{(t)}$ vs $^{87}Sr/^{86}Sr_{(t)}$. DM: Depleted Mantle; CHUR: Chondritic Uniform Reservoir. The green areas represent the isotopic evolution with time of the TTG rocks. Data from the literature are 3.45 TTG (Barton et al., 1983b; Robb et al., 1986); 3.23 TTG (Schoene et al., 2009); GMS suite (Yearron, 2003; Moyen et al., 2021). ... **Error! Bookmark not defined.**

Figure 2-12. Comparison of the modeled cumulate rock compositions and the natural BAC rocks. A) TAS diagram (Middlemost, 1994). B) Binary diagram K_2O vs Na_2O (wt%) with potassic and sodic series field delimitation of Middlemost (1975). C) Peralkalinity vs Alumina Saturation Index (Shand, 1943). ..... **Error! Bookmark not defined.**

Figure 2-13. Crystal accumulation modeling. A) Phase proportion stabilized from initial granitic melts with $K_2O+Na_2O > 9.3$ wt%. B) Phase proportion stabilized from initial granitic melts with $K_2O+Na_2O < 9.3$ wt%. Titanite is stabilized but its volumes are too low to be expressed in this illustration. C-D) Spider diagram for trace elements and REE with the mean trace element contents of initial granitic melt with $K_2O+Na_2O > 9.3$, compared with the cumulus rock modeled and the composition range of the natural syenites and quartz monzonites. Primitive Mantle normalized (McDonough and Sun, 1995) and chondrite normalized (Nakamura, 1974). .. **Error! Bookmark not defined.**

Figure 3-1. Simplified geological map of the Barberton Granite-Greenstone Terrane showing the GMS suite and surrounding units (after de Ronde and de Wit, 1994; Clemens et al., 2010; Schoene and Bowring, 2010). The insert shows the location of the Kaapvaal Craton. SIFS: Saddleback-Inyoka Fault System; WSZ: Welverdiend Shear Zone. **Error! Bookmark not defined.**

Figure 3-2. Geological map of the Boesmanskop Alkaline Complex illustrating the spatial distribution of main facies and sample locations (black stars). A) Kees Zyn Doorns pluton intrusive into ca. 3.2 Ga TTG suite. B) Boesmanskop Head and Boesmanskop Tail plutons intrusive into ca. 3.5 Ga TTG suite (after Anhaeusser and Robb, 1983 and Westraat et al., 2005). C) Representative texture of coarse-grained quartz monzonite with mineral lineation. D) Representative texture of the coarse-grained syenite with K-feldspar phenocrysts. ..... **Error! Bookmark not defined.**

Figure 3-3. Photomicrography of representative accessory minerals textures. A-B) Porphyritic syenite with subhedral titanite crystals hosting zircon and in contact with amphibole. C-D) Coarse-grained syenites with apatite hosted by amphibole. Interstitial Fe-Ti oxide minerals and K-feldspar phenocrysts are also observed. E) Titanite crystal hosting allanite, zircon and Fe-Ti oxides in a coarse-grained quartz monzonite. These inclusions are clustered in the overgrown rims. All: allanite; Amph: amphibole; Ap: apatite; Ilm: Ilmenite; Kfs: K-feldspar; Pl: plagioclase; Qz: quartz; Ttn: titanite; Zrc: zircon..... **Error! Bookmark not defined.**

Figure 3-4. BSE images display the main textures of the accessory minerals in syenites (A-D) and quartz monzonites (E-F) of BAC. A) Acicular apatite. B) Euhedral blocky apatite crystals in a mafic cluster of biotite, ilmenite, and magnetite. C) Apatite inclusion in amphibole with biotite rims and surrounded by anhedral titanite and Fe-Ti oxides. D) Euhedral titanite crystal with a homogeneous bright interior which has been overgrown at the rim and replaced by a BSE darker titanite. E) Euhedral titanite crystal with a homogeneous bright core that has been overgrown by a BSE darker rim. F) Titanite crystal with concentric zonation on its core and overgrown rim. All: allanite; Amph: amphibole; Ap: apatite; Ilm: Ilmenite; Kfs: K-feldspar; Mt: Magnetite; Pl: plagioclase; Qz: quartz; Rt: rutile; Ttn: titanite; Zrc: zircon..... **Error! Bookmark not defined.**

Figure 3-5. CL images of representative zircon crystals hosted in the coarse-grained quartz monzonite (sample KZD01) and age correlation with Ti contents. White circles

indicate $^{207}Pb/^{206}Pb$ ages (Ma) and uncertainties (2σ), while green circles indicate trace elements analyses. The bright crystals within the zircon are apatite..... **Error! Bookmark not defined.**

Figure 3-6. Illustration of the chemistry of the zircon crystals in the BAC syenites and quartz monzonites and the Ti in zircon thermometry results. A) Chondrite normalized (Nakamura, 1974) zircon REE plot. B) ΣLREE vs ΣHREE. C) Hf vs Ti. D) Apparent crystallization temperatures inferred using the Ti-in-zircon thermometer of Ferry and Watson (2007), with $a TiO_2 = 0.65$ and $a SiO_2 = 0.95$. E) Nb/Yb vs U/Yb ratios. F) Ce/Sm vs Yb/Gd ratios. The vectors of mineral fractionation and mantle array were defined by Grimes et al. (2015). The Mpuluzi granite and TTG suite data were obtained from Murphy (2015) and Laurent et al. (2022). ..... **Error! Bookmark not defined.**

Figure 3-7. Diagrams illustrating the chemical distinctions of the two apatite populations described in this study. A) Chondrite normalized (Nakamura, 1974) spider diagram. B) Fe vs Mn. C) Ce/Ce* vs Eu/Eu*. D) Ce/Sm vs Yb/Gd ratios. E) ∑LREE vs ∑HREE; F) Th/U ratio vs Sr. ..... **Error! Bookmark not defined.**

Figure 3-8. Chemical diagrams for the titanite crystals of the BAC rocks subdivided according to their chemical signatures. A-B) Chondrite-normalized REE diagram (Nakamura, 1974) with plot of the syenite-hosted crystals and quartz monzonite-hosted crystals, respectively. C) Yb/Gd vs Ce/Sm ratios. D) Gd vs Eu/Eu*. E) Zr vs ∑REE. F) Zr-in-titanite temperature for the BAC and TTG crystals. The literature data are the primary titanite hosted on the TTG suite reported by Mühlberg (2022)..... **Error! Bookmark not defined.**

Figure 3-9. U-Pb concordia $^{206}Pb/^{238}U$ vs $^{207}Pb/^{235}U$ diagram plots for the coarse-grained quartz monzonite of the BAC (sample KZD01). A) Inherited cores. B) Crystallization zircon ages. The ellipses uncertainties are reported as 2σ. MSWD: mean square of weighted deviates..... **Error! Bookmark not defined.**

Figure 3-10. Graphical abstract illustrating the crystallization order of the accessory minerals investigated and their REE signatures..... **Error! Bookmark not defined.**

Figure 4-1. Geological map of the Salisbury Kop batholith displaying the sample locations and surrounding units. The dashed line represents the inferred limits of the pluton (after Kamo and Davis, 1994; Robb et al., 2006). B) Representation of rolled block

outcrops of the SB. C) Representative texture of the coarse-grained granodiorite. ..... **Error! Bookmark not defined.**

Figure 4-2. Photomicrographs illustrating representative textures of the SB granodiorites (A-D) and granites (E-F), displaying angulous plagioclase, K-feldspar (microcline), anhedral quartz (Qz) euhedral biotite (Bt), euhedral diamond-shaped titanite (Ttn). Images A, C, and E were captured under plane-polarized light, while B, D, and F were taken under cross-polarized light. ..... **Error! Bookmark not defined.**

Figure 4-3. Classification diagrams with plot of rock compositions of the SB and GMS suite. A) Plot of total alkalis vs. silica (TAS) diagram (Middlemost, 1994). B) K_2O vs Na_2O (wt%) diagram with the potassic and sodic series fields of Middlemost (1975). C) Peralkalinity vs Alumina Saturation Index diagram of Shand (1943), A/CNK: $Al_2O_3/(CaO+Na_2O+K_2O)$; A/NK: $Al_2O3/(Na_2O+K_2O)$ (molar ratio). The gray symbols represent the GMS suite samples according to their chemical classification. The GMS suite literature data were obtained from Anhaeusser and Robb, 1983; Westraat et al. (2005); Moyen et al. (2021) and Leandro et al. (2024). ..... **Error! Bookmark not defined.**

Figure 4-4. Binary diagrams for relevant major oxides (wt%) and trace elements (ppm). A) TiO_2 vs SiO_2; B) Al_2O_3 vs SiO_2; C) FeO_T vs SiO_2; D) MgO vs SiO_2; E) CaO vs SiO_2; F) K_2O vs SiO_2; G) Na_2O vs SiO_2; H) TiO_2 vs FeO_T +MgO vs SiO_2; I) Sr vs Rb (ppm). Symbols and references are the same as those used in Figure 4-3.. **Error! Bookmark not defined.**

Figure 4-5. Spider diagram showing trace element and REE data for SB samples, normalized to the Primitive Mantle (McDonough and Sun, 1995) and chondrite (Nakamura, 1974), respectively. The gray area indicates the compositional range of granodiorites from the GMS suite reported by Westraat et al. (2005) and Moyen et al. (2021). ..... **Error! Bookmark not defined.**

Figure 4-6. A) Representative cathodoluminescence images of zircon crystals from the coarse-grained granodiorite (sample SB02), with white circles marking analyzed areas along with their $^{207}Pb/^{206}Pb$ ages (Ma) and associated 2σ uncertainties. B) U-Pb concordia diagram for the coarse-grained granodiorite of the SB, not corrected for common Pb. The insert show the $^{207}Pb/^{206}Pb$ mean age of the concordant spots. MSWD: Mean Square Weighted Deviates..... **Error! Bookmark not defined.**

Figure 4-7. Tera-Wasserburg concordia diagram for titanite, showing a low intercept age of 3100 ± 11 Ma (uncorrected for ^{204}Pb). Insert: BSE image illustrating titanite crystals

analyzed. Ap: apatite; Kfs: K-feldspar; Mt: magnetite; Pl: plagioclase; Qz: quartz; Ttn: titanite. ..... **Error! Bookmark not defined.**

Figure 5-1. Representative U-Pb crystallization ages for the GMS suite delimitating the age range of the suite, shown with 2σ uncertainty bars. The literature ages are reported by Maphalala and Kröner (1993), Kamo and Davis (1994), Zeh et al. (2009), and Moyen et al. (2021). ..... **Error! Bookmark not defined.**

Figure 5-2. Schematic illustration of intra-crustal magma generation model during decompression of a previously thickened crust, based on Moyen et al. (2021b). Mantle upwelling and ascent of mafic magmas triggered localize crustal melting. The upward movement of magma to shallower levels was enabled by weak transcrustal structures. ..... **Error! Bookmark not defined.**

Abbreviations and nomenclature

ρ	Correlation coefficient between the isotopic ratios $^{206}Pb/^{238}U$ and $^{207}Pb/^{235}U$
$^{143}Nd/^{144}Nd_{(t)}$	Neodymium initial ratios
2σ	Two standard deviation
$^{87}Sr/^{86}Sr_{(t)}$	Strontium initial ratios
A/CNK	Molar Al/(2*Ca+Na+K)
A/NK	Molar Al/(Na+K)
Ab	Albite
AGC	Ancient Gneiss Complex
All	Allanite
Amph	Amphibole
An	Anorthite
An%	Anorthite percentage of feldspar
Ap	Apatite
apfu	Atoms per Formula Unit
$a SiO_2$	SiO_2 activity
$a TiO_2$	TiO_2 activity
BAC	Boesmanskop Alkaline Complex
BGB	Barberton Greenstone Belt
BGGT	Barberton Granite-Greenstone Terrane
BH	Boesmanskop Head pluton
BSE	Backscattered Electron
BT	Boesmanskop Tail pluton
Bt	Biotite
BuCoMO	Building Continents - From Mantle to Ore
ca.	*Circa* (approximately)
Ca-Amph	Calcium amphibole
CAF	Central Analytical Facilities
CL	Cathodoluminescence
Cpx	Clinopyroxene
e.g.	*Exempli gratia*
EDS	Energy Dispersive X-Ray Spectrometry
En	Enstatite
FeO_T	Total iron oxides ($FeO+Fe_2O_3$)
FE-SEM	Field Emission Scanning Electron Microscope
fO_2	Oxygen fugacity
Fs	Ferrosilite
GMS suite	Granodiorite-Monzogranite-Syenogranite suite
HFSE	High-Field-Strength Elements
HREE	Heavy Rare Earth Elements
ICP-MS	Inductively Coupled Plasma Mass Spectrometry
Ilm	Ilmenite
IRP	International Research Project
Kfs	K-feldspar
KZD	Kees Zyn Doorns
LILE	Large-ion Lithophile Elements
LREE	Light Rare Earth Elements
Mg#	Magnesium number
MREE	Middle Rare Earth Elements
MSWD	Mean square of weighted deviates
Mt	Magnetite
NKFMASH	Na_2O-K_2O-FeO–MgO–Al_2O_3–SiO_2-H_2O
NRF	National Research Foundation
NW	Northwest
Or	Orthoclase
Pl	Plagioclase
P-T-X	Pressure-Temperature-Composition
Q ICP-MS	Quadrupole Inductively Coupled Plasma Mass Spectrometry
Qz	Quartz
REE	Rare Earth Elements
s.s.	*Sensu stricto* (strict sense)
SARChI	South African Research Chairs Initiative
SCLM	Sub-continental lithospheric mantle
SEM	Scanning Electron Microscope
Ser	Sericite
SIFS	Saddleback-Inyoka Fault System
SB	Salisbury Kop batholith
TAS	Total Alkali-Silica diagram
TREE	Trace and Rare Earth Elements
TTG suite	Tonalite-Trondhjemite-Granodiorite suite
Ttn	Titanite
WDS	Wavelength dispersive X-ray Spectrometer
Wo	Wollastonite
WSZ	Welverdiend Shear Zone
Zrc	Zircon
Σ	Summation

Units

°C	Degree Celsius
cps	Counts per second
µm	Micrometer
cm	Centimetre
Ga	Billion years
Hz	Hertz
kbar	Kilobar
kbar	Kilobar
km	Kilometres
kV	Kilovolt
m	Meters
Ma	Million years
mm	Millimeter
nA	Nanoampere
nm	Nanometer
ppm	Parts per million
wt%	Weight percentage

Pedras sonhando pó na mina;
Pedras sonhando com britadeiras.
Cada ser tem sonhos à sua maneira.

Pedro Luis Teixeira De Oliveira and Luiz Filho

CHAPTER 1. INTRODUCTION

1.1. Definitions of Alkaline rocks

Alkaline rocks form a diverse group of both plutonic and volcanic varieties, characterized by a wide range of geochemical and textural characteristics. According to Shand (1943) alkaline rocks are characterized by a molecular ratio of Na + K that exceeds the available Al and Si in a proportion of 1:1:6, preventing all Na and K from being accommodated within feldspar. A widely applied classification system that divides igneous rocks into two categories - alkaline and subalkaline - based on the relationship between silica (SiO_2) content and total alkalis ($K_2O + Na_2O$) content is used in this research (e.g., Miyashiro, 1978). This classification is visually represented in the Total Alkalis vs Silica (TAS) diagram (e.g., Sørensen, 1974; Miyashiro, 1978; Fitton and Upton, 1987). According to this broader division, alkaline rocks include two main groups. The first group is silica-saturated peralkaline rocks, in which quartz may coexist with K-feldspar. The second group is silica-undersaturated types, which can be either peralkaline or metaluminous, that contain feldspathoids (e.g., Shand, 1943; Sørensen, 1974; Marks et al., 2011). Felsic silica-undersaturated alkaline rocks often are spatially and temporally associated with carbonatitic rocks. According to the IUGS classification, a rock is defined as carbonatitic if it contains more than 50% modal primary carbonate minerals and typically less than 20 wt% SiO_2 (Le Maitre, 2002). These rocks are considered to have a magmatic origin (sensu lato), commonly derived from mantle sources (Sørensen, 1974; Bailey, 1993).

Alkaline rocks are typically characterized by high concentrations of large-ion lithophile elements (LILE) and rare earth elements (REE). Most of the world's REE deposits are associated with alkaline and carbonatitic complexes, making them crucial to mineral resource exploration (e.g., Hou et al., 2015; Dostal, 2017; Hussain et al., 2020; Beard et al., 2023). Additionally, alkaline complexes are potential deposits of high-field strength elements (HFSE), fluorine, and phosphorus, further underscoring their economic importance (e.g., Vielreicher et al., 2000; Beard et al., 2023).

Accessory minerals play a fundamental role in controlling the trace elements and REE budget in their host rocks (e.g., Conceição et al., 1991; Sørensen, 1974; Duan et al., 2019; Bruand et al., 2020). In the metaluminous and peraluminous rocks, REE and HFSE can be accommodated in accessory minerals commonly found in sub-alkaline rocks (e.g., zircon, titanite, and Fe-Ti oxides). On the other hand, in peralkaline rocks, these trace elements are accommodated in exotic phases (e.g., eudialyte, aenigmatite, astrophyllite, wöhlerite) (Sørensen, 1974; Marks et al., 2011). Therefore, the chemical and isotopic characterization of these minerals is crucial for understanding the formation of evolved magmas with high

trace element concentrations (e.g., Rosa et al., 2001; Bea et al., 2013; Bruand et al., 2016; Bruand et al., 2020). Furthermore, alkaline rocks petrogenesis are indispensable for understanding Earth's thermal and geodynamic evolution, as they contain high concentrations of radioactive elements such as U, Th, and K (e.g., Sørensen, 1974; Marks et al., 2011; Mikkola et al., 2011).

1.2. Geodynamic settings of alkaline magmatism

Felsic alkaline magmatism is often linked to mantle-crust interactions, continental crust growth, and occurs in most geodynamic settings (e.g., Fitton and Upton, 1987; Blichert-Toft et al., 1996; Balashov and Glaznev, 2006). In subduction zones, high-K magmatism typically emerges when slab-derived fluids and melts metasomatize the mantle wedge, enriching it in potassium and other incompatible elements (e.g., Fitton and Upton, 1987). In post-collisional settings, crustal thickening followed by lithospheric delamination or convective removal of the lithospheric roots can trigger partial melting of metasomatized mantle domains, generating high-K melts (e.g., Bonin, 1998). Similarly, in continental rift and extensional settings, decompression melting of enriched lithospheric mantle sources can produce K-rich volcanic and plutonic rocks (e.g., Fitton and Upton, 1987; Blichert-Toft et al., 1996; Lauri et al., 2006). Despite the wide range of possible geodynamic configurations that give rise to alkaline magmas, these rocks are typically found in stable regions, with their ascent and emplacement often controlled by rift structures and zones of abrupt continental lithosphere thinning (e.g., Kogarko et al., 2006; Lauri et al., 2006; Mageswarii et al., 2024).

Possible sources for the alkali-rich magmas range from the lower mantle-core boundary (associated with hot spots) to shallow crustal depths (e.g., Courtillot et al., 2003; Tchameni et al., 2001; Lauri et al., 2006; Bea et al., 2014; Chagondah et al., 2023).

The mantle source hypothesis involves the fractional crystallization of alkali basaltic or tholeiitic magmas, with or without crustal assimilation, leading to the production of alkali-rich rocks (Fitton and Upton, 1987; Turner et al., 1992; Wickham et al., 1995). Another possibility is the low degree of partial melting of upper mantle peridotite under anhydrous conditions, influenced by mantle-derived halogens (Collins et al., 1982; Clemens et al., 1986). The crust source hypothesis focuses on low degrees of partial melting of granulites (Clemens et al., 1986; Whalen et al., 1987), melting of I-type tonalites (Patiño Douce, 1997), or melting of the lower crust metasomatized by mantle-derived fluids (Fitton and Upton, 1978; Taylor et al., 1980). The processes acting within the magma chamber (e.g., fractional crystallization, mineral accumulation and liquid immiscibility) may also play a significant role in producing alkaline rocks (e.g., Farina et al., 2012; Paterson et al., 2005; Rocher et al., 2018; Yu et al., 2023).

Understanding the origin, nature, and stabilization of Earth's first crustal segments requires thorough research, especially given the scarcity and overprinting of Archean remnants (e.g., Moyen et al., 2006; Anhaeusser, 2014; Kröner et al., 2016). A detailed study of plutonic alkaline rocks, including bulk rock analysis, isotopic compositions and mineral chemistry assessment can provide valuable insights into early crustal formation and the thermal and chemical conditions that influenced cratonic growth and stabilization (e.g., Anhaeusser et al., 1983; Clemens et al., 2010; Laurent et al., 2014; Moyen et al., 2021).

1.3. The Onset of High-K Magmatism on Earth

The Zimbabwe and Kaapvaal Cratons in southern Africa and the Pilbara and Yilgarn Cratons in Australia host some of the oldest remnants of the Archean Eon, attracting many researchers investigating early Earth processes (e.g., Nelson et al., 1999; Cavosie et al., 2007; Anhaeusser, 2014; Van Kranendonk et al., 2014; Kröner et al., 2016; Robb et al., 2021). Archean crustal fragments can be summarized as three major rock groups: (i) greenstone belts composed of supracrustal metamorphosed volcanic and sedimentary rocks, typically metamorphosed under greenschist to amphibolite facies conditions (e.g., Laurent et al., 2014; Anhaeusser, 2014). (ii) gray gneisses, which are a complex and deformed assemblage of metamorphosed sedimentary and igneous rocks, mainly composed of granitoid gneisses from the Tonalite - Trondhjemite - Granodiorite (TTG) suite, which might be the dominant granitoid in the Archean crust (e.g., Moyen et al., 2019). (iii) Late-stage high-K granitoid plutons, intrusive into the older gray gneisses and greenstone belts (e.g., Laurent et al., 2014; Moyen et al., 2019; Robb et al., 2006).

Some researchers suggest that the compositional transition from Archean sodic TTGs to regionally extensive granites (*sensu stricto*) marks the stabilization of cratons and the establishment of modern-style plate tectonics (e.g., Blichert-Toft et al., 1995; Schoene et al., 2008, 2009; Farina et al., 2015 Howarth et al., 2019; Moyen et al., 2019). The transition from low-K to high-K magmatism in a given region can also signal shifts from juvenile crust formation to reworking of older continental lithosphere (e.g., Laurent et al., 2014). This transition is diachronous, occurring between 3.1 and 2.5 Ga across different cratons, generally about 500 Ma after the formation of the oldest associated TTG suite rocks (e.g., Peucat et al., 1993; Robb et al., 2006; Moyen et al., 2019). The Barberton Granite-Greenstone Terrane (BGGT) in the Eastern Kaapvaal Craton registers this shift earlier than most cratons and contains well-preserved, diverse high-K rocks, making it an ideal unit for studying the evolution of early cratonic nuclei (e.g., Lowe and Byerly, 2007; Anhaeusser, 2014; Agangi et al., 2018; Moyen et al., 2021).

1.4. Archean alkaline rocks

Records of alkaline complexes are rare in the Archean geological record, in contrast to the more commonly preserved TTG suites and greenstone terranes, especially those older than 2.7 Ga (e.g., Blichert-Toft et al., 1995; Kogarko et al., 2006). This scarcity may be due to their destruction by later tectonic-thermal processes or because likely higher Archean mantle temperatures were unfavorable for producing alkaline magmatism (e.g., Blichert-Toft et al., 1996).

Syenites are classical examples of K-rich plutonic rocks. The compilation of ages of syenitic magmatism (which includes syenites, monzonites, and foid-bearing analogs) by Balashov and Glaznev (2006) illustrates the increase in the number of occurrences from the Late Archean to the Phanerozoic. These authors identified significant peaks in syenitic magmatism at three points of geological time: 2680 Ma, 2040 Ma, and 1120 Ma, as illustrated in Figure 1-1. The oldest syenitic magmatism is recorded at ca. 3105 Ma syenites and quartz monzonites in the Kaapvaal Craton (Kamo and Davis, 1994) and ca. 3048 Ma trachyte tuffs in the Pilbara Craton (Nelson et al., 1999; Balashov and Glaznev, 2006).

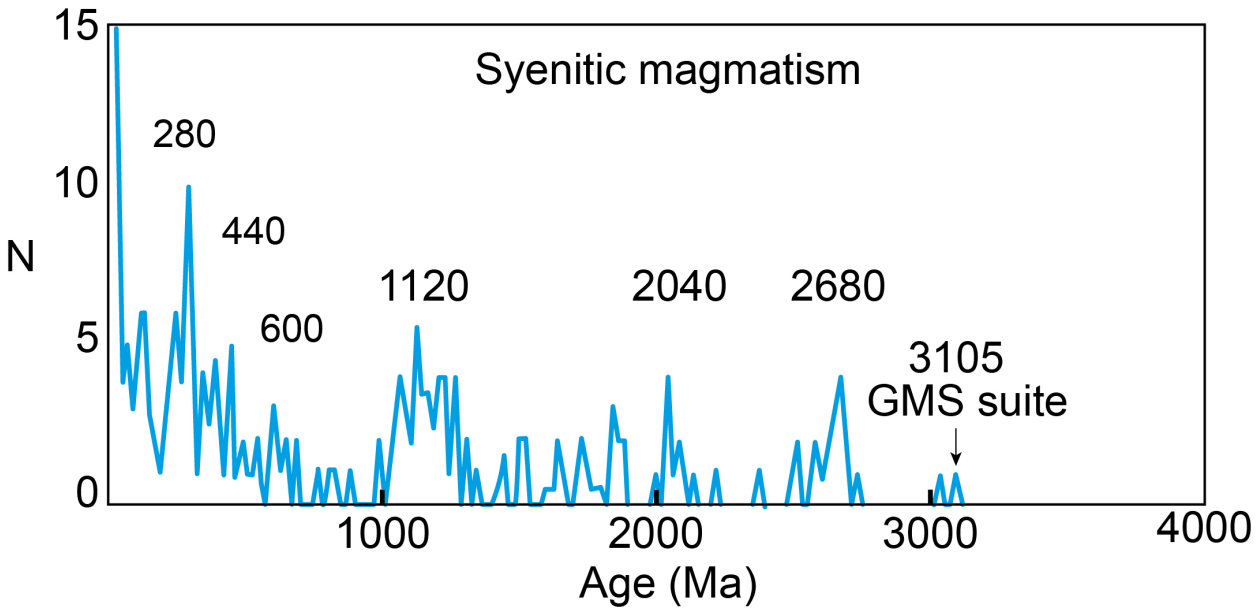

Figure 1-1. Evolution of syenitic magmatism. The averaging step is 20 Ma and N is the number of dates in the compilation (Balashov and Glaznev, 2006). GMS: Granodiorite-Monzogranite-Syenogranite suite.

1.5. Alkaline complexes in the Kaapvaal Craton

The Kaapvaal Craton hosts well-preserved Meso to Neoarchean rocks, including the world's oldest recorded syenites and well-known alkaline complexes, many of which are associated with shear zone structures (Figure 1-2) (e.g., Kamo and Davis, 1994; Vielreicher et al., 2000). The Paleoproterozoic Schiel Alkaline Complex (2060 - 2050 Ma, Graupner et al., 2018; Laurent and Zeh, 2015), found in the southern portion of the Limpopo Belt is a small alkaline complex consisting mainly of nepheline syenites and pyroxenites (Höss et al., 2024). Radiogenic isotope signatures (positive εNd and εHf values) reported for

the cogenetic pyroxenites and gabbros have been interpreted as evidence of a mantle source (Höss et al., 2024).

The Phalaborwa and Pilanesberg complexes occur adjacent to the Thabazimbi-Murchison Lineament, a major crustal-scale shear zone (Good and de Wit, 1997). The ca. 2060 Ma Phalaborwa Complex (e.g., Wu et al., 2011) is a carbonatite-alkaline concentrically zoned complex famous for its economic resources such as copper and phosphates intrusive into Archean gneisses at the eastern edge of the Kaapvaal Craton (e.g., Vielreicher et al., 2000). It consists predominantly of clinopyroxenites, syenites and carbonatites derived from decompression melting of metasomatized mantle (e.g., Wu et al., 2011; Vielreicher et al., 2000).

The Pilanesberg Complex located in the western Bushveld region is one of the largest known alkaline ring complexes and includes volcanic (e.g., trachytes and phonolites) and intrusive rocks, such as syenites and nepheline syenites (Elburg et al., 2017). Its age (1395+10/−11 Ma) suggests emplacement in an intraplate setting, Sr isotopes and trace-element patterns, without Nb anomalies indicate mantle-derived parental magmas (Elburg et al., 2017).

The ca. 3105 Ma Boesmanskop Alkaline Complex (BAC) located at the southwestern portion of the Barberton Greenstone Belt (BGB) is submitted to the Barberton lineament (Kamo and Davis, 1994). The BAC consists of three plutons composed of syenites, quartz monzonites and leucogranites. These plutons intrude both the surrounding greenstones and the 3500–3400 Ma TTG gneisses (Anhaeusser et al., 1983). The BAC rocks exhibit several geochemical and petrological features that cast doubt on their source and origin. They are Si-saturated, display both positive and negative εNd values, and notably lack feldspathoids, carbonatitic and mafic cogenetic rocks (e.g., Anhaeusser et al., 1983; Yearron, 2003), which are key indicators of direct mantle input. These characteristics suggest a larger contribution of crustal material to the BAC source compared to the other alkaline complexes in the Kaapvaal Craton (e.g., Anhaeusser et al., 1983; Yearron, 2003; Moyen et al., 2021).

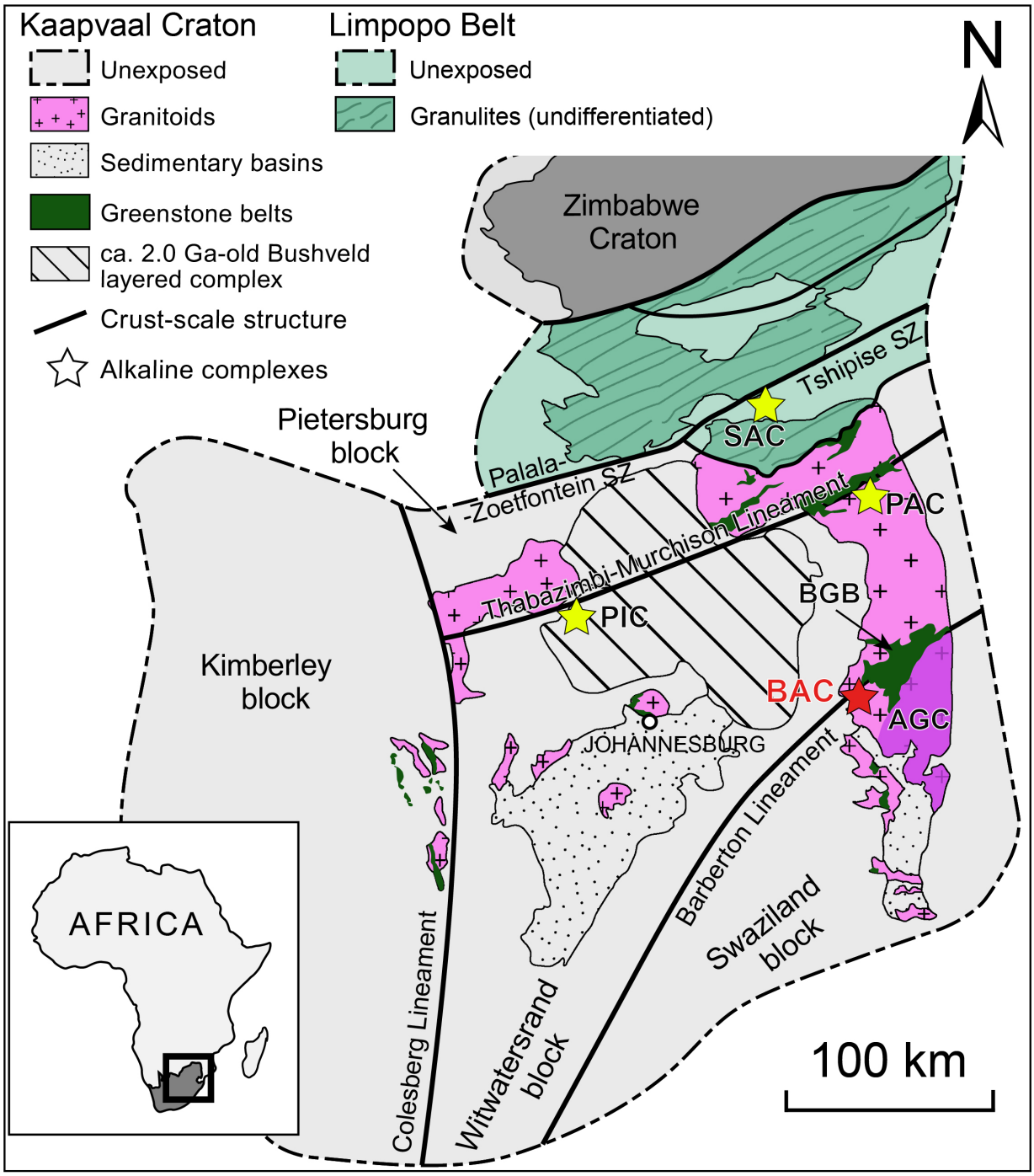

Figure 1-2. Geological setting of the Kaapvaal craton, South Africa and adjacent Limpopo Belt (after Eglington and Armstrong, 2004 and Laurent et al., 2014), showing the major structures and the location of relevant alkaline complexes. AGC: Ancient Gneiss Complex; BAC: Boesmanskop Alkaline Complex; BGB: Barberton Greenstone Belt; PAC: Phalaborwa Complex; PIC: Pilanesberg Complex; SAC: Schiel Alkaline Complex; SZ: Shear zone.

1.6. Local Geology Overview

1.6.1. Basement

The Ancient Gneiss Complex (ACG) is located at the south and southeast of the BGB, eastern portion of the Kaapvaal Craton. The ACG is a complex deformed and metamorphism terrane composed of ca. 3.68–3.55 Ga TTG gneisses (e.g., Compston and Kröner, 1988; Zeh et al., 2011). The 3.6 Ga rocks

register reworking of early-formed crust (T_{DM}Hf of 3.77-4.08 Ga; Zeh et al., 2011), followed by magmatic events at 3.54, 3.45, and 3.32 Ga which introduced juvenile material, whereas later reworking at 3.23, 3.1, and 2.7 Ga occurred without significant juvenile input (Zeh et al., 2011).

The BGB greenstones, dating from 3550 to 3220 Ma, are typically divided into three lithostratigraphic groups: Onverwacht, Fig Tree, and Moodies (e.g., Lowe and Byerly, 2007; Heubeck et al., 2022). The Onverwacht Group (3550 - 3280 Ma) comprises ultramafic to mafic successions and felsic volcanoclastic units (Kröner et al., 1996; Kohler and Anhaeusser, 2002; Kröner et al., 2016). The Fig Tree Group (3259 - 3225 Ma) is composed of clastic and volcanoclastic sediments, the Moodies Group (< 3220 Ma) is a sequence of sandstones, and polymict conglomerate (e.g., Kröner et al., 1996; Kohler and Anhausser, 2002).

The greenstone sequences of the BGB are intruded by a contemporaneous suite of TTGs (e.g., Anhaeusser and Robb, 1983; Kamo and Davis, 1994; Moyen et al., 2019). The TTG-greenstone basement was subsequently intruded by voluminous K-rich alkaline plutons at ca. 3105 ± 10 Ma, termed Granodiorite-Monzogranite-Syenogranite (GMS) suite (e.g., Anhaeusser and Robb, 1983; Kamo and Davis, 1994; Yearron, 2003; Clemens et al., 2010; Laurent et al., 2014).

1.6.2. TTG suite

The oldest TTG pluton in the region is the Steynsdorp pluton (3550 - 3500 Ma), while most Na-rich plutons were generated during two major magmatic events at ca. 3450 Ma and 3290 - 3210 Ma (Kamo and Davis, 1994; Kröner et al., 1996), associated with the main NW-SE crustal shortening and subsequent NE-SW extension during the proto-Kaapvaal craton assembly (e.g., de Ronde and de Wit, 1994; Kröner et al., 1996; Kisters et al., 2003; Westraat et al., 2005).

The earliest expression of the shift from Na- to K-dominated magmatism in the BGGT is represented by the Dalmein pluton and the Usutu Suite (Anhaeusser et al., 1983). The Dalmein pluton (3215 ± 2 Ma) is composed predominantly of porphyritic granodiorite, intrusive into 3450 Ma TTG gneiss and lithologies of the southern BGB. Although the Dalmein pluton shares textural and chemical similarities with the GMS suite - such as LREE enrichment relative to HREE and the absence of Eu anomalies (e.g., Yearron, 2003), which agrees with the idea of Moyen et al. (2011) that granodiorites, potassic rocks, should be distinguished from the tonalite and trondhjemite (conventional Archean sodic granitoids) - its older age has led some studies to classify it as the most differentiated phase of the TTG suite (e.g., Kamo and Davis, 1994; Robb et al., 2006). The ca. 3.23 Ga Usutu Suite within the Ancient Gneiss Complex comprises coarse-grained granodiorites, gabbros, and diorites (e.g., Kamo and Davis, 1994; Schoene and Bowring, 2010).

1.6.3. GMS suite

The GMS suite includes granites, quartz monzonite, granodiorites, and smaller volumes of syenites, representing shallow-crustal laccoliths, often occurring as batholiths with massive cores and sheeted rims (Westraat et al., 2005; Clemens et al., 2010). Internally, these plutons are texturally and geochemically heterogeneous (e.g., Clemens et al., 2010; Moyen et al., 2021; Robb et al., 2021). These mostly undeformed plutons have sharp contacts with the TTG suite and greenstone basement (e.g., Belcher and Kisters, 2006; Robb et al., 2006; Moyen et al., 2021).

The south of the GMS suite is covered by volcano-sedimentary sequences of the Pongola supergroup, which exhibits intracratonic characteristics (e.g., Wilson and Zeh, 2018). The maximum depositional ages of 3074 ± 12 Ma reported for sandstones of the Nsuze Group containing the lower formations of the Pongola supergroup and brittle intrusion of dolerite dykes ca. 2.98 Ga suggests that the GMS suite represents the final stages of Kaapvaal Craton stabilization (e.g., Anhaeusser et al., 1983; Wilson and Zeh, 2018). The GMS suite and Pongola supergroup are intruded by discrete granitic plutons with North-South alignment and emplaced predominantly between 2830 Ma and 2720 Ma, known as post-Pongola Granites (e.g., Robb et al., 2006; Robb et al., 2021).

Although some GMS intrusions such as the Mpuluzi and Heereveen batholiths have been studied in detail (e.g., Westraat et al., 2005; Clemens et al., 2010; Moyen et al., 2021), other intrusions such as the Pigg's Peak batholith, Salisbury Kop batholith, and Boesmanskop Alkaline Complex, remain under-investigated. This lack of data hinders a complete understanding of the regional geodynamic conditions during the stabilization of the Kaapvaal craton. Thus, this study focuses on Mesoarchean high-K alkaline rocks of the ca. 3105 Ma Boesmanskop Alkaline Complex (BAC) and ca. 3109 Ma Salisbury Kop batholith (SB) (e.g., Kamo and Davis, 1994; Moyen et al., 2021), to unravel their petrogenesis and contribute to the understanding of crustal differentiation processes and the stabilization of the local crust.

1.7. Objectives

The main objective of this research is to investigate the magmatic processes responsible for generating the K_2O and incompatible elements enriched magmatism that produced the BAC and SB Mesoarchean rocks. Thus, this research examines the petrography, mineral chemistry, U-Pb zircon dating, and Rb-Sr, Sm-Nd isotopic compositions of the Boesmanskop Alkaline Complex, with a focus on the syenites and quartz monzonites. Phase equilibrium modeling experiments were conducted under upper-crust conditions to assess the hypothesis proposed based on the dataset obtained. This study also

investigates the petrography, mineral chemistry, whole-rock compositions, and U-Pb zircon dating of the granites and granodiorites of the Salisbury Kop batholith, coeval to the syenites. The data collected allowed me to reassess previously proposed ideas about the GMS suite origin and introduce new ideas about the magmatic processes responsible for producing the ca. 3105 Ma alkaline rocks. To achieve the main objective, several steps were followed:

i. Compilation of data available in the literature for the GMS rocks and their basement;
ii. Mapping of lithological relationships, field descriptions and sample collection in the Boesmanskop Alkaline Complex and Salisbury Kop batholith;
iii. Petrographic description of sampled rocks;
iv. Whole-rock compositional analysis, including major, trace, and REE elements;
v. Rb-Sr and Sm-Nd isotope analysis of representative rocks in the BAC;
vi. Characterization of accessory minerals textures and their major, trace and REE compositions;
vii. U-Pb zircon and titanite geochronological dating;
viii. Phase equilibrium modeling to test the proposed petrogenetic hypothesis;

1.8. Structure of the Thesis

This thesis comprises six chapters. The first chapter introduces the research topic, provides an overview of the local geology, and outlines the research objectives. Chapter 2 presents a research paper covering the main features of the BAC rocks, submitted to *Lithos*, which is undergoing peer review. Chapter 3 presents a research paper tackling the mineral chemistry of BAC rocks to refine the models proposed in Chapter 2. This manuscript was submitted to the *Journal of Petrology*, which is undergoing peer review. Chapter 4 is a research paper manuscript regarding the main petrographic and geochemical features of the SB rocks and is in preparation for submission to the *South African Journal of Geology*. Chapter 5 presents the general conclusions drawn from the entire dataset produced in this research. Chapter 6 provides the supplementary data produced in this study.

1.9. References - Chapter 1

1. Agangi, A., Hofmann, A., and Elburg, M.A., 2018. A review of Palaeoarchaean felsic volcanism in the eastern Kaapvaal craton: Linking plutonic and volcanic records. *Geoscience Frontiers*, *9(3)*, 667-688. https://doi.org/10.1016/j.gsf.2017.08.003

2. Anhaeusser, C.R., 2014. Archaean greenstone belts and associated granitic rocks–a review. *Journal of African Earth Sciences*, *100*, 684-732. https://doi.org/10.1016/j.jafrearsci.2014.07.019

3. Anhaeusser, C.R., and Robb, L.J., 1983. Geological and geochemical characteristics of the Heerenveen and Mpuluzi batholiths south of the Barberton greenstone belt and preliminary thoughts on their petrogenesis. In: Anhaeusser, C.R.

(Ed.), Contributions to the Geology of the Barberton Mountain Land. *Geological Society of South Africa Special Publication, 9*, 131-152.

4. Anhaeusser, C.R., Robb, L.J., and Barton, J.M., 1983, Mineralogy, petrology and origin of the Boesmanskop Syenite-Granite complex, Barberton Mountain Land, South Africa*, Geological Society of South Africa, Special Publication, 9*, 169-183.

5. Bailey, D.K., 1993. Carbonate magmas. Journal of the Geological Society of London, 150(4), 637-651. https://doi.org/10.1144/gsjgs.150.4.0637

6. Balashov, Y.A., and Glaznev, V.N., 2006. Cycles of alkaline magmatism. *Geochemistry International*, *44*, 274-285. https://doi.org/10.1134/S0016702906030050

7. Bea, F., Montero, P., Haissen, F., and El Archi, A., 2013. 2.46 Ga kalsilite and nepheline syenites from the Awsard pluton, Reguibat Rise of the West African Craton, Morocco. Generation of extremely K-rich magmas at the Archean–Proterozoic transition. Precambrian Research, 224, 242-254. https://doi.org/10.1016/j.precamres.2012.09.024

8. Bea, F., Montero, P., Haissen, F., Rjimati, E., Molina, J.F., and Scarrow, J.H., 2014. Kalsilite-bearing plutonic rocks: The deep-seated Archean Awsard massif of the Reguibat Rise, South Morocco, West African Craton. *Earth-Science Reviews*, *138*, 1-24. https://doi.org/10.1016/j.earscirev.2014.08.003

9. Beard, C.D., Goodenough, K.M., Borst, A.M., Wall, F., Siegfried, P.R., Deady, E.A., Pohl, C., Hutchison, W., Finch, A.A., Walter, B.F., Elliott, H.A.L., and Brauch, K., 2023. Alkaline-silicate REE-HFSE systems. Economic Geology, 118(1), 177-208. https://doi.org/10.5382/econgeo.4956

10. Belcher, R.W., and Kisters, A.F.M., 2006. Syntectonic emplacement and deformation of the Heerenveen batholith: conjectures on the structural setting of the 3.1 Ga granite magmatism in the Barberton granite-greenstone terrain, South Africa. *Geological Society of America, Special Publication, 405,* 211–231. https://doi.org/10.1130/2006.2405(12)

11. Blichert-Toft, J., Arndt, N.T., and Ludden, J.N., 1996. Precambrian alkaline magmatism. *Lithos*, *37*(2-3), 97-111. https://doi.org/10.1016/0024-4937(95)00031-3

12. Blichert-Toft, J., Rosing, M.T., Lesher, C.E., Chauvel, C., 1995. Geochemical constraints on the origin of the late Archean Skjoldungen alkaline igneous province, SE Greenland. Journal of Petrology, 36(2), 515-561. https://doi.org/10.1093/petrology/36.2.515

13. Bonin, B., Azzouni-Sekkal, A., Bussy, F., and Ferrag, S., 1998. Alkali-calcic and alkaline post-orogenic (PO) granite magmatism: petrologic constraints and geodynamic settings. Lithos, 45(1-4), 45-70.https://doi.org/10.1016/S0024-4937(98)00025-5

14. Bruand, E., Fowler, M., Storey, C., Laurent, O., Antoine, C., Guitreau, M., Heilimo, E., and Nebel, O., 2020. Accessory mineral constraints on crustal evolution: elemental fingerprints for magma discrimination. Geochemical Perspectives Letters, 13, 7-12. https://doi.org/10.7185/geochemlet.2006

15. Bruand, E., Storey, C., and Fowler, M., 2016. An apatite for progress: Inclusions in zircon and titanite constrain petrogenesis and provenance. Geology, 44(2), 91-4. https://doi.org/10.1130/G37301.1

16. Cavosie, A.J., Valley, J.W., and Wilde, S.A., 2007. The oldest terrestrial mineral record: a review of 4400 to 4000 Ma detrital zircons from Jack Hills, Western Australia. *Developments in Precambrian Geology, 15*, 91-111. https://doi.org/10.1016/S0166-2635(07)15025-8

17. Chagondah, G.S., Hofmann, A., Elburg, M.A., Iaccheri, L.M., Kramers, J.D., and Wilson, A.H., 2023. Petrogenesis of potassic granite suites along the southern margin of the Zimbabwe Craton. *South African Journal of Geology 2023*, *126(1)*, 1-28. https://doi.org/10.25131/sajg.126.0004

18. Clemens J.D., Holloway J.R., and White A.J.R., 1986. Origin of an A-type granite: experimental constraints. *American Mineralogist, 71*, 317–324.

19. Clemens, J.D., Belcher, R.W., and Kisters, A.F., 2010. The Heerenveen batholith, Barberton Mountain Land, South Africa: Mesoarchaean, potassic, felsic magmas formed by melting of an ancient subduction complex. *Journal of Petrology, 51(5)*, 1099-1120. https://doi.org/10.1093/petrology/egq014

20. Collins W.J., Beams S.D., White A.J.R., and Chappell B.W., 1982. Nature and origin of A-type granites with particular reference to southeastern Australia. *Contributions to Mineralogy and Petrology, 80*, 189-200. https://doi.org/10.1007/BF00374895

21. Compston, W., and Kröner, A., 1988. Multiple zircon growth within early Archaean tonalitic gneiss from the Ancient Gneiss Complex, Swaziland. *Earth and Planetary Science Letters, 87(1-2)*, 13-28. https://doi.org/10.1016/0012-821X(88)90061-1

22. Conceição, H., Sabaté, P., and Bonin, B., 1991. The Itiúba alkaline syenite massif, Bahia State (Brazil): mineralogical, geochemical and petrological constraints - relation to the genesis of rapakivi magmatism. Precambrian Research, 51(1-4), 283-314. https://doi.org/10.1016/0301-9268(91)90105-J

23. Courtillot, V., Davaille, A., Besse, J., and Stock, J., 2003. Three distinct types of hotspots in the Earth's mantle. *Earth and Planetary Science Letters, 205(3-4)*, 295-308. https://doi.org/10.1016/S0012-821X(02)01048-8

24. De Ronde, C.E., and de Wit, M.J., 1994. Tectonic history of the Barberton greenstone belt, South Africa: 490 million years of Archean crustal evolution. Tectonics, 13(4), 983-1005. https://doi.org/10.1029/94TC00353

25. Dostal, J., 2017. Rare earth element deposits of alkaline igneous rocks. Resources, 6(3), 34. https://doi.org/10.3390/resources6030034https://doi.org/10.3390/resources6030034

26. Duan, X.X., Chen, B., Sun, K.K., Wang, Z.Q., Yan, X., and Zhang, Z., 2019. Accessory mineral chemistry as a monitor of petrogenetic and metallogenetic processes: a comparative study of zircon and apatite from Wushan Cu-and Zhuxiling W (Mo)-mineralization-related granitoids. Ore Geology Reviews, 111, 102940. https://doi.org/10.1016/j.oregeorev.2019.102940

27. Eglington, B.M., and Armstrong, R.A., 2004. The Kaapvaal Craton and adjacent orogens, southern Africa: a geochronological database and overview of the geological development of the craton. South African Journal of Geology, 107(1-2), 13-32. https://doi.org/10.2113/107.1-2.13

28. Elburg, M.A., and Cawthorn, R.G., 2017. Source and evolution of the alkaline Pilanesberg Complex, South Africa. Chemical Geology, 455, 148-165. https://doi.org/10.1016/j.chemgeo.2016.10.007

29. Farina, F., Albert, C., and Lana, C., 2015. The Neoarchean transition between medium-and high-K granitoids: Clues from the Southern São Francisco Craton (Brazil). Precambrian Research, 266, 375-394.http://dx.doi.org/10.1016/j.precamres.2015.05.038

30. Fitton, J.G., and Upton, B.G., 1987. Alkaline igneous rocks. *Geological Society, London, special publications, 30,* 568.

31. Good, N., and De Wit, M. J., 1997. The Thabazimbi-Murchison lineament of the Kaapvaal craton, South Africa: 2700 Ma of episodic deformation. Journal of the Geological Society, 154(1), 93-97. https://doi.org/10.1144/gsjgs.154.1.009

32. Graupner, T., Klemd, R., Henjes-Kunst, F., Goldmann, S., Behnsen, H., Gerdes, A., Dohrmann, R., Barton Jr., J.M., and Opperman, R., 2018. Formation conditions and REY enrichment of the 2060 Ma phosphorus mineralization at Schiel (South Africa): geochemical and geochronological constraints. Mineralium Deposita, 53, 1117-1142. https://doi.org/10.1007/s00126-018-0791-7

33. Heubeck, C., Drabon, N., Byerly, G., Leisgang, I., Linnemann, U., Lowe, D., Mertz-Kraus, R., Gonzalez-Pinzon, A., Thomsen, T.B., Zeh, A., Rojas-Agramonte, Y., and Kröner, A., 2022. Detrital zircon provenance of the Archean Moodies Group, Barberton Greenstone Belt, South Africa and Eswatini. American Journal of Science, *322(2)*, 65-107. https://doi.org/10.2475/02.2022.01

34. Höss, A., Klemd, R., Bolhar, R., Haase, K. M., Ramos, J., Geiger, E., Brandt, S., Graupner, T., 2024. Magmatic evolution of the Schiel Alkaline Complex, Bushveld large igneous province, South Africa. Lithos, 466, 107464. https://doi.org/10.1016/j.lithos.2023.107464

35. Hou, Z., Liu, Y., Tian, S., Yang, Z., and Xie, Y., 2015. Formation of carbonatite-related giant rare-earth-element deposits by the recycling of marine sediments. Scientific reports, 5(1), 10231. https://doi.org/10.1038/srep10231

36. Howarth, G.H., Moore, A.E., Harris, C., van der Meer, Q.H.A., and le Roux, P., 2019. Crustal versus mantle origin of carbonate xenoliths from Kimberley region kimberlites using C-O-Sr-Nd-Pb isotopes and trace element abundances. *Geochimica et Cosmochimica Acta 266(1),* 258-273. https://doi.org/10.1016/j.gca.2019.03.026

37. Hussain, A., Zhao, K-D., Arif, M., Palmer, M.R., Chen, W., Zhang, Q., Li, Q., Jiang, S., and Girei, M.B., 2020. Geochronology, mineral chemistry and genesis of REE mineralization in alkaline rocks from the Kohistan Island Arc, Pakistan. Ore Geology Reviews, 126, 103749. https://doi.org/10.1016/j.oregeorev.2020.103749

38. Kamo, S.L., and Davis, D.W., 1994. Reassessment of Archaean crustal development in the Barberton mountain land, South Africa, based on U-Pb dating. *Tectonics, 13(1)*, 167-192. https://doi.org/10.1029/93TC02254

39. Kisters, A.F., Stevens, G., Dziggel, and A. Armstrong, R.A., 2003. Extensional detachment faulting and core-complex formation in the southern Barberton granite–greenstone terrain, South Africa: evidence for a 3.2 Ga orogenic collapse. *Precambrian Research*, *127(4)*, 355-378. https://doi.org/10.1016/j.precamres.2003.08.002

40. Kogarko, L.N., 2006. Alkaline magmatism and enriched mantle reservoirs: Mechanisms, time, and depth of formation. *Geochemistry International*, *44*, 3-10. https://doi.org/10.1134/S0016702906010022

41. Kohler, E.A., and Anhaeusser, C.R., 2002. Geology and geodynamic setting of Archaean silicic metavolcaniclastic rocks of the Bien Venue Formation, Fig Tree Group, northeast Barberton greenstone belt, South Africa. *Precambrian Research, 116(3-4)*, 199-235. https://doi.org/10.1016/S0301-9268(02)00021-9

42. Kröner, A., Anhaeusser, C.R., Hoffmann, J.E., Wong, J., Geng, H., Hegner, E., Xie, H., Yang, J. and Liu, D., 2016. Chronology of the oldest supracrustal sequences in the Palaeoarchaean Barberton Greenstone Belt, South Africa and Swaziland. *Precambrian Research*, *279*, 123-143. https://doi.org/10.1016/j.precamres.2016.04.007

43. Kröner, A., Hegner, E., Wendt, J.I., and Byerly, G.R., 1996. The oldest part of the Barberton granitoid-greenstone terrain, South Africa: evidence for crust formation between 3.5 and 3.7 Ga. *Precambrian Research, 78(1-3)*, 105-124. https://doi.org/10.1016/0301-9268(95)00072-0

44. Laurent, O., and Zeh, A., 2015 A linear Hf isotope-age array despite different granitoid sources and complex Archean geodynamics: example from the Pietersburg block (South Africa). Earth and Planetary Science Letters, 430, 326–338. https://doi.org/10.1016/j.epsl.2015.08.028

45. Laurent, O., Martin, H., Moyen, J.F., and Doucelance, R., 2014. The diversity and evolution of late-Archean granitoids: Evidence for the onset of "modern-style" plate tectonics between 3.0 and 2.5 Ga. *Lithos*, *205*, 208-235. https://doi.org/10.1016/j.lithos.2014.06.012

46. Lauri, L.S., Rämö, O.T., Huhma, H., Mänttäri, I., and Räsänen, J., 2006. Petrogenesis of silicic magmatism related to the∼ 2.44 Ga rifting of Archean crust in Koillismaa, eastern Finland. *Lithos*, *86(1-2)*, 137-166. https://doi.org/10.1016/j.lithos.2005.03.016

47. Le Maitre, R.W., Streckeisen, A., Zanettin, B., Le Bas, M.J., Bonin, B., and Bateman, P., 2002. Igneous rocks: a classification and glossary of terms. Cambridge University Press, Cambridge, U.K. 236 pp.

48. Lowe, D.R., and Byerly, G.R., 2007. An overview of the geology of the Barberton Greenstone Belt and vicinity: implications for early crustal development. *Developments in Precambrian geology, 15*, 481-526. 10.1130/0091-7613(1994)022<1099:ahotab>2.3.co;2

49. Mageswarii, G., Mishra, M., Srivastava, V., Srivastava, H.B., Satyanarayanan, M., and Shrivastava, J.P., 2024. Palaeoproterozoic rift-related alkaline magmatism in Bari area, Son valley, Central India. *Geosystems and Geoenvironment, 3(1),* 100222.

50. Marks, M.A., Hettmann, K., Schilling, J., Frost, B. R., and Markl, G., 2011. The mineralogical diversity of alkaline igneous rocks: critical factors for the transition from miaskitic to agpaitic phase assemblages. *Journal of Petrology, 52(3),* 439-455. https://doi.org/10.1093/petrology/egq086

51. Mikkola, P., Salminen, P., Torppa, A., and Huhma, H., 2011. The 2.74 Ga Likamännikkö complex in Suomussalmi, East Finland: lost between sanukitoids and truly alkaline rocks? *Lithos, 125(1-2),* 716-728. https://doi.org/10.1016/j.lithos.2011.04.002

52. Moyen, J.F., 2011. The composite Archaean grey gneisses: petrological significance, and evidence for a non-unique tectonic setting for Archaean crustal growth. Lithos, 123(1-4), 21-36. https://doi.org/10.1016/j.lithos.2010.09.015

53. Moyen, J.F., Stevens, G., and Kisters, A.F.M, 2006. Record of mid-Archaean subduction from metamorphism in the Barberton terrain, South Africa. *Nature*, *442(7102)*, 559-562. https://doi.org/10.1038/nature04972

54. Moyen, J.F., Stevens, G., Kisters, A.F.M., Belcher, R.W., and Lemirre, B., 2019. TTG Plutons of the Barberton Granitoid-Greenstone Terrain, South Africa. *Developments in Precambrian Geology, 15*, 607-667. https://doi.org/10.1016/S0166-2635(07)15056-8

55. Moyen, J.F., Zeh, A., Cuney, M., Dziggel, A., and Carrouée, S., 2021. The multiple ways of recycling Archaean crust: A case study from the ca. 3.1 Ga granitoids from the Barberton Greenstone Belt, South Africa. *Precambrian Research, 353,* 105998. https://doi.org/10.1016/j.precamres.2020.105998

56. Nelson, D.R., Trendall, A.F., and Altermann, W., 1999. Chronological correlations between the Pilbara and Kaapvaal cratons. *Precambrian Research*, *97*(3-4), 165-189. https://doi.org/10.1016/S0301-9268(99)00031-5
57. Patiño Douce, A.E., 1997. Generation of metaluminous A-type granites by low-pressure melting of calc-alkaline granitoids. Geology, 25(8), 743-746. https://doi.org/10.1130/0091-7613(1997)025<0743:GOMATG>2.3.CO;2

58. Peucat, J.J., Mahabaleswar, B., Jayananda, M., 1993. Age of younger tonalitic magmatism and granulitic metamorphism in the South Indian transition zone (Krishnagiri area); comparison with older Peninsular gneisses from the Gorur–Hassan area. *Journal of Metamorphic Geology, 11(6)*, 879-88. https://doi.org/10.1111/j.1525-1314.1993.tb00197.x

59. Robb, L.J., Brandl, G., Anhaeusser, C.R., Poujol, M., Johnson, M.R., and Thomas, R.J., 2006. Archaean granitoid intrusions. In: Johnson, M.R., Anhaeusser, C.R., Thomas, R.J. (Eds.), *The Geology of South Africa*, 57-94.

60. Robb, L.J., Meyer, F.M., Hawkesworth, C.J., and Gardiner, N.J., 2021. Petrogenesis of Archaean granites in the Barberton region of South Africa as a guide to early crustal evolution. *South African Journal of Geology*, *124(1)*, 111-140. https://doi.org/10.25131/sajg.124.0021

61. Rosa, M.L.S., Conceição, H., Leal, L.R., Macamibra, M.J., Scheller, T., and Martin, H., 2001. Idade Pb-Pb e assinatura isotopica Rb-Sr e Sm-Nd do magmatismo sienitico paleoproterozoico no sul do Cinturão movel Salvador- Curaçá: Maciço Sienitico de São Felix, Bahia. *Revista Brasileira de Geociencias, 1*, 31.

62. Schoene, B., de Wit, M. J., Bowring, S.A., 2008. Mesoarchean assembly and stabilization of the eastern Kaapvaal craton: A structural-thermochronological perspective. *Tectonics, 27(5)*. https://doi.org/10.1029/2008TC002267

63. Schoene, B., Dudas, F.O., Bowring, S.A., and De Wit, M., 2009. Sm–Nd isotopic mapping of lithospheric growth and stabilization in the eastern Kaapvaal craton. *Terra Nova, 21(3)*, 219-228. https://doi.org/10.1111/j.1365-3121.2009.00877.x

64. Sørensen, H., 1974. The Alkaline Rocks. *Cambridge University Press, London*, 622. https://doi.org/10.1017/S0016756800045994

65. Taylor, R.P., Strong, D.F., and Kean, B.F., 1980. The Topsails igneous complex: Silurian – Devonian peralkaline magmatism in western Newfoundland. Canadian Journal of Earth Sciences, 17, 425-439. https://doi.org/10.1139/e80-040

66. Tchameni, R., Mezger, K., Nsifa, N.E., and Pouclet, A., 2001. Crustal origin of Early Proterozoic syenites in the Congo craton (Ntem complex), South Cameroon. *Lithos, 57(1)*, 23-42. https://doi.org/10.1016/S0024-4937(00)00072-4

67. Van Kranendonk, M.J., Kröner, A., Hoffmann, J.E., Nagel, T., and Anhaeusser, C.R., 2014. Just another drip: Re-analysis of a proposed Mesoarchean suture from the Barberton Mountain Land, South Africa. *Precambrian Research, 254*, 19-35. https://doi.org/10.1016/j.precamres.2014.07.022

68. Vielreicher, N.M., Groves, D.I., and Vielreicher, R.M., 2000. The Phalaborwa (Palabora) deposit and its potential connection to iron-oxide copper-gold deposits of Olympic Dam type. In Porter, T.M. (Ed.), Hydrothermal Iron Oxide Copper-Gold and Related Deposits: A Global Perspective, PGC Publishing, Australia, 1, pp 321-329.

69. Westraat, J.D., Kisters, A.F.M., Poujol, M., and Stevens, G., 2005. Transcurrent shearing, granite sheeting and incremental construction of the tabular 3.1 Ga Mpuluzi batholith, Barberton granite-greenstone terrane, South Africa. *Journal of the Geological Society, 162(2)*, 373-388. https://doi.org/10.1144/0016-764904-026

70. Whalen, J.B., Currie, K.L., and Chappell, B.W., 1987. A-type granites: geochemical characteristics, discrimination and petrogenesis. *Contributions to Mineralogy and Petrology, 95*, 407–419. https://doi.org/10.1007/BF00402202

71. Wickham, S.M., Litvinovsky, B.A., Zanvilevich, A.N., and Bindeman, I.N., 1995. Geochemical evolution of Phanerozoic magmatism in Transbaikalia, East Asia: A key constraint on the origin of K-rich silicic magmas and the process of cratonization. *Journal of Geophysical Research: Solid Earth, 100(B8)*, 15641-15654. https://doi.org/10.1029/95JB00035

72. Wilson, A.H., and Zeh, A., 2018. U-Pb and Hf isotopes of detrital zircons from the Pongola Supergroup: Constraints on deposition ages, provenance and Archean evolution of the Kaapvaal craton. *Precambrian Research, 305*, 177-196. https://doi.org/10.1016/j.precamres.2017.12.020

73. Wu, F.Y., Yang, Y.H., Li, Q.L., Mitchell, R.H., Dawson, J.B., Brandl, G., and Yuhara, M., 2011. In situ determination of U–Pb ages and Sr–Nd–Hf isotopic constraints on the petrogenesis of the Phalaborwa carbonatite Complex, South Africa. Lithos, 127(1-2), 309-322. https://doi.org/10.1016/j.lithos.2011.09.005

74. Yearron, L.M., 2003. Archaean granite petrogenesis and implications for the evolution of the Barberton Mountain Land, South Africa. Doctoral dissertation, Kingston University.

75. Zeh, A., Gerdes, A. and Millonig, L., 2011. Hafnium isotope record of the Ancient Gneiss Complex, Swaziland, southern Africa: evidence for Archaean crust–mantle formation and crust reworking between 3.66 and 2.73 Ga. Journal of the Geological

CHAPTER 2. PRESENTATION OF RESEARCH PAPER 1 - ARCHEAN SYENITES BY INTRACRUSTAL PROCESSES: THE BOESMANSKOP ALKALINE COMPLEX, EASTERN KAAPVAAL CRATON

This manuscript, first authored by Marcel Vinicius Santos Leandro was submitted to *Lithos* and is currently under peer review (DOI: http://dx.doi.org/10.2139/ssrn.4972697). The following aspects of the research were done independently by Marcel Vinicius Santos Leandro while receiving standard supervision by his supervisors Gary Stevens, Jean-François Moyen and Alex F.M. Kisters: (i) fieldwork and sampling; (ii) sample preparation; (iii) petrographic description; (iv) SEM imaging and EDS analysis of major elements of pertinent minerals; (v) phase equilibrium modeling; (vi) generation of figures; (vii) writing of the manuscript.

Contribution Roles Taxonomy (CRediT) classification - **Marcel V.S. Leandro**: Data curation; Formal Analysis; Investigation; Methodology; Visualization; Writing – Original Draft Preparation. **Gary Stevens**: Conceptualization; Data Curation; Funding Acquisition; Project Administration; Resources; Supervision; Validation; Writing – Review & Editing. **Jean-François Moyen**: Data Curation; Funding Acquisition; Resources; Supervision; Validation; Writing – Review & Editing. **Alex F.M. Kisters**: Supervision; Validation; Writing – Review & Editing. **Alanielson Ferreira**: Visualization; Validation; Writing – Review & Editing.

Archean syenites by intracrustal processes: the Boesmanskop Alkaline Complex, Eastern Kaapvaal Craton

Marcel V.S. Leandro[a]*, Gary Stevens[a], Jean-François Moyen[b], Alex F.M. Kisters[a], Alanielson Ferreira[c]

1 Stellenbosch University, Department of Earth Sciences, Private Bag X1, Matieland, 7602, Stellenbosch, South Africa; 2 Université Jean-Monnet, Laboratoire Magmas et Volcans, UCA-CNRS-IRD, Aubière F-63170, France; 3 University of Brasília, Institute of Geosciences, Brasília-DF, 70910-900, Brazil

*Corresponding author: marcel.leandro@hotmail.com; https://orcid.org/0000-0002-5177-890X

Abstract

Alkaline rocks are volumetrically a minor component of the geological record, with Archean examples being remarkably rare. The oldest syenites on Earth occur in the ca. 3.1 Ga Boesmanskop Alkaline Complex (BAC), located on the eastern margin of the Kaapvaal Craton, where they form part of a voluminous Granodiorite-Monzogranite-Syenogranite suite (GMS). The rocks of the BAC include syenite, quartz monzonite, and leucogranite. This study draws upon newly acquired data, encompassing field observations, petrological analysis, mineral chemistry, whole-rock geochemistry including Rb-Sr and Sm-Nd isotope ratios, and phase equilibrium modeling, with the aim of better understanding the petrogenesis of the BAC rocks. These syenitic rocks display coarse-grained porphyritic textures with K-feldspar phenocrysts as cumulus phase and clinopyroxene, Ca-amphibole, plagioclase, titanite, and scarce quartz as the main intercumulus phases. The syenite is only deformed at the contact with the Tonalite–Trondhjemite–Granodiorite (TTG) suite basement, displaying SC fabrics and mineral lineation parallel with the pluton edges and concordant with the basement kinematic indicators. In other outcrops, the syenite intrudes the TTG suite with sharp contacts and overlay syenitic dyke swarms connected to sill intrusions with hypabyssal textures, which suggest a shallow emplacement of the magmas along an active shear zone. The BAC rocks are silica-saturated with high K_2O+Na_2O (< 11.2 wt%), low MgO (< 1.6 wt%) and low CaO (<3.4 wt%). They also have low transition element contents, high Ba and Sr contents and negative Nb, Ta, and Ti anomalies in the primitive mantle-normalized trace element diagrams, indicative of crustal sources. The BAC rocks have initial εNd values that overlap those of the host TTG suite basement. The data obtained indicate that the syenites represent K-feldspar-dominated crystal cumulates left behind by the extraction of rhyolitic melts from the magma chamber, formed from magmas that crystallized high-temperature K-feldspar before plagioclase and quartz. The viability of this hypothesis has been tested by phase equilibrium modeling, which has demonstrated that a subset of GMS granite compositions with high K_2O+Na_2O (> 9.3 wt%) do produce high-temperature K-feldspar as the first tectosilicate when cooling under low-pressure conditions. Thus, the syenitic cumulates are proposed to be produced by a structurally assisted accumulation of K-feldspar from hot granitic magma produced by fluid-absent anatexis of the lower crust, contributing to the craton stabilization by the transfer of radioactive elements to shallow depths.

Keywords: Cumulus rocks; high-temperature K-feldspar; Phase equilibrium modeling;

2.1. Introduction

Alkaline igneous rocks comprise a compositionally broad group of rocks characterized by alkali concentrations that exceed the capacity of their feldspar to fully accommodate the alkali elements (Fitton and Upton, 1987; Frost and Frost, 2008). A broader, commonly applied classification that is also used in this study, classifies igneous rocks as either alkaline or subalkaline, based on the relationship between SiO_2 and the combined alkali content, as expressed in the Total Alkali vs Silica diagram (e.g., Sørensen, 1974; Miyashiro, 1978; Fitton and Upton, 1987). Alkaline rocks often contain high LILE, HFSE, and REE contents, which attract the attention of petrologists (e.g., Sørensen, 1974; Fitton and Upton, 1987; Marks et al., 2011; Mikkola et al., 2011). The REE and HFSE in metaluminous and peraluminous alkaline plutonic rocks can be accommodated in the same minerals that host these elements in sub-alkaline rocks (e.g., apatite, epidote, Fe-Ti oxides, monazite, titanite, and zircon). In contrast, in peralkaline rocks, typically higher concentrations of these incompatible elements can result in the formation of unusual silicates (i.e., eudialyte, aenigmatite, astrophyllite, wöhlerite), in which case the rocks are agpaitic (e.g., Sørensen, 1974; Marks et al., 2011).

Syenites are typical examples of alkaline rocks and occur is both peralkaline and alkaline varieties. Hypotheses to explain their origin can be divided into two categories: the first focusing on the role of mantle-derived silica-undersaturated magmas and the second focusing on the role of fractional crystallization from crustal-derived felsic magmas (e.g., Wickham et al., 1995; Tchameni et al., 2001). The mantle source hypothesis involves (i) fractional crystallization of alkali basaltic magmas with varying degrees of crustal assimilation (e.g., Fitton and Upton, 1987; Turner et al., 1992), and (ii) mixing of basaltic magmas with felsic melts followed by fractional crystallization (e.g., Wickham et al., 1995). Many hypotheses invoking crustal sources have been proposed, including (i) low degrees of partial melting of granulitic lower crust (e.g., Clemens et al., 1986; Whalen et al., 1987), (ii) melting of I-type tonalites (Patiño Douce, 1997), (iii) melting of the lower crust with the source or resultant magma metasomatized by mantle-derived fluids (e.g., Fitton and Upton, 1978; Taylor et al., 1980). Furthermore, some researchers have postulated that magma chamber processes might be as important as source processes in the production of syenites (e.g., Farina et al., 2012; Paterson et al., 2005; Rocher et al., 2018; Yu et al., 2023).

Alkaline rocks are particularly scarce in the Archean rock record, and almost all Archean examples are Neoarchean (e.g., Blichert-Toft et al., 1995; Balashov and Glaznev, 2006). Well-

described examples include the ca. 2.70 Ga Poohbah Lake complex on the Superior Craton and the ca. 2.74 Ga Likamännikkö complex on the Karelian Craton (e.g., Mikkola et al., 2011). Mesoarchean alkaline rocks worldwide are rare (e.g., Fitton and Upton, 1987; Blichert-Toft et al., 1995). To date, the oldest syenites on Earth form part of the ca. 3.1 Ga Boesmanskop Alkaline Complex, located to the south of the Barberton Greenstone Belt (BGB), one of the best-preserved Paleoarchean volcano-sedimentary sequences on Earth (e.g., Anhaeusser and Robb, 1983; Kamo and Davis, 1994; Blichert-Toft et al., 1995; Balashov and Glaznev, 2006). This raises the following questions: Are the classic hypotheses proposed to explain Proterozoic syenite genesis applicable to the oldest syenites on Earth, given the fact that Archean syenites predates the emergence of cratons and possibly the differentiation of the mantle? Thus, this study draws upon newly acquired data, encompassing field observations, petrological analysis, mineral major and trace element chemistry, whole-rock geochemical data including Rb-Sr and Sm-Nd isotope ratios, and phase equilibrium modeling to investigate the petrogenesis of these ca. 3.1 Ga syenites. The data were obtained primarily for the Boesmanskop Alkaline Complex rocks but also include data from the adjacent and contemporaneous ca. 3.1 Ga Heerenveen batholith (HE). Furthermore, previously published whole-rock isotopic, major and trace element data for the GMS suite (e.g., Barton et al., 1983a; Yearron, 2003; Westraat et al., 2005; Anhaeusser and Robb, 1983; Murphy, 2015; Moyen et al., 2021) were integrated with the dataset generated from this study.

2.2. Geological Background

2.2.1. Barberton Granite-Greenstone Terrane overview

Archean crustal fragments are complex geological domains consisting of Tonalite–Trondhjemite–Granodiorite (TTG) gneisses and greenstone belt sequences made up of meta-volcanic and metasedimentary supracrustal units (Moyen et al., 2019). Globally, the intrusion of voluminous granites *sensu stricto* (*s.s.*) into the TTG crust is widely considered to mark the local stabilization of the craton and the transition to a modern style plate tectonic regime (e.g., Schoene et al., 2008; 2009; Howarth et al., 2019). This event is diachronous, occurring between 3.1 and 2.5 Ga in different areas, but generally, it occurs ca. 500 Ma after the formation of the oldest associated TTGs (e.g., Peucat et al., 1993; Robb et al., 2006; Moyen et al., 2019).

The Barberton Granite-Greenstone Terrane (BGGT) and the Ancient Gneiss Complex (AGC) form the Eastern portion of the Kaapvaal Craton in South Africa and Eswatini and preserve well-exposed and pristine Archean rocks that share a common geological history from

3.23 Ga, result of the collision of two of more microcontinental blocks (e.g., de Wit et al., 1992; de Ronde and de Wit, 1994 Schoene and Bowring, 2010). The BGGT includes ca. 3.55 - 3.45 Ga and 3.29 - 3.21 Ga TTG plutons, and ca. 3.23 Ga high-pressure amphibolite facies rocks that appear coeval with granulite facies rocks in the AGC, and records a history of polyphase deformation (e.g., Lowe, 1994; Kröner et al., 1996; Lowe and Byerly, 2007). The main regional deformation is characterized by NW-SE directed horizontal crustal shortening, with the main deformational phase occurring between 3.23 and 3.22 Ga, coeval with or closely followed by an NE–SW directed extension of the mid-crustal sequences (e.g., de Ronde and de Wit, 1994; Kamo and Davis, 1994; Kisters et al., 2003; Westraat et al., 2005). These features are associated with the collision that amalgamated the AGC with the western margin of the proto-Kaapvaal Craton (e.g., Kröner et al., 1996; Schoene and Bowring et al., 2010).

The BGGT and the AGC were intruded by a suite of Mesoarchean felsic potassic rocks termed the Granodiorite-Monzogranite-Syenogranite suite (GMS), (e.g., Anhaeusser and Robb, 1983; Kröner et al., 1996; Kisters et al., 2003; Yearron, 2003). The GMS suite occurs as several sheet-like plutons of substantial areal extent (Figure 2-1), (e.g., Anhaeusser and Robb, 1983; Robb et al., 2006).

The volcano-sedimentary succession of the Dominion group (ca. 3.07 Ga) and Pongola Supergroup (< 2.99 Ga) displaying excellent preservation of unmetamorphosed or burial metamorphosed cover sequences, along with the brittle intrusion of dolerite dykes (< 2.98 Ga) indicate that the Kaapvaal Craton was a stable entity after the 3.1 Ga magmatic event., leading many authors to interpret the voluminous potassic GMS magmatism to represent the final stages of the Kaapvaal Craton stabilization (e.g., Kamo and Davis, 1994; Anhaeusser and Robb, 1983; Clemens et al., 2010; Gumsley et al., 2015; Wilson and Zeh, 2018).

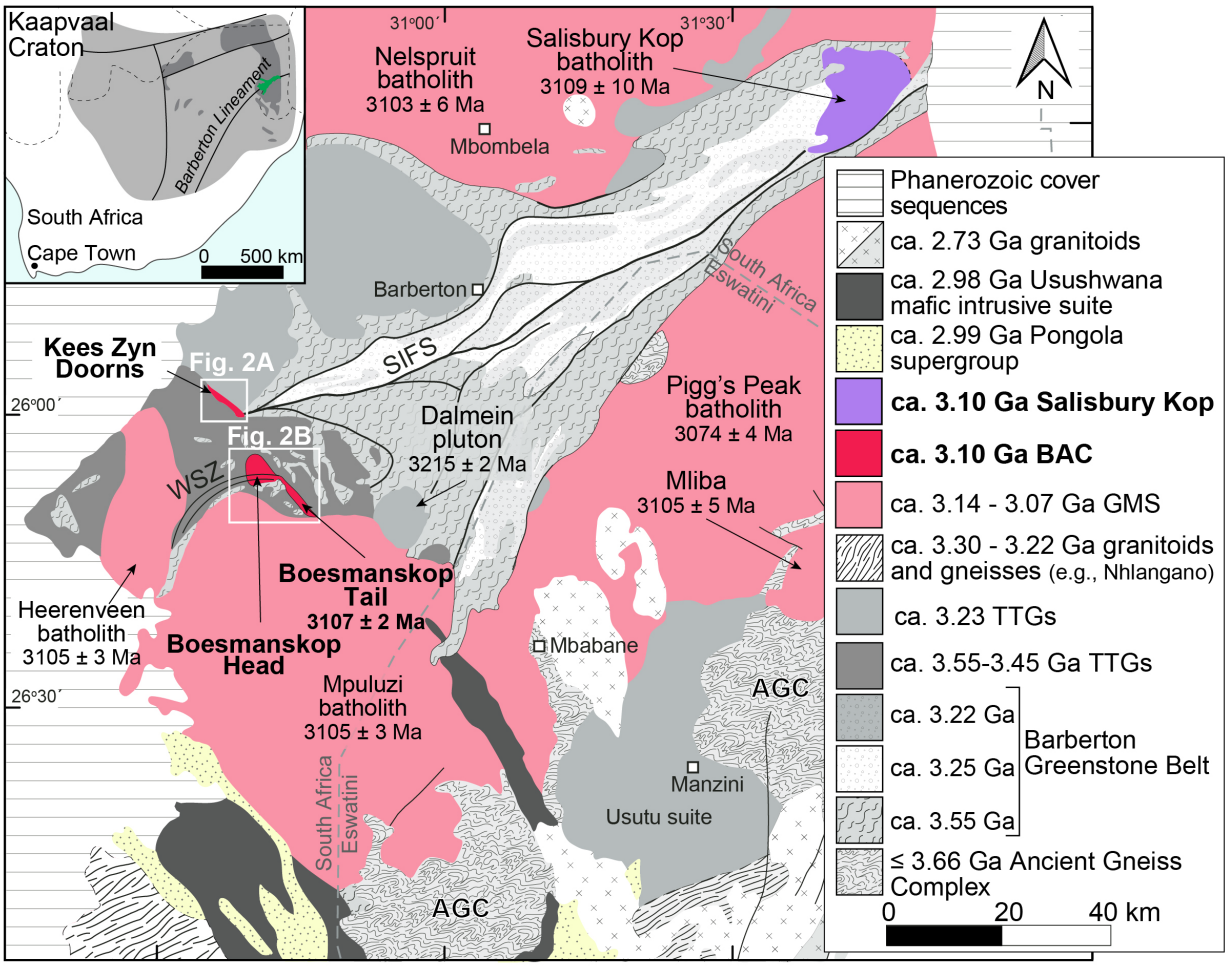

Figure 2-1. Simplified geological map of the Barberton Granite-Greenstone Terrane showing the GMS suite and surrounding units (after de Ronde and de Wit, 1994; Clemens et al., 2010; Schoene and Bowring, 2010). Insert: location of the Kaapvaal Craton. AGC: Ancient Gneiss Complex; SIFS: Saddleback-Inyoka Fault System; WSZ: Welverdiend Shear Zone.

2.2.2. Granodiorite-Monzogranite-Syenogranite suite overview

The Granodiorite-Monzogranite-Syenogranite suite was emplaced between 3140 and 3074 Ma and exhibits considerable compositional heterogeneity, including syenites, quartz monzonites and voluminous granites *s.s.* (e.g., Kamo and Davis, 1994; Anhaeusser and Robb, 1983; Robb et al., 2006). This suite represents a significant shift in the chemistry of the regional magmatism, which transitioned from pre- to syn-tectonic Na-rich compositions, typical of the Archean continental crust, to a syn- to post-tectonic potassic magmatism (e.g., Anhaeusser and Robb, 1983; Robb et al., 2006; Chen et al., 2023). This shift did not begin with the GMS suite; rather, it started approximately 100 Ma earlier with the intrusion of the Dalmein pluton into the southern portion of the BGB and the development of the Usutu suite in the AGC. The Dalmein pluton (3215 ± 2 Ma) is predominantly composed of porphyritic granodiorite and the Usutu suite comprises ca. 3.23 Ga coarse-grained granodiorites, gabbros and diorites (e.g.,

Kamo and Davis, 1994; Schoene and Bowring, 2010). Despite the chemical similarities of the Damein pluton with the GMS suite (e.g., LREE-enriched in comparison with the HREE, with no Eu anomalies), its older ages lead some studies to consider it as the most differentiated phase of the TTG suite (e.g., Robb et al., 2006).

The GMS suite consists of several plutons distributed across the BGGT, and intrusive into the basement with sharp contacts (e.g., Anhaeusser and Robb, 1983; Robb et al., 1983). Notable examples that outcrop in the south of the BGB include the different bodies that comprise the Boesmanskop Alkaline Complex (ca. 3107 ± 2 Ma), Mpuluzi batholith (ca. 3105 ± 3 Ma) and the Heerenveen batholith (ca. 3105 ± 3 Ma). These plutons have been reasonably well characterized by a number of previous studies (e.g., Anhaeusser, 1980; Anhaeusser and Robb, 1983; Westraat et al., 2005; Clemens et al., 2010; Moyen et al., 2021) and intruded as sub-horizontal tabular generally quartz-monzonite to granite *s.s.* bodies, with intrusion initiated by syn-magmatically deformed sheeted dykes of granodioritic to syenitic composition that are visible on some of the margins of the plutons (e.g., Westraat et al., 2005; Belcher and Kisters, 2006; Clemens et al., 2010). Zircon crystals with ca. 3.6 - 3.2 Ga U-Pb ages interpreted as inherited crystals and Hf and Nd T_{DM} ages of ca. 4.13 - 3.48 Ga and 3.64 - 3.23 Ga, respectively, that have been identified in the Mpuluzi and Heerenveen batholiths suggests a contribution of the TTGs and/or AGC materials to the GMS suite sources (e.g., Murphy, 2015; Moyen et al., 2021).

The Nelspruit batholith (ca. 3104 ± 3 Ma) and Salisbury Kop batholith (ca. 3109 ± 10 Ma) occur in the north of the belt, while the oldest GMS suite rocks occur within the Pigg's Peak batholith (3144 - 3074 ± 4 Ma) outcropping in the east of the BGB (e.g., Kamo and Davis,1994; Robb et al., 2006; Lowe and Byerly, 2007; Clemens et al., 2010).

Internally, the GMS plutons exhibit a range of different textures and chemistries (i.e., granodiorites, monzonites, quartz-monzonites, syenites and granites, fine-grained to pegmatitic, low- to high-K, metaluminous to peraluminous rocks) reflecting the complex magmatic history of the GMS suite, most likely including a range of different magma sources (e.g., Anhaeusser and Robb,1983; Clemens et al., 2010; Moyen et al., 2021).

2.2.3. Study area

The Boesmanskop Alkaline Complex (BAC) is spatially a minor component of the GMS suite and encompasses the Boesmanskop Head (BH), Boesmanskop Tail (BT), and Kees Zyn Doorns (KZD) plutons, which are topographically well distinguished from the lower-lying TTG

suite rocks they intrude by forming mountains and hills. They are composed of quartz monzonites, leucogranites, and syenites (e.g., Anhaeusser, 1980; Anhaeusser and Robb, 1983). The BH main outcrop is defined by the Boesmanskop mountain with its eastern end connected with the BT, while the BT and KZD outcrop as linear, dyke-like structures with NW-SE alignment (e.g., Anhaeusser and Robb, 1983). A very similar trend is followed by the ca. 2.98 Ga dykes of the Usushwana mafic intrusive suite (e.g., Gumsley et al., 2015).

The KZD intrudes along the contact of the Badplaas and Nelshoogte TTG suite plutons (3290-3230 Ma and 3236 ±1 Ma, respectively; de Ronde and Kamo, 2000; Kisters et al., 2010) with its southern end intersecting the rocks of the BGB in the Stolzburg syncline (Figure 2-2 A). The Boesmanskop Head and Boesmanskop Tail (3107 ± 4 Ma) plutons intrude the TTG suite gneisses of the 3450 Ma Stolzburg pluton (Figure 2-2 B), (Kamo and Davis, 1994; Mühlberg et al., 2021). The BH and BT are in the vicinity of the HE to the west, and the Mpuluzi batholith to the south, and they share several textural and chemical similarities. The ages, petrography, and chemistry similarities of the BAC, Herenveen, and Mpuluzi batholiths suggest they may have formed through the same multi-batch assembly event (e.g., Robb et al., 2006; Moyen et al., 2021).

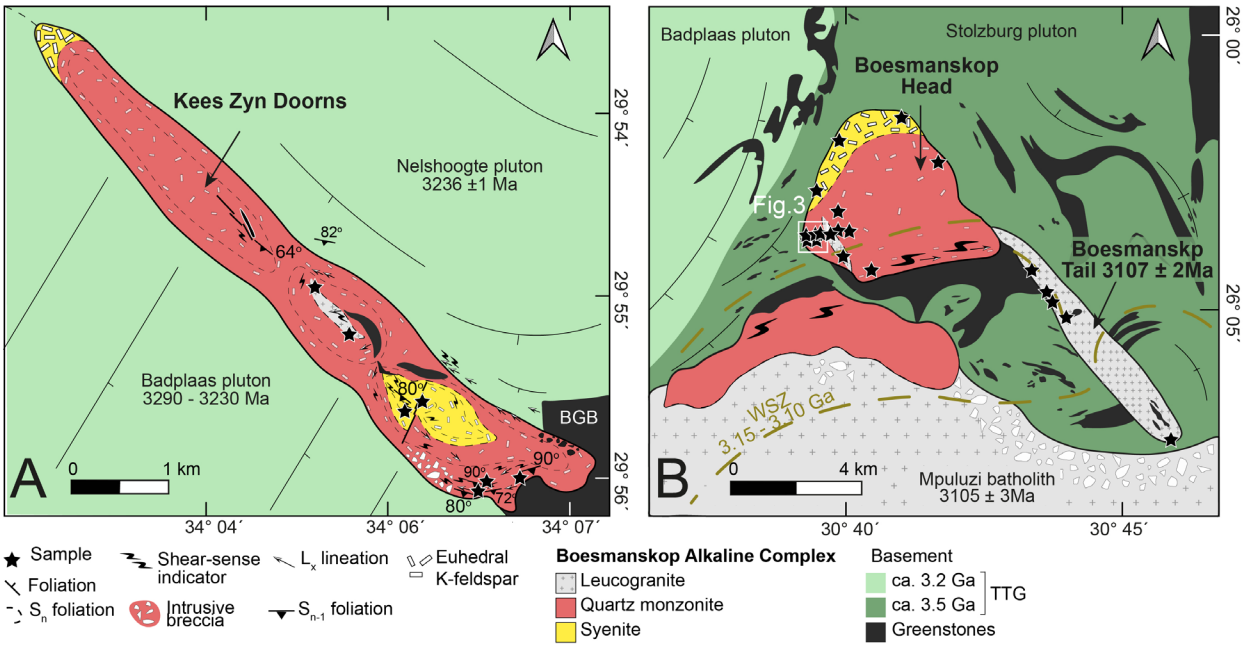

Figure 2-2. Simplified geological map of the Boesmanskop Alkaline Complex illustrating the spatial distribution of main rock types and sample locations. A) Kees Zyn Doorns pluton. B) Boesmanskop Head and Boesmanskop Tail plutons (after Anhaeusser and Robb, 1983; Westraat et al., 2005). BGB: Barberton Greenstone Belt.

2.3. Materials and Methods

2.3.1. Sample preparation

The sample preparation was conducted at the Central Analytical Facility (CAF), Stellenbosch University, except for the thin sections, which were produced by Lab Crystals, Lucknow, India. The bulk rock samples were crushed with a jaw crusher and milled with a tungsten carbide ring mill. The sample powder was fused into glass disks in an autofluxer, with lithium borate flux (ratio 1/10 sample/flux) without a heavy absorber. The glass disks were utilized for the analysis of major oxide and trace elements.

2.3.2. Petrography and mineral chemistry

The sample localities are indicated in Figure 2-2, and their coordinates are presented in Table 2-1. Petrographic investigation of the thin sections utilized an optical microscope, cathodoluminescence (CL), and backscattered electron (BSE) images collected using a Zeiss Merlin Field Emission Scanning Electron Microscope at the CAF. The images were acquired utilizing an accelerating voltage of 10 kV and 11 nA probe current, with a working distance of 9.5 mm. Quantitative chemical analysis of mineral compositions was conducted utilizing a Zeiss EVO SEM with an Oxford Instruments × Max 20 mm^2 energy dispersive spectroscopy (EDS) detector, an Oxford Instruments wavelength dispersive X-ray spectrometer (WDS) detector, and Oxford INCA software installed. The beam conditions were 20 kV accelerating voltage and 1.0 A probe current, with a working distance of 8.5 mm and a specimen beam current of -20.0 nA. The counting time was 10 s live-time for the EDS detector and 60 s peak, with 30 s off-peak for the WDS detector.

The *in situ* REE analysis of amphibole, pyroxene and titanite was performed using a Resolution 193 nm Excimer laser from Applied Spectra connected to an Agilent 7700 Q ICP-MS at the CAF with laser spot sizes of 40 µm, frequency of 8 Hz and 45 s of sample ablation time. The JJG1424 clinopyroxene (Zhao et al., 2020) was utilized as a calibration standard, bracketing 15 analyses of the unknowns, and BCR-2G and BHVO-2G glasses (Jochum et al., 2005) as quality control standards. The Si was used as an internal standard, with values determined through EDS-SEM measurements in this study. The Si content considered was 14.1% for titanite, 24.1% for amphibole, and 24.6% for clinopyroxene.

Table 2-1. Sample coordinates and facies of the Boesmanskop Alkaline Complex and correlated potassic samples of the Heerenveen batholith.

Sample	Pluton	Latitude (dec)	Longitude (dec)	Primary assemblage	Facies
BH03	Boesmanskop Head	-26.0430556	30.6577778	Kfs + Pl + Amph + Qz + Mt + Ilm+ Ttn + Cpx + Ap+ All+ Zrc	Syenite
BH04	Boesmanskop Head	-26.0286111	30.6641667	Kfs + Pl + Cpx + Qz + Amph + Mt + Ilm+ Ttn + Ap+ All+ Zrc	
BH18	Boesmanskop Head	-26.0206667	30.6850333	Kfs + Pl + Qz + Amph + Mt + Ilm + Ttn + Cpx + Ap+ All+ Zrc	
HE03	Heereveen	-26.1842402	30.4364831	Kfs + Pl + Qz + Amph + Ilm + Mt + Ilm + Ap + Ttn + Zrc	
KZD03	Kees Zyn Dorns	-25.9590562	30.6458904	Kfs + Pl + Cpx + Amph +Qz+ Mt + Ilm + Ttn + Ap + Ep + Zrc	
KZD04	Kees Zyn Dorns	-25.9525189	30.6362462	Kfs + Pl + Amph +Qz+ Mt + Ilm + Ttn + Ap + Ep + Zrc	
BH02	Boesmanskop Head	-26.0566667	30.6569444	Kfs + Pl + Qz + Mt + Ilm+ Ttn + Ap + All+ Zrc	Quartz monzonite
BH05	Boesmanskop Head	-26.0344444	30.6961111	Kfs + Pl + Qz + Cpx + Amph + Mt + Ilm + Ttn + Ap+ All+ Zrc	
BH06A	Boesmanskop Head	-26.0541332	30.6644431	Kfs + Pl + Qz + Amph + Mt + Ilm + Ttn + Ap + Zrc	
BH06B	Boesmanskop Head	-26.0541332	30.6644431	Kfs + Pl + Qz + Mt + Ilm+ Ttn + Ap + Zrc	
BH07	Boesmanskop Head	-26.0541250	30.6670919	Kfs + Pl + Qz + Amph + Mt + Ttn + Ap + Zrc + All	
BH09	Boesmanskop Head	-26.0488118	30.6639188	Kfs + Pl + Qz + Mt + Ilm+ Ttn + Cpx + Ap + Zrc + All	
BH11	Boesmanskop Head	-26.0658333	30.6752778	Kfs + Pl + Qz + Mt + Ilm+ Ttn + Ap + Zrc + Ep	
BH13	Boesmanskop Head	-26.0566667	30.6569444	Kfs + Pl + Qz + Mt + Ilm + Ttn + Ep + Ap + Zrc	
BH14	Boesmanskop Head	-26.0567000	30.6571000	Kfs + Pl + Qz + Cpx + Mt + Ilm+ Ttn + Ap+ Ep+ Zrc	
BH16	Boesmanskop Head	-26.0572222	30.6547222	Kfs + Pl + Qz + Mt + Ilm + Ap + All + Zrc	
BH1A	Boesmanskop Head	-26.0574000	30.6551833	Kfs + Pl + Qz + Mt + Ilm+ Ttn + Ap + Zrc + All	
HE02	Heereveen	-26.1721474	30.4435493	Kfs + Pl + Qz + Ttn + Mt + Ilm + Ap + Zrc	
HE05	Heereveen	-26.1684833	30.4833167	Kfs + Pl + Qz + Amph + Mt + Ilm Ttn + Ap + Ep + Zrc	
KZD1A	Kees Zyn Dorns	-25.9589833	30.6459333	Kfs + Pl + Qz + Cpx + Mt + Ilm + Ttn + Ap + Ep + Mnz	
KZD09	Kees Zyn Dorns	-25.9603400	30.6414285	Kfs + Pl + Qz + Cpx + Mt + Ilm+ Ttn + Ap+ All+ Zrc	
KZD02	Kees Zyn Dorns	-25.9598667	30.6427333	Kfs + Pl + Qz + Cpx + Mt + Ilm + Ttn + Ap + Ep	

Table 2-1. Sample coordinates and facies of the Boesmanskop Alkaline Complex and correlated potassic samples of the Heerenveen batholith (continued).

Sample	Pluton	Latitude (dec)	Longitude (dec)	Primary assemblage	Facies
BH08A	Boesmanskop Head	-26.5479280	30.6631144	Kfs + Pl + Qz + Ap + Mt	Low-K leucogranite
KZD05	Kees Zyn Dorns	-25.9412796	30.6249336	Pl + Kfs+ Qz + Bt	
KZD06	Kees Zyn Dorns	-25.9445215	30.6272057	Kfs + Pl + Qz + Bt	
BH17*	Boesmanskop Tail	-26.0308833	30.7127667	Pl + Kfs + Qz + Cpx + Ep	
BH12	Boesmanskop Head	-26.0614000	30.6612300	Kfs + Pl + Qz + Ap + Zrc	Medium-K leucogranite
BT01	Boesmanskop Tail	-26.0736111	30.7335000	Kfs + Pl + Qz + Bt	
BT03A	Boesmanskop Tail	-26.0781500	30.7383167	Pl + Kfs + Qz	
BT04A	Boesmanskop Tail	-26.0782667	30.7399667	Kfs + Pl + Qz	
HE04	Heereveen Batholith	-26.1932726	30.4594745	Kfs + Pl + Qz + Mt + Ilm + Ap	

2.3.3. Whole-rock compositions

The major oxide compositions of the thirty-one samples were analyzed by X-ray Fluorescence Spectrometry on glass disks at the CAF laboratory following the method of Eggins (2003). The standards utilized were BE-N, JB-1, BHVO-1, JG-1 and WITS-G. A well-characterized composition, HUSG1, was used for quality control and was analyzed as an unknown after every 15 samples.

Trace elements were analyzed on glass disks by a 193 nm Excimer laser ablation system from Applied Spectra coupled to an Agilent 7700 ICP-MS. The reference materials utilized were the BCR-2, BCR-2G, BHVO-1, and BHVO-2G also made into fluxed fused disks. The reference materials were run at the beginning and the end of each sample in a sample bracketing mode after every five sample measurements. Drift corrections were applied, and all measurements were made in duplicate. Whole-rock compositions are presented in Tables 2-2 and 2-3. The standard average measurements and relative standard deviation are presented in the supplementary material.

2.3.4. Isotopic analysis

Whole-rock Nd and Sr isotope ratios of six samples were obtained at the Department of Geological Sciences at the University of Cape Town using a NuPlasma HR multi-collector

inductively coupled plasma mass spectrometer equipped with a DSN-100 desolvating nebulizer in the MC-ICP-MS facility. Isotopic abundances were determined in solution mode, obtaining present-day $^{87}Sr/^{86}Sr$ and $^{143}Nd/^{144}Nd$ ratios, according to Ódri et al. (2020) and Howarth et al. (2019). Column chromatography was used to separate Sr and REE. Initial Sr and Nd ratios were calculated based on the whole-rock Rb, Sr, Sm and Nd concentrations obtained with XRF and sample ages from literature (e.g., Kamo and Davis, 1994).

The NIST987 carbonate was applied as a bracketing reference material normalized to a $^{87}Sr/^{86}Sr$ value of 0.710255 for the Sr isotope ratios analysis with 0.2% HNO_3 solutions at a concentration of 200 ppb. The measured signal for ^{85}Rb and the natural $^{85}Rb/^{87}Rb$ ratio were utilized to correct the Sr isotopic data for Rb interference and the instrumental mass fractionation correction was carried out using exponential law and an $^{86}Sr/^{88}Sr$ value of 0.1194. Internal 2σ analytical uncertainty for $^{87}Sr/^{86}Sr$ was <0.000013. The Nd data were normalized to a $^{143}Nd/^{144}Nd$ value of 0.512115 (Tanaka et al., 2000) for the bracketing standard JNdi-1 and Nd isotope ratios were measured as 50 ppb 2% HNO_3 solutions. Internal 2σ analytical uncertainties for $^{143}Nd/^{144}Nd$ varied from 0.000009 to 0.000016. The measured signal for ^{147}Sm and ^{140}Ce, and natural Sm and Ce isotope abundances were applied to correct Sm and Ce interference of Nd isotope data. Instrumental mass fractionation was corrected using exponential law and a $^{146}Nd/^{144}Nd$ value of 0.7219.

2.3.5. Phase equilibrium modeling

The phase equilibrium modeling experiments in the system NKFMASH were conducted with Rcrust software utilizing the Meemum function of PERPLE_X to calculate phase stabilities for the set P-T-X space according to gridded Gibbs free energy minimization (Janoušek et al., 2015; Mayne et al., 2016). The Rcrust software was chosen due to its capacity to simulate path-dependent open-system processes such as the removal/addition of phases during the experiments, which is very suitable to model systems experiencing fractional crystallization and melt loss (Mayne et al., 2016).

The trace element modeling was conducted on an Excel spreadsheet, based on the mass balance equations and partition coefficient provided by Laurent (2012) to felsic melts and the accessory mineral volume of the syenites.

2.4. Results

2.4.1. Field relationships

2.4.1.1. Boesmanskop Head pluton

The dominant rocks of the BH are pinkish leucocratic quartz monzonites ranging from coarse-grained to fine-grained with high volumes of K-feldspar phenocrysts. The NW of the Boesmanskop mountain is composed of porphyritic syenites, reflected by the high modal proportion of euhedral angular K-feldspar (Figure 2-3 F). The BH presents well-developed magmatic layering towards the western edge of the pluton. The mafic mineralogy is represented by clinopyroxene, amphibole, and titanite. The syenite becomes finer-grained from the north towards the southern portions of the BH pluton and gradationally changes to quartz monzonite whilst the euhedral angular K-feldspar becomes scarce and progressively more altered. At the southern edge of the BH, a deformed quartz monzonite displays SC fabric, magmatic layering, and mineral lineation parallel with the edges of the intrusion and concordant with the basement kinematic indicators.

The Theespruit River cuts through the BH, exposing sharp contacts with amphibolite schist and TTG suite gneisses of the Stolzburg pluton (Figure 2-3 A-B). The riverbed outcrops consist of fine- to medium-grained quartz monzonite dykes with sub-vertical magmatic mineral alignment and magmatic layering at the edges of the pluton. These outcrops are cut by quartz-feldspathic veins creating a stockwork pattern and by fine-grained leucogranites. Amphibolite xenoliths, occasionally rounded, are scattered throughout the outcrops with sharp contacts with the BAC. The dyke structures feed a quartz monzonite sill with hypabyssal texture, dipping eastward (ca. 10^{o}).

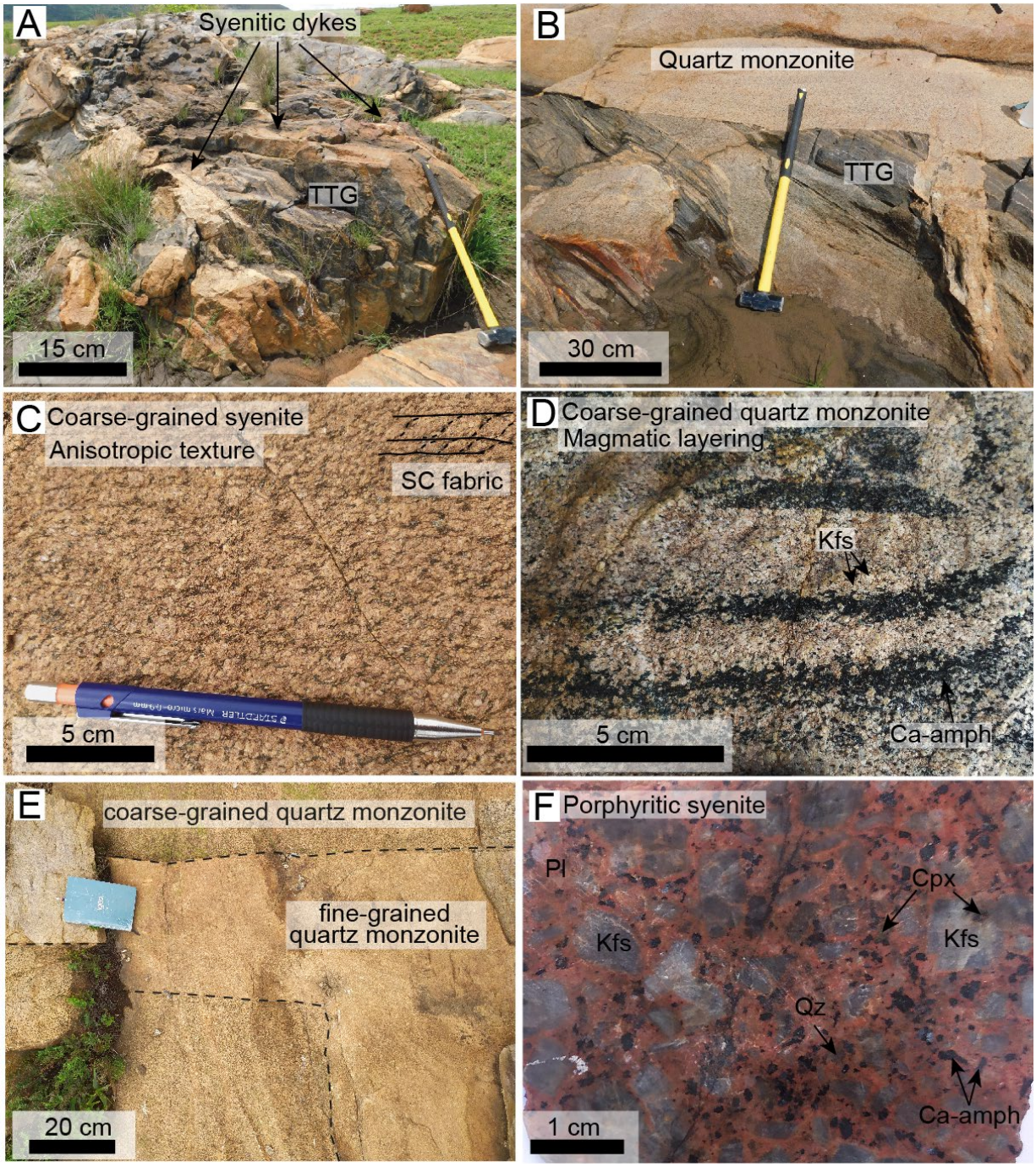

Figure 2-3. Field features of the BAC. A-B) Syenitic dykes intruding the TTG suite with sharp contacts. C) SC fabric in cumulus syenite. D) Magmatic layering on the quartz monzonite. E) fine-grained quartz monzonite dyke intruding the coarse-grained quartz monzonite. F) Porphyritic syenite with angular euhedral K-feldspar (Kfs) phenocrysts surrounded by smaller K-feldspar, plagioclase (Pl), quartz (Qz) and amphibole (Ca-amph).

2.4.1.2. Kees Zyn Doorns pluton

The Kees Zyn Doorns pluton predominantly consists of coarse-grained pinkish quartz monzonite, which displays sharp contacts with the TTG suite basement. The quartz monzonite contains pervasive rounded whitish K-feldspar phenocrysts, surrounded by a matrix of pink feldspar and with amphibole as the main mafic mineral. Throughout the outcrops, the coarse-grained quartz monzonite is intruded by fine-grained quartz monzonite dykes with lower contents of mafic minerals and displaying sharp contacts (Figure 2-3 E). Due to the narrow width of the dykes, they are not displayed on the simplified geological map. In the central portions of the pluton, the quartz monzonite is isotropic, while at the edges, it exhibits planar and linear magmatic fabric (SC fabric, asymmetric fold, and mineral alignment; Figure 2-3 D), mylonitic and cataclastic textures. The magmatic fabric is parallel to the boundary of the pluton and dips outward with angles ranging from 60° to sub-vertical. Representative measurements are illustrated on the geological map (Figure 2-2).

Bodies of coarse-grained isotropic syenite with abundant rounded K-feldspar crystals, akin to those reported for the quartz monzonite, occur in the central portions of the KZD pluton and exhibit gradational contacts with the host quartz monzonite. Similar to what was observed for the quartz monzonite, the coarse-grained syenites are also intruded with sharp and gradational contacts by more leucocratic syenites with lower mafic minerals contents. Porphyritic syenite with angular euhedral K-feldspar phenocrysts texturally akin to the porphyritic syenite from the BH, occurs at the northern extremity of the pluton.

The KZD leucogranite consists of fine to medium-grained rocks, which display a magmatic foliation defined by biotite. The leucogranite intrudes the quartz monzonite with gradational contacts. It is texturally similar to the quartz monzonite, due to the presence of rounded K-feldspar phenocrysts but differs in its quartz contents and the presence of biotite as the main mafic mineral.

2.4.1.3. Boesmanskop Tail pluton

The Boesmanskop Tail is an elongated pluton characterized by homogeneous and anisotropic pinkish-to-grayish granites. These rocks are fine to coarse-grained and are predominantly leucocratic, with biotite as the main mafic mineral. Magmatic layering and foliation are observed at the SW margins of the pluton, concordant with the Welverdiend Shear Zone (WSZ). Abundant pegmatitic quartz veins and TTG lenses are present at central portions of the BT, with the TTG xenoliths.

2.4.2. Petrography

2.4.2.1. Quartz monzonite

All described rocks contain modal quartz and most preserve near-pristine igneous textures. The predominant rock within the BAC is the medium- to coarse-grained pinkish quartz monzonite, characterized by pervasive rounded whitish K-feldspar phenocrysts (< 1.5 cm), frequently displaying concentric zonation and patches of tartan twinning characteristic of microcline and perthitic textures. This is interpreted to reflect incomplete conversion from the magmatic orthoclase to microcline, during cooling. Small anhedral microcline crystals are also common as a matrix component (Figure 2-4 C-D). The K-feldspar phenocrysts display irregular and interlocked boundaries with other K-feldspar crystals, indicating they are cumulus crystals. Sericitization is common in the cores of the K-feldspar phenocrysts.

The quartz monzonite also contains smaller volumes of anhedral plagioclase with sericitized cores, anhedral Ca-amphibole, subhedral clinopyroxene, and euhedral diamond-shaped titanite as phenocrysts. Additionally, subhedral to anhedral quartz, Ca-amphibole, clinopyroxene, small microcline, and plagioclase crystals occur as intercumulus phases (Figure 2-4 A-B).

Anhedral amphibole is the predominant mafic mineral, found in mafic clusters with magnetite, ilmenite, and titanite. Two types of amphiboles occur: a green anhedral amphibole, which replaces clinopyroxene, and a brown subhedral amphibole with poikilitic texture including apatite, epidote, titanite, zircon, and magnetite, interpreted as primary. The quartz monzonite described in the Theespruit riverbed exhibits scarce anhedral, highly sericitized, and zoned K-feldspar phenocrysts in a fine-grained matrix (Figure 2-4-D). The matrix is composed of anhedral and altered feldspar, quartz, and titanite. Sericite and white mica often completely replace the K-feldspar phenocrysts and create pseudomorphs.

The quartz monzonites from KZD have mylonitic and allotriomorphic textures, indicating solid-state deformation. They present mafic minerals (i.e., titanite, Ca-amphibole), ribbon quartz, augen feldspar, and biotite fish aligned to the edges of the pluton (Figure 2-4 E-F). The accessory mineralogy is represented by euhedral to subhedral diamond-shaped titanite, apatite, ilmenite, magnetite, and zircon, with scarce epidote. Zircon and epidote are included in amphibole and feldspar crystals. The epidote occurs as subhedral crystals, in mafic mineral clusters and anhedral micrometric allanite crystals within titanite. The most common alteration minerals are sericite and muscovite, which replace feldspar; biotite, which has replaced

amphibole; epidote filling late fractures; chlorite, which has replaced biotite; and rutile, derived from titanite breakdown.

The quartz monzonites of the HE also have a K-feldspar cumulus texture, with Ca-amphibole as the main mafic intercumulus mineral. They are texturally similar to the coarse quartz monzonite from the KZD.

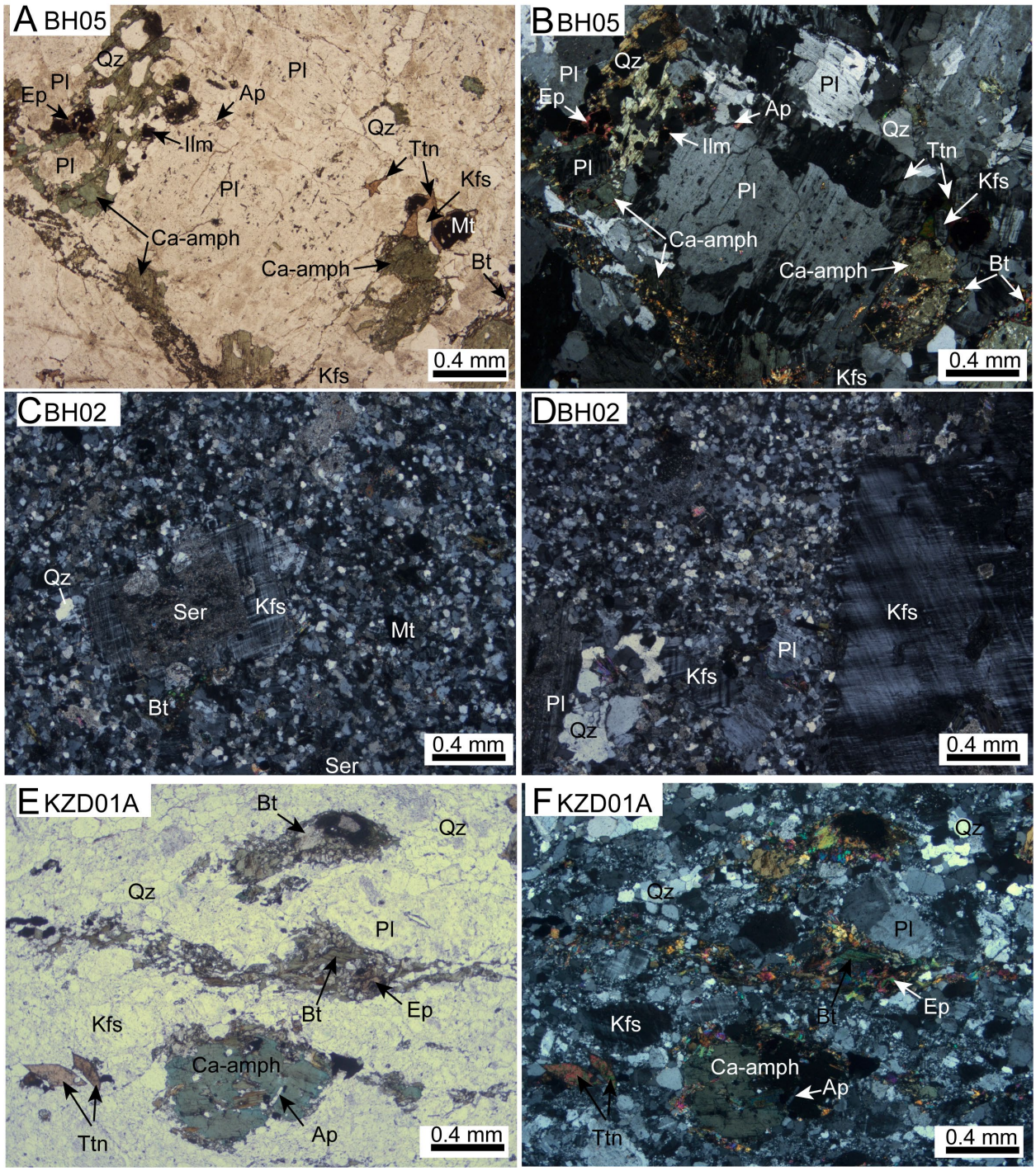

Figure 2-4. Photomicrographs of representative textures of the quartz monzonite from BAC. A-B) Illustration of the intercumulus anhedral crystals filling gaps between the K-feldspar and plagioclase in a medium-grained rock, under plane- and cross-polarized light, respectively. C-D) Quartz monzonite with a fine-grained matrix showing K-feldspar phenocrysts with variable alteration degree, under cross-polarized light. The fine-grained matrix is predominantly composed of anhedral plagioclase, K-feldspar, and quartz. E-F) Mylonitized quartz monzonite, with the generation of mineral alignment, augen crystals, quartz ribbon, and a matrix composed of recrystallized crystals, under plane-

and cross-polarized light. Ap: Apatite; Bt: Biotite; Ep: Epidote; Ilm: Ilmenite; Mt: Magnetite; Ser: Sericite; Ttn: Titanite.

2.4.2.2. Syenites

The syenites display coarse-grained porphyritic and textures defined by abundant angular euhedral K-feldspar phenocrysts, up to 3.0 cm, with perthitic, microperthitic and tartan exsolution (Figure 2-5 A-B), scarce homogeneous orthoclase (up to 2 cm) with Carlsbad twinning (Figure 2-5 C) and anhedral microcline which is altered (mottled texture), and exhibit myrmekite texture on its edges. The angular K-feldspar phenocryst exsolutions attest to its destabilization to microcline at low temperatures. The orthoclase phenocrysts display cumulus textures, whereas the subhedral to anhedral clinopyroxene and Ca-amphibole, subhedral to euhedral titanite and scarce anhedral quartz are the main intercumulus components (Figure 2-5 A-D). The K-feldspar phenocrysts display irregular and interlocked contacts with other crystals characteristic of cumulus textures (Figure 2-5 C) more often than what was reported for the quartz monzonites. Inclusions of previously crystallized minerals (e.g., apatite, opaque minerals, zircon) define growth zones on the larger K-feldspar crystals.

The matrix is composed of small anhedral microcline, anhedral plagioclase and scarce quartz crystals. The mafic minerals are anhedral to subhedral clinopyroxene, amphibole, and scarce biotite flakes. Biotite occurs rimming clinopyroxene, Ca-amphibole, Fe-Ti oxide minerals (ilmenite and magnetite), and filling fractures, suggesting its secondary origin. The accessory mineralogy is constituted by euhedral to subhedral diamond-shaped titanite, prismatic apatite, ilmenite, magnetite, zircon, and subhedral epidote.

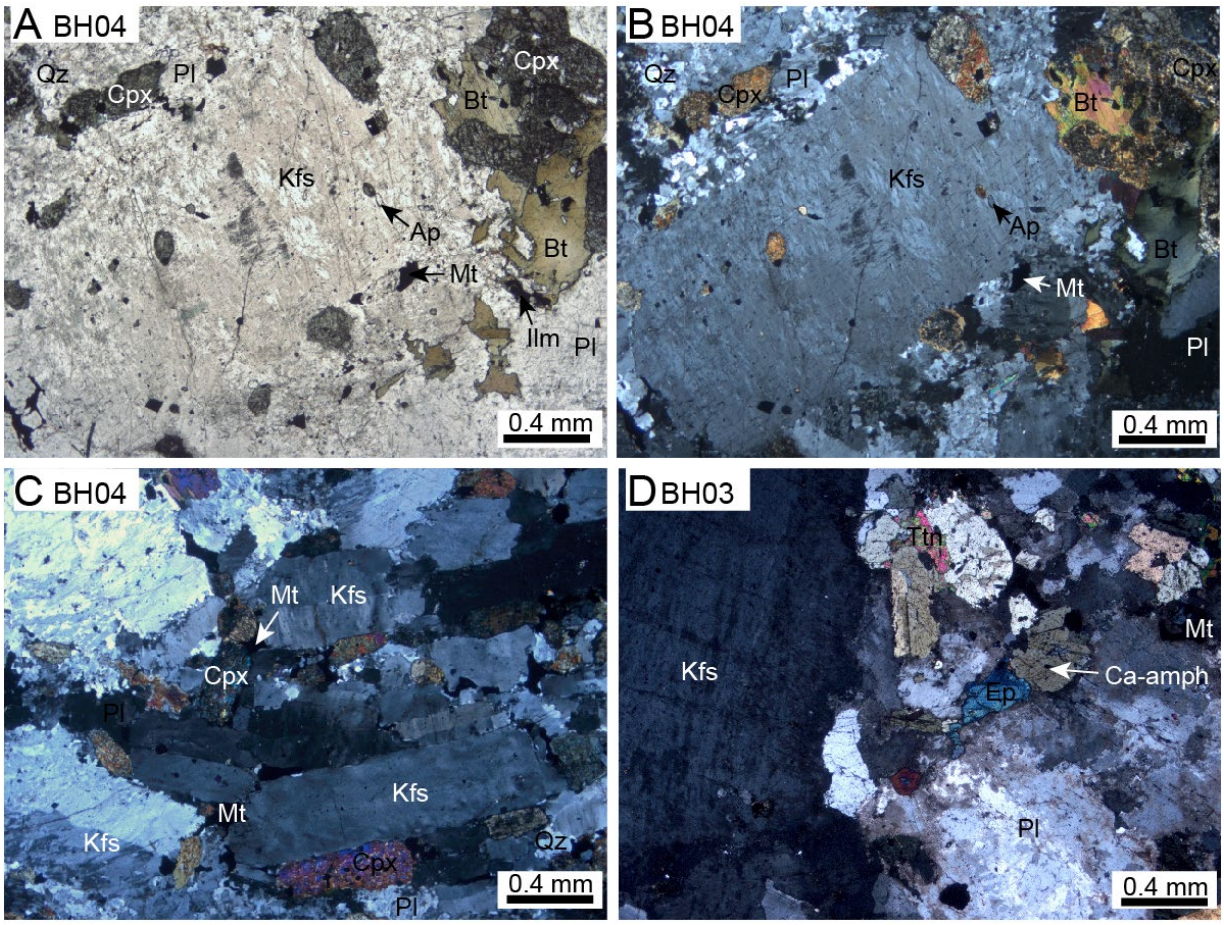

Figure 2-5. Photomicrography of representative textures of the porphyritic syenites. A-B) Angular euhedral K-feldspar phenocryst with perthite exsolution, apatite, and clinopyroxene inclusions under plane- and cross-polarized light, respectively. C) Homogeneous K-feldspar phenocrysts with interlocked contacts and mafic minerals as intercumulus phases under cross-polarized light. The clinopyroxene is partially replaced by amphibole. D). Titanite, epidote, and magnetite filling the feldspar interstices, under cross-polarized light.

2.4.2.3. Granite

The homogeneous granite carries anhedral K-feldspar phenocrysts (< 1.0 cm) but lacks the angular euhedral K-feldspar phenocrysts and cumulus textures described for the other rock types. The K-feldspar is mottled and poikilitic with small plagioclase inclusions. The subhedral and anhedral plagioclase phenocrysts (< 1.0 cm) exhibit very altered cores and myrmekitic texture on their edges. The quartz crystals occur as subhedral phenocrysts (< 0.6 cm) and anhedral crystals in the matrix. Anhedral microcline and plagioclase also constitute the matrix. The main mafic mineral is biotite, occurring as small flakes (< 2.0 mm). Accessory minerals include euhedral prismatic apatite, ilmenite, magnetite, pyrite, titanite, zircon, and rutile. Alteration minerals are muscovite and epidote from the feldspar alteration and chlorite from the biotite destabilization. The anisotropic granites are characterized by mineral alignment and polycrystalline quartz ribbons.

2.4.3. Whole-rock major and trace element geochemistry

The BAC rocks are classified as syenite, quartz monzonite, and granite (Table 2-2). Subsequently, the BAC granites were subdivided into two groups (low-K leucogranites and medium-K leucogranites) according to their major oxide signatures. The HE samples, on the chemical diagrams, clustered with the BAC rocks, in agreement with the textural similarities described.

Table 2-2. Whole-rock major element compositions (wt%) of the Boesmanskop Alkaline Complex and associated high-K rocks of the Heerenveen batholith.

Sample	Facies	SiO_2	TiO_2	Al_2O_3	FeO_T	MnO	MgO	CaO	K_2O	Na_2O	P_2O_5	LOI	Total	Mg#	$K_2O + Na_2O$	K_2O/Na_2O
BH03	Syenite	62.8	0.7	16.7	4.3	0.1	0.9	2.2	5.8	5.4	0.4	0.69	99.9	27.7	11.2	1.1
HE03		60.9	0.8	16.9	5.9	0.1	1.1	2.2	6.0	4.3	0.4	1.28	99.7	24.4	10.3	1.4
KZD03		64.4	0.7	15.6	4.8	0.1	1.2	2.2	5.1	4.8	0.4	0.84	100.3	30.9	10.0	1.1
BH18		63.0	0.7	16.7	4.5	0.1	1.0	2.2	5.8	5.4	0.4	0.54	100.4	29.0	11.2	1.1
KZD04		63.7	0.8	15.4	5.2	0.1	1.4	2.2	5.4	4.6	0.5	0.86	100.0	31.8	10.1	1.2
BH04		59.0	0.9	16.5	6.7	0.2	1.5	3.2	5.2	5.4	0.6	0.74	99.8	29.0	10.6	1.0
BH02	Quartz monzonite	68.8	0.4	15.8	2.7	0.1	0.5	1.2	4.5	4.8	0.2	1.06	99.9	24.9	9.3	0.9
KZD09		65.2	0.7	16.3	3.8	0.1	1.2	1.3	5.0	5.1	0.4	1.00	100.0	35.2	10.0	1.0
BH11		68.4	0.5	15.0	3.3	0.1	0.7	1.4	4.7	4.6	0.3	0.89	99.8	27.3	9.3	1.0
BH09		67.7	0.5	15.2	3.7	0.1	0.8	1.6	4.8	4.8	0.3	0.83	100.2	26.7	9.5	1.0
BH14		66.8	0.5	16.0	3.3	0.1	0.8	1.7	4.8	4.7	0.2	1.67	100.5	28.6	9.5	1.0
KZD02		67.3	0.6	15.2	3.8	0.1	0.9	1.7	4.8	4.5	0.3	0.69	100.0	30.3	9.4	1.1
BH1A		68.6	0.6	15.0	3.6	0.1	0.8	1.8	3.7	4.7	0.3	0.83	100.0	28.5	8.4	0.8
BH13		67.4	0.4	16.1	3.1	0.1	0.6	1.9	5.0	4.6	0.2	0.50	99.7	26.8	9.5	1.1
BH06A		66.0	0.7	15.6	4.1	0.1	0.9	1.9	4.9	4.6	0.4	0.94	100.0	27.9	9.6	1.1
BH06B		65.6	0.8	15.5	4.3	0.1	1.0	2.1	4.8	4.6	0.4	1.15	100.2	28.1	9.4	1.1
KZD01A		67.1	0.6	15.1	3.7	0.1	0.8	2.1	4.8	4.6	0.3	0.71	99.9	26.8	9.4	1.0
BH07		65.1	0.7	15.5	4.5	0.1	1.0	2.2	4.9	4.7	0.4	0.81	99.9	28.5	9.6	1.0
BH16		66.2	0.7	15.5	4.0	0.1	0.9	2.2	4.9	4.2	0.3	0.85	99.8	29.5	9.1	1.2
HE02		63.7	0.7	16.7	4.6	0.1	0.9	2.5	4.3	5.0	0.4	0.91	99.7	26.2	9.2	0.9
HE05		63.5	0.6	16.6	4.6	0.1	0.8	2.5	4.9	5.0	0.4	0.70	99.8	24.4	9.9	1.0
BH05		62.8	0.9	15.3	5.4	0.1	1.5	3.0	4.9	4.7	0.6	0.76	99.9	32.6	9.6	1.1
HE04	Medium-K leucogranite	71.0	0.3	14.9	2.5	0.0	0.4	0.8	4.6	4.2	0.2	1.09	100.0	23.5	8.8	1.1
BT03A		76.7	0.0	13.6	0.5	0.0	0.0	0.3	2.7	5.5	BD	1.06	100.3	0.0	8.2	0.5
BH12		71.6	0.3	14.3	3.1	0.0	0.3	1.0	4.2	4.1	0.1	1.10	100.0	12.9	8.3	1.0
BT01		73.7	0.3	14.2	1.6	0.0	0.2	1.2	3.3	4.6	0.1	0.78	100.0	17.2	7.9	0.7
BT04A		74.0	0.2	14.9	1.1	0.0	0.1	1.2	3.0	5.0	0.0	1.02	100.6	15.9	8.0	0.6
KZD06	Low-K leucogrante	71.7	0.2	16.0	2.0	0.0	0.4	2.9	1.2	5.3	0.1	0.49	100.3	27.7	6.5	0.2
KZD05		71.0	0.2	16.3	1.8	0.0	0.5	2.9	1.4	5.3	0.1	0.91	100.5	34.2	6.7	0.3
BH08A		69.0	0.4	16.6	1.4	0.0	0.7	3.4	0.8	6.7	0.1	1.15	100.3	45.1	7.5	0.1
BH17*		69.3	0.2	17.2	1.8	0.0	0.7	2.8	1.2	6.5	0.1	0.49	100.3	41.0	7.7	0.2

FeO_T = FeO + Fe_2O_3; LOI = Loss on ignition; Mg# = cationic Mg/(Mg+Fe)

2.4.3.1. Major elements

The BAC samples have low degrees of alteration (loss on ignition < 1.7 wt%) and are silica-saturated, with the syenites predictably representing the rock type with the lowest normative Qz values (supplementary material). Despite the small geographic extent of the BAC in comparison with the whole GMS suite, its geochemistry exhibits significant variability, encompassing most of the compositional range reported for the entire GMS suite (Figure 2-6 A).

The rocks described petrographically as syenites have SiO_2 contents ranging from 58.9 to 64.4 wt% and plot within the syenite field of the TAS diagram, except for one sample (sample KZD03), which plots in the quartz monzonite field, close to the boundary with the syenite field. The syenites have Mg#s ranging from 24 to 32. Their K_2O+Na_2O values range from 9.9 to 11.2 wt%, while the K_2O/Na_2O range from 1.0 to 1.4 (Table 2-2).

The quartz monzonites classify as alkaline and have SiO_2 contents that vary from 62.8 to 68.8 wt%, K_2O+Na_2O < 10.0 wt%, Mg#s varying from 24 to 35 wt%, and K_2O/Na_2O ratios from 0.8 to 1.2. The single exception is sample HE04, which has higher SiO_2 (70.9 wt%), less K_2O+Na_2O (8.8 wt%) and classifies as subalkaline.

The BAC granite samples were subdivided into two geochemical types, following the Moyen et al. (2021) classification: low-K leucogranite (0.75 to 1.5 wt% K_2O) and medium-K leucogranite (2.7 to 4.2 wt% K_2O). The low-K leucogranites are characterized by SiO_2 values that vary from 69.0 to 71.7 wt%, K_2O+Na_2O ranging from 6.5 to 7.7 wt% and Mg#s from 28 to 45, whilst the medium-K leucogranites SiO_2 values range from 71.5 to 76.7 wt%, with higher total alkali contents (7.9 to 8.3 wt%) and lower Mg#s (< 17).

The syenite, quartz monzonite, and medium-K leucogranite rocks belong to the potassic series, whereas low-K leucogranites plot on the sodic series (Figure 2-6 B). The studied quartz monzonites, syenites, and low-K leucogranites are metaluminous. On the other hand, the medium-K leucogranite is metaluminous to slightly peraluminous (Figure 2-6 C).

On Harker diagrams, the BAC rocks are characterized by low MgO content (< 1.6 wt%), low CaO (<3.41 wt%) and low Mg#s relative to the broader GMS suite (Figure 2-7 A-F), the low-K leucogranite data plot off the main BAC trend and the syenite and quartz monzonite Na_2O and K_2O contents remain relatively constant within the SiO_2 interval for each rock type (Figure 2-7 B-C).

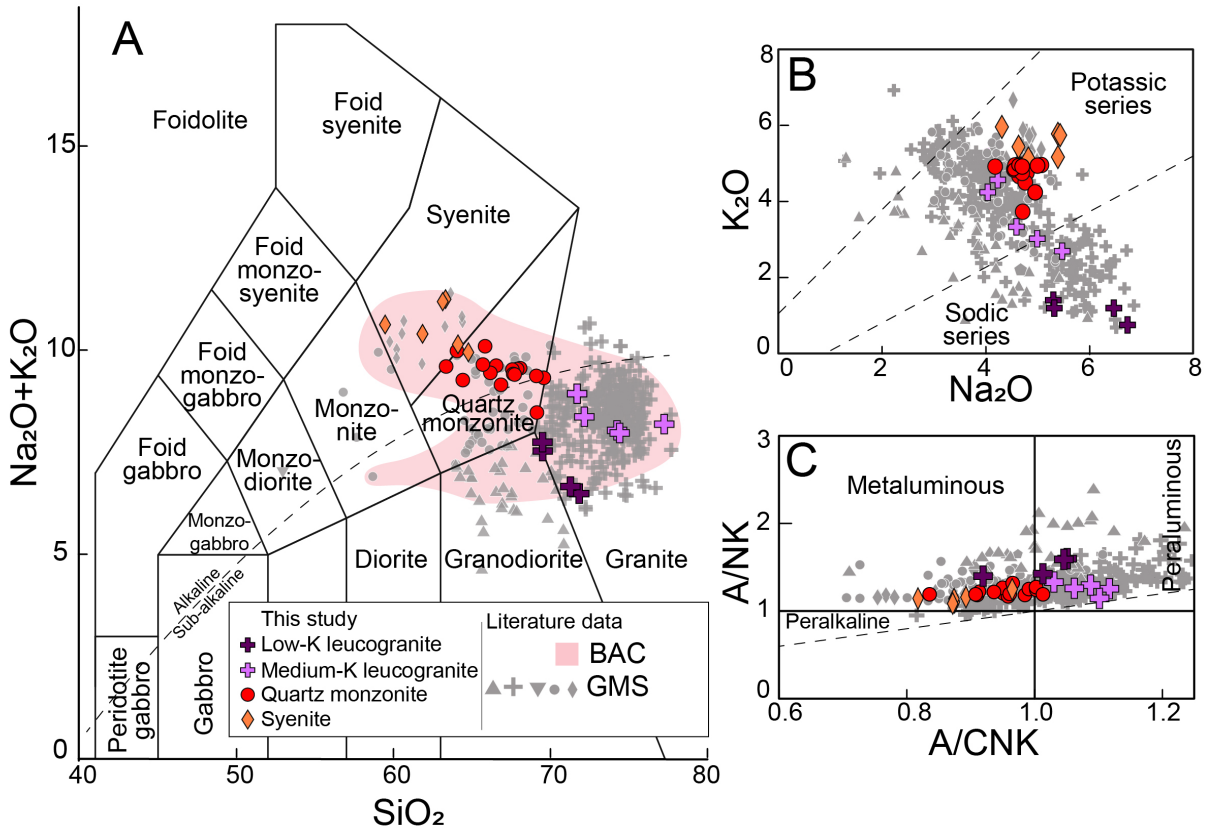

Figure 2-6. Chemical classification diagrams of BAC rocks. A) Plot of total alkalis vs silica (TAS) diagram (Middlemost, 1994) showing BAC and GMS suite compositions. B) K_2O vs Na_2O (wt%) diagram with the potassic and sodic series fields of Middlemost (1975). C) Peralkalinity vs Alumina Saturation Index diagram of Shand (1943); A/CNK = molar Al/(2*Ca+Na+K); A/NK = molar Al/(Na+K). The GMS data are from Anhaeusser and Robb, 1983; Westraat et al., 2005; Moyen et al., 2021. The shapes of the symbols correspond to the chemical classification of the rocks.

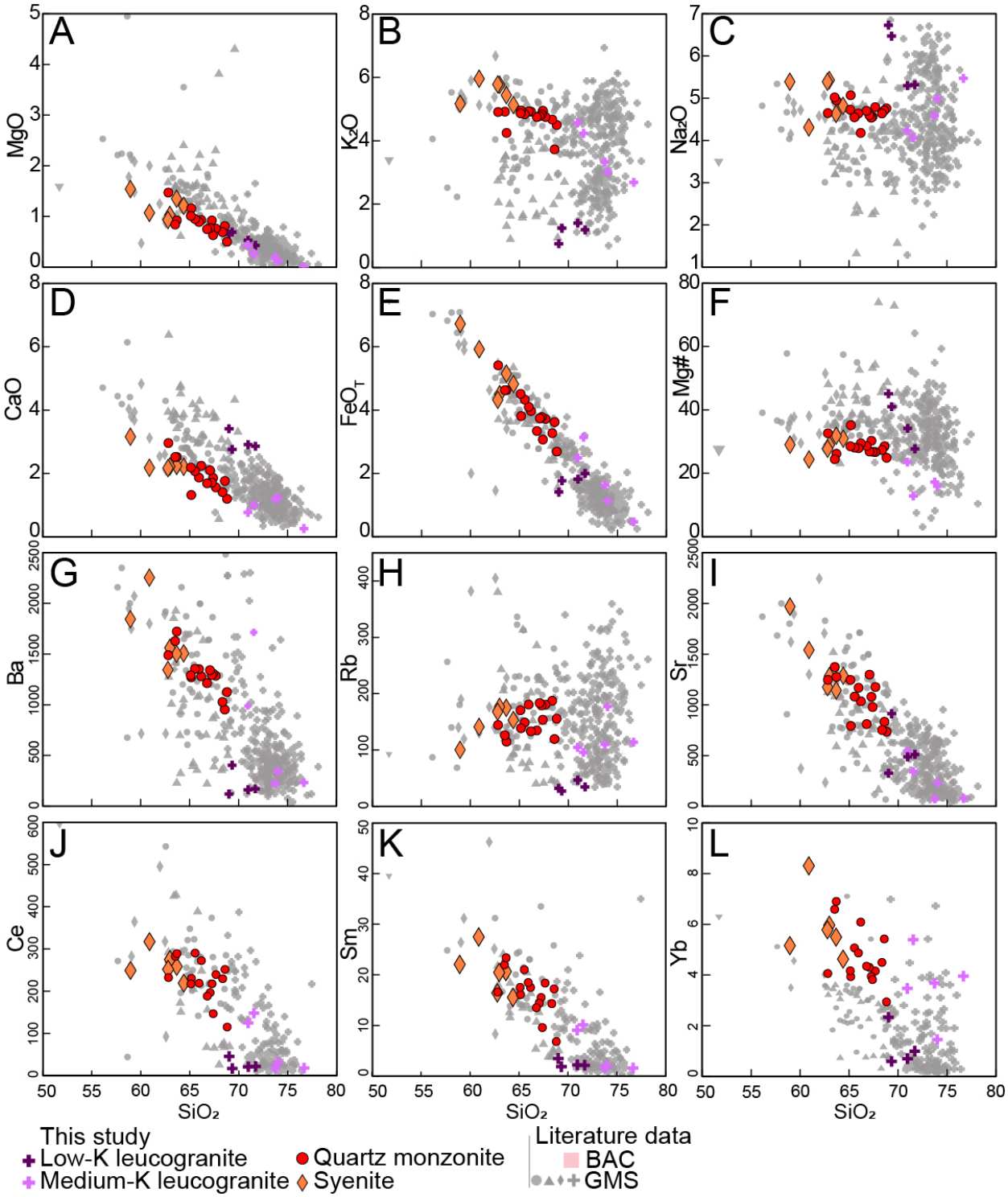

Figure 2-7. The data from Fig. 2-6 plotted on Harker diagrams for relevant major (wt%), trace element (ppm) and REE (ppm) vs SiO_2 (wt%). The graphs illustrate that the BAC rocks do have the highest contents of trace element except for Rb, and high REE relative to the GMS rocks. A) MgO vs SiO_2; B) K_2O vs SiO_2; C) Na_2O vs SiO_2; D) CaO vs SiO_2; E) FeO_T vs SiO_2; F) Mg# vs SiO_2; G) Ba vs SiO_2; H) Rb vs SiO_2; I) Sr vs SiO_2; J) Ce vs SiO_2; K) Sm vs SiO_2; L) Yb vs SiO_2. Mg# = cationic Mg/(Mg+Fe).

2.4.3.2. Trace elements

All BAC rock types present low contents of transition elements (i.e., V, Cr, Ni), with Ni, ranging from 23.2 to 5.6 ppm and Cr from 23.6 to 6.0 ppm and high LILE contents (Table 2-3). The syenites contain high Sr and Ba contents, with Sr < 1970 ppm and Ba < 2260 ppm, which is higher or similar amounts to those found in the quartz monzonite (Sr< 1380 ppm, Ba < 1730 ppm; Figure 2-7 G-I). The trace elements and REE exhibit negative trends with SiO_2 (Figure 2-7). The BAC syenites and quartz monzonites have the highest contents of incompatible elements within the GMS suite. The only exception is the granite data from the literature, which have higher reported Rb contents than the samples analyzed for this study (Figure 2-7 H). The low-K leucogranite shows low Rb contents (< 50 ppm), whereas the medium-K leucogranite has Rb contents between 95 and 180 ppm.

The syenite and quartz monzonite have similar REE and incompatible element patterns, marked by preferential enrichment of LREE over HREE, $(La/Yb)_{CN}$ ratios from 24.7 to 36.6 for the syenites and 23.5 to 42.0 for the quartz monzonites, strong negative HFSE anomalies for Nb, Ta, P, and Ti, positive anomalies for Rb, Ba, Th, Pb, and Sr. They present a weak negative Eu anomaly (Eu/Eu* 0.6 to 1.0), (Figure 2-8 A-D).

The heterogeneous nature of the granites is corroborated by their REE and trace element signatures; however, all of them are characterized by LREE enrichment over HREE and Nb, Ta, P and Ti negative anomalies (Figure 2-8 E-F). The low-K leucogranites contain the lowest REE contents from the BAC. These granites are the only BAC rocks with positive Eu anomaly (Eu/Eu* from 1.4 to 1.9) and strong Pb positive anomaly.

The medium-K leucogranites exhibit two distinct REE signatures that can be linked to their K_2O content. The leucogranites with K_2O from 5 to 4 wt% present weak Pb enrichment, akin to the signature observed at the quartz monzonite and syenites. Meanwhile, medium-K leucogranites with K_2O from 3.5 to 2.5 wt% present a signature similar to that of low-K leucogranite. They also exhibit a REE seagull-like pattern with negative Eu anomaly (Eu/Eu* 0.5 to 0.6).

Table 2-3. Whole-rock relevant trace element contents (ppm).

Sample	Facies	Sc	V	Cr	Ni	Cu	Rb	Sr	Y	Zr	Nb	Ba	Ce	Sm	Eu	Yb	Th	U	Eu/Eu*
BH03	Syenite	7	45	9	7	17	168	1175	36	641	29	1344	253	17	4	3	14	3	0.9
BH04		10	84	10	10	15	100	1969	41	449	9	1844	250	22	6	3	3	1	1.0
HE03		8	64	8	9	22	141	1541	52	548	26	2254	319	28	6	4	11	3	0.8
KZD03		8	57	14	12	16	153	1287	26	431	22	1507	220	16	4	2	14	3	0.9
KZD04		8	58	14	13	22	175	1143	41	436	25	1502	260	21	5	3	17	4	0.8
BH18		11	50	11	10	82	177	1284	47	633	29	1560	276	21	5	3	17	4	0.9
BH02	Quartz monzonite	6	26	10	8	12	156	736	15	257	17	1125	115	7	2	2	12	3	0.9
BH05		9	68	18	16	22	144	1246	31	396	21	1489	233	17	4	2	15	4	0.8
BH06A		7	45	11	11	18	181	1169	36	373	22	1352	220	19	4	2	16	4	0.8
BH06B		7	48	12	10	24	149	1081	39	383	27	1354	292	21	5	3	17	4	0.8
BH07		7	49	12	11	17	171	1246	33	400	22	1290	218	18	4	2	19	5	0.8
BH09		7	42	11	11	22	181	1177	25	339	16	1286	240	19	5	2	17	4	0.9
BH11		6	33	9	10	19	187	752	30	334	24	1028	230	14	3	2	29	6	0.7
BH13		6	29	10	8	15	154	979	24	272	16	1307	147	10	2	2	11	3	0.8
BH14		6	36	9	8	41	135	810	28	298	18	1213	189	14	3	2	13	3	0.8
BH16		7	45	15	12	19	133	1035	39	444	32	1280	273	18	4	3	17	3	0.8
BH1A		7	42	12	10	16	119	833	38	399	27	953	253	17	3	3	18	3	0.6
HE02		6	53	8	10	21	115	1275	60	442	21	1722	290	24	6	4	15	4	0.8
HE05		7	53	10	9	20	126	1373	52	426	23	1629	283	22	5	3	15	4	0.8
KZD01A		6	42	10	10	10	183	1298	30	343	20	1342	197	14	3	2	25	5	0.9
KZD02		6	41	11	9	14	179	1079	29	367	22	1294	218	16	4	2	22	5	0.8
KZD09		7	42	16	9	5	139	792	30	386	26	1271	231	16	4	2	23	5	0.9
BH12	Medium-K leucogranite	7	16	6	9	21	96	342	35	393	13	1715	148	10	3	3	19	4	0.9
BT01		4	7	17	19	5	110	73	14	41	12	222	17	2	0	2	6	3	0.6
BT03A		4	7	16	23	5	114	76	14	44	12	232	17	2	0	2	6	3	0.5
BT04A		4	11	6	7	7	177	230	8	77	7	341	31	2	0	1	6	2	0.6
HE04		4	26	7	8	20	105	543	18	216	13	988	125	9	2	2	10	3	0.9
BH17*	Low-K leucogrante	10	18	18	18	65	27	912	2	108	2	404	16	1	1	0	1	0	1.9
BH08A		5	34	24	19	22	32	325	10	436	7	119	45	3	1	1	6	3	1.4
KZD05		4	21	10	9	5	46	487	3	95	2	161	20	1	1	0	1	1	1.5
KZD06		4	18	6	6	11	34	512	2	100	2	170	21	1	1	0	2	0	1.5

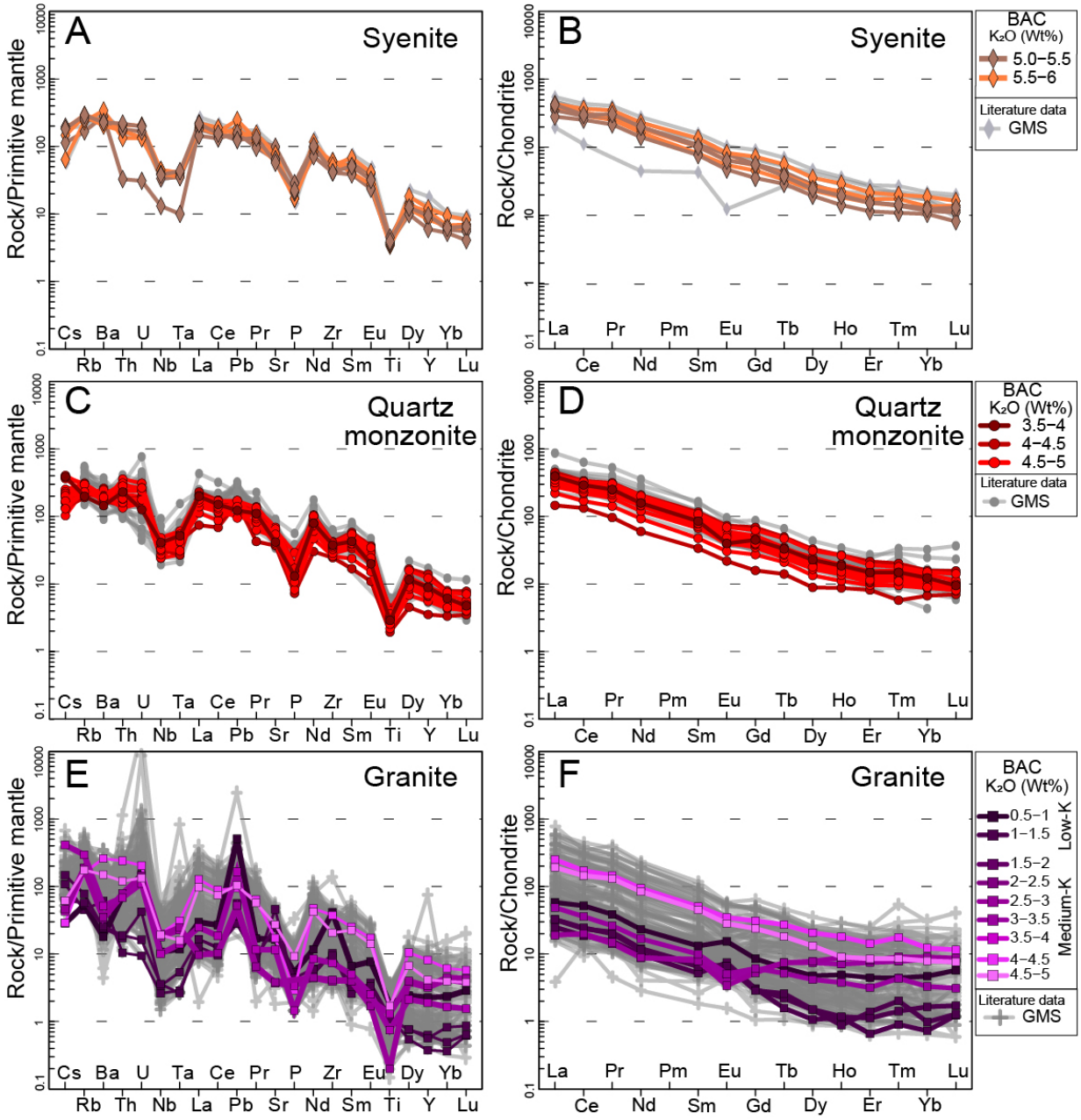

Figure 2-8. Spider diagram for trace elements and REE normalized to the Primitive Mantle (McDonough and Sun, 1995) and chondrite (Nakamura, 1974), respectively. A-B) Plot of the syenite compositions. C-D) Plot of the quartz monzonite compositions. E-F) Plot of the BAC granite compositions. The BAC rocks are subdivided according to their K_2O content.

2.4.4. Mineral compositions

2.4.4.1. Mafic minerals

Clinopyroxene in the syenites and quartz monzonites is diopside ($Wo_{43-48}En_{39-42}Fs_{10-15}$), (Figure 2-9 A). The clinopyroxene crystals have high MREE, in comparison with the LREE and exhibit a prominent negative Eu anomaly, indicating crystallization from a melt composition shaped by prior crystallization of feldspar (Figure 2-10 A).

The primary amphibole in the syenites is predominantly Mg-hornblende and Mg-hastingsite, with a minor population of pargasite crystals. These distinct populations often coexist within the same sample. The secondary amphibole is edenite and actinolite (Figure 2-9 B). This chemical diversity is also evident in the REE signatures, with primary crystals with high LREE over the HREE, whereas the secondary crystals are

depleted in the LREE over the HREE (Figure 2-10 B). Moreover, titanite crystals contain high LREE in comparison with the HREE, with the LREE values exceeding chondrite values by 10,000 times, demonstrating that this mineral is an important phase controlling the REE contents of the syenites and quartz monzonites.

Following the classification of Tischendorf et al. (1999), the leucogranites contain Fe-biotite, and the syenites and quartz monzonites contain Mg-biotite crystals. The nature of the biotite can be inferred by the TiO_2, FeO + MnO, and MgO (wt%) contents as proposed by Nachit et al. (2005). The low Ti contents of the Mg-biotite from syenites suggest they are secondary crystals, which agrees with their described texture (Figure 2-5). The biotite of the quartz monzonites exhibits compositions of reequilibrated crystals and the Fe-biotite of the leucogranites preserves primary chemical compositions (Figure 2-9 C). The correlation of these textures and oxides suggests that the biotite in the leucogranites crystallized directly from the parental magma, whereas the biotite in the quartz monzonites and syenites represents crystals formed by post-magmatic breakdown of earlier Fe-Mg crystals (e.g., pyroxene, amphibole). Hence, the parental magmas of the leucogranites crystalized within the stability field of biotite. In contrast, the magmas that formed the syenites and quartz monzonites were either too hot or too H_2O-poor to form primary biotite (e.g., Nachit et al., 2005), clearly as K-feldspar rich rocks they contained sufficient K_2O.

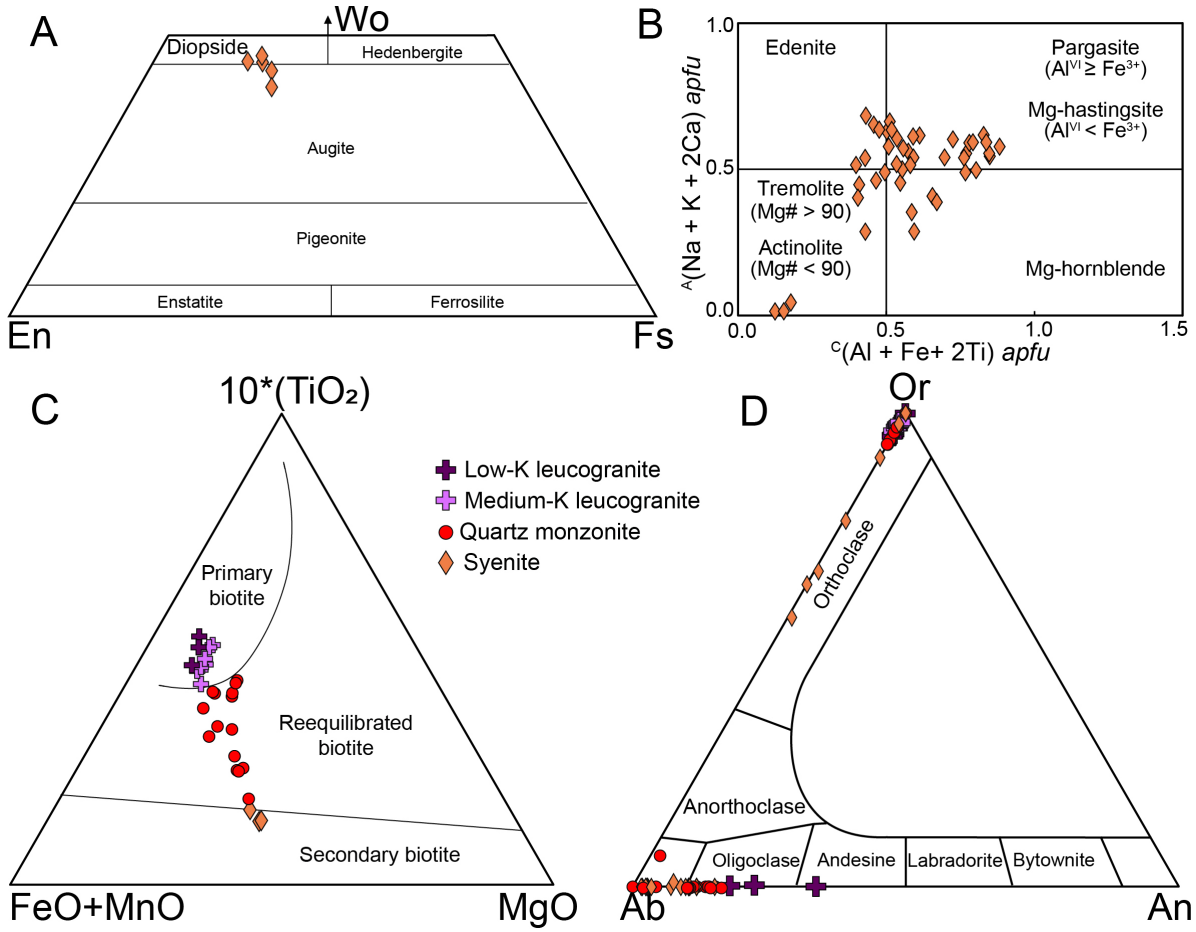

Figure 2-9. A) BAC pyroxene compositions plotted on a Wollastonite-Enstatite-Ferrosillite (Wo-En-Fs) ternary diagram for pyroxene classification (Morimoto, 1988). B) Amphibole compositions plotted on the classification diagram (Hawthorne et al., 2012). C) Biotite compositions plotted on a ternary biotite classification diagram of Nachit et al. (2005). D) BAC feldspar

compositions plotted on an Albite-Anorthite-Orthoclase (Ab-An-Or) ternary diagram illustrating the low calcium content of the plagioclase in the syenitic rocks relative to the granites. Apfu: atoms per formula unit.

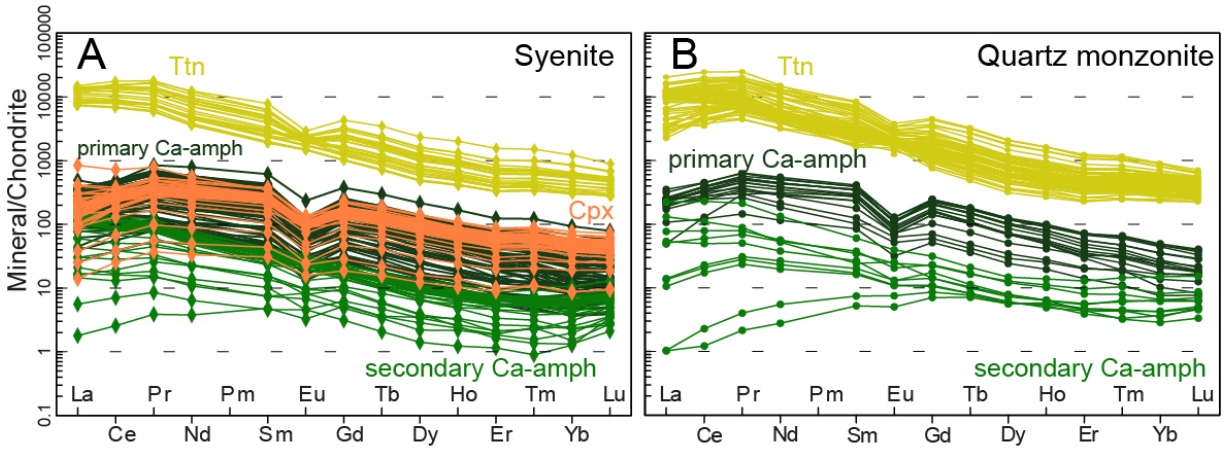

Figure 2-10. REE spider diagram for titanite, clinopyroxene, and amphibole in the A) syenite and B) quartz monzonite Chondrite normalized (Nakamura, 1974).

2.4.4.2. Feldspar

The alkali-feldspar is commonly perthitic and microperthitic, with the exsolved components plotting close to pure endmember compositions (Figure 2-9 D). Nevertheless, in the syenite and quartz monzonite, homogeneous K-feldspar occurs with compositions in the range of Or_{77-56}. These crystals are orthoclase and commonly present more albitic rims. The K-feldspar crystals in the quartz monzonite have BaO contents up to 0.75 wt%; in the syenites, this value is up to 1.07 wt%. The most common plagioclase in all the BAC rocks is oligoclase and has anorthite values up to 22. However, plagioclase with higher anorthite contents is found in the low-K leucogranite ($<An_{34}$).

2.4.5. Sr and Nd isotopic ratios

The syenites and quartz monzonites have low $^{143}Nd/^{144}Nd_{(t)}$ ratios that range from 0.50851 to 0.50864 with $\varepsilon Nd_{(t)}$ values between –1.7 and +0.8, using a crystallization age of 3107 ±2 Ma (Kamo and Davis, 1994); T_{DM} ages lie between 3.37 to 3.18 Ga. The $^{87}Sr/^{86}Sr_{(t)}$ ratios range from 0.70240 to 0.70134 (Table 2-4; Figure 2-11). The BAC medium-K leucogranite has the lowest $^{143}Nd/^{144}Nd_{(t)}$ ratio of 0.50847, an $\varepsilon Nd_{(t)}$ value of -2.6, and a T_{DM} age of 3.49 Ga.

The $\varepsilon Nd_{(t)}$ values gathered from the literature for the GMS granites are negative, and the $^{87}Sr/^{83}Sr_{(t)}$ exhibit a wider range than the values recorded from syenites and quartz monzonites of this study (Figure 2-11 B). The Nd and Sr isotopic data available in the literature for TTG suite gneisses of the BGGT were mostly produced during the 1980s and contain some very unlikely values, such as $^{87}Sr/^{86}Sr_{(t)}$ below 0.700 (e.g., Barton et al., 1983a,b; Robb et al., 1986). Nevertheless, $^{143}Nd/^{144}Nd_{(t)}$ values range from 0.50789 to 0.50878 and $\varepsilon Nd_{(t)}$ from -5.0 to 7.4 (Barton et al., 1983b; Robb et al., 1986; Yearron, 2003; Schoene et al., 2009). These isotopic values overlap those of the GMS suite and the BAC rocks.

Table 2-4. Rb/Sr and Sm/Nd isotopic data of representative rocks, for 3107 Ma crystallization age.

Sample	Rb (ppm)	Sr (ppm)	$^{87}Rb/^{86}Sr$	±1σ internal	$^{87}Sr/^{86}Sr$ measured	±2σ internal	$^{87}Sr/^{86}Sr_{(t)}$	error (abs)	$\varepsilon Sr_{(t)}$		
KZD09	138.6	791.8	0.5073	0.0051	0.724266	0.00001	0.70138	0.00023	279		
BH07	170.7	1245.7	0.3970	0.0040	0.719630	0.00001	0.70172	0.00018	213		
HE05	126.1	1373.2	0.2658	0.0027	0.714400	0.00001	0.70241	0.00012	139		
BH03	167.7	1174.6	0.4137	0.0041	0.720004	0.00001	0.70134	0.000274	219		
BH04	100.2	1969.3	0.1473	0.0015	0.707990	0.00001	0.70135	0.000211	48		
Sample	**Sm (ppm)**	**Nd (ppm)**	$^{147}Sm/^{144}Nd$	error (%)	$^{143}Nd/^{144}Nd$ measured	±2σ internal	$^{143}Nd/^{144}Nd_{(t)}$	error (abs)	$\varepsilon Nd_{(t)}$	error	T_{DM} (Ga)
KZD09	16.2	99.5	0.09833	0.00010	0.51053	0.00001	0.5085	0.000021	-1.8	0.42	3.4
BH07	17.6	105.6	0.10087	0.0010	0.51065	0.00001	0.5086	0.000023	-0.5	0.46	3.3
HE05	22.1	126.9	0.10527	0.0010	0.51076	0.00001	0.5086	0.000025	0.0	0.49	3.2
BH03	16.5	103.9	0.09610	0.0010	0.51062	0.00001	0.5086	0.000023	0.9	0.44	3.2
BH04	22.2	125.0	0.10722	0.0010	0.51077	0.00001	0.5086	0.000025	-0.5	0.48	3.3
BT04A	2.0	10.6	0.11514	0.0011	0.51083	0.00001	0.5085	0.000026	-2.6	0.50	3.5

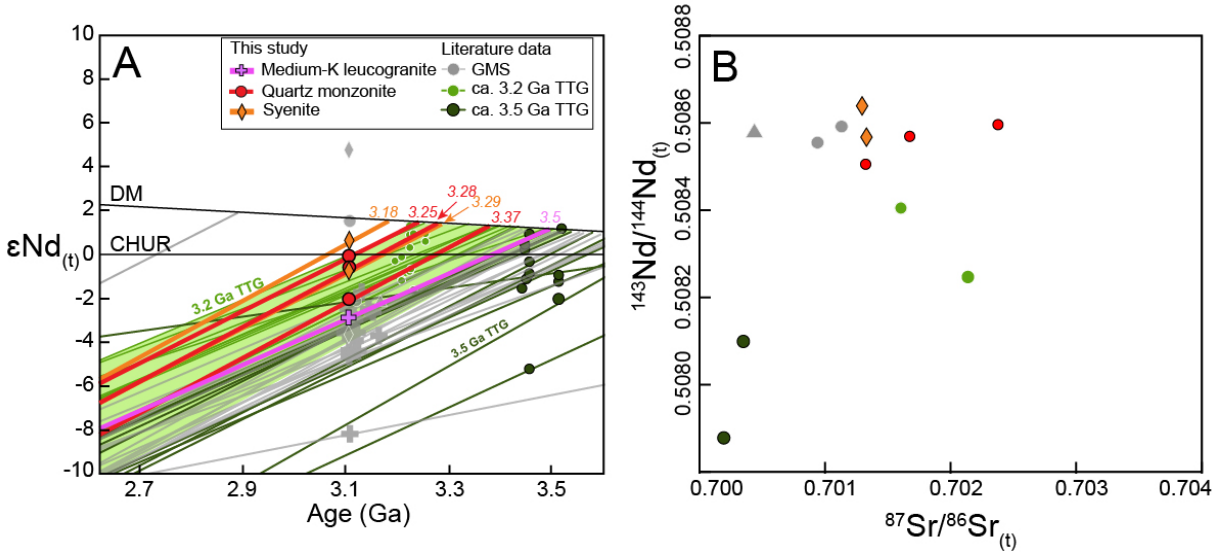

Figure 2-11. Binary diagrams depicting the relevant radiogenic isotope compositions of the BAC and spatially related TTG and GMS suite. A) εNd(t) vs U-Pb age. B) $^{143}Nd/^{144}Nd_{(t)}$ vs $^{87}Sr/^{86}Sr_{(t)}$. DM: Depleted Mantle; CHUR: Chondritic Uniform Reservoir. The green areas represent the isotopic evolution with time of the TTG rocks. Data from the literature are 3.45 TTG (Barton et al., 1983b; Robb et al., 1986); 3.23 TTG (Schoene et al., 2009); GMS suite (Yearron, 2003; Moyen et al., 2021).

2.4.6. Modeling fractional crystallization processes

2.4.6.1. Input parameters

The absence of mafic rocks that are cogenetic with the syenites, coupled with their very low Mg#s, Cr and Ni contents, as well as their generally quartz-normative character, suggests that the BAC syenitic rocks likely originated from crustal sources. To investigate this hypothesis, phase equilibrium modeling experiments were conducted to explore the possibility of producing cumulus syenites and quartz monzonites through fractional crystallization (FC) of granitic magmas under upper-crust conditions.

To simulate the FC process, the Rcrust software was set to remove the melt from the system whenever the crystal volume reached 20%. All but 1% of the melt was removed to simulate a small amount of interstitial melt trapped between crystals. During these modeling experiments the early-formed mineral assemblage would represent the cumulus rocks formed by melt loss from the system. In this context, K-

feldspar needs to be the predominant tectosilicate phase to form during the early stages of crystallization to produce rocks akin to the K_2O-rich syenites of the BAC.

The temperature interval of the experiments was set to range from 950 to 800 °C. While the modeling was set at 1.5 kbar, in agreement with the brittle fracture features, hypabyssal textures, dyke, and horizontal sheet structures that were observed at the lower portions of the BH, suggesting magma emplacement at low pressure (Figure 2-3).

The presence of primary amphibole and secondary biotite in the syenites and quartz monzonites indicate a relatively water-poor magma. This idea is reinforced by the work of Bonin et al. (1998), which proposes that in water-poor magmas, amphibole will crystallize, and silica-saturated to oversaturated alkaline trends will be produced. Consequently, the magmas were modeled using 1.5 wt% of H_2O in the initial bulk composition, as this was the maximum water content that allowed the system to remain H_2O-undersaturated. To investigate the effect of lower water contents, experiments were also conducted using 1.0 and 0.5 wt% H_2O.

Despite the wide compositional range that characterizes the GMS suite, granites are the predominant rock type of the suite and frequently occur as fine-grained rocks, as reported for the BT and BH sill. Furthermore, the Mg# of the melt in equilibrium with the composition of the clinopyroxene in the syenites was estimated as ranging from 37 to 42 (based on Kd(cpx-liq)(Fe-Mg) = 0.23); this suggests equilibrium with felsic magmas (e.g., Bédard, 2010). These characteristics led us to utilize the more potassic GMS granite compositions as possible initial melts in the modeling. Additionally, the CaO content should be sufficient to allow the crystallization of clinopyroxene, while the alkalis should be high enough to crystalize K-feldspar as an early tectosilicate. Consequently, the granodiorites of the GMS suite were not suitable as potential parental melts to the syenites nor quartz monzonites due to their high CaO contents relative to K_2O.

2.4.6.2. Crystal cumulates modeled

The modeling experiments using a GMS granite subset with $K_2O+Na_2O > 9.3$ wt% and low CaO (<1.4 wt%) stabilized significant volumes of K-feldspar prior to plagioclase and the K-feldspar coexisted with a mineral assemblage matching that observed in the BAC syenites and quartz monzonites (Figure 2-13 A). These experiments suggest that FC of granitic magmas with compositions similar to common GMS rocks produced K-feldspar-rich cumulate rocks that are compositionally akin to the BAC syenites and quartz monzonite under the specified intracrustal conditions (Figure 2-12). Conversely, magma compositions with $K_2O+Na_2O < 9.3$ wt% stabilized plagioclase before K-feldspar, which suggests they are likely not suitable to represent parental magmas for the syenites and quartz monzonites (Figure 2-13 B).

Two initial compositions of samples of the Mpuluzi batholith reported by Anhaeusser and Robb (1983) are plotted on the TAS diagram (Figure 2-12) to illustrate the K_2O+Na_2O values that are theoretically

capable of producing paragenesis and cumulus rock geochemistry compatible with the natural syenites and quartz monzonite within the set P-T-X conditions (sample MF1 and JG8; Table 2-5). The sample MF1 contains a higher total alkali amount (10.24 wt%) than sample JG8 (9.34 wt%). For these two compositions, the lowest water content composition (0.5 wt%) produced its first crystal extraction between 945 and 935 °C whilst the higher water content composition (1.5 wt%) experienced its first crystal extraction between 855 and 835 °C.

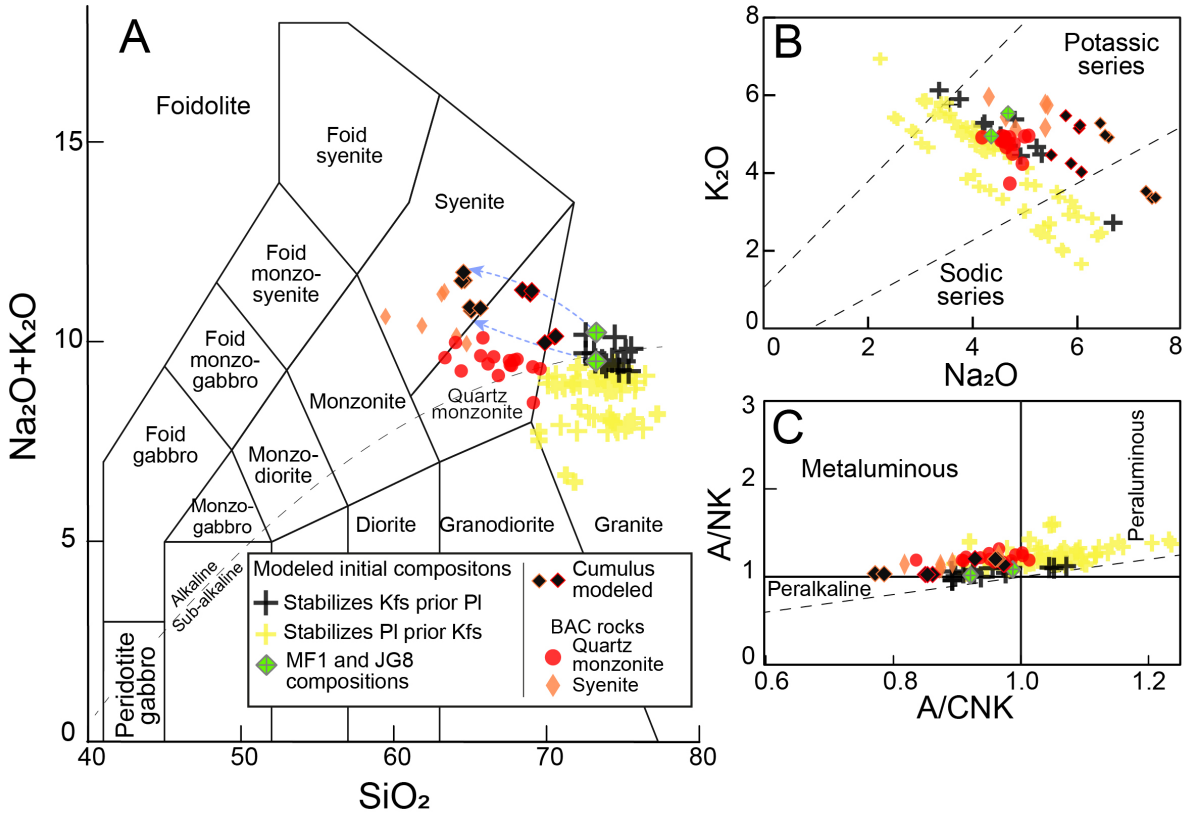

Figure 2-12. Comparison of the modeled cumulate rock compositions and the natural BAC rocks. A) TAS diagram (Middlemost, 1994). B) Binary diagram K_2O vs Na_2O (wt%) with potassic and sodic series field delimitation of Middlemost (1975). C) Peralkalinity vs Alumina Saturation Index (Shand, 1943).

Table 2-5. Whole-rock composition of representative initial melts modeled that can crystalize K-feldspar prior plagioclase and compositions of theoretical cumulus rocks produced by the FC with three initial H_2O contents.

Phases	Initial H_2O	SiO_2	TiO_2	Al_2O_3	FeO_T	MgO	CaO	K_2O	Na_2O	Mg#	K_2O + Na_2O
Initial composition - MF1	-	*73.4*	*0.2*	*14.0*	*1.1*	*0.4*	*0.8*	*5.5*	*4.7*	*36.1*	*10.2*
1st extraction	0.5	64.6	0.8	16.8	2.0	1.1	3.1	4.9	6.6	49.3	11.5
1st extraction	1.0	64.4	0.8	16.8	2.2	1.1	3.1	5.0	6.5	46.9	11.5
1st extraction	1.5	64.5	0.7	16.9	2.1	1.0	2.9	5.3	6.4	46.3	11.7
2nd extraction	0.5	68.9	0.4	16.0	1.1	0.6	1.8	5.1	6.0	49.2	11.2
2nd extraction	1.0	68.4	0.4	16.1	1.3	0.6	1.8	5.2	6.1	46.8	11.3
2nd extraction	1.5	69.0	0.4	15.9	1.2	0.6	1.6	5.5	5.8	46.1	11.2
Initial composition - JG8	-	*71.9*	*0.3*	*13.6*	*2.2*	*0.1*	*0.7*	*5.0*	*4.4*	*7.5*	*9.3*
1st extraction	0.5	65.1	1.1	19.2	1.5	0.1	2.3	3.3	7.4	9.8	10.8
1st extraction	1.0	65.0	1.0	19.3	1.4	0.1	2.2	3.4	7.5	9.2	10.9
1st extraction	1.5	65.7	0.9	19.0	1.3	0.1	2.1	3.5	7.3	7.6	10.8
2nd extraction	0.5	70.4	0.6	16.5	0.8	0.1	1.4	4.0	6.1	9.7	10.1
2nd extraction	1.0	70.5	0.6	16.4	0.9	0.1	1.4	4.2	5.9	8.7	10.1
2nd extraction	1.5	69.8	0.5	15.8	2.4	0.1	1.3	4.5	5.5	7.0	10.0

The first extraction of cumulate crystals from both MF1 and JG8 produces syenitic compositions, while the second extraction of crystals produces quartz monzonitic compositions. A third FC step increases the quartz content and lowers the bulk rock K_2O contents of the cumulus, leading to the production of granites. This suggests that the process of step-wise fractional crystallization within the context of a dynamic deformational system, which can move melt away from the cumulates, can explain much of the geochemical diversity of the BAC rocks.

The K_2O, Al_2O_3, SiO_2, TiO_2 and CaO contents of the modeled cumulates are close to the compositions of the relevant BAC rocks (Table 2-5), whereas the FeO_T modeled is lower and the Na_2O is higher than the values analyzed for the BAC. The MF1 sample has a Mg# of 36.1, which is close to the inferred Mg# of the melt in equilibrium with the clinopyroxene compositions. On the other hand, the JG8 sample has a very low Mg# (7.5) and is not representative of the magmas that formed the BAC in this regard.

The modeling records the mineral assemblage present in the magmas as it cools, with the cumulate assemblage being the assemblage that existed at the time melt separates from the crystals and a new effective bulk composition is established in the melt-dominated and crystal-dominated systems. The melt extraction events occur at high temperatures and involve clinopyroxene as the ferromagnesian phase. This is in reasonably good agreement with the petrographic observations. There is a potential discrepancy with the existence of magmatic amphibole in some of the rocks interpreted to be cumulates, but it needs to be considered that the melt-bearing crystal cumulate will continue to crystalize new phases as it cools towards the solidus. The involvement of more melt in the cumulus produced would favour the crystallization of amphibole and biotite while keeping their composition with high alkalis. However, this scenario has not been modeled in this study.

2.4.6.3. Trace element modeling

The modeling of the major elements highlights the necessity for the magmas to crystalize K-feldspar as the first tectosilicate if syenite is to be the ultimate product of crystal accumulation. Translating this behaviour into a robust model for the corresponding trace element behaviour is not straightforward because no current thermodynamically constrained phase equilibrium modeling approach can deal with the whole accessory mineral assemblage, which plays a crucial role in the trace element and REE budget of the system (e.g., Bruand et al., 2020). Thus, the mean trace element values of granite samples from literature with $K_2O + Na_2O > 9.3$ wt% (n = 3) were utilized in the modeling combined with the volume of each accessory mineral as determined by petrographic analysis of the syenites, and the proposed felsic magma partition coefficients of Laurent (2012). Note that in this method, the abundance and composition of the major minerals are thermodynamically constrained and agree well with the natural rocks, but the accessory mineral proportions are based on observation. Consequently, there is some degree of circularity

in the trace element argument. Nonetheless, the resultant modeled cumulate rocks produced trace element signatures that are in reasonable agreement with the documented whole-rock compositions of the syenites and quartz monzonites (Figure 2-13 C-D). The most significant point of discrepancy is the strong negative anomalies of Eu and Sr produced in the modeling, which exist but are weaker in the BAC syenitic rocks. This distinction could originate from underestimations of allanite and apatite abundances in the cumulate; however, even with unrealistically high values, the addition of these accessory minerals failed to eliminate these anomalies. This suggests that the parental magma for the syenitic rocks had higher Eu and Sr contents than the most alkali-rich rock compositions from the GMS suite.

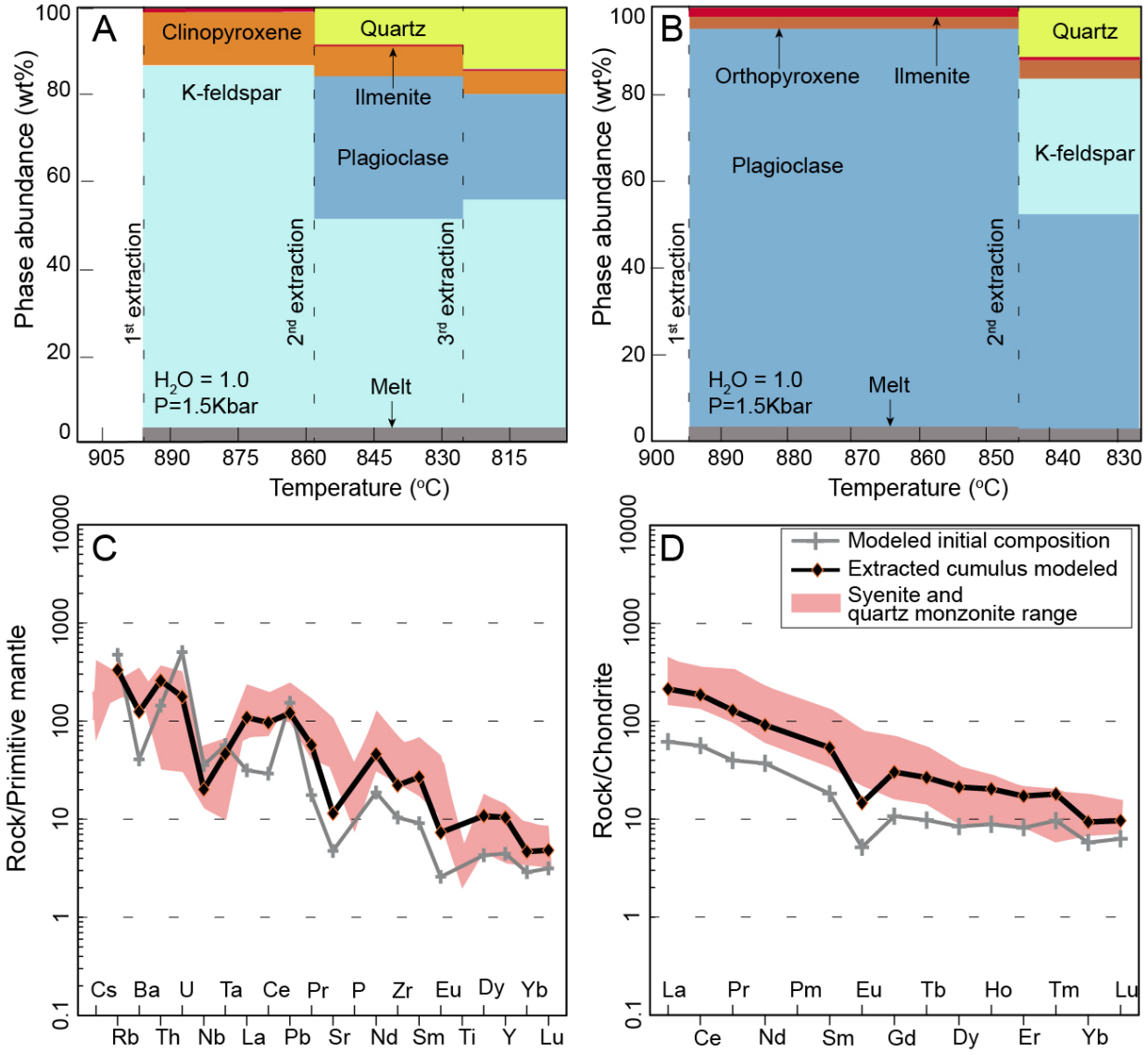

Figure 2-13. Crystal accumulation modeling. A) Phase proportion stabilized from initial granitic melts with K_2O+Na_2O > 9.3 wt%. B) Phase proportion stabilized from initial granitic melts with K_2O+Na_2O < 9.3 wt%. Titanite is stabilized but its volumes are too low to be expressed in this illustration. C-D) Spider diagram for trace elements and REE with the mean trace element contents of initial granitic melt with K_2O+Na_2O > 9.3, compared with the cumulus rock modeled and the composition range of the natural syenites and quartz monzonites. Primitive Mantle normalized (McDonough and Sun, 1995) and chondrite normalized (Nakamura, 1974).

2.5. Discussion

2.5.1. Constraints on the origin of the feldspar phenocrysts

The sampled BAC rocks preserve magmatic textures without significant secondary overprints. Within these rocks, the syenites and quartz monzonite display textural evidence for K-feldspar accumulation, as shown in Figure 2-4 and Figure 2-5. The K-feldspar occurs as angular euhedral phenocrysts with concentric zonation, textures associated with magmatic crystals (e.g., Vernon and Paterson, 2008).

The existence of homogeneous orthoclase phenocrysts with interlocked contact and the results of the phase equilibrium modeling support the primary crystallization of K-feldspar at high temperatures. The plagioclase, abundant as intercumulus crystals with low anorthite contents, suggests a crystallization at lower temperatures (e.g., Vernon and Paterson, 2008). Therefore, the K_2O content in the parental magma was high enough to allow K-feldspar crystallization prior to plagioclase. These features indicate that the mechanical accumulation of high-temperature K-feldspar is an important process in assembling the BAC plutons. The presence of magmatic layering at the edge of the plutons (Figure 2-3D), sub-vertical mineral alignment in dykes, and emplacement into an active shear zone are features that also reinforce the relevance of mechanical accumulation to produce the syenites and quartz monzonites (e.g., Vernon and Collins, 2011; Yu et al., 2023).

Melt loss from the crystal-mush can cause the rocks to have low Rb contents. This can explain the lower Rb contents of the syenitic rocks relative to the granites (e.g., Lee and Morton, 2015). Moreover, Kd_{Sr} and Kd_{Ba} can be significantly higher than 1 for K-feldspar (Henderson and Pierozynski, 2012; Laurent, 2012), leading to high Ba and Sr contents in the BAC rocks with K-feldspar accumulation, along with the high contents of K_2O and Na_2O that are almost constant over the relevant SiO_2 range (Henderson and Pierozynski, 2012; Farina et al., 2012; Lee and Morton, 2015; Laurent et al., 2020). Thus, the K-feldspar/melt separation can explain the behavior of Rb, Ba, and the alkali elements as a function of SiO_2 (Figure 2-7).

2.5.2. Tectonic setting and emplacement mechanisms

The large, sheet-like batholiths of the GMS suite and the intrusions of the BAC were emplaced during a phase of NW-SE directed subhorizontal shortening of the BGGT (e.g., Kamo and Davis, 1994; de Ronde and de Witt, 1994; Westraat et al., 2005). Despite this, the intrusions of the BAC describe two distinct geometries and orientations, suggesting different controls on their emplacement. The KZD and BT form northwesterly trending, elongate, dyke-like bodies, at high angles to the BGB (Figure 2-2). The BH, in contrast, is sheet-like at its base. It is underlain by older, highly deformed TTGs, that are cross-cut by a network of granitic and syenitic dykes that have ostensibly formed the feeders to the overlying syenite sheet (Figure 2-3).

The dyke-like geometry and orientation of the KZD and BT correspond to their emplacement during the episode of NW-SE shortening and orthogonal extension. Notably, both intrusions occur on a structural

trend parallel to the strike that has been exploited at later times by the large Usushwana mafic intrusive suite (e.g., Gumsley et al., 2015). This may indicate the presence of a weak transcrustal structural trend that has allowed for the emplacement of deeply sourced magmas at different times.

The BH, in contrast, is located at the northern termination of the WSZ. The shear zone is part of a regional system of syn-magmatic, conjugate shear zones that not only determined the distribution and geometry of the GMS plutons but also acted as feeders of the granitic magmas (e.g., Belcher and Kisters et al., 2006). Given the dextral transpressional kinematics along the WSZ (Westraat et al., 2005), intrusion of the subhorizontal BH sheet occurred in the compressive sector of the WSZ termination. The contrasting setting and structural controls of the KZD and BT and the coeval BH may explain the different geometries of the intrusions, but clearly underscores the syn-kinematic emplacement of the BAC.

The occurrence of K-feldspar (a low-density mineral) and high-density minerals (e.g., titanite, pyroxene) as cumulus phases and the relatively small difference in density between the K-feldspar crystals and granitic melts does not support a K-feldspar accumulation by sinking or floatation within the magmatic chamber (Hack and Thompson, 2011). Instead, structurally assisted segregation of crystals from the melt is a more plausible scenario (e.g., Paterson et al., 2005; Vernon and Collins, 2011; Rocher et al., 2018; Farina et al., 2020), particularly given the location of the BAC rocks relative to the syn-magmatic shear zones. Deformation along the southern margins of particularly the BH and, to a lesser extent, the KZD may have led to filter-pressing like processes and the structurally promoted expulsion of melt. The assembly of the BAC through multiple magma batches could increase flow differentiation within the chamber, thereby promoting the accumulation of minerals (e.g., Farina et al., 2012; Rocher et al., 2018; Yu et al., 2023). These processes would favour the accumulation of high-temperature K-feldspar (orthoclase) alongside mafic minerals and facilitate the extraction of rhyolitic melt from the crystal-mush (e.g., Paterson et al., 2005; Vernon and Collins, 2011; Rocher et al., 2018), giving rise to syenites and quartz monzonites with prominent cumulus textures. It is not clear whether the buoyancy-driven melt extraction was pervasive or along distinct conduits since the higher levels of the intrusions are not preserved.

2.5.3. Chemical and isotopic assessment

Proterozoic shoshonitic igneous rocks characterized by high LILE contents and negative anomalies of HFSE compared to the primitive mantle, along with positive and negative $\varepsilon Nd_{(t)}$ and $\varepsilon Hf_{(t)}$ values, are typically considered to reflect magmas derived from heterogeneous metasomatized Subcontinental Lithospheric Mantle (SCLM) reservoirs enriched by the recycling of ancient crust materials (e.g., Foley and Peccerillo, 1992; Blichert-Toft et al., 1995; Wang et al., 2017). Similarly, Archean alkaline rocks with these geochemical features are often interpreted as being derived from partial melting of the SCLM (i.e., Wang et al., 2017; Mikkola et al., 2011; Gao et al., 2018; Chen et al., 2023). However, in the case of the Archean examples, this interpretation relying on geochemical and isotopic data can be a function of the short time

elapsed between the formation of the TTG crust from mantle-derived metamafic rocks (e.g., Moyen et al., 2019; Moyen et al., 2021) and the formation of the alkaline rocks. This is particularly so for the BAC, which formed at ca 3.1 Ga in a terrane where the preserved TTG crust was produced between 3.55 and 3.23 Ga. This initial crust-mantle differentiation may produce Archean rocks with ambiguous geochemical signatures (e.g., Yearron, 2003; Moyen and Laurent, 2018; Moyen et al., 2021).

The dataset collected in this research, combined with the GMS suite whole-rock compilation from the literature, highlights the absence of comagmatic mafic rocks with the BAC rocks; all rocks with SiO_2 < 63 wt% are syenites and quartz monzonites. The few positive $\varepsilon Nd_{(t)}$ values suggest a minor contribution of mantle materials to the source of the ca. 3.1 Ga magmatic event. On the other hand, the predominant negative $\varepsilon Nd_{(t)}$ supports the conclusion that the BAC syenitic parental melts were derived from partial melting of sources with isotopic compositions similar to the local TTGs, which agrees with published zircon Lu-Hf data from the GMS and TTG suite which is compatible with the local lower crust being a probable source for the GMS (e.g., Zeh et al., 2009; Tchameni et al., 2001; Moyen et al., 2021). The hypothesis that the TTG suite basement is the main source of the BAC is also supported by the GMS T_{DM} values that are coeval with BGGT TTG suite crystallization ages, as well as the presence of inherited 3.2 Ga zircon crystals in the quartz monzonites of the Heerenveen and Mpuluzi batholiths (e.g., Zeh et al., 2009; Murphy, 2015; Moyen et al., 2021). Thus, the 3.48 – 3.28 Ga T_{DM} values of the BAC may represent the age range of this crustal source, while the younger 3.25 – 3.18 Ga T_{DM} values may reflect the fertilization of this source during the tectonic events that postdate the youngest TTGs (e.g., Westraat et al., 2005; Schoene et al., 2008; Kisters et al., 2010; Brey and Shu, 2018). The isotopic data suggesting the source of the BAC is predominantly crustal are corroborated by the voluminous granites composing the GMS suite, the high LILE content of the rocks, their negative Nb, Ta, and Ti anomalies, as well as the low Mg#s, low CaO and low Cr, Ni, and V contents of BAC syenites and quartz monzonites (e.g., Tchameni et al., 2001; Weng et al., 2022; Yu et al., 2023). Furthermore, the positive Th, U, and Pb anomalies in the BAC rocks with higher K_2O contents might demonstrate the low-degree partial melting of the lower crust, enriching the melt in incompatible elements (e.g., Fitton and Upton, 1987). These features suggest that the hot granitic parental magmas that evolved to form the BAC were likely generated directly by fluid-absent anatexis of lower crust rocks with variable K_2O contents (dominated by TTG gneisses; Clemens et al., 2010; Moyen et al., 2021), rather than fractional crystallization of mafic melts at low pressure.

This anatexis might have formed small melt batches which facilitated the structurally assisted crystal accumulation and could explain the low volumes of syenites in the GMS suite. The progressive increase in the melting rates, which might involve distinct and more fertile sources, could have produced the voluminous granitic magmas that built up the extensive GMS plutons. During this process, radioactive elements were extracted from the lower crust and transferred to the upper crust, contributing to the

stabilization of the craton. This scenario can explain the diverse chemistry of the BAC and the similar Nd isotopic evolution seen in the BAC and TTG gneisses.

The crustal origin hypothesis is further supported by the phase equilibrium modeling, which demonstrates that it is possible to produce syenites and monzogranites that are chemically and petrographically similar to the BAC rocks by crystal accumulation and melt loss, as long as granitic magmas with K_2O+Na_2O >9.3 wt% are involved. Such compositions are reasonably common within the GMS suite (Figure 2-12). The trace element modeling also indicates that the parental magmas require Eu and Sr contents above the values reported for the GMS granites, which indicates that direct equivalents of the real parental magmas are not preserved in the suite.

The high REE values recorded by the syenitic rocks of the BAC are possibly the result of the clinopyroxene, Ca-amphibole, titanite, and apatite accumulation alongside the K-feldspar. The geochemical heterogeneities within the BAC plutons (i.e., trace element contents and Mg#s variation) could reflect the chemical diversity of the source rocks with similar major element compositions but distinct trace element contents produced compositionally variable magma batches that assembled into heterogeneous plutons at shallow depths (e.g., Belcher and Kisters, 2006; Clemens et al., 2009; 2010; Yu, 2023).

Furthermore, the leucogranites are a chemically diverse group, as shown by the distinct features of the low-K and medium-K groups, including multiple REE signatures. Their genesis could not be due to a single process and likely involves various evolutionary pathways, including partial melting of crustal materials, variable degrees of FC, country rock assimilation, and possible melt loss from the magma chambers (e.g., Clemens et al., 2009; Moyen et al., 2021).

2.6. Conclusion

The dataset produced in this study suggests the syenites and quartz monzonites of the Boesmanskop Alkaline Complex are primarily K-feldspar cumulate rocks. Orthoclase crystallized at high temperatures prior to plagioclase and quartz. This early crystallization, along with the accumulation of K-feldspar and early phases (clinopyroxene, titanite, and amphibole), strongly controls the geochemical signatures observed in these rocks.

Geochemical evidence, including negative $\varepsilon Nd_{(t)}$ values, low MgO, Cr, and Ni, along with negative Nb, Ta, and Ti anomalies of the BAC rocks, suggests a predominantly lower crust source for the BAC, isotopically resembling the TTG suite basement. Sporadic positive $\varepsilon Nd_{(t)}$ values reported for the syenites indicate a minor mantle contribution. Additionally, the degree of melting had to be small to enrich the melt in incompatible elements and outside the stability field of the biotite. Therefore, it is proposed the alkaline rocks of the BAC originated from granitic melts produced by low degrees of fluid-absent anatexis of the lower crust, which resulted in low volumes of melt batches.

The dyke-like features of the KZD and BT, as well as the sheet-like BH, reflect the influence of regional shear zones on the pluton geometries and emplacement mechanisms. The dyke-like structures described below the BH served as conduits for granitic magmas to be emplaced at shallow depths and the pluton assembly by multiple melt-batches. The syn-kinematic emplacement of these magmas prompted structurally assisted crystal segregation and melt loss from the magma chambers via a filter-pressing like mechanism. The transfer of incompatible elements to shallow crustal depts contributed to the Kaapvaal Craton stabilization.

The phase equilibrium and trace element modeling conducted in upper-crust, fluid-absent conditions corroborate that K-feldspar could have crystallized at high temperatures from a granitic magma rich in alkalis and low in CaO, consistent with a geochemical subset of rocks found in the GMS suite. A subsequent accumulation of the early crystallized phases alongside melt removal could theoretically produce cumulus rocks chemically akin to the syenites and quartz monzonites of the BAC.

2.7. Acknowledgment

This research was supported by an RSA NRF grant to Gary Stevens via the SARChI program and by IRP BuCoMO, a collaborative research project funded by the CNRS and the NRF. This is BuCoMO contribution A15. We thank Riana Rossouw for XRF analyses, Madelaine Frazenburg for assistance with SEM analyses, and Petrus Le Roux for assistance with Sr, Nd isotope measurements.

2.8. References – Chapter 2

1. Anhaeusser, C.R., 1980. A geological investigation of the Archaean granite-greenstone terrane south of the Boesmanskop syenite pluton, Barberton Mountain Land. *South African Journal of Geology, 83(1)*, 93-106. https://hdl.handle.net/10520/AJA10120750_1070

2. Anhaeusser, C.R., and Robb, L.J., 1983. Geological and geochemical characteristics of the Heerenveen and Mpuluzi batholiths south of the Barberton greenstone belt and preliminary thoughts on their petrogenesis. In: Anhaeusser, C.R. (Ed.), Contributions to the Geology of the Barberton Mountain Land. *Geological Society of South Africa Special Publication, 9*, 131-152.

3. Balashov, Y.A., and Glaznev, V.N., 2006. Cycles of alkaline magmatism. *Geochemistry International*, *44*, 274-285. https://doi.org/10.1134/S0016702906030050

4. Barton Jr, J.M., Robb, L.J., Anhaeusser, C.R., and Van Nierop, D.A., 1983a. Geochronologic and Sr-isotopic studies of certain units in the Barberton Granite-Greenstone Terrane, South Africa. *In*: Anhaeusser, C.R. (Ed.), Contributions to the Geology of the Barberton Mountain Land. *Geological Society of South Africa Special Publication, 9*, 131-152.

5. Barton Jr, J.M., Hunter, D.R., Jackson, M.P. A., and Wilson, A.C., 1983b. Geochronologic and Sr-isotopic studies of certain units in the Barberton granite-greenstone terrane, Swaziland. *South African Journal of Geology*, *86(2)*, 71-80. https://hdl.handle.net/10520/EJC-111616268f

6. Bédard, J.H., 2010. Parameterization of the Fe= Mg exchange coefficient (Kd) between clinopyroxene and silicate melts. *Chemical Geology, 274(3-4)*, 169-176. https://doi.org/10.1016/j.chemgeo.2010.04.003

7. Belcher, R.W., and Kisters, A.F.M., 2006. Syntectonic emplacement and deformation of the Heerenveen batholith: conjectures on the structural setting of the 3.1 Ga granite magmatism in the Barberton granite-greenstone terrain, South Africa. *Geological Society of America, Special Publication, 405,* 211–231. https://doi.org/10.1130/2006.2405(12)

8. Blichert-Toft, J., Rosing, M.T., Lesher, C.E., and Chauvel, C., 1995. Geochemical constraints on the origin of the late Archean Skjoldungen alkaline igneous province, SE Greenland. *Journal of Petrology, 36(2)*, 515-561. https://doi.org/10.1093/petrology/36.2.515

9. Bonin, B., Azzouni-Sekkal, A., Bussy, F., and Ferrag, S., 1998. Alkali-calcic and alkaline post-orogenic (PO) granite magmatism: petrologic constraints and geodynamic settings. *Lithos, 45(1-4)*, 45-70. https://doi.org/10.1016/S0024-4937(98)00025-5

10. Brey, G.P., and Shu, Q., 2018. The birth, growth and ageing of the Kaapvaal subcratonic mantle. *Mineralogy and Petrology, 112*, 23-41. https://doi.org/10.1007/s00710-018-0577-8

11. Bruand, E., Fowler, M., Storey, C., Laurent, O., Antoine, C., Guitreau, M., E. Heilimo, and Nebel, O., 2020. Accessory mineral constraints on crustal evolution: elemental fingerprints for magma discrimination. Geochemical Perspectives Letters, 13, 7-12. https://doi.org/10.7185/geochemlet.2006

12. Chen, S., Li, J., Yuan, F., Jowitt, S.M., Li, L., Deng, Y., Liu, H., and Jiang, R., 2023. Modern-style subduction during the late Neoarchean to early Paleoproterozoic? Geochemical evidence from ca. 2.45 Ga arc-type magmatism in the Feidong Complex, northeastern Yangtze Craton, South China. *Precambrian Research, 388,* 106999. https://doi.org/10.1016/j.precamres.2023.106999

13. Clemens, J.D., Belcher, R.W., and Kisters, A.F., 2010. The Heerenveen batholith, Barberton Mountain Land, South Africa: Mesoarchaean, potassic, felsic magmas formed by melting of an ancient subduction complex. *Journal of Petrology, 51(5)*, 1099-1120. https://doi.org/10.1093/petrology/egq014

14. Clemens, J.D., Helps, P.A., and Stevens, G., 2009. Chemical structure in granitic magmas–a signal from the source? *Earth and Environmental Science Transactions of the Royal Society of Edinburgh, 100(1-2)*, 159-172. https://doi.org/ 10.1017/S1755691009016053

15. Clemens, J.D., Holloway, J.R., and White, A.J.R., 1986. Origin of an A-type granite; experimental constraints. *American Mineralogist, 71(3-4)*, 317-324.

16. De Ronde, C.E., and de Wit, M.J., 1994. Tectonic history of the Barberton greenstone belt, South Africa: 490 million years of Archean crustal evolution. *Tectonics, 13(4)*, 983-1005. https://doi.org/10.1029/94TC00353

17. De Wit, M.J., Roering, C., Hart, R.J., Armstrong, R.A., de Ronde, C.E.J., Green, R.W.E., Tredoux, M., Peberdy, E., and Hart, R.A., 1992, Formation of an Archean continent. *Nature,357*, 553–562. https://doi.org/10.1038/357553a0

18. Eggins, S.M., 2003. Laser ablation ICP-MS analysis of geological materials prepared as lithium borate glasses. *Geostandards Newsletter, 27(2)*, 147-162. https://doi.org/10.1111/j.1751-908X.2003.tb00642.x

19. Farina, F., Mayne, M.J., Stevens, G., Soorajlal, R., Frei, D., and Gerdes, A., 2020. Phase equilibria constraints on crystallization differentiation: insights into the petrogenesis of the normally zoned Buddusò Pluton in north-central Sardinia. *Geological Society, London, Special Publications, 491(1)*, 243-265. https://doi.org/10.1144/SP491-2019-3

20. Farina, F., Stevens, G., and Villaros, A., 2012. Multi-batch, incremental assembly of a dynamic magma chamber: the case of the Peninsula pluton granite (Cape Granite Suite, South Africa). *Mineralogy and Petrology, 106*, 193-216. https://doi.org/10.1007/s00710-012-0224-8

21. Fitton, J.G., and Upton, B.G., 1987. Alkaline igneous rocks. *Geological Society, London, special publications, 30,* 568.

22. Foley, S.F., and Peccerillo, A., 1992. Potassic and ultrapotassic magmas and their origin. *Lithos, 28*, 181–185. https://doi.org/10.1016/0024-4937(92)90005-J

23. Gao, L., Liu, S., Sun, G., Guo, R., Hu, Y., Fu, J., Wang, M., Ma, C., and Hu, F., 2018. Petrogenesis of late Neoarchean high-K granitoids in the Western Shandong terrane, North China Craton, and their implications for crust-mantle interactions. *Precambrian Research, 315*, 138-61. https://doi.org/10.1016/j.precamres.2018.07.006

24. Gumsley, A., Olsson, J., Söderlund, U., de Kock, M., Hofmann, A., and Klausen, M., 2015. Precise U-Pb baddeleyite age dating of the Usushwana Complex, southern Africa–Implications for the Mesoarchaean magmatic and sedimentological evolution of the Pongola Supergroup, Kaapvaal Craton. *Precambrian Research, 267,* 174-185. https://doi.org/10.1016/j.precamres.2015.06.010

25. Hack, A.C., and Thompson, A.B., 2011. Density and viscosity of hydrous magmas and related fluids and their role in subduction zone processes. *Journal of Petrology, 52(7-8)*, 1333-1362. https://doi.org/10.1093/petrology/egq048

26. Hawthorne, F.C., Oberti, R., Harlow, G.E., Maresch, W.V., Martin, R.F., Schumacher, J.C., and Welch, M.D., 2012. Nomenclature of the amphibole supergroup. *American Mineralogist, 97(11-12)*, 2031-2048. https://doi.org/10.2138/am.2012.4276

27. Henderson, C.M.B., and Pierozynski, W.J., 2012. An experimental study of Sr, Ba and Rb partitioning between alkali feldspar and silicate liquid in the system nepheline–kalsilite–quartz at 0.1 GPa P (H2O): a revisitation and reassessment. *Mineralogical Magazine, 76(1)*, 157-190. https://doi.org/10.1180/minmag.2012.076.1.157

28. Howarth, G.H., Moore, A.E., Harris, C., van der Meer, Q.H.A., and le Roux, P., 2019. Crustal versus mantle origin of carbonate xenoliths from Kimberley region kimberlites using C-O-Sr-Nd-Pb isotopes and trace element abundances. *Geochimica et Cosmochimica Acta 266(1),* 258-273. https://doi.org/10.1016/j.gca.2019.03.026

29. Janoušek, V., Moyen, J.F., Martin, H., Erban, V., and Farrow, C., 2015. Geochemical modelling of igneous processes: principles and recipes in R language, *Springer,* 257, https://doi.org/10.1007/978-3-662-46792-3

30. Jochum, K.P., Nohl, U., Herwig, K., Lammel, E., Stoll, B., and Hofmann, A.W., 2005. GeoReM: a new geochemical database for reference materials and isotopic standards. *Geostandards and Geoanalytical Research, 29(3),* 333-338. https://doi.org/10.1111/j.1751-908X.2005.tb00904.x

31. Kamo, S.L., and Davis, D.W., 1994. Reassessment of Archaean crustal development in the Barberton mountain land, South Africa, based on U-Pb dating. *Tectonics, 13(1)*, 167-192. https://doi.org/10.1029/93TC02254

32. Kisters, A.F., Belcher, R.W., Poujol, M., and Dziggel, A., 2010. Continental growth and convergence-related arc plutonism in the Mesoarchaean: Evidence from the Barberton granitoid-greenstone terrain, South Africa. *Precambrian Research, 178(1-4)*, 15-26. https://doi.org/10.1016/j.precamres.2010.01.002

33. Kisters, A.F., Stevens, G., Dziggel, A., and Armstrong, R.A., 2003. Extensional detachment faulting and core-complex formation in the southern Barberton granite–greenstone terrain, South Africa: evidence for a 3.2 Ga orogenic collapse. *Precambrian Research*, *127*(4), 355-378. https://doi.org/10.1016/j.precamres.2003.08.002

34. Kröner, A., Hegner, E., Wendt, J.I., and Byerly, G.R., 1996. The oldest part of the Barberton granitoid-greenstone terrain, South Africa: evidence for crust formation between 3.5 and 3.7 Ga. *Precambrian Research, 78(1-3)*, 105-124. https://doi.org/10.1016/0301-9268(95)00072-0

35. Laurent, O., 2012. *Les changements géodynamiques à la transition Archéen-Protérozoïque: étude des granitoïdes de la marge Nord du craton du Kaapvaal (Afrique du Sud)*. Doctoral dissertation, Université Blaise Pascal-Clermont-Ferrand II.

36. Laurent, O., Björnsen, J., Wotzlaw, J.F., Bretscher, S., Pimenta Silva, M., Moyen, J.F., Ulmer, P., and Bachmann, O., 2020. Earth's earliest granitoids are crystal-rich magma reservoirs tapped by silicic eruptions. *Nature Geoscience, 13(2)*, 163-169. https://doi.org/10.1038/s41561-019-0520-6

37. Lee, C.T.A., and Morton, D.M., 2015. High silica granites: Terminal porosity and crystal settling in shallow magma chambers. *Earth and Planetary Science Letters*, *409*, 23-31. https://doi.org/10.1016/j.epsl.2014.10.040

38. Lowe, D.R., 1994. Accretionary history of the Archean Barberton greenstone belt (3.55-3.22 Ga), southern Africa. *Geology, 22(12),* 1099-1102.

39. Lowe, D.R., and Byerly, G.R., 2007. An overview of the geology of the Barberton Greenstone Belt and vicinity: implications for early crustal development. *Developments in Precambrian geology, 15*, 481-526. 10.1130/0091-7613(1994)022<1099:ahotab>2.3.co;2

40. Marks, M.A., Hettmann, K., Schilling, J., Frost, B.R., and Markl, G., 2011. The mineralogical diversity of alkaline igneous rocks: critical factors for the transition from miaskitic to agpaitic phase assemblages*. Journal of Petrology, 52(3),* 439-455. https://doi.org/10.1093/petrology/egq086

41. Mayne, M.J, Moyen, J.F., Stevens, G., and Kaislaniemi, L., 2016. Rcrust: A tool for calculating path-dependent open system processes and application to melt loss. *Journal of Metamorphic Geology, 34(7)*, 663-82. https://doi.org/10.1111/jmg.12199

42. McDonough, W.F., and Sun, S.S., 1995. The composition of the Earth. *Chemical Geology, 120*, 223-253. https://doi.org/10.1016/0009-2541(94)00140-4

43. Middlemost, E.A., 1975. The Basalt Clan. *Earth-Science Reviews, 11(4)*, 337-564. http://dx.doi.org/10.1016/0012-8252(75)90039-2

44. Middlemost, E.A., 1994. Naming materials in the magma/igneous rock system. *Earth-science reviews, 37(3-4)*, 215-224. https://doi.org/10.1016/0012-8252(94)90029-9

45. Mikkola, P., Salminen, P., Torppa, A., and Huhma, H., 2011. The 2.74 Ga Likamännikkö complex in Suomussalmi, East Finland: lost between sanukitoids and truly alkaline rocks? *Lithos, 125(1-2),* 716-728. https://doi.org/10.1016/j.lithos.2011.04.002

46. Miyashiro, A., 1978. Nature of alkalic volcanic rock series. Contributions to *Mineralogy and Petrology, 66*, 91-104. https://doi.org/10.1007/BF00376089

47. Morimoto, N., 1988. Nomenclature of pyroxenes. *Mineralogy and Petrology, 39(1)*, 55-76. https://doi.org/10.1007/BF01226262

48. Moyen, J.F., and Laurent, O., 2018. Archaean tectonic systems: a view from igneous rocks. *Lithos. 302*, 99-125. https://doi.org/10.1016/j.lithos.2017.11.038

49. Moyen, J.F., Stevens, G., Kisters, A.F.M., Belcher, R.W., and Lemirre, B., 2019. TTG Plutons of the Barberton Granitoid-Greenstone Terrain, South Africa. *Developments in Precambrian Geology, 15*, 607-667. https://doi.org/10.1016/S0166-2635(07)15056-8

50. Moyen, J.F., Zeh, A., Cuney, M., Dziggel, A., and Carrouée, S., 2021. The multiple ways of recycling Archaean crust: A case study from the ca. 3.1 Ga granitoids from the Barberton Greenstone Belt, South Africa. *Precambrian Research, 353,* 105998. https://doi.org/10.1016/j.precamres.2020.105998

51. Mühlberg, M., Stevens, G., Moyen, J.F., Kisters, A.F., and Lana, C., 2021. Thermal evolution of the Stolzburg Block, Barberton granitoid-greenstone terrain, South Africa: Implications for Paleoarchean tectonic processes. *Precambrian Research, 359*, 106082. https://doi.org/10.1016/j.precamres.2020.106082

52. Murphy, R.C., 2015. *Stabilising a craton: the origin and emplacement of the 3.1 Ga Mpuluzi Batholith*. Doctoral dissertation, Macquarie University.

53. Nachit, H., Ibhi, A., Abia, E.H., and Ohoud, M.B., 2005. Discrimination between primary magmatic biotites, reequilibrated biotites and neoformed biotites. *Comptes Rendus Geoscience, 337(16),* 1415-1420. https://doi.org/10.1016/j.crte.2005.09.002

54. Ódri, A., Harris, C., and Le Roux, P., 2020. The role of crustal contamination in the petrogenesis of nepheline syenite to granite magmas in the Ditrău Complex, Romania: evidence from O-, Nd-, Sr- and Pb-isotopes. *Contributions to Mineralogy and Petrology 175*, 1-25. https://doi.org/10.1007/s00410-020-01738-5.

55. Paterson, S.R., Vernon, R.H., and Zak, J., 2005. Mechanical instabilities and physical accumulation of K-feldspar megacrysts in granitic magma, Tuolumne batholith, California, USA. J*ournal of the Virtual Explorer, 18,* 1–18. https://doi.org/10.3809/jvirtex.2005.00114

56. Patiño Douce, A.E., 1997. Generation of metaluminous A-type granites by low-pressure melting of calc-alkaline granitoids. *Geology, 25(8)*, 743-746. https://doi.org/10.1130/0091-7613(1997)025<0743:GOMATG>2.3.CO;2

57. Peucat, J.J., Mahabaleswar, B., and Jayananda, M., 1993. Age of younger tonalitic magmatism and granulitic metamorphism in the South Indian transition zone (Krishnagiri area); comparison with older Peninsular gneisses from the Gorur–Hassan area. *Journal of Metamorphic Geology, 11(6)*, 879-88. https://doi.org/10.1111/j.1525-1314.1993.tb00197.x

58. Robb, L.J., Barton Jr, J.M., Kable, E.J.D., and Wallace, R.C., 1986. Geology, geochemistry and isotopic characteristics of the Archaean Kaap Valley pluton, Barberton mountain land, South Africa. *Precambrian Research, 31(1)*, 1-36. https://doi.org/10.1016/0301-9268(86)90063-X

59. Robb, L.J., Brandl, G., Anhaeusser, C.R., Poujol, M., Johnson, M.R., and Thomas, R.J., 2006. Archaean granitoid intrusions *In*: Johnson, M.R., Anhaeusser, C.R., Thomas, R.J. (Eds.), *The Geology of South Africa*, 57-94.

60. Rocher, S., Alasino, P., Grande, M.M., Larrovere, M.A., and Paterson, S.R., 2018. K-feldspar megacryst accumulations formed by mechanical instabilities in magma chamber margins, Asha pluton, NW Argentina. *Journal of Structural Geology*, *112*, 154-173. https://doi.org/10.1016/j.jsg.2018.04.017

61. Schoene, B., de Wit, M.J., and Bowring, S.A., 2008. Mesoarchean assembly and stabilization of the eastern Kaapvaal craton: A structural-thermochronological perspective. *Tectonics, 27(5)*. https://doi.org/10.1029/2008TC002267

62. Schoene, B., Dudas, F.O., Bowring, S.A., and De Wit, M., 2009. Sm–Nd isotopic mapping of lithospheric growth and stabilization in the eastern Kaapvaal craton. *Terra Nova, 21(3)*, 219-228. https://doi.org/10.1111/j.1365-3121.2009.00877.x

63. Schoene, B. and Bowring, S.A., 2010. Rates and mechanisms of Mesoarchean magmatic arc construction, eastern Kaapvaal craton, Swaziland. *Bulletin, 122(3-4)*, 408-429. https://doi.org/10.1130/B26501.1

64. Shand, S.J., 1943. Eruptive rocks: their genesis, composition, classification, and their relation to ore deposits, with a chapter on meteorites. *Journal of Geology, 56(6)*, 593-593. https://doi.org/10.1086/625564

65. Sørensen, H., 1974. The Alkaline Rocks. *Cambridge University Press, London*, 622. https://doi.org/10.1017/S0016756800045994

66. Tanaka, T., Togashi, S., Kamioka, H., Amakawa, H., Kagami, H., Hamamoto, T., Yuhara, M., Orihashi, Y., Yoneda, S., Shimizu, H., Kunimaru, T., Takahashi K., Yanagi, T., Nakano, T., Fujimaki, H., Shinjo, R., Asahara, Y., Tanimizu, M., and Dragusanu, C., 2000. JNdi-1: a neodymium isotopic reference in consistency with LaJolla neodymium. *Chemical Geology, 168(3-4)*, 279-281. https://doi.org/10.1016/S0009-2541(00)00198-4

67. Taylor, R.P., Strong, D.F., and Kean, B.F., 1980. The Topsails igneous complex: Silurian – Devonian peralkaline magmatism in western Newfoundland. *Canadian Journal of Earth Sciences, 17*, 425-439. https://doi.org/10.1139/e80-040

68. Tchameni, R., Mezger, K., Nsifa, N.E., and Pouclet, A., 2001. Crustal origin of Early Proterozoic syenites in the Congo craton (Ntem complex), South Cameroon. *Lithos, 57(1)*, 23-42. https://doi.org/10.1016/S0024-4937(00)00072-4

69. Tischendorf, G., Förster H.J., and Gottesmann, B., 1999. The correlation between lithium and magnesium in trioctahedral micas: Improved equations for Li_2O estimation from MgO data. *Mineralogical Magazine, 63(1)*, 57-74. https://doi.org/10.1180/002646199548312

70. Turner, S.P., Foden, J.D., and Morrison, R.S., 1992. Derivation of some A-type magmas by fractionation of basaltic magma: an example from the Pathway ridge, South Australia. *Lithos, 28,* 151-179. https://doi.org/10.1016/0024-4937(92)90029-X

71. Vernon, R.H., and Collins, W.J., 2011. Structural criteria for identifying granitic cumulates. *The Journal of Geology, 119(2)*, 127-142. https://doi.org/10.1086/658198

72. Vernon, R.H., and Paterson, S.R., 2008. How late are K-feldspar megacrysts in granites? *Lithos, 104(1-4)*, 327-336. https://doi.org/10.1016/j.lithos.2008.01.001

73. Wang, K., Liu, S., Wang, M., and Yan, M., 2017. Geochemistry and zircon U-Pb-Hf isotopes of the late Neoarchean granodiorite-monzogranite-quartz syenite intrusions in the Northern Liaoning Block, North China Craton: Petrogenesis and implications for geodynamic processes. *Precambrian Research, 295*, 151-71. https://doi.org/10.1016/j.precamres.2017.04.021

74. Weng, Q., Niu, H.C., Qu, P., Li, N.B., Shan, Q., and Yang, W.B., 2022. Controlling factors of prolonged REE mineralization in the Maoniuping REE deposit: constraints from alkaline granite in the syenite–carbonatite complex. *Ore Geology Reviews, 142*, 104705. https://doi.org/10.1016/j.oregeorev.2022.104705

75. Westraat, J.D., Kisters, A.F.M., Poujol, M., and Stevens, G., 2005. Transcurrent shearing, granite sheeting and incremental construction of the tabular 3.1 Ga Mpuluzi batholith, Barberton granite-greenstone terrane, South Africa. *Journal of the Geological Society, 162(2)*, 373-388. https://doi.org/10.1144/0016-764904-026

76. Whalen, J.B., Currie, K.L., and Chappel, B.W., 1987. A-type granites: geochemical characteristics, discrimination and petrogenesis. *Contributions to Mineralogy and Petrology, 95,* 407–419. https://doi.org/10.1007/BF00402202

77. Wickham, S.M., Litvinovsky, B.A., Zanvilevich, A.N., and Bindeman, I.N., 1995. Geochemical evolution of Phanerozoic magmatism in Transbaikalia, East Asia: A key constraint on the origin of K-rich silicic magmas and the process of cratonization. *Journal of Geophysical Research: Solid Earth, 100(B8)*, 15641-15654. https://doi.org/10.1029/95JB00035

78. Wilson, A.H., and Zeh, A., 2018. U-Pb and Hf isotopes of detrital zircons from the Pongola Supergroup: Constraints on deposition ages, provenance and Archean evolution of the Kaapvaal craton. *Precambrian Research, 305*, 177-196. https://doi.org/10.1016/j.precamres.2017.12.020

79. Yu, Y., Luo, B., Zhang, H., Xu, W., Yang, H., Pan, F., Guo, L., Li, J., Ruan, B., Lai, K., Zhang, Y., and Cao, Z., 2023. Origin of K-feldspar megacrysts of Quxu batholith in Gangdese belt, South Tibet: Implication for magma rejuvenation in a crystal mush reservoir. *Lithos, 438*, 107019. https://doi.org/10.1016/j.lithos.2023.107019

80. Zeh, A., Gerdes, A., and Barton Jr, J.M., 2009. Archean accretion and crustal evolution of the Kalahari Craton—the zircon age and Hf isotope record of granitic rocks from Barberton/Swaziland to the Francistown Arc. *Journal of Petrology, 50(5)*, 933-966. https://doi.org/10.1093/petrology/egp027

81. Zhao, H., Zhao, X., Le Roux, P.J., Zhang, W., Wang, H., Xie, LW., Huang, C., Wu, ST., Yang, JH., Wu, FY., Yang, YH., 2020. Natural Clinopyroxene Reference Materials for *in situ* Sr Isotopic Analysis via LA-MC-ICP-MS. *Frontiers in Chemistry*, *8*, 594316. https://doi.org/10.3389/fchem.2020.594316

CHAPTER 3. PRESENTATION OF RESEARCH PAPER 2 - ACCESSORY MINERAL CHEMISTRY OF CA. 3.1 GA SYENITES AND QUARTZ MONZONITES OF THE BOESMANSKOP ALKALINE COMPLEX, KAAPVAAL CRATON: INSIGHTS INTO MAGMATIC PROCESSES DURING CRATON STABILIZATION

This manuscript, first authored by Marcel Vinicius Santos Leandro, was submitted to the *Journal of Petrology* and is currently under peer review. The following aspects of the research were done independently by Marcel Vinicius Santos Leandro while receiving standard supervision by his supervisors Gary Stevens, Jean-François Moyen, and Alex F.M. Kisters: (i) sample preparation; (ii) petrographic description; (iii) SEM imaging and EDS analysis of major oxides of pertinent minerals; (iv) mineral picking; (v) generation of figures; (vi) writing of the manuscript. Riana Rossouw acquired U-Pb, trace element, and REE data by LA-ICP-MS.

Contribution Roles Taxonomy (CRediT) classification - **Marcel V.S. Leandro**: Conceptualization; Data curation; Formal Analysis; Investigation; Methodology; Visualization; Writing – Original Draft Preparation. **Gary Stevens**: Data Curation; Funding Acquisition; Project Administration; Resources; Supervision; Validation; Writing – Review & Editing. **Jean-François Moyen:** Data Curation; Funding Acquisition; Resources; Supervision; Validation; Writing – Review & Editing. **Ariela O. Mazoz:** Visualization; Validation; Writing – Review & Editing.

Accessory mineral chemistry of ca. 3.1 Ga syenites and quartz monzonites of the Boesmanskop Alkaline Complex, Kaapvaal Craton: Insights into magmatic processes during craton stabilization

Marcel V.S. Leandro [a]*, Gary Stevens [a], Jean-François Moyen [b], Ariela O. Mazoz[a]

[a] Department of Earth Sciences, Stellenbosch University, Private Bag X1, Matieland, 7602, Stellenbosch, South Africa

[b] Université Jean-Monnet, Laboratoire Magmas et Volcans, UCA-CNRS-IRD, Aubière F-63170, France

*Corresponding author: marcel.leandro@hotmail.com; https://orcid.org/0000-0002-5177-890X

Abstract

Investigating trace and rare earth elements (TREE) in accessory minerals provides insights into the magmatic evolution of their host rocks. This research focuses on the TREE compositions of apatite, titanite, and zircon of syenites and quartz monzonites obtained by LA-ICP-MS, along with *in situ* U-Pb zircon ages of the quartz monzonites from the Boesmanskop Alkaline Complex (BAC), located in the Barberton Granite-Greenstone Terrane, South Africa. Zircon crystals for the quartz monzonite show high Ti contents, reflecting high-temperature crystallization (up to 915 °C). The syenite and quartz monzonite have large diamond-shaped titanite crystals exhibiting chemical zonation; their cores contain high MREE and the rims exhibit lower MREE, registering apparent crystallization temperatures from 756 °C to 684 °C. The elevated MREE patterns in BAC F-apatite and titanite cores represent the pristine compositions of these early-formed minerals and the hot REE-rich nature of the magma they crystallized. Their parental melts were likely derived from low degrees of fluid-absent partial melting of the lower crust, leaving behind a refractory residuum. U-Pb data for the quartz monzonite yielded a crystallization age of 3118 ± 9/32 Ma (2s; MSWD = 1.1; n = 24) and an inherited age of 3220 ± 13/35 Ma (2s; MSWD = 0.24; n = 14), indicating the contribution of ancient crustal material. The BAC syenites and quartz monzonites might represent the initial stages of the partial melting that produced the high-K magmatism that finalized the Kaapvaal Craton stabilization.

Keywords: Accessory mineral chemistry; U-Pb dating; high-Ti zircon; Archean syenite

3.1. Introduction

Apatite, zircon, and titanite are common accessory minerals in plutonic rocks and play a crucial role in controlling the trace and rare earth element (TREE) budget of the rocks. The chemistry of these minerals can reflect intensive parameters during crystallization, such as temperature, oxygen fugacity, and melt compositions (e.g., Belousova et al., 2002; Claiborne et al., 2006; Bruand et al., 2020). Consequently, they serve as important tools for reconstructing the magmatic and metamorphic crustal evolution processes, as well as for determining the mineral provenance in sedimentary rocks (e.g., Hoskin and Ireland, 2000; Belousova et al., 2002; Bruand et al., 2016, 2020; Duan et al., 2019). Additionally, the increasing precision and

cost reduction of *in situ* TREE analysis by LA-ICP-MS, have enhanced their use as petrogenetic indicators (e.g., Piccoli et al., 2000; McLeod et al., 2011; Duan et al., 2019; Bruand et al., 2020; Belousova et al., 2002).

The TREE of accessory minerals is particularly important for petrogenetic studies of Archean rocks, given the limited dataset that can be obtained for this Eon. *In situ* TREE analyses are also crucial for investigating the genesis of cumulus rocks, where bulk-rock chemistry does not represent the magma composition, and fractional crystallization plays a fundamental role (e.g., Hoskin and Ireland, 2000; Belousova et al., 2002; Bruand et al., 2014; Buard et al., 2016). Thus, this technique is essential to investigate the Archean K-feldspar cumulus rocks of the Boesmanskop Alkaline Complex (BAC) (e.g., Anhaeusser et al., 1983; Leandro et al., 2024).

The BAC is a volumetrically minor component of the Granodiorite-Monzogranite-Syenogranite (GMS) suite, located along the eastern margin of the Kaapvaal Craton (Figure 3-1) (e.g., Anhaeusser and Robb, 1983; Yearron, 2003; Robb et al., 2021). The GMS suite represents an important change in the nature of the felsic magmas involved in crustal development (e.g., Schoene et al., 2009). The sodic magmatism producing trondhjemite, tonalite, and granodiorite (TTG) suite between 3.55 to 3.21 Ga (e.g., Kröner et al., 1996) shift to potassium-high magmatism, leading to the generation of the voluminous ca. 3105 Ma granites *sensu stricto* (*s.s.*) and associated phases of the GMS suite, which marks the final stages of the Kaapvaal Craton stabilization (e.g., Anhaeusser et al., 1983; Anhaeusser and Robb, 1983; Lowe, 1994; Lowe and Byerly, 2007; Schoene et al., 2008, 2009; Moyen et al., 2021; Chen et al., 2023).

Few studies cover the accessory mineral chemistry of the GMS suite, with most of them discussing only zircon compositions (e.g., Yearron, 2003; Murphy, 2015). Moreover, the TREE behavior of the apatite and titanite, ubiquitous accessory minerals of the GMS suite are still vague. Thus, this research investigates the trace element and REE compositions of apatite, titanite, and zircon of the syenites and related quartz monzonites of the BAC to constrain their magmatic evolution. By analyzing the TREE patterns of accessory minerals within the 3.1 Ga GMS suite, we aim to enhance the understanding of the processes that generated magmas enriched in incompatible elements forming syenites and quartz monzonite of the BAC.

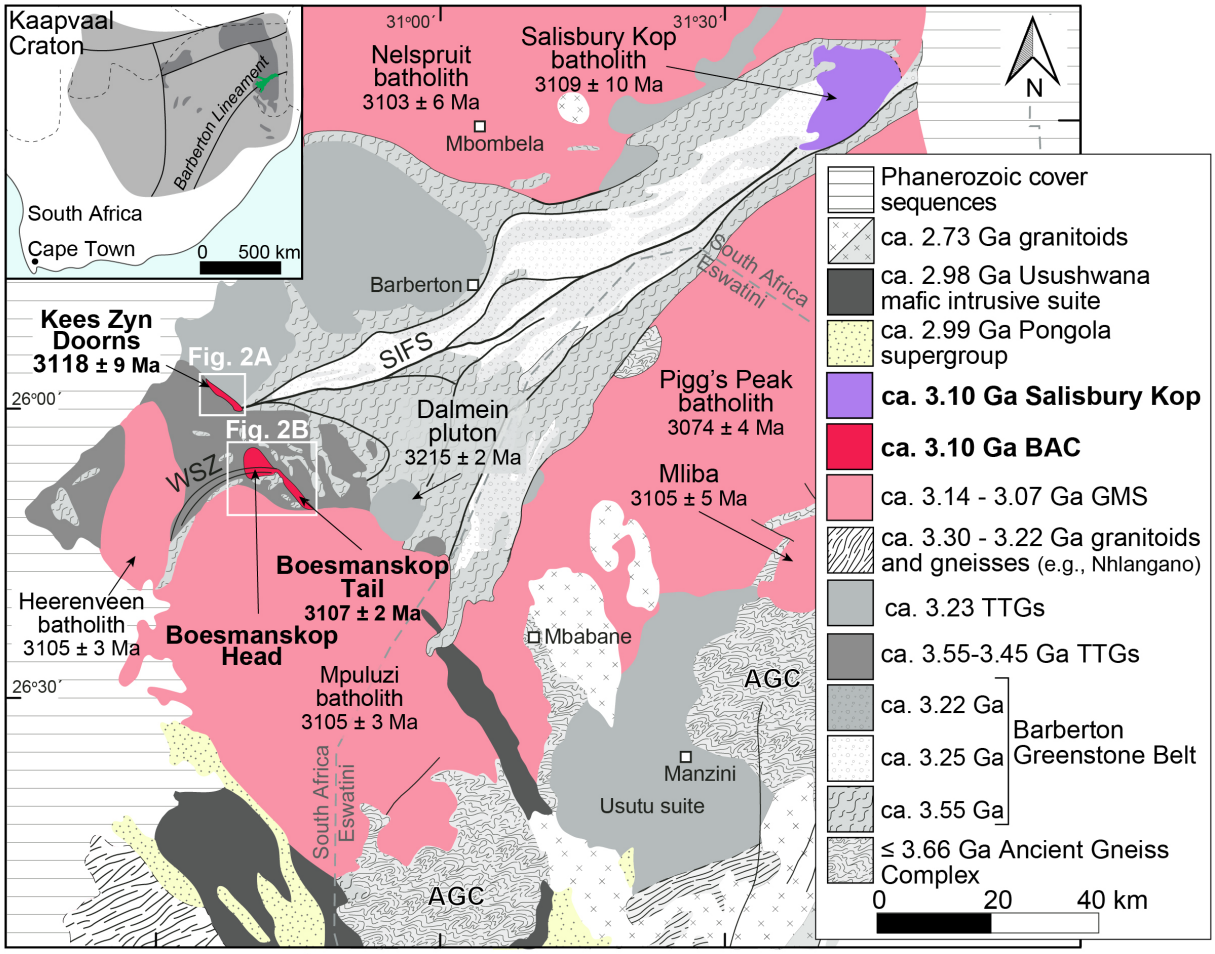

Figure 3-1. Simplified geological map of the Barberton Granite-Greenstone Terrane showing the GMS suite and surrounding units (after de Ronde and de Wit, 1994; Clemens et al., 2010; Schoene and Bowring, 2010). The insert shows the location of the Kaapvaal Craton. SIFS: Saddleback-Inyoka Fault System; WSZ: Welverdiend Shear Zone.

3.2. Analytical Methods

3.2.1. Sample preparation

The apatite, titanite, and zircon crystals were extracted from three representative samples of syenite (BH03, BH04 and KZD04) and two representative samples of quartz monzonite (KZD01 and KZD09) of the BAC. The sample preparation for crystals mounted in epoxy was conducted at the Central Analytical Facilities (CAF) of Stellenbosch University, South Africa, and the thin section preparation was performed by Lab Crystals in Lucknow, Uttar Pradesh, India.

The samples were crushed with a jaw crusher and milled with a disk mill, producing a rock powder sieved in distinct grain size fractions. The heavy minerals were concentrated from the < 350 µm fraction with a Frantz magnetic separator, followed by heavy liquid separation using tetrabromoethane. The zircon, apatite, and titanite crystals were handpicked, mounted in epoxy resin discs, and polished with a Rotopol-35 for chemical analyses. Titanite and zircon

were also analyzed *in situ* within thin sections, allowing the track of their textural relationship with the surrounding minerals.

3.2.2. Imaging acquisition

The petrography of the accessory minerals, as well as related textural associations in the thin sections, were investigated by optical microscopy, backscattered electron (BSE) imaging, and cathodoluminescence (CL) imaging using a Zeiss Merlin Field Emission Scanning Electron Microscopes (FE-SEM) at the CAF. The mineral mounts and thin sections were coated with carbon, and images were acquired using an accelerating voltage of 20 kV, 11 nA probe current, specimen current between 19.5 and 20.5 nA, and a 9.5 mm working distance. These images enabled the distinction and selection of pristine areas of the crystals of interest for chemical and isotopic analyses, avoiding cracks, inclusions, and domains modified by post-magmatic processes.

3.2.3. Mineral compositions and U-Pb zircon dating

The major elements of the accessory minerals were measured at the CAF using a Zeiss EVO MA15 SEM with an Oxford Instruments X-Max 20 mm^2 Energy Dispersive X-Ray Spectrometry detector (EDS) and INCA Oxford software. The beam conditions used an accelerating voltage of 20 kV, 11 nA probe current, specimen current between 19.5 and 20.5 nA, and a working distance of 8.5 mm.

The *in situ* TREE analysis of zircon was performed using a Resolution 193 nm Excimer laser from Applied Spectra connected to an Agilent 7700 Q ICP-MS at the CAF with laser spot sizes of 30 and 40 μm, frequency of 8 Hz and 45 s of sample ablation time. The Si and Ca were used as internal standards, with values determined through EDS-SEM measurements in this study. The Si content considered was 14.1% for titanite, 24.1% for amphibole, and 24.6% for clinopyroxene. The Ca content considered was 37.0% for apatite and 19.0% for titanite. All calibration standards were analyzed every 15 spots. The JJG1424 clinopyroxene (Zhao et al., 2020), was utilized as a calibration standard, bracketing 15 analyses of the unknowns, and BCR-2G and BHVO-2G glasses (Jochum et al., 2005) as quality control standards. Madagascar (Young et al., 1969; Thomson et al., 2012) and Durango (Chew et al., 2016) apatite were used as additional quality control for the TREE analysis. The accuracy obtained on repeated analyses of the reference materials is better than 15%.

U–Pb zircon ages were determined for a quartz monzonite sample at CAF using a Thermo Scientific Element 2 sector field ICP-MS, paired with a Resolution 193 nm Excimer laser

ablation system from Applied Spectra. The analysis sequence was done in sample bracketing mode. The masses measured included ^{202}Hg, ^{204}Pb, ^{206}Pb, ^{207}Pb, ^{208}Pb, ^{238}Th, and ^{238}U. The U-Pb isotopic composition of zircon was obtained using the GJ-1 zircon (Jackson et al., 2004; Horstwood et al., 2016) as primary reference material and the 91500 (Wiedenbeck et al., 1995) and Plešovice zircon (Sláma et al., 2008) as quality control. The data reduction was conducted using the U-Pb Saturn software (Silva et al., 2023). The concordia diagram was plotted with the IsoplotR (Vermeesch, 2018). The obtained values for the 91500 and Plešovice zircon secondary reference materials produced concordia ages of 1064 ± 14/18 Ma (2s; MSWD = 2.2; n = 6) and 339 ± 3/5 Ma (2s; MSWD = 1.5; n = 7), respectively, consistent with the published reference values (Wiedenbeck et al., 1995; Sláma et al. 2008). The final age uncertainties are reported as 2 sigma (2s) and quoted as α/β (without/with systematic uncertainties; Horstwood et al., 2016).

The accessory mineral compositions from this project were compared with the TREE compositions of the zircon, apatite, and titanite crystals of various TTG rocks of the BAC basement (Laurent et al., 2022; Mühlberg, 2022) and zircon from granites of the ca. 3105 Ma Mpuluzi batholith (Moyen et al., 2021; Laurent et al., 2022; Mühlberg, 2022).

The REE values were normalized by the chondrite composition ($_{CN}$) of Nakamura (1974). The zircon analyses with $La_{CN} > 2$ and $Pr_{CN} < 15$ were considered to reflect altered or metamorphic grains and were removed from the database (e.g., Hoskin, 2005; Laurent et al., 2022). This filter was also applied to the zircon compositions gathered from the literature. The dataset is available in the supplementary material.

3.2.4. Thermometry

The Ti-in-zircon and Zr-in-titanite temperatures were calculated using the equations proposed by Ferry and Watson (2007) and Hayden et al. (2008). The SiO_2 activity ($a SiO_2$) and TiO_2 activity ($a TiO_2$) values used in these equations were 0.95 and 0.65, respectively, as proposed for granitoid magmas that crystallized titanite and Ti-magnetite in the absence of primary rutile (e.g., Claiborne et al., 2006; Ferry and Watson, 2007).

3.3. Local Geology

The BAC is located to the south of the Barberton Granite-Greenstone Terrane in South Africa (Figure 3-1). This complex comprises three kilometric plutons, the Boesmanskop Head (BH) and the elongated Kees Zyn Doorns (KZD) and Boesmanskop Tail (BT) (Figure 3-2 A). Kamo and Davis (1994) reported a $^{207}Pb/^{206}Pb$ age of 3107 ± 2 Ma as the crystallization age of the BT,

which is often extrapolated as the BH and KZD ages. They comprise syenites, leucogranites, and quartz monzonites, often with high REE contents (e.g., Anhaeusser et al., 1983; Anhaeusser and Robb, 1983; Moyen et al., 2021; Leandro et al., 2024). The GMS batholiths neighboring the BAC occur as tabular intrusions displaying a wide range of rock textures and compositions, from granodiorite to granites, and are predominantly composed of leucogranites (e.g., Westraat et al., 2005; Robb et al., 2006; Clemens et al., 2010; Moyen et al., 2021).

The syenites and quartz monzonites of the BAC are famous for their high volumes of K-feldspar phenocrysts and high contents of incompatible elements (e.g., LREE, LILE), predominantly higher than what is reported on the other GMS intrusions (e.g., Anhaeusser and Robb, 1983; Robb et al., 2006; Moyen et al., 2021). Although the BAC plutons are significantly smaller than the surrounding ca. 3105 Ma GMS plutons (e.g., Mpuluzi and Heereveen batholiths), they display a wide geochemical variation (e.g., Kamo and Davis, 1994; Moyen et al., 2021; Leandro et al., 2024).

The sheet-like structures, which can contain hypabyssal textures, at the lower levels of the BH overlay a network of granitic and syenitic dykes, suggesting the emplacement of the BAC at shallow levels (e.g., Leandro et al., 2024). The BAC intrusions are governed by the syn-magmatic shear zone dynamics that are partially recorded in the Saddleback-Inyoka Fault System and the Welverdiend Shear Zone, which is reflected in the Kees Zyn Doorns and Boesmanskop plutons, respectively (e.g., de Ronde and Wit, 1994; Lowe, 1994; Belcher and Kisters, 2006; Leandro et al., 2024).

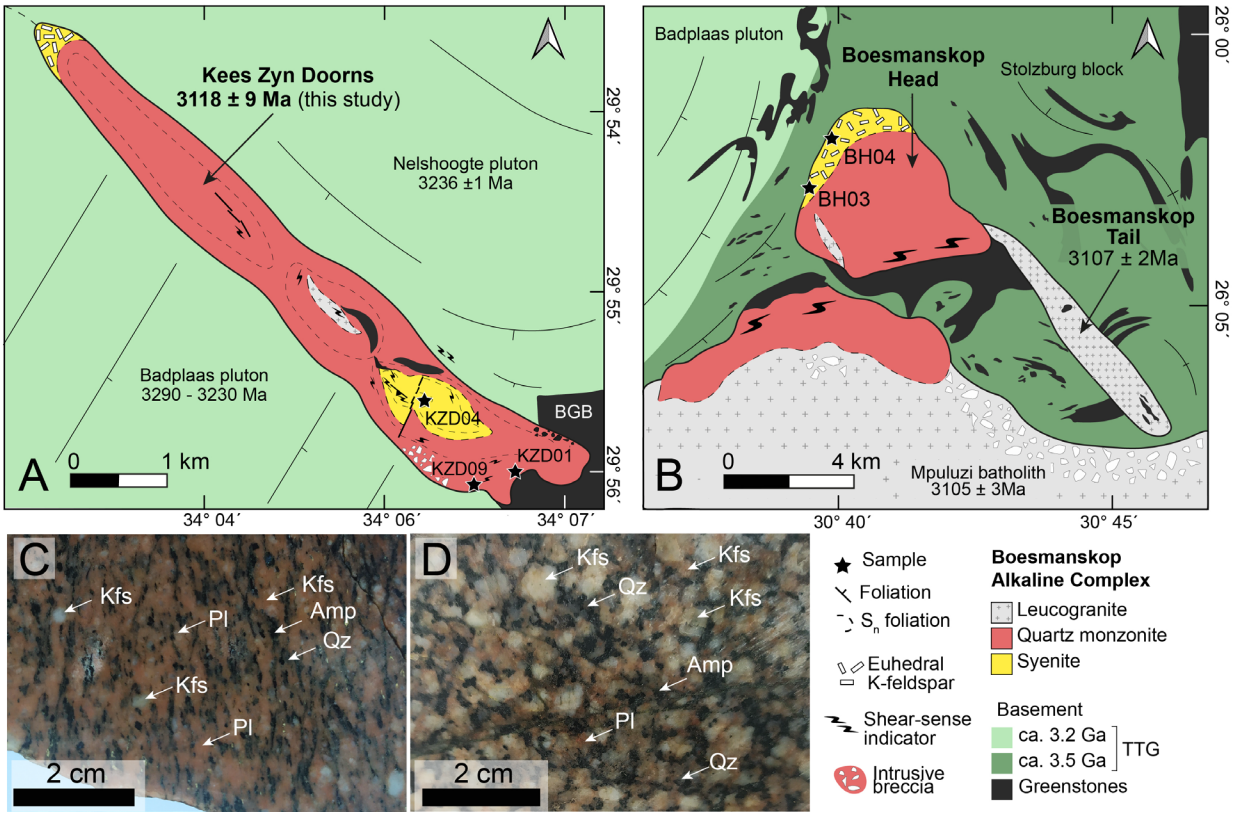

Figure 3-2. Geological map of the Boesmanskop Alkaline Complex illustrating the spatial distribution of main facies and sample locations (black stars). A) Kees Zyn Doorns pluton intrusive into ca. 3.2 Ga TTG suite. B) Boesmanskop Head and Boesmanskop Tail plutons intrusive into ca. 3.5 Ga TTG suite (after Anhaeusser and Robb, 1983 and Westraat et al., 2005). C) Representative texture of coarse-grained quartz monzonite with mineral lineation. D) Representative texture of the coarse-grained syenite with K-feldspar phenocrysts.

3.4. Whole-rock Chemistry

The syenite and quartz monzonite samples investigated in this study range in SiO_2 between 58.9 and 65.5 wt% (anhydrous and 100% normalized) and are characterized by high total alkalis (K_2O + Na_2O between 11.2 and 10.0 wt%) (Leandro et al., 2024). These rocks are metaluminous and contain high concentrations of large ion lithophile elements (LILE), such as Sr + Ba contents < 3813 parts per million (ppm), low concentrations of high field strength element (HFSE), and high ΣREE (from 586 to 620 ppm) (Leandro et al., 2024). The high LILE associated with the low HFSE (e.g., Nb, Ta, and Ti) has been interpreted to reflect a predominantly crustal magma source (e.g., Leandro et al., 2024; Yearron, 2003). The high alkalis contents were interpreted to reflect K-feldspar accumulation by mechanical processes associated with rhyolitic melt loss from the magma chamber due to the dynamic setting of intrusion (e.g., Leandro et al., 2024).

3.5. Results

3.5.1. Petrography

A detailed description of the essential mineral assemblage and whole-rock composition data of the BAC rocks used in this study is presented by Leandro et al. (2024). Here we focus on the main textural features related to the accessory minerals.

The syenites and quartz monzonites contain similar mineral assemblages and textures (Figure 3-2 C-D). Both types of rocks show pervasive K-feldspar cumulus textures with intercumulus pyroxene, amphibole, and titanite. The syenites and quartz monzonites exhibit high proportions of euhedral K-feldspar phenocrysts (orthoclase partially replaced by microcline), anhedral plagioclase phenocrysts (predominantly oligoclase), and low contents of quartz, occurring commonly as small, anhedral crystals in a medium to coarse-grained matrix. The main mafic minerals are Ca-amphibole, clinopyroxene (diopside and augite), and Fe-Ti oxides (magnetite and ilmenite). Biotite appears in minor amounts as small crystals with texture and chemistry (low Ti content) consistent with a secondary origin (Leandro et al., 2024). The accessory minerals are represented by titanite, prismatic apatite, and euhedral zircon (Figure 3-3).

Apatite is the only phosphate of the BAC rocks and occurs as short prismatic crystals (Figure 3-4). The apatite hosted within titanite contains weak chemical zonation and the apatite hosted within the other silicates is homogeneous. Some prismatic apatite is also hosted as inclusions within zircon crystals, indicating the early saturation of the magma with apatite. Rare elongated acicular apatite crystals are present within K-feldspar, amphibole, titanite, and clinopyroxene (Figure 3-4 A).

Titanite crystals occur as large euhedral to subhedral diamond-shaped crystals, which can be homogeneous (Figure 3-4 D-E) or with concentric zonation in the BSE electron images (Figure 3-4 F), and as smaller subhedral to anhedral crystals (Figure 3-4 C). The larger crystals display thin to well-developed overgrown rims (Figure 3-3 E) that host inclusions of Fe-Ti oxides (ilmenite and magnetite), allanite, and apatite. These overgrown rims are observed as darker rims in the BSE electron images (Figure 3-4 E-F). Rutile occurs as anhedral crystals strictly within titanite, suggesting their secondary origin (Figure 3-4 E).

Epidote group minerals also occur as rare, small anhedral crystals of allanite associated with titanite (Figure 3-3 E; Figure 3-4 F). The small dimensions of allanite and sporadic occurrence in the samples investigated precluded its TREE analysis.

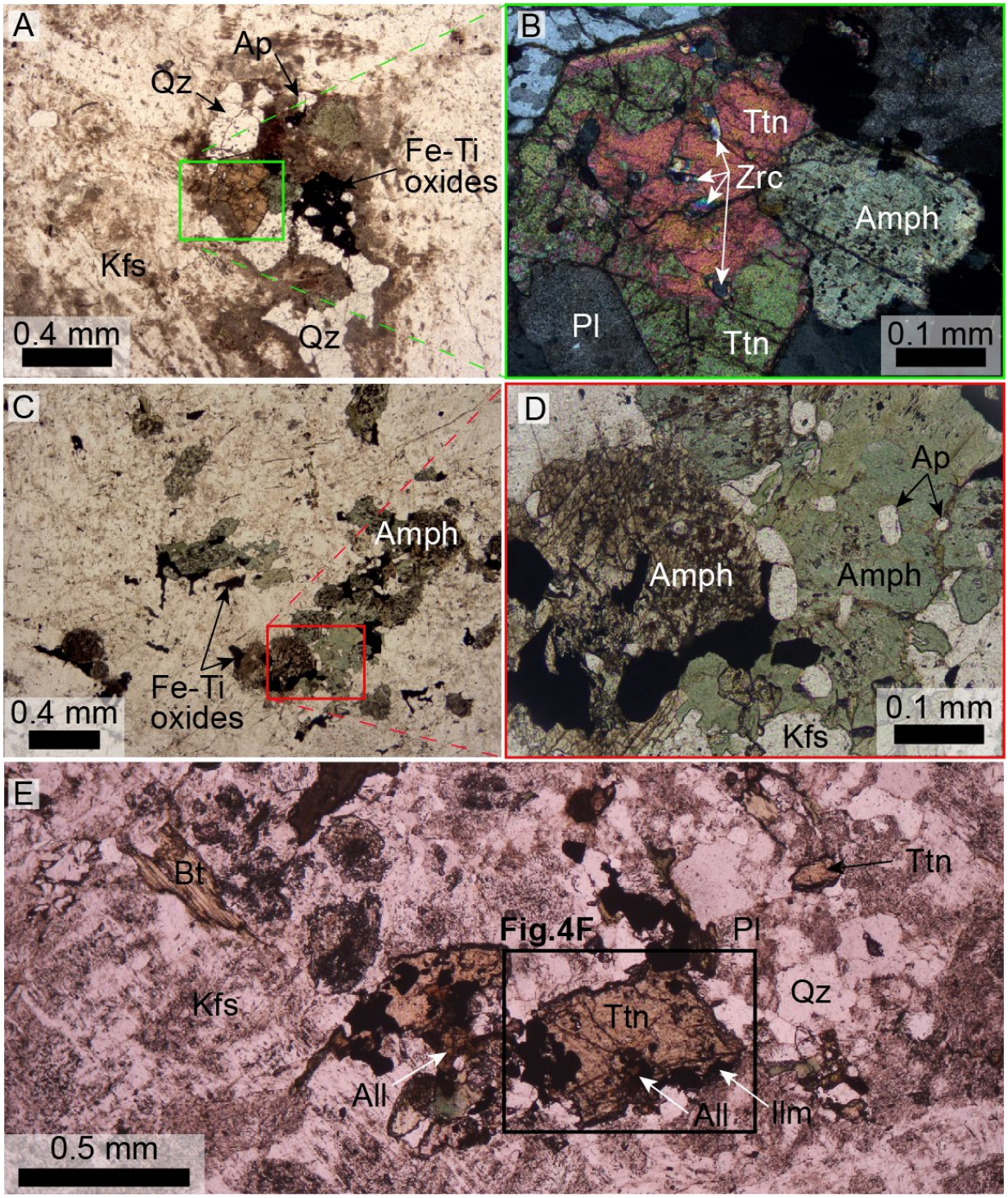

Figure 3-3. Photomicrography of representative accessory minerals textures. A-B) Porphyritic syenite with subhedral titanite crystals hosting zircon and in contact with amphibole. C-D) Coarse-grained syenites with apatite hosted by amphibole. Interstitial Fe-Ti oxide minerals and K-feldspar phenocrysts are also observed. E) Titanite crystal hosting allanite, zircon and Fe-Ti oxides in a coarse-grained quartz monzonite. These inclusions are clustered in the overgrown rims. All: allanite; Amph: amphibole; Ap: apatite; Ilm: Ilmenite; Kfs: K-feldspar; Pl: plagioclase; Qz: quartz; Ttn: titanite; Zrc: zircon.

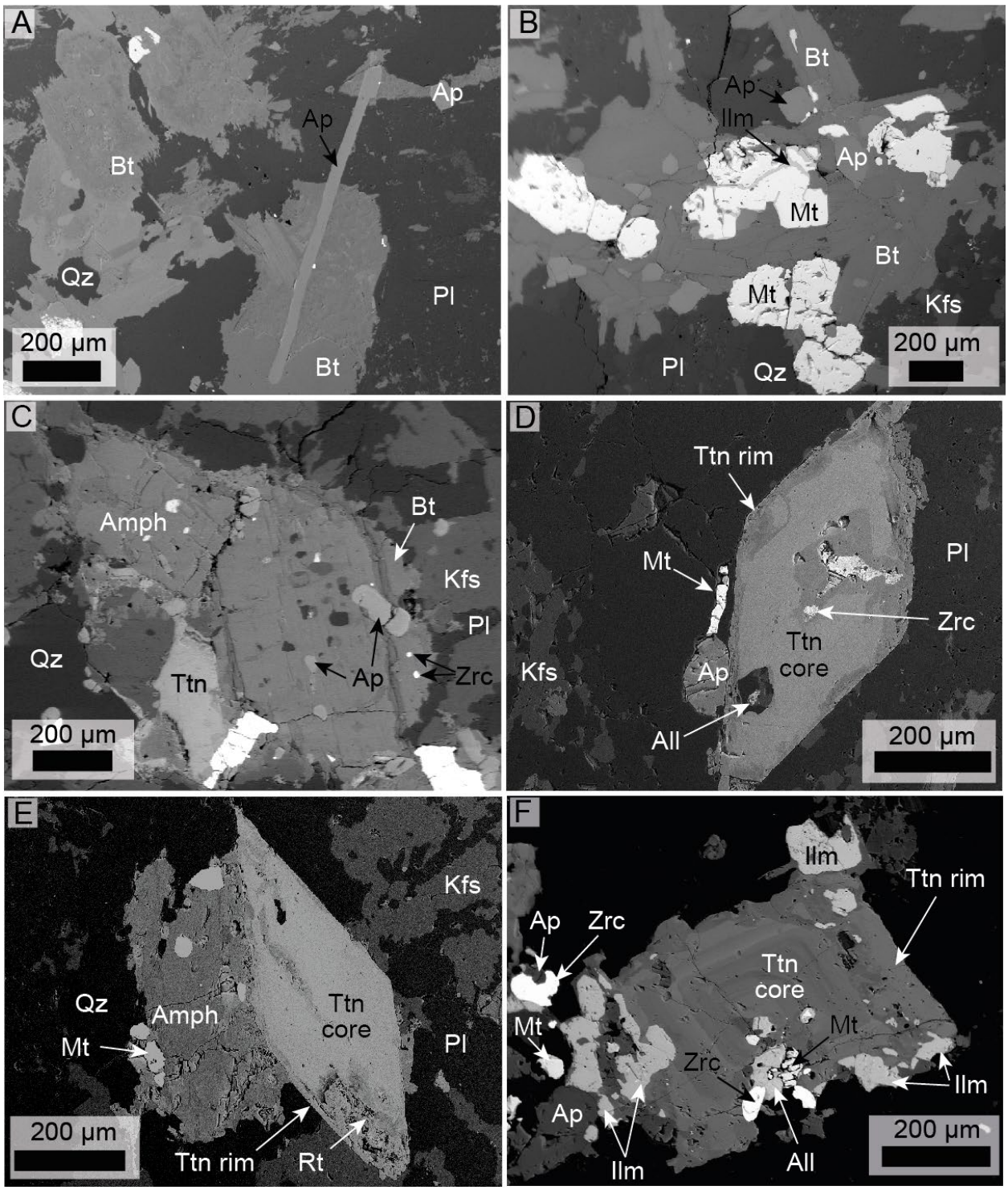

Figure 3-4. BSE images display the main textures of the accessory minerals in syenites (A-D) and quartz monzonites (E-F) of BAC. A) Acicular apatite. B) Euhedral blocky apatite crystals in a mafic cluster of biotite, ilmenite, and magnetite. C) Apatite inclusion in amphibole with biotite rims and surrounded by anhedral titanite and Fe-Ti oxides. D) Euhedral titanite crystal with a homogeneous bright interior which has been overgrown at the rim and replaced by a BSE darker titanite. E) Euhedral titanite crystal with a homogeneous bright core that has been overgrown by a BSE darker rim. F) Titanite crystal with concentric zonation on its core and overgrown rim. All: allanite; Amph: amphibole; Ap: apatite; Ilm: Ilmenite; Kfs: K-feldspar; Mt: Magnetite; Pl: plagioclase; Qz: quartz; Rt: rutile; Ttn: titanite; Zrc: zircon.

3.5.2. Zircon chemistry

Zircon in the BAC syenites and quartz monzonites are brown to pink in color, prismatic euhedral to subhedral crystals, and range between 10 and 160 µm in length. Most of the zircon crystals analyzed in the CL images in this study are characterized by concentric oscillatory zoning (Figure 3-5). Some rare crystals contain cores with zonation truncated by overgrowths and may thus represent inherited cores.

The zircon crystals from both samples display HREE enrichment over the LREE, with positive Ce anomalies (Figure 3-6 A-B), negative Eu anomaly (from 0.69 to 0.36), and Th/U ratios varying from 0.5 to 1.2 (Table 3-1). The Hf content from the syenite and quartz monzonite-hosted zircon ranges from 6346 ppm to 9833 ppm and is inversely proportional to the Ti contents (Figure 3-6 C). The Ti content is highly variable, ranging from 39.5 ppm to 6.7 ppm, with the higher values representing crystal cores, while the lower values are linked to the rims.

The Ti-in-zircon geothermometer (Ferry and Watson, 2007) indicates high apparent crystallization temperatures ranging from 915 °C to 750 °C, from core to rim. This geothermometer is pressure-dependent and assumes that zircon was in equilibrium with the surrounding magma at the time of crystallization, which may introduce an uncertainty of up to 50 ^{o}C to the estimation (Ferry and Watson, 2007). The higher temperatures are registered for the syenite-hosted zircon crystals (Figure 3-6 D). The zircon analyses report U/Yb from 0.2 to 2.6 (Figure 3-6 E), and Yb/Gd from 1.5 to 12.6 (Figure 3-6 F).

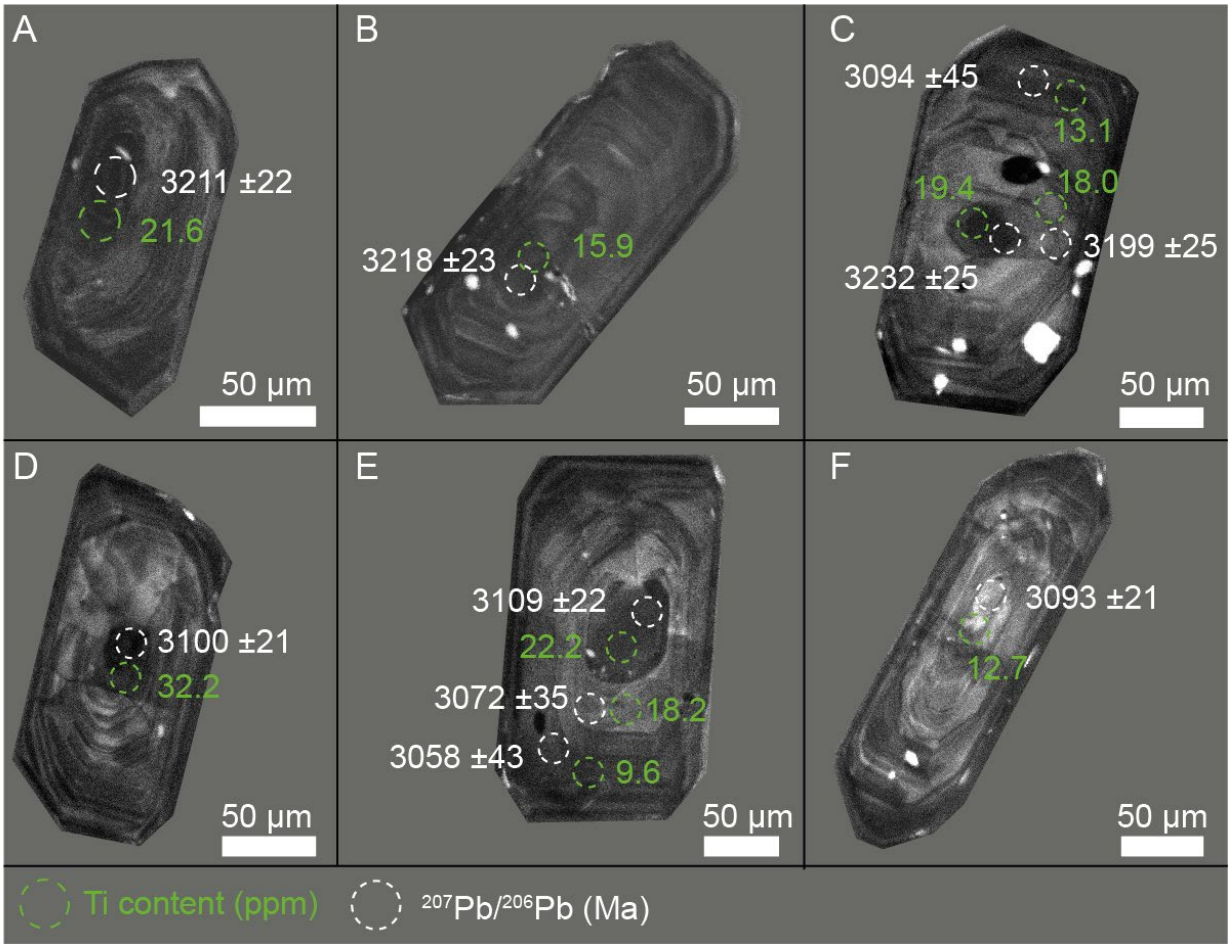

Figure 3-5. CL images of representative zircon crystals hosted in the coarse-grained quartz monzonite (sample KZD01) and age correlation with Ti contents. White circles indicate $^{207}Pb/^{206}Pb$ ages (Ma) and uncertainties (2σ), while green circles indicate trace elements analyses. The bright crystals within the zircon are apatite.

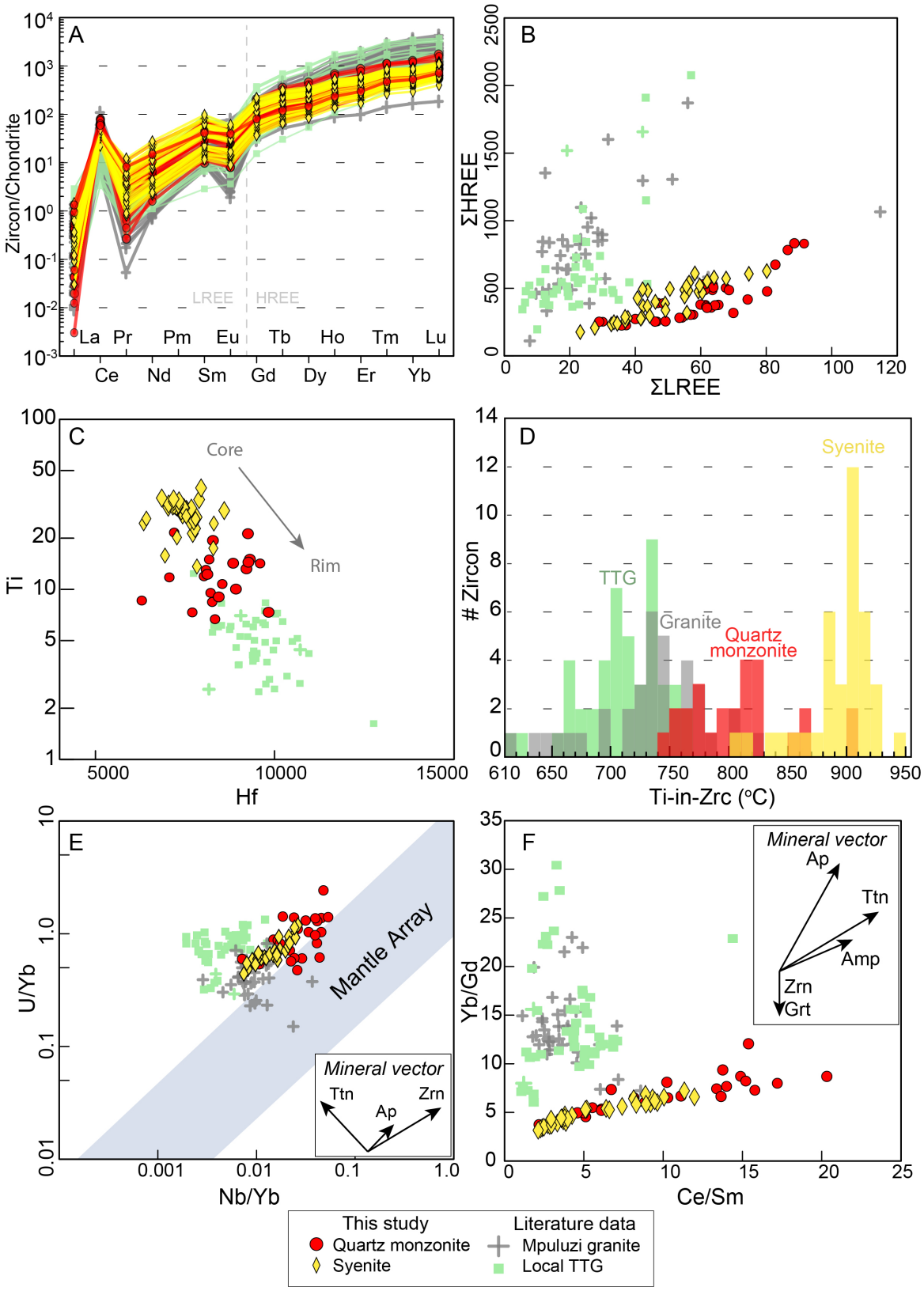

Figure 3-6. Illustration of the chemistry of the zircon crystals in the BAC syenites and quartz monzonites and the Ti in zircon thermometry results. A) Chondrite normalized (Nakamura, 1974) zircon REE plot. B) ΣLREE vs ΣHREE. C) Hf vs Ti. D) Apparent crystallization temperatures inferred using the Ti-in-zircon thermometer of Ferry and Watson (2007), with $a\mathrm{TiO_2}$ = 0.65 and $a\mathrm{SiO_2}$ = 0.95. E) Nb/Yb vs U/Yb ratios. F) Ce/Sm vs Yb/Gd ratios. The vectors of mineral fractionation and mantle array were defined by Grimes et al. (2015). The Mpuluzi granite and TTG suite data were obtained from Murphy (2015) and Laurent et al. (2022).

Table 3-1. Representative trace and rare earth element analyses (ppm) of zircon hosted in the BAC quartz monzonites and syenites.

Facies	Syenite						Quartz monzonite						
Sample	BH03			BH04			KZD09			KZD1			
Portion	**Rim**	**Core**	**Core**	**Rim**	**Core**	**Core**	**Core**	**Core**	**Rim**	**Rim**	**Rim**	**Core**	**Core**
Ti	13.6	26.9	26.1	22.8	33.7	39.5	21.3	30.2	9.0	13.1	8.5	28.7	14.3
Rb	0.1	0.2	0.2	0.1	0.3	0.2	0.1	0.2	0.1	0.1	0.3	0.1	0.3
Sr	0.2	0.3	0.2	0.2	0.2	0.2	0.6	0.3	0.2	0.2	0.1	BD	BD
Y	484	878	617	438	981	747	483	611	387	557	503	873	588
Nb	2.0	1.5	1.4	2.7	1.8	1.7	3.0	1.4	2.4	4.3	6.2	4.3	6.4
Ba	BD	0.0	BD	0.0	BD	0.1	0.3	0.2	0.0	BD	0.2	BD	< BD
La	0.0	0.2	0.2	0.0	0.1	0.1	0.4	0.3	0.0	0.4	0.2	0.1	0.0
Ce	49.3	40.9	34.2	36.0	41.8	36.4	51.0	30.1	45.9	53.8	51.1	32.6	56.8
Pr	0.2	0.7	0.4	0.1	1.2	0.7	0.9	0.6	0.1	0.6	0.3	1.2	0.2
Nd	2.2	8.7	4.6	2.0	14.8	9.8	9.3	6.7	1.0	3.1	2.1	14.9	3.3
Sm	4.1	11.4	6.7	3.9	16.9	12.3	8.4	9.1	2.3	4.0	3.2	15.0	4.1
Eu	1.3	3.6	2.4	1.1	4.1	3.3	3.1	2.6	0.6	1.4	0.9	3.8	0.8
Gd	17.8	41.4	26.5	17.4	54.2	41.1	22.1	32.0	11.6	18.4	16.1	44.0	18.6
Tb	5.4	11.1	7.4	5.0	13.8	10.4	5.6	8.3	3.6	5.1	4.6	10.9	6.0
Dy	50.7	97.7	67.1	47.7	118.6	89.9	49.7	72.2	37.0	54.0	46.8	96.8	56.0
Ho	17.2	31.8	21.9	15.6	35.2	27.6	16.3	22.3	13.1	18.1	16.1	27.4	20.5
Er	70.2	121.0	87.2	61.7	130.7	101.3	66.7	82.9	55.2	79.1	65.2	108.1	83.3
Tm	14.4	23.5	17.5	12.6	24.8	19.3	14.1	16.3	11.7	15.2	13.9	18.5	17.5
Yb	117.5	183.2	139.9	102.2	188.6	152.1	115.0	127.7	100.7	136.2	116.8	164.4	142.1
Lu	24.8	38.3	29.7	21.2	36.6	30.2	24.3	26.2	21.5	27.6	24.0	31.6	28.5
Hf	7833.9	7534.0	6422.1	7781.5	7894.8	7950.0	9256.3	7426.7	8445.8	8078.8	8251.8	7331.5	9590.3
Ta	0.8	0.7	0.6	1.0	0.8	0.7	1.0	0.5	1.0	0.8	1.4	0.7	0.7
^{208}Pb	28.0	30.0	28.2	30.6	34.6	30.2	23.2	21.6	26.1	44.0	32.9	33.3	31.0
Th	85.0	100.9	81.8	89.8	119.1	103.6	81.4	68.8	72.8	128.1	89.0	94.4	108.4
^{238}U	110.6	89.0	83.4	121.8	109.3	93.6	126.7	68.5	140.0	178.8	163.9	78.2	147.2
Eu/Eu*	0.5	0.5	0.5	0.4	0.4	0.4	0.7	0.5	0.4	0.5	0.4	0.5	0.3
Ce/Ce*	296.4	25.6	29.9	231.1	26.7	33.8	19.4	17.4	1561.3	26.1	46.5	23.6	297.9
Th/U	0.8	1.1	1.0	0.7	1.1	1.1	0.6	1.0	0.5	0.7	0.5	1.2	0.7
Yb/Gd	6.6	4.4	5.3	5.9	3.5	3.7	5.2	4.0	8.7	7.4	7.3	3.7	7.6
Ce/Sm	12.0	3.6	5.1	9.2	2.5	3.0	6.1	3.3	20.3	13.4	15.8	2.2	14.0
ΣLREE	57	66	48	43	79	62	73	49	50	63	58	68	65
ΣHREE	300	507	371	266	548	431	292	356	243	335	287	458	354
Ti-in-zircon (°C)	815	893	889	873	921	942	865	907	772	810	766	901	820

CN = Chondrite Normalized (Nakamura, 1974); BD = Below detection limit; $Eu/Eu^* = Eu_{CN}/(Sm_{CN}*Gd_{CN})^{\wedge 0.5}$; $Ce/Ce^* = Ce_{CN}/(La_{CN}*Pr_{CN})^{\wedge 0.5}$

3.5.3. Apatite chemistry

Apatite crystals in the rocks investigated are F-apatite (F <1.38 atoms per formula unit; supplementary material), which is typical of magmatic crystals (e.g., Duan et al., 2019). They are Ce-La rich, with higher REE contents in their cores (Figure 3-7 A). The apatite Mn content ranges from 695 ppm down to 232 ppm, while the Fe ranges from 1594 ppm to 112 ppm, with mean values of 364 ppm and 253 ppm, respectively (Figure 3-7 B).

Two apatite populations can be distinguished based on their TREE (Figure 3-7). One population presents an upward-convex REE signature due to high middle rare earth elements (MREE) contents. A second apatite population contains low MREE, obtained from crystals hosted by or in contact with titanite and amphibole.

The apatite population with a high MREE signature displays negative Eu anomalies (Eu/Eu* from 0.80 to 0.27; Figure 3-7 C) and predominantly positive Ce anomalies (Ce/Ce* from 0.97 to 1.17). The apatite with low MREE presents a weak negative Eu anomaly (Eu/Eu* from 0.97 to 0.57), and a slight negative Ce anomaly (from 0.94 to 0.99), predominantly. The MREE content distinction between the two apatite populations is evidenced by the correlation between the Ce/Sm and Yb/Gd ratios (Figure 3-7 D).

The high MREE apatite population displays high ∑HREE up to 1377 ppm (Figure 3-7 E; Table 3-2) and high and variable Sr (1085 to 2894 ppm), as well as Th/U ratios between 6.9 and 1.8 (Figure 3-7 F). The low MREE apatite population, in contrast, has lower ∑HREE (up to 615 ppm), Th/U ratios (6.2 to 4.5), as well as lower and less variable Sr (1823 to 894 ppm).

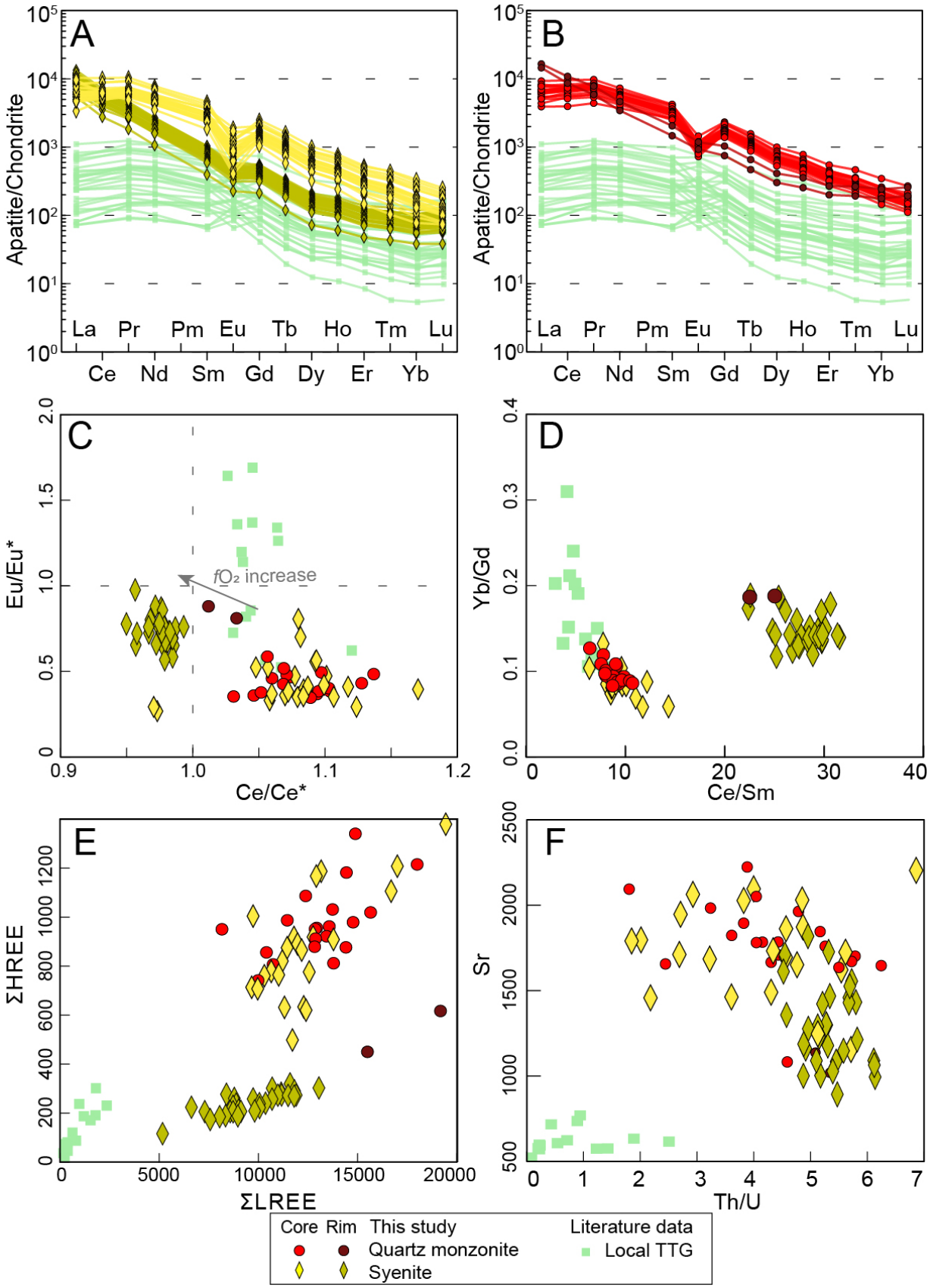

Figure 3-7. Diagrams illustrating the chemical distinctions of the two apatite populations described in this study. A) Chondrite normalized (Nakamura, 1974) spider diagram. B) Fe vs Mn. C) Ce/Ce* vs Eu/Eu*. D) Ce/Sm vs Yb/Gd ratios. E) ∑LREE vs ∑HREE; F) Th/U ratio vs Sr.

Table 3-2. Representative trace and rare earth element analyses (ppm) of apatite hosted in the BAC quartz monzonites and syenites.

Facies	Syenite			Syenite			Quartz monzonite				
Sample	BH04			BH03			KZD09				
Signature	**High MREE**			**Low MREE**			**High MREE**				
Na	635.2	417.9	654.2	351.9	426.2	458.6	293.7	203.3	750.2	453.6	616.6
Al	BD	6.6	BD	3.9	0.3	BD	0.4	167.4	2.9	BD	8.3
Ti	0.8	0.2	BD	BD	0.5	0.4	BD	1.1	0.9	BD	0.7
V	7.5	4.0	6.8	9.9	9.4	7.6	6.9	5.9	7.1	6.7	7.0
Mn	485.7	338.3	249.0	357.2	475.1	303.1	366.6	285.9	329.5	373.7	409.8
Fe	261.1	268.0	185.4	308.2	289.3	113.9	112.3	473.9	269.9	188.6	235.6
Ni	0.2	0.2	0.2	BD	BD	BD	0.3	0.6	0.7	BD	0.3
Cu	0.1	0.4	1.4	0.2	BD	BD	0.3	0.7	3.2	BD	1.4
Zn	0.9	BD	BD	BD	BD	BD	1.9	1.5	0.7	BD	1.4
Ga	176.3	118.0	102.7	94.5	70.7	42.8	161.7	135.8	135.5	143.4	166.1
Rb	0.2	0.2	0.1	0.1	0.1	0.0	0.1	1.1	0.2	0.1	0.2
Sr	1626	1795	1656	1463	1472	1190	1022	1789	1713	1765	1706
Y	1515	1327	618	392	291	138	784	1526	1027	1044	1278
Zr	3.3	1.5	0.3	0.6	0.3	0.1	4.1	0.9	0.9	1.3	1.4
Nb	0.1	0.0	0.0	0.0	0.0	0.0	0.0	0.1	0.0	0.0	0.0
Ba	0.2	0.4	0.1	0.5	0.4	0.5	0.4	0.6	0.3	0.2	0.3
La	3406.5	1913.7	2123.0	3790.5	2899.0	1789.9	5450.8	2225.5	2569.3	2606.2	3063.2
Ce	8876.4	5683.5	5231.4	5426.9	4082.9	2396.3	9372.8	6519.8	6740.9	7193.0	8239.4
Pr	1167.6	816.8	663.1	469.7	354.7	205.5	872.3	955.8	894.9	958.5	1094.5
Nd	4906.9	3604.1	2745.4	1626.2	1182.1	670.6	2922.6	4197.8	3765.3	4051.8	4606.7
Sm	937.7	746.5	474.7	207.9	149.8	80.3	416.4	839.5	684.7	730.1	860.1
Eu	94.5	118.7	48.4	45.3	33.5	17.4	91.4	111.7	81.4	74.3	90.5
Gd	688.5	570.5	340.7	152.3	109.5	58.6	286.6	642.5	500.0	526.2	625.8
Tb	77.1	64.9	35.4	15.8	11.3	5.6	30.9	74.0	53.9	56.3	67.2
Dy	347.8	296.7	151.2	72.1	51.2	24.7	141.8	343.2	241.4	248.6	298.7
Ho	54.4	47.0	23.2	12.6	8.9	4.2	25.0	54.7	37.7	38.6	46.5
Er	120.2	105.4	48.3	31.0	22.2	10.7	60.8	123.5	82.9	85.2	102.1
Tm	13.1	11.8	4.9	3.9	2.8	1.3	8.0	14.0	8.9	9.0	10.6
Yb	68.0	62.0	23.6	26.0	17.5	8.4	53.5	76.6	46.8	47.7	55.7
Lu	7.9	7.2	2.7	4.3	2.9	1.3	8.8	9.2	5.4	5.6	6.4
^{208}Pb	30.1	9.1	11.2	45.4	23.9	12.7	49.3	19.9	15.9	19.2	26.0
Th	97.0	19.8	26.2	139.1	68.9	24.4	165.2	59.4	40.8	61.0	81.6
^{238}U	17.5	10.7	5.5	24.5	12.9	5.0	30.9	14.3	9.2	11.6	14.1
Eu/Eu	0.36	0.56	0.37	0.78	0.80	0.78	0.81	0.46	0.43	0.37	0.38
Ce/Ce	1.07	1.09	1.06	0.98	0.97	0.95	1.03	1.07	1.07	1.09	1.08
Yb/Gd	0.1	0.1	0.1	0.2	0.2	0.1	0.2	0.1	0.1	0.1	0.1
Ce/Sm	9.5	7.6	11.0	26.1	27.3	29.8	22.5	7.8	9.8	9.9	9.6
Th/U	5.5	1.9	4.8	5.7	5.3	4.9	5.3	4.2	4.4	5.3	5.8
ΣLREE	19390	12883	11286	11567	8702	5160	19126	14850	14737	15614	17954
ΣHREE	1377	1166	630	318	226	115	615	1338	977	1017	1213

CN = Chondrite Normalized (Nakamura, 1974); BD = Below limit of detection; Eu/Eu* = $Eu_{CN}/(Sm_{CN}*Gd_{CN})^{\wedge 0.5}$; Ce/Ce* = $Ce_{CN}/(La_{CN}*Pr_{CN})^{\wedge 0.5}$

3.5.4. Titanite chemistry

Titanite crystals are characterized by a systematic decrease in their TREE contents from the homogeneous bright areas in the core to the darker rims in BSE images, which contain Fe-Ti oxides and apatite inclusions (Figure 3-4 E-F). The homogeneous and brighter cores contain higher MREE contents than the darker rims (Figure 3-8 A-B). The titanite crystals can be divided in three distinct groups according to their texture and chemical compositions (core, rim and small titanite crystals). The bright cores exhibit an upward-convex REE signature due to the high MREE contents and a negative Eu anomaly (Eu/Eu* from 0.5 to 0.8). The darker rims of the titanite display lower MREE contents and a negative to positive Eu anomaly (Eu/Eu* from 0.8 to 1.7), (Figure 3-8 D). The smaller subhedral crystals are chemically distinct from the larger ones, exhibiting lower LREE contents than titanite rims, while displaying similar fractionation patterns for the HREE (Figure 3-8 B). Furthermore, the anhedral and smaller crystals have lower REE (Figure 3-8 E) and predominantly negative Eu anomaly (from 0.7 to 1.1).

Despite the distinct REE contents, the three titanite groups contain Fe and Al concentrations within the same range (Table 3-3). Fe content is relatively high (28413 ppm to 15206 ppm) and the Al content is low (16704 ppm to 6655 ppm). Zr contents in the core are up to 1365 ppm and decrease towards the crystal rims (down to 364 ppm). The lower Zr contents are reported for the anhedral and smaller titanite crystals (573 to 158 ppm).

The Zr-in-titanite geothermometer was calculated for the titanites in the syenite and quartz monzonite samples following the equation proposed by Hayden et al. (2008). The results provided a wide range of apparent temperatures, varying from 756 °C for the cores to 684 °C for the rims (Figure 3-8). The smaller crystals express the lower temperatures (707 to 643 °C).

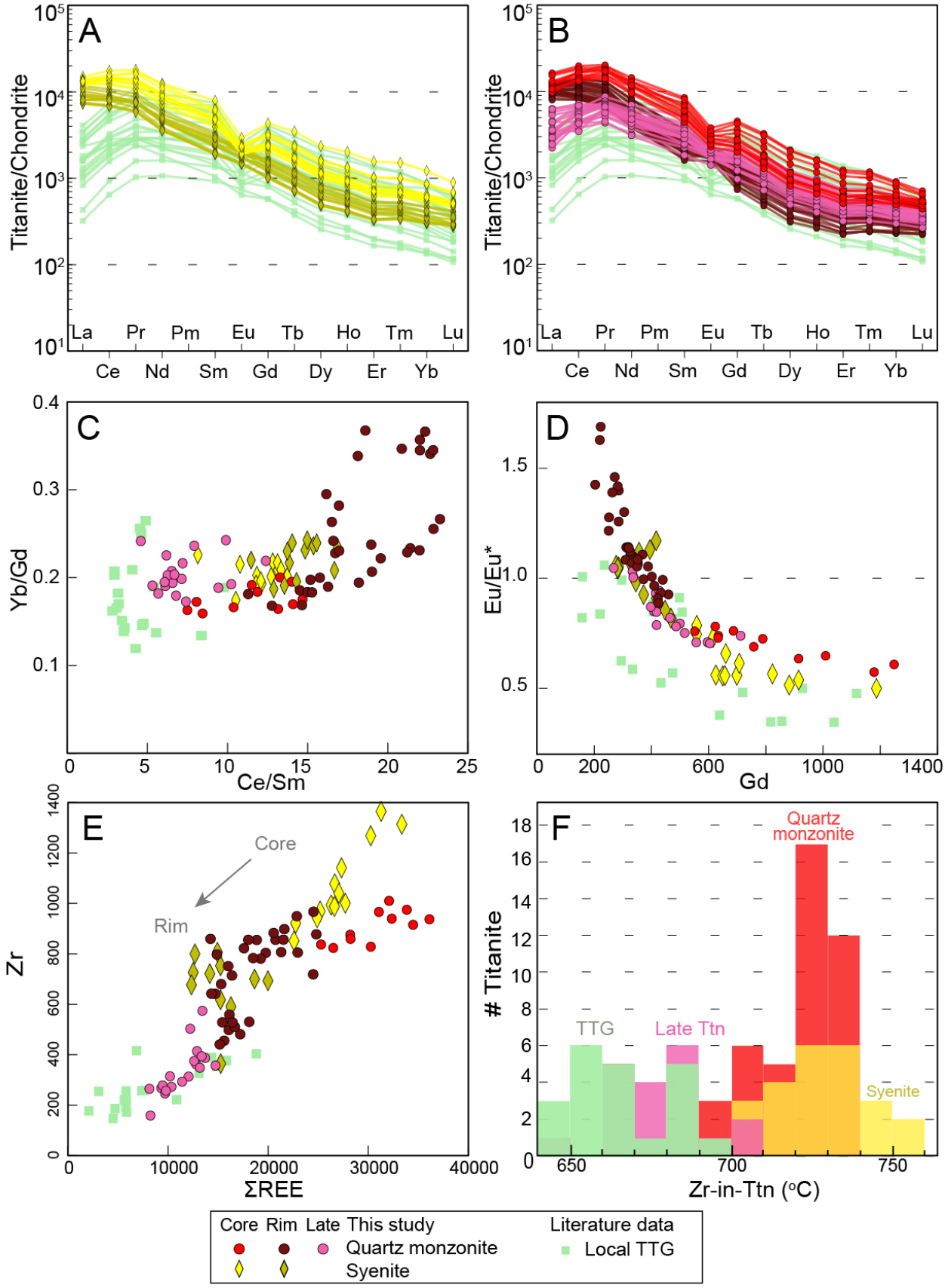

Figure 3-8. Chemical diagrams for the titanite crystals of the BAC rocks subdivided according to their chemical signatures. A-B) Chondrite-normalized REE diagram (Nakamura, 1974) with plot of the syenite-hosted crystals and quartz monzonite-hosted crystals, respectively. C) Yb/Gd vs Ce/Sm ratios. D) Gd vs Eu/Eu*. E) Zr vs ∑REE. F) Zr-in-titanite temperature for the BAC and TTG crystals. The literature data are the primary titanite hosted on the TTG suite reported by Mühlberg (2022).

Table 3-3. Representative trace and rare earth element analyses (ppm) of titanite hosted in the BAC quartz monzonites and syenites.

Facies	Syenite				Quartz monzonite				Quartz monzonite	
Sample	BH03				KZD09				KZD01	
Signature	**High MREE**		**Low MREE**		**High MREE**		**Low MREE**	**Late**	**Late**	**Low MREE**
V	324.0	355.9	361.8	435.7	393.8	372.5	367.5	389.9	491.1	349.0
Cr	10.1	11.1	50.8	21.8	9.4	11.7	11.4	20.7	15.4	9.6
Mn	1441.4	1567.5	1336.1	1081.5	1284.9	1256.3	1196.4	1207.4	885.8	1242.0
Al	8199	7913	8775	9297	9632	8820	9715	11395	10640	8187
Fe	20901	23600	20948	20568	20229	18608	18693	19655	21891	19444
Ni	0.3	BD	0.2	0.6	BD	BD	1.3	0.7	BD	0.3
Cu	31.4	2.5	12.1	3.2	2.2	2.2	2.3	2.6	1.6	1.5
Zn	32.2	5.1	10.0	6.7	7.2	5.6	32.3	21.3	1.3	2.7
Ga	195.3	295.5	170.8	132.3	277.4	228.8	130.2	118.1	56.1	159.1
Rb	0.6	0.4	0.2	0.3	0.7	0.5	0.5	3.2	0.2	0.2
Sr	109	81	82	85	139	112	101	90	94	110
Y	1488	2552	1287	1173	2224	1298	861	911	883	1150
Zr	851.3	1314.1	693.2	364.5	1010.2	823.3	455.6	573.8	264.8	949.5
Nb	1304.3	2871.8	1117.2	1235.2	1643.4	1576.7	991.5	1060.5	549.2	1716.3
Cs	0.2	BD	0.0	0.1	0.0	0.1	0.0	0.1	0.0	0.0
Ba	19.7	0.3	7.1	1.9	3.5	8.6	16.1	4.0	1.4	0.4
La	4227.7	4921.6	3843.2	2652.1	4116.5	4050.5	3250.9	2081.5	961.0	3958.0
Ce	10447.8	15166.4	9310.9	6849.6	14311.9	12667.2	7369.2	6205.0	3279.8	11420.8
Pr	1212.0	2010.1	1064.9	839.7	2023.0	1612.1	798.1	790.7	487.3	1317.2
Nd	4425.3	7631.6	3825.6	3165.0	8022.5	5909.5	2784.5	2938.6	2025.8	4391.4
Sm	795.9	1282.0	672.1	597.1	1379.1	905.1	485.6	500.9	455.2	629.8
Eu	162.5	190.3	150.2	148.4	233.0	175.2	140.5	134.8	131.4	170.5
Gd	558.0	914.6	468.5	417.0	914.3	551.2	331.8	336.2	333.6	388.4
Tb	69.6	113.6	58.1	53.5	105.5	60.0	41.7	40.1	43.0	44.2
Dy	334.9	556.3	286.8	263.9	500.4	276.4	203.9	196.1	210.4	214.7
Ho	57.3	93.5	48.2	43.9	81.0	45.7	32.8	32.4	35.2	37.9
Er	138.1	230.3	118.8	108.5	194.9	114.2	78.3	81.2	87.5	115.1
Tm	18.1	29.5	15.5	14.2	24.7	15.7	10.2	11.2	11.7	18.8
Yb	116.5	185.3	101.6	91.7	151.9	107.6	65.5	73.6	72.2	131.4
Lu	15.7	22.6	13.9	12.0	19.0	14.9	8.7	10.8	10.0	18.9
Hf	62.1	96.5	49.7	32.6	64.0	63.3	38.0	44.7	32.8	68.5
Ta	57.5	213.2	49.2	52.2	196.0	152.7	58.1	69.1	22.5	186.1
^{208}Pb	246.4	139.2	180.0	72.5	131.4	124.1	159.0	86.8	38.9	109.3
Th	568.1	445.1	476.6	231.9	416.5	407.0	415.6	292.2	124.2	384.0
^{238}U	138.0	66.0	167.6	188.0	68.8	90.8	109.5	107.5	134.3	67.6
Eu/Eu*	0.7	0.5	0.8	0.9	0.6	0.8	1.1	1.0	1.0	1.1
Ce/Ce*	1.1	1.2	1.1	1.1	1.2	1.2	1.1	1.2	1.2	1.2
Yb/Gd	0.2	0.2	0.2	0.2	0.2	0.2	0.2	0.2	0.2	0.3
Ce/Sm	13.1	11.8	13.9	11.5	10.4	14.0	15.2	12.4	7.2	18.1
ΣREE	22579	33348	19978	15256	32078	26505	15602	13433	8144	22857
Zr-in-titanite (°C)	729	754	718	684	739	727	696	708	668	735

3.5.5. Geochronology

U-Pb zircon dating has confirmed fourteen individual spots on inherited cores out of a total of thirty-eight individual spots. They yielded an upper intercept age of 3220 ± 13/35 Ma (2s, MSWD = 0.24). The U-Pb concordia diagram exhibits clear Pb loss, as reflected by the ages plotting alongside a steep discordia line (Figure 3-9 A).

Twenty-four individual spots on concentric oscillatory zoned zircon crystals yielded an upper intercept age of 3118 ± 9/32 Ma (2s; MSWD = 1.1; Table 3-4), illustrated in Figure 3-9 B. These grains also experienced Pb loss recorded predominantly on the crystal rims. Within the data that reflect BAC crystallization ages, the higher Ti measured on their cores reaches 32 ppm (Figure 3-5 D).

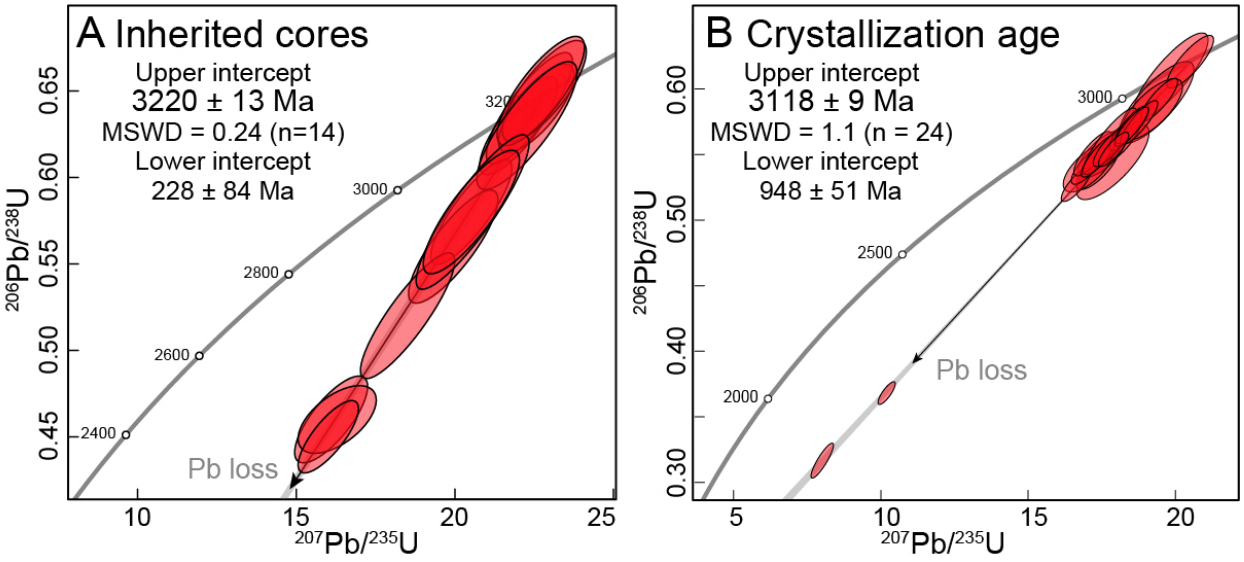

Figure 3-9. U-Pb concordia $^{206}Pb/^{238}U$ vs $^{207}Pb/^{235}U$ diagram plots for the coarse-grained quartz monzonite of the BAC (sample KZD01). A) Inherited cores. B) Crystallization zircon ages. The ellipses uncertainties are reported as 2σ. MSWD: mean square of weighted deviates.

Table 3-4. U-Pb isotopic data of zircon hosted in the coarse-grained quartz monzonite yielding crystallization ages. The inherited ages are presented in the supplementary materials.

Sample KZD01	Concentration (ppm)			Radiogenic ratios							Calculated age (Ma)						Concordance	
Spot	**U**	**Th**	**Th/U**	**$^{207}Pb/^{206}Pb$**	2σ (%)	**$^{207}Pb/^{235}U$**	2σ (%)	**$^{206}Pb/^{238}U$**	2σ (%)	***ρ***	**$^{206}Pb/^{238}U$**	2σ (abs)	**$^{207}Pb/^{235}U$**	2σ (abs)	**$^{207}Pb/^{206}Pb$**	2σ (abs)	**206/238 x 207/235**	**207/206 x 206/238**
1	144.2	69.5	0.5	0.24	1.72	20.50	3.13	0.62	2.61	0.83	3113	65	3115	34	3117	28	100	100
2	166.4	92.3	0.0	0.24	2.81	19.83	5.18	0.61	4.35	0.84	3069	107	3083	54	3093	46	100	99
3	268.6	72.2	0.0	0.24	2.99	19.19	4.39	0.58	3.22	0.73	2967	77	3052	46	3108	48	97	95
4	373.4	155.7	0.4	0.24	1.36	18.22	2.55	0.56	2.16	0.85	2866	50	3001	28	3093	22	95	93
5	127.2	63.6	0.5	0.24	1.40	19.44	2.62	0.59	2.22	0.85	2996	53	3064	28	3109	22	98	96
6	186.7	100.4	0.5	0.23	2.16	17.36	3.36	0.54	2.57	0.76	2786	58	2955	35	3072	35	94	91
7	135.1	56.7	0.4	0.23	2.70	17.52	3.76	0.55	2.61	0.70	2827	60	2963	39	3058	44	95	92
8	190.6	47.0	0.2	0.23	1.44	17.82	2.82	0.56	2.42	0.86	2852	56	2980	30	3067	23	96	93
9	213.2	75.3	0.4	0.23	2.94	17.04	4.02	0.54	2.74	0.68	2782	62	2937	42	3045	48	95	91
10	190.5	61.9	0.3	0.23	1.41	16.63	2.43	0.53	1.97	0.81	2729	44	2914	26	3043	23	94	90
11	240.0	134.8	0.6	0.23	1.62	17.03	2.66	0.54	2.11	0.79	2789	48	2936	28	3038	26	95	92
12	121.7	38.3	0.3	0.23	1.73	17.19	3.02	0.55	2.47	0.82	2828	57	2946	32	3027	28	96	93
13	2142.9	1537.2	0.7	0.18	1.81	8.01	3.84	0.32	3.39	0.88	1773	53	2232	37	2684	30	79	66
14	255.6	74.3	0.3	0.23	1.93	17.78	4.12	0.56	3.64	0.88	2867	85	2978	43	3053	31	96	94
15	81.3	24.9	0.3	0.24	3.56	17.87	5.55	0.54	4.25	0.77	2802	97	2983	57	3107	58	94	90
16	241.7	126.4	0.5	0.23	1.48	17.40	2.78	0.55	2.35	0.85	2820	54	2957	30	3052	24	95	92
17	666.1	119.7	0.2	0.20	1.32	10.20	2.31	0.37	1.89	0.82	2020	33	2453	24	2833	22	82	71
18	244.9	137.9	0.6	0.23	1.40	18.31	2.45	0.57	2.01	0.82	2896	47	3006	27	3081	23	96	94
19	314.9	81.1	0.3	0.23	1.51	17.79	2.63	0.56	2.15	0.82	2849	50	2978	28	3067	24	96	93
20	215.7	90.2	0.4	0.23	1.45	18.54	2.49	0.57	2.03	0.81	2919	48	3018	27	3084	23	97	95
21	188.5	57.6	0.3	0.24	1.35	18.76	2.72	0.57	2.36	0.87	2925	56	3030	29	3100	22	97	94
22	270.7	31.6	0.1	0.24	3.24	19.34	5.36	0.59	4.26	0.80	2988	103	3059	56	3106	53	98	96
23	493.1	165.8	0.3	0.24	1.29	18.51	2.46	0.57	2.10	0.85	2912	49	3016	27	3086	21	97	94
24	357.5	146.8	0.4	0.23	1.28	17.90	2.29	0.55	1.90	0.83	2841	44	2984	25	3082	21	95	92

ρ = Correlation coefficient between the isotopic ratios $^{206}Pb/^{238}U$ and $^{207}Pb/^{235}U$

3.6. Discussion

3.6.1. Zircon chemistry

Zircon is a ubiquitous accessory mineral in the syenites and quartz monzonites of the BAC. They exhibit textures and geochemical signatures indicative of igneous crystals (Figure 3-5, Figure 3-6) (e.g., Hoskin and Ireland, 2000; Grimes et al., 2015; Duan et al., 2019). The zircon low ∑HREE compared to ∑LREE contents (Figure 3-6 B), plot outside the zircon mantle array (Figure 3-6 E) defined by Grimes et al. (2015), along with the trends observed on the Ce/Sm vs Yb/Gd diagram (Figure 3-6 F) suggest the melt was depleted in HREE since its early stages. These signatures may reflect the preferential partitioning of the LREE into the melt during source incongruent melting, while HREE are retained in refractory phases (e.g., pyroxene and garnet) left behind in the source (e.g., Fitton and Upton, 1987; Clemens et al., 2012; Clemens et al., 2020). The U-Pb age results confirmed that most zircon analyzed from the quartz monzonite is ca. 3.1 Ga. However, some zircon chemical analyses do not have U-Pb associated ages, and the presence of a few inherited zircon compositions might explain the plot of some spots within the mantle array on the U/Yb vs Nb/Yb diagram.

The increase in Ce/Sm and Yb/Gd ratios in zircon can result from the preferential removal of MREE from the melt compared to LREE and HREE during fractional crystallization (e.g., Lee et al., 2017). A steep increase in these ratios, as observed for the ca. 3.46 Ga TTG suite basement (Figure 3-6 B), may be associated with apatite crystallization. Conversely, a flatter trend in Ce/Sm vs Yb/Gd ratios might indicate early crystallization of amphibole or titanite in varying proportions (e.g., Grimes et al., 2015; Lee et al., 2017; Duan et al., 2019). Therefore, the shallow increase of these ratios observed in the syenite and quartz monzonite zircons suggests the co-crystallization of zircon with amphibole and titanite (e.g., Grimes et al., 2015; Duan et al., 2019), which agrees with the textural observations in this study (Figure 3-3 B).

The temperature range registered by the Ti-in-zircon may reflect the continuous crystallization from the zircon saturation down to the solidus temperatures (e.g., Claiborne et al., 2006; Bea et al., 2007). The spatially coupled U-Pb and trace element analysis indicate that the crystals reporting crystallization ages for the quartz monzonite contain high Ti amounts (up to 32 ppm), suggesting an early zircon saturation within hot magmas as it is required to produce zircon-bearing rocks as K-feldspar dominated cumulates (e.g., Leandro et al., 2024) and progressive crystallization over a range of ca. 200 °C. At the same time, the increase of Hf in zircon associated with the systematic decrease of Ti indicates that the crystals from the syenites

are derived from hotter and less evolved melts than those crystallizing the quartz monzonites (Figure 3-6 C-D). These features associated with a positive correlation between U/Yb and Nb/Yb ratios (Figure 3-6 E) reflect the changes in melt composition during the cooling of the magma and progressive crystallization of zircon alongside the early phases (e.g., Claiborne et al., 2006; Lee et al., 2017). This is consistent with the fractional crystallization hypothesis producing the BAC proposed by Leandro et al. (2024).

The zircons hosted in ca. 3105 Ma granites of the Mpuluzi batholith and the TTG suite basement exhibit Ti concentrations ranging from 14.2 to 1.2 ppm and 8.3 to 1.9 ppm, respectively (Murphy, 2015; Laurent et al., 2022). These Ti concentrations consequently indicate lower apparent temperatures than the zircon hosted in the syenites and quartz monzonites, with values between 820 °C and 667 °C for the granites and 800 °C to 720 °C for the local TTG suite (Murphy, 2015; Laurent et al., 2022). The TTG suite basement and Mpuluzi granite zircon display higher HREE and lower LREE contents than the zircon in the BAC syenites and quartz monzonites (Figure 3-6 B). This feature may reflect the origin of the TTG suite from hydrated mafic sources within the garnet stability field (e.g., Clemens et al., 2006) whereas the granite might be derived from high degrees of partial melting hindering the enrichment of the magma in incompatible elements (e.g., Moyen et al., 2021).

3.6.2. Apatite chemistry

Apatite hosted in zircon and acicular crystals suggests that apatite and zircon crystallized contemporaneously at an early stage of the crystallization history. The early nature of the apatite allows it to register the magmatic history and thus provide insight into the magma evolution (e.g., Carvalho et al., 2012; Buand et al., 2016; Duan et al., 2019). The apatite crystals in the BAC are euhedral, well-developed, and hosted in early crystallized silicates (e.g., amphibole, pyroxene), indicating they are primary. Furthermore, apatite with the same signature in the samples from Kees Zyn Doorns and Boesmanskop Head reinforces the findings that they are cogenetic and derived from compositionally similar parental magmas.

The abrupt change in apatite composition between the low and high MREE populations suggests these chemical changes are not a result of the progressive crystallization during magma cooling (e.g., Bruand et al., 2016). The higher Kd for the MREE, compared with LREE and HREE, can cause the concave-upward signature of apatite observed in the REE diagram (Watson and Green, 1981; Duan et al., 2019). This hypothesis may explain the higher MREE contents of the coarse-grained rocks. Another possibility to explain an apparent enrichment of MREE is the

depletion of LREE in the source. However, the MREE-high and MREE-low apatite populations in this study often contain similar contents of LREE (Figure 3-7 E), demonstrating that the LREE contents were not affected by the process that caused the MREE decoupling. Additionally, the Mn and Fe content of the two distinct populations of apatite chemistry are within the same range in the syenites and quartz monzonites (Table 3-2) despite the differences in the whole-rock SiO_2 and alumina saturation index contents of these rocks. This suggests that the parental magma composition is not the primary factor influencing the observed MREE variations described in the apatite.

The crystallization of other phases that can absorb MREE is a plausible explanation for the two different apatite REE compositions. The early crystallization of titanite can reduce the MREE relative to LREE and HREE and produce apparent positive Eu anomalies in the apatite once Sm and Gd are preferentially incorporated into titanite (e.g., Watson and Green, 1981; Duan et al., 2019). Thus, the apatite with high MREE contents is interpreted as the pristine compositions of early crystallized apatite prior to titanite saturation. In contrast, the apatite crystals with lower MREE initiated their crystallization after the titanite, zircon, and amphibole, explaining their lower MREE and HREE contents (Figure 3-7 D-E).

The higher Sr and lower Th/U in the high MREE apatite group also support the previous interpretation. The MREE-low apatite displays a negative Ce anomaly, suggesting they crystallized in a slightly more oxidizing magma (Figure 3-7 C). The lower Sr contents of this apatite population indicate higher volumes of coexisting feldspar (Figure 3-7 F), and its higher Th/U ratio (Figure 3-7 F) indicates more felsic magmas than those that formed the early crystallized apatite (e.g., Duan et al., 2019; Belousova et al., 2002).

The two apatite signatures in the BAC rocks differ from those hosted in the TTG suite. The latter has lower TREE contents, which might be a signature inherited from their mafic source (e.g., Clemens et al., 2006).

3.6.3. Titanite chemistry

Titanite in the BAC rocks occur predominantly as relatively large, euhedral to subhedral crystals. This, in combination with their high Fe and low Al character (Table 3-3), suggests that these crystals are magmatic and early crystallized (e.g., Gros et al., 2020; Kowallis et al., 2022). On the other hand, the smaller subhedral to anhedral titanite crystals are textures of late crystallized crystals.

The homogeneous zones, which are brighter in BSE images and commonly form the crystal cores, contain higher MREE contents and preserves higher temperatures than the overgrow rims (Figure 3-8 E-F). These MREE-rich zones are interpreted as the pristine compositions of the early crystallized titanite. The decrease in TREE from core to rim may reflect the evolving composition of the melt during the magma. The titanite overgrowths may reflect changes in the intensive parameters acting on the system (e.g., Piccoli et al., 2000; Hayden et al., 2008; McLeod et al., 2011; Bruand et al., 2014; Gros et al., 2020). Progressive magma crystallization causes the MREE-rich titanite to be in disequilibrium in the magma, leading to its destabilization, precipitation of ilmenite and allanite, and regrowth of titanite rims with lower MREE on the phenocryst rims (Figure 3-4 F and Figure 3-8).

The thin recrystallized rims observed on the borders of homogeneous crystals demonstrate that they experienced small degrees of destabilization-reprecipitation, while the titanite crystals with more inclusions contain wider MREE-depleted areas, indicating that they are more susceptible to destabilization-reprecipitation than the homogeneous crystals. Additionally, the texture demonstrating euhedral titanite crystallizing simultaneously with the amphibole, together with the Zr-in-titanite thermometry, points to titanite saturation at high temperatures. This suggests the temperature range from 754 °C down to 644 °C obtained for the large crystals represents crystallization temperatures (Figure 3-8 F). The lower temperatures (< 707 °C) reported for the smaller crystals reinforce that they are late crystallized directly from the magma.

3.6.4. Source inferences

The analysis of a zircon grain population of n = 24 shows the precision and repeatability of the U-Pb ages reported in this study (Figure 3-9). The 3118 ± 9/32 Ma (2s) crystallization age obtained for the quartz monzonite of the KZD is slightly older than the 3107 ± 2 Ma (n = 3) age of the BT and the ca. 3105 Ma batholiths of the GMS suite (e.g., Kamo and Davis, 1994; Moyen et al., 2021). This suggests that the BAC quartz monzonite was crystallized at the beginning of the magmatic event that assembled the GMS rocks.

The crystallization of a substantial fraction of the magmatic zircon analyzed in this research at very high temperatures (often above 850 °C) argues for a Zr-rich parental magma able to reach zircon saturation at high temperatures and avoid the complete dissolution of crystals inherited from the source or country rocks. This is evidenced by the preservation of ca. 3.2 Ga inherited cores. The zircon from the syenites and quartz monzonites contain more Ti and

less Hf than zircon in the TTG suite, which suggests the magmas crystallizing the zircon from the syenites and quartz monzonites are hotter than the TTG magmas (e.g., Clemens et al., 2006; Claiborne et al., 2006).

The geochemical signature of the primary apatite and titanite indicates that the initial melts that crystallized the syenites and quartz monzonites carried high LREE, MREE, Ti, and Zr but relatively low HREE contents. The signature of these accessory minerals resembles the compositions of the crystals hosted in high Ba-Sr rocks (Bruand et al., 2020) rather than the signature characteristic of the Archean TTG suite, supporting their origin from felsic magmas.

The BAC syenites and quartz monzonites have chemical characteristics consistent with derivation from granitic magmas, such as low transition element concentrations, low MgO, CaO, and Mg#s, and $\varepsilon Nd_{(t)}$ -4.6 to 4.8 that cluster around -3 (e.g., Murphy, 2015; Moyen et al., 2021; Leandro et al., 2024). These chemical features suggest magma sources derived from crustal materials (predominantly TTG-like) with minor mantle contributions (Yearron, 2003; Moyen et al., 2021; Robb et al., 2021; Leandro et al., 2024). The shear zone settings active during the BAC emplacement caused localized extensional dynamics and crustal thinning (de Ronde and de Wit, 1994), which might have allowed mantle heat input into the lower crust and triggered partial melting (e.g., Fitton and Upton, 1987; Kogarko et al., 2006; Robb et al., 2021). The partial melting prompted by the breakdown of high-Ti biotite under mid- to lower-crust conditions and high temperatures can produce large volumes of granitic melts that contain high contents of incompatible elements, including U, Th, K, LREE, and low contents of HREE, leaving behind a more refractory residuum (e.g., Clemens et al., 2012; Clemens et al., 2020).

The volume of melt produced is constrained by the contents of hydrous phases in the source (Stevens and Clemens, 1993; Clemens et al., 2020). A relatively low biotite content in the source would cause low degrees of partial melting (e.g., Stevens and Clemens, 1993; Clemens and Watkins, 2001; Bea et al., 2007). This is a classic process invoked to explain syenite production (e.g., Fitton and Upton, 1987; Tchameni et al., 2001; Kogarko et al., 2006; Lauri et al., 2006; Mageswarii et al., 2024). Thus, low degrees of fluid-absent partial melting of the lower crust could produce high-temperature LREE-rich granitic melts (e.g., Stevens and Clemens, 1993; Clemens et al., 2001). These melts ascend as buoyant, hot batches through local shear zones emplaced in the upper crust (e.g., Belcher and Kisters, 2006). The formation of a relatively small magma chamber within an active shear zone setting would promote mechanical K-feldspar accumulation and rhyolitic melt loss from this magma chamber (Figure 3-10), resulting in cumulus syenites and quartz monzonites of the BAC with relatively low CaO

contents and explaining their scarcity within the voluminous GMS suite (e.g., Leandro et al., 2024). This can be attributed to the low contents of high-Ti biotite and the presence of refractory minerals, which inhibited partial melting, resulting in low volumes of melts. Conversely, building up the GMS batholiths with a high proportion of leucogranites requires substantial melt production. This indicates that the K-high magmatism recorded in the GMS suite likely began by melting a deep and dry refractory lower crust. As the heat propagates upward, more fertile, shallower crustal layers melt, producing the extensive granitic magmatism observed in the GMS suite. The large magma chambers hindered the action of mechanical mineral accumulation. This hypothesis agrees with the older and hotter zircon hosted in the quartz monzonites compared to the neighbor granites.

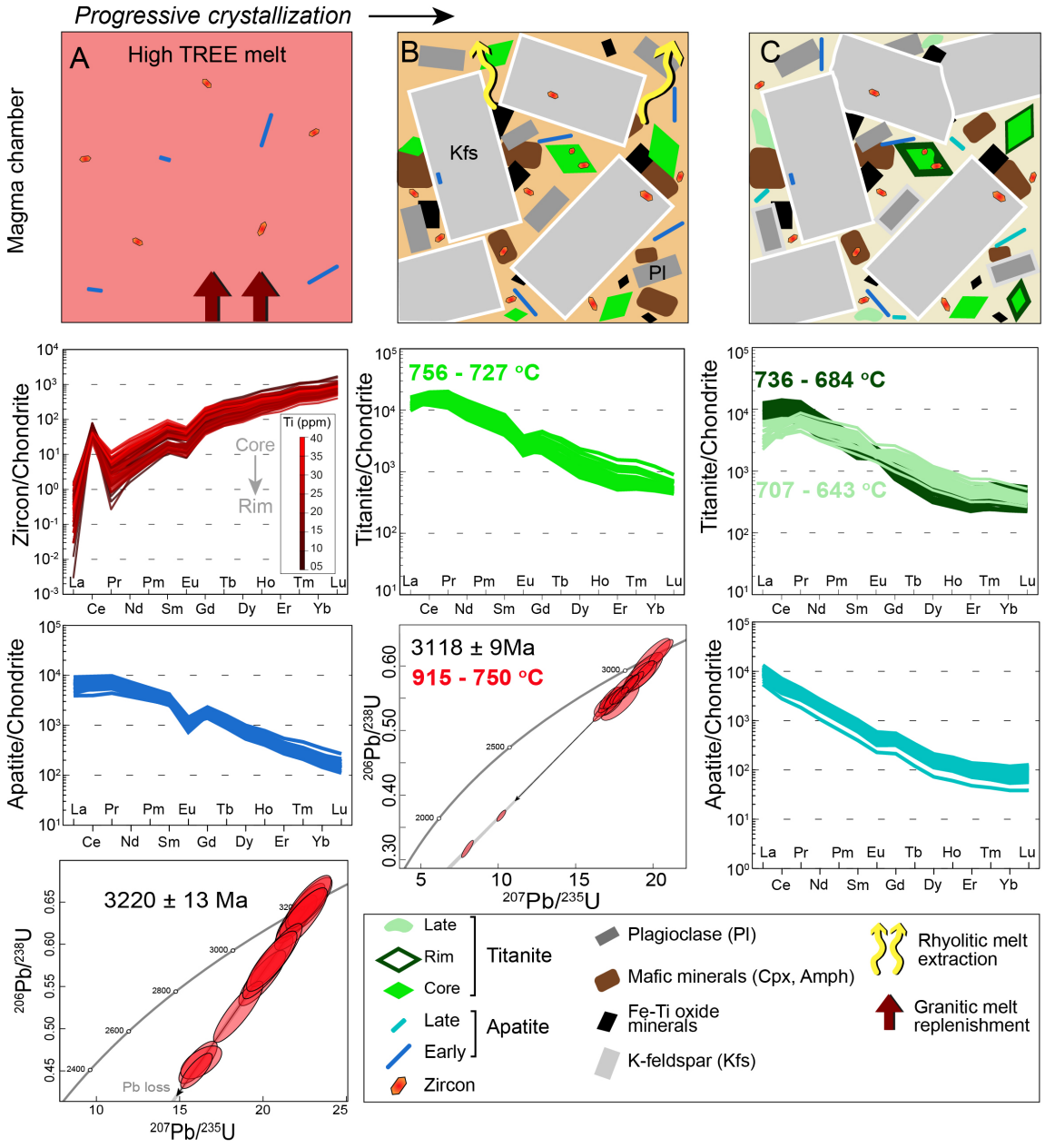

Figure 3-10. Graphical abstract illustrating the crystallization order of the accessory minerals investigated and their REE signatures.

3.7. Conclusion

Titanite and apatite are early-crystallized phases that primarily control the LREE and MREE concentration. At the same time, zircon is the phase hosting most of the HREE in the syenites and quartz monzonites of the BAC. The high TREE contents in the F-apatite and titanite crystal cores are interpreted as pristine signatures of these early-formed minerals, indicating that they crystallized from hot REE-rich felsic magmas. The systematic decrease of REE towards the crystal rims likely reflects progressive magma crystallization, reducing their availability for the later crystallized zones.

The overgrowth rims of titanite, associated with allanite and ilmenite precipitation, suggest that the chemical differences between cores and rims may result from the dissolution of the primary titanite and reprecipitation as REE-depleted rims. Meanwhile, the small titanite crystals are formed later, directly from REE-impoverished magmas.

The zircon and titanite hosted in the syenites register higher temperatures than the crystals hosted in the quartz monzonite, indicating the syenites were likely produced before the quartz monzonites. The presence of the inherited zircon cores highlights the contribution of ca. 3.2 Ga ancient crustal materials at the magma source of the syenites and quartz monzonites. The zircon U-Pb crystallization ages obtained for the Kees Zyn Doorns quartz monzonite of 3118 ± 9 Ma. Thus, the syenites and quartz monzonites likely were formed by fluid-absent, low-degree partial melting of the lower crust, which produced the hot, granitic, and TREE-rich melts required to produce the BAC cumulus rocks. The progressive increase of partial melting of a shallower source could have produced the voluminous leucogranites of the GMS batholiths, which contain lower-temperature zircons and are slightly younger than the cumulus rocks of the BAC.

3.8. Acknowledgment

We thank Riana Rossouw for LA-ICP-MS analyses and Madelaine Frazenburg for assistance with SEM analyses. This research was supported by an RSA NRF grant to Gary Stevens via the SARChI program and IRP BuCoMO, a collaborative research project funded by the CNRS and the NRF. This is BuCoMO contribution A15.

3.9. Data Availability

The data underlying this article are available in EarthChem Library, at https://doi.org/10.60520/IEDA/113562

3.10. References – Chapter 3

1. Anhaeusser, C.R., and Robb, L.J., 1983. Geological and geochemical characteristics of the Heerenveen and Mpuluzi batholiths south of the Barberton greenstone belt and preliminary thoughts on their petrogenesis. In: Anhaeusser, C.R. (Ed.), Contributions to the Geology of the Barberton Mountain Land. *Geological Society of South Africa Special Publication*, *9*, 131-152.

2. Anhaeusser, C.R., Robb, L.J., and Barton, J.M., 1983. Mineralogy, petrology and origin of the Boesmanskop Syenite-Granite complex, Barberton Mountain Land, South Africa. *Geological Society of South Africa, Special Publication*, *9*, 169-183.

3. Balashov, Y.A., and Glaznev, V.N., 2006. Cycles of alkaline magmatism. *Geochemistry International*, *44*, 274-285. https://doi.org/10.1134/S0016702906030050

4. Bea, F., Montero, P., González-Lodeiro, F., and Talavera, C., 2007. Zircon inheritance reveals exceptionally fast crustal magma generation processes in Central Iberia during the Cambro-Ordovician. *Journal of petrology, 48(12)*, 2327-2339. https://doi.org/10.1093/petrology/egm061

5. Belcher, R.W., and Kisters, A.F., 2006. Progressive adjustments of ascent and emplacement controls during incremental construction of the 3.1 Ga Heerenveen batholith, South Africa. *Journal of Structural Geology, 28(8)*, 1406-1421. https://doi.org/10.1016/j.jsg.2006.05.001

6. Belousova, E.A., Griffin, W.L., O'Reilly, S.Y., and Fisher, N.I., 2002. Apatite as an indicator mineral for mineral exploration: trace-element compositions and their relationship to host rock type. *Journal of Geochemical Exploration, 76(1)*, 45-69. https://doi.org/10.1016/S0375-6742(02)00204-2

7. Blichert-Toft, J., Rosing, M.T., Lesher, C.E., and Chauvel, C., 1995. Geochemical constraints on the origin of the late Archean Skjoldungen alkaline igneous province, SE Greenland. *Journal of Petrology, 36(2)*, 515-561. https://doi.org/10.1093/petrology/36.2.515

8. Boehnke, P., Watson, E.B., Trail, D., Harrison, T. M., and Schmitt, A.K., 2013. Zircon saturation re-revisited. *Chemical Geology, 351*, 324-334. https://doi.org/10.1016/j.chemgeo.2013.05.028

9. Bruand, E., Fowler, M., Storey, C., Laurent, O., Antoine, C., Guitreau, M., Heilimo, E., and Nebel, O., 2020. Accessory mineral constraints on crustal evolution: elemental fingerprints for magma discrimination. *Geochemical Perspectives Letters, 13*, 7-12. https://doi.org/10.7185/geochemlet.2006

10. Bruand, E., Storey, C., and Fowler, M., 2014. Accessory mineral chemistry of high Ba–Sr granites from northern Scotland: constraints on petrogenesis and records of whole-rock signature. *Journal of Petrology*, *55(8)*, 1619-1651. https://doi.org/10.1093/petrology/egu037

11. Bruand, E., Storey, C., and Fowler, M., 2016. An apatite for progress: Inclusions in zircon and titanite constrain petrogenesis and provenance. *Geology, 44(2)*, 91-94. https://doi.org/10.1130/G37301.1

12. Chew, D.M., Babechuk, M.G., Cogne, N., Mark, C., O'Sullivan, G.J., Henrichs, I.A., Doepke, D., and McKenna, C.A., 2016. (LA, Q)-ICPMS trace-element analyses of Durango and McClure Mountain apatite and implications for making natural LA-ICPMS mineral standards. *Chemical Geology, 435*, 35-48. https://doi.org/10.1016/j.chemgeo.2016.03.028

13. Claiborne, L.L., Miller, C.F., Walker, B.A., Wooden, J.L., Mazdab, F.K., and Bea, F., 2006. Tracking magmatic processes through Zr/Hf ratios in rocks and Hf and Ti zoning in zircons: an example from the Spirit Mountain batholith, Nevada. *Mineralogical Magazine*, *70*(5), 517-543. https://doi.org/10.1180/0026461067050348

14. Clemens, J., and Watkins, J.M., 2001. The fluid regime of high-temperature metamorphism during granitoid magma genesis. *Contributions to Mineralogy and Petrology*, *140*(5), 600-606. https://doi.org/10.1007/s004100000205

15. Clemens, J.D., 2012. Granitic magmatism, from source to emplacement: a personal view. *Applied Earth Science, 121(3),* 107-136. https://doi.org/10.1179/1743275813Y.0000000023

16. Clemens, J.D., Belcher, R.W., and Kisters, A.F., 2010. The Heerenveen batholith, Barberton Mountain Land, South Africa: Mesoarchaean, potassic, felsic magmas formed by melting of an ancient subduction complex. *Journal of Petrology, 51(5)*, 1099-1120. https://doi.org/10.1093/petrology/egq014

17. Clemens, J.D., Stevens, G., and Bryan, S.E., 2020. Conditions during the formation of granitic magmas by crustal melting–hot or cold; drenched, damp or dry?. *Earth-Science Reviews, 200, 102982*. https://doi.org/10.1016/j.earscirev.2019.102982

18. Clemens, J.D., Yearron, L.M., and Stevens, G., 2006. Barberton (South Africa) TTG magmas: geochemical and experimental constraints on source-rock petrology, pressure of formation and tectonic setting. *Precambrian Research*, *151*(*1-2*), 53-78. https://doi.org/10.1016/j.precamres.2006.08.001

19. De Ronde, C.E., and de Wit, M.J., 1994. Tectonic history of the Barberton greenstone belt, South Africa: 490 million years of Archean crustal evolution. *Tectonics, 13(4)*, 983-1005. https://doi.org/10.1029/94TC00353

20. Duan, X.X., Chen, B., Sun, KK., Wang, Z. Q., Yan, X., and Zhang, Z., 2019. Accessory mineral chemistry as a monitor of petrogenetic and metallogenetic processes: a comparative study of zircon and apatite from Wushan Cu-and Zhuxiling W (Mo)-mineralization-related granitoids. *Ore Geology Reviews*, *111*, 102940. https://doi.org/10.1016/j.oregeorev.2019.102940

21. Ferry, J.M., and Watson, E.B., 2007. New thermodynamic models and revised calibrations for the Ti-in-zircon and Zr-in-rutile thermometers. *Contributions to Mineralogy and Petrology, 154(4)*, 429-437. https://doi.org/10.1007/s00410-007-0201-0

22. Fitton, J.G., and Upton, B.G., 1987. Alkaline igneous rocks. *Geological Society, London, special publications, 30,* 568.

23. Grimes, C.B., Wooden, J.L., Cheadle, M.J., and John, B.E., 2015. "Fingerprinting" tectono-magmatic provenance using trace elements in igneous zircon. *Contributions to Mineralogy and Petrology*, *170*, 1-26. https://doi.org/10.1007/s00410-015-1199-3

24. Gros, K., Słaby, E., Birski, Ł., Kozub-Budzyń, G., and Sláma, J., 2020. Geochemical evolution of a composite pluton: insight from major and trace element chemistry of titanite. *Mineralogy and Petrology*, *114*, 375-401. https://doi.org/10.1007/s00710-020-00715-x

25. Hayden, L.A., Watson, E.B., and Wark, D.A., 2008. A thermobarometer for sphene (titanite). *Contributions to Mineralogy and Petrology, 155,* 529-540. https://doi.org/10.1007/s00410-007-0256-y

26. Horstwood, M.S., Košler, J, Gehrels, G., Jackson, S.E., McLean, N.M., Paton, C., Pearson, N.J., Sircombe, K., Sylvester, P., Vermeesch, P., Bowring, J.F. and Schoene, B., 2016. Community-derived standards for LA-ICP-MS U-(Th-) Pb geochronology–Uncertainty propagation, age interpretation and data reporting. *Geostandards and Geoanalytical Research, 40(3)*, 311-332. https://doi.org/10.1111/j.1751-908X.2016.00379.x

27. Hoskin, P.W., 2005. Trace-element composition of hydrothermal zircon and the alteration of Hadean zircon from the Jack Hills, Australia. *Geochimica et cosmochimica acta, 69(3)*, 637-48. https://doi.org/10.1016/j.gca.2004.07.006

28. Hoskin, P.W., and Ireland, T.R., 2000. Rare earth element chemistry of zircon and its use as a provenance indicator. *Geology, 28(7),* 627-630. https://doi.org/10.1130/0091-7613(2000)28<627:REECOZ>2.0.CO;2

29. Howarth, G.H., Moore, A.E., Harris, C., van der Meer, Q.H.A., and le Roux, P., 2019. Crustal versus mantle origin of carbonate xenoliths from Kimberley region kimberlites using C-O-Sr-Nd-Pb isotopes and trace element abundances. *Geochimica et Cosmochimica Acta 266(1),* 258-273. https://doi.org/10.1016/j.gca.2019.03.026

30. Jackson, S.E., Pearson, N.J., Griffin, W.L., and Belousova, E.A., 2004. The application of laser ablation-inductively coupled plasma-mass spectrometry to in situ U-Pb zircon geochronology. *Chemical Geology, 211*, 47-69. https://10.1016/j.chemgeo.2004.06.017

31. Jochum, K.P., Nohl, U., Herwig, K., Lammel, E., Stoll, B., and Hofmann, A.W., 2005. GeoReM: a new geochemical database for reference materials and isotopic standards. *Geostandards and Geoanalytical Research, 29(3),* 333-338. https://doi.org/10.1111/j.1751-908X.2005.tb00904.x

32. Kamo, S.L., and Davis, D.W., 1994. Reassessment of Archaean crustal development in the Barberton mountain land, South Africa, based on U-Pb dating. *Tectonics, 13(1)*, 167-192. https://doi.org/10.1029/93TC02254

33. Kogarko, L.N., 2006. Alkaline magmatism and enriched mantle reservoirs: Mechanisms, time, and depth of formation. *Geochemistry International*, *44*, 3-10. https://doi.org/10.1134/S0016702906010022

34. Kowallis, B.J., Christiansen, E.H., Dorais, M.J., Winkel, A., Henze, P., Franzen, L., and Mosher, H., 2022. Variation of Fe, Al, and F substitution in titanite (sphene). *Geosciences*, *12(6)*, 229. https://doi.org/10.3390/geosciences12060229

35. Kröner, A., Hegner, E., Wendt, J.I., and Byerly, G.R., 1996. The oldest part of the Barberton granitoid-greenstone terrain, South Africa: evidence for crust formation between 3.5 and 3.7 Ga. *Precambrian Research, 78(1-3)*, 105-124. https://doi.org/10.1016/0301-9268(95)00072-0

36. Laurent, O., Moyen, J. F., Wotzlaw, J. F., Björnsen, J., and Bachmann, O., 2022. Early Earth zircons formed in residual granitic melts produced by tonalite differentiation. *Geology*, *50*(4), 437-441. https://doi.org/10.1130/G49232.1

37. Lauri, L.S., Rämö, O.T., Huhma, H., Mänttäri, I., and Räsänen, J., 2006. Petrogenesis of silicic magmatism related to the ~ 2.44 Ga rifting of Archean crust in Koillismaa, eastern Finland. *Lithos*, *86*(1-2), 137-166. https://doi.org/10.1016/j.lithos.2005.03.016

38. Leandro, M.V.S., Stevens, G., Moyen, J.F., Kisters A.F.M., and Ferreira, A., 2024. Generating Archean syenites by intracrustal processes: A review of the Boesmanskop Alkaline Complex, Eastern Kaapvaal Craton. *Lithos, in press. http://dx.doi.org/10.2139/ssrn.4972697*

39. Lee, R.G., Dilles, J.H., Tosdal, R.M., Wooden, J.L., and Mazdab, F.K., 2017. Magmatic evolution of granodiorite intrusions at the El Salvador porphyry copper deposit, Chile, based on trace element composition and U/Pb age of zircons. *Economic Geology*, *112(2)*, 245-273. https://doi.org/10.2113/econgeo.112.2.245

40. Lowe, D.R., 1994. Accretionary history of the Archean Barberton greenstone belt (3.55-3.22 Ga), southern Africa. *Geology, 22(12),* 1099-1102. https://doi.org/10.1130/0091-7613(1994)022<1099:AHOTAB>2.3.CO;2

41. Mageswarii, G., Mishra, M., Srivastava, V., Srivastava, H.B., Satyanarayanan, M., and Shrivastava, J.P., 2024. Palaeoproterozoic rift-related alkaline magmatism in Bari area, Son valley, Central India. *Geosystems and Geoenvironment, 3(1),* 100222. https://doi.org/10.1016/j.geogeo.2023.100222

42. McLeod, G.W., Dempster, T.J., and Faithfull, J.W., 2011. Deciphering magma-mixing processes using zoned titanite from the Ross of Mull Granite, Scotland. *Journal of Petrology*, *52(1)*, 55-82. https://doi.org/10.1093/petrology/egq071

43. Moyen, J.F., Zeh, A., Cuney, M., Dziggel, A., and Carrouée, S., 2021. The multiple ways of recycling Archaean crust: A case study from the ca. 3.1 Ga granitoids from the Barberton Greenstone Belt, South Africa. *Precambrian Research, 353,* 105998. https://doi.org/10.1016/j.precamres.2020.105998

44. Mühlberg, M., 2022. *Magmatic and metamorphic evolution of the Stolzburg Block, Barberton Granitoid-Greenstone Terrain*. Doctoral dissertation, Stellenbosch University.

45. Murphy, R.C., 2015. *Stabilising a craton: the origin and emplacement of the 3.1 Ga Mpuluzi Batholith*. Doctoral dissertation, Macquarie University.

46. Nakamura, N., 1974. Determination of REE, Ba, Fe, Mg, Na and K in carbonaceous and ordinary chondrites. *Geochimica et cosmochimica acta, 38(5)*, 757-775. https://doi.org/10.1016/0016-7037(74)90149-5

47. Paterson, S.R., Vernon, R.H., and Zak, J., 2005. Mechanical instabilities and physical accumulation of K-feldspar megacrysts in granitic magma, Tuolumne batholith, California, USA. J*ournal of the Virtual Explorer, 18,* 1–18. https://doi.org/10.3809/jvirtex.2005.00114

48. Piccoli, P., Candela, P., and Rivers, M., 2000. Interpreting magmatic processes from accessory phases: titanite—a small-scale recorder of large-scale processes. *Earth and Environmental Science Transactions of the Royal Society of Edinburgh*, *91(1-2)*, 257-267. https://doi.org/10.1017/S0263593300007422

49. Robb, L.J., Brandl, G., Anhaeusser, C.R., Poujol, M., Johnson, M.R., and Thomas, R.J., 2006. Archaean granitoid intrusions. In: Johnson, M.R., Anhaeusser, C.R., Thomas, R.J. (Eds.), *The Geology of South Africa*, 57-94.

50. Robb, L.J., Meyer, F.M., Hawkesworth, C.J., and Gardiner, N.J., 2021. Petrogenesis of Archaean granites in the Barberton region of South Africa as a guide to early crustal evolution. *South African Journal of Geology 2021*, *124*(1), 111-140. https://doi.org/10.25131/sajg.124.0021

51. Schoene, B., and Bowring, S.A., 2010. Rates and mechanisms of Mesoarchean magmatic arc construction, eastern Kaapvaal craton, Swaziland. *Bulletin, 122(3-4)*, 408-429. https://doi.org/10.1130/B26501.1

52. Schoene, B., de Wit, M. J., and Bowring, S.A., 2008. Mesoarchean assembly and stabilization of the eastern Kaapvaal craton: A structural-thermochronological perspective. *Tectonics, 27(5)*. https://doi.org/10.1029/2008TC002267

53. Schoene, B., Dudas, F.O., Bowring, S.A., and De Wit, M., 2009. Sm–Nd isotopic mapping of lithospheric growth and stabilization in the eastern Kaapvaal craton. *Terra Nova, 21(3)*, 219-228. https://doi.org/10.1111/j.1365-3121.2009.00877.x

54. Silva, J.P., Lana, C., Mazoz, A., Buick, I., and Scholz, R., 2023. U-Pb Saturn: New U-Pb/Pb-Pb Data Reduction Software for LA-ICP-MS. *Geostandards and Geoanalytical Research*, *47*(1), 49-66. https://doi.org/10.1111/ggr.12474

55. Sláma, J., Košler, J., Condon, D.J., Crowley, J.L., Gerdes, A., Hanchar, J.M., Horstwood, M.S.A., Morris, G.A., Nasdala, L., Norberg, N., Schaltegger, U., Schoene, B., Tubrett, M.N., and Whitehouse, M.J., 2008. Plešovice zircon - a new natural reference material for U-Pb and Hf isotopic microanalysis. *Chemical Geology, 249,* 1-35. https://10.1016/j.chemgeo.2007.11.005

56. Stevens, G., and Clemens, J.D., 1993. Fluid-absent melting and the roles of fluids in the lithosphere: a slanted summary? *Chemical Geology, 108(1-4)*, 1-7. https://doi.org/10.1016/0009-2541(93)90314-9

57. Tchameni, R., Mezger, K., Nsifa, N.E., and Pouclet, A., 2001. Crustal origin of Early Proterozoic syenites in the Congo craton (Ntem complex), South Cameroon. *Lithos, 57(1)*, 23-42. https://doi.org/10.1016/S0024-4937(00)00072-4

58. Thomson, S. N., Gehrels, G.E., Ruiz, J., and Buchwaldt, R., 2012. Routine low-damage apatite U-Pb dating using laser ablation–multicollector–ICPMS. *Geochemistry, Geophysics, Geosystems*, *13*(2). https://doi.org/10.1029/2011GC003928

59. Vermeesch, P., 2018. IsoplotR: A free and open toolbox for geochronology. *Geoscience Frontiers, 9(5)*, 1479-1493. https://doi.org/10.1016/j.gsf.2018.04.001

60. Watson, E.B. and Green, T.H., 1981. Apatite/liquid partition coefficients for the rare earth elements and strontium. *Earth and Planetary Science Letters, 56*, 405–421. https://doi.org/10.1016/0012-821X(81)90144-8

61. Westraat, J.D., Kisters, A.F.M., Poujol, M., and Stevens, G., 2005. Transcurrent shearing, granite sheeting and incremental construction of the tabular 3.1 Ga Mpuluzi batholith, Barberton granite-greenstone terrane, South Africa. *Journal of the Geological Society, 162(2)*, 373-388. https://doi.org/10.1144/0016-764904-026

62. Wiedenbeck, M., Allé, P., Corfu, F., Griffin, W.L., Meier, M., Oberli, F., Von Quadt, A., Roddick, J.C., and Spiegel, W., 1995. Three natural zircon standards for U-Th-Pb, Lu-Hf, trace element and REE analysis. *Geostandards and Geoanalytical Research, 19,* 1-23. https://10.1111/j.1751-908X.1995.tb00147.x

63. Yearron, L.M., 2003. *Archaean granite petrogenesis and implications for the evolution of the Barberton Mountain Land, South Africa*. Doctoral dissertation, Kingston University.

64. Young, E.J., Myers, A.T., Munson, E.L., and Conklin, N.M., 1969, Mineralogy and geochemistry of fluorapatite from Cerro de Mercado, Durango, Mexico: U.S. Geological Survey *Professional* Paper, 650D, 84–93.

65. Zhao, H., Zhao, X., Le Roux, P.J., Zhang, W., Wang, H., Xie, LW., Huang, C., Wu, ST., Yang, JH., Wu, FY., Yang, YH., 2020. Natural Clinopyroxene Reference Materials for *in situ* Sr Isotopic Analysis via LA-MC-ICP-MS. *Frontiers in Chemistry*, *8*, 594316. https://doi.org/10.3389/fchem.2020.594316

CHAPTER 4. PRESENTATION OF RESEARCH PAPER 3 – U-PB ZIRCON GEOCHRONOLOGY AND CHEMICAL CHARACTERIZATION OF THE MESOARCHEAN SALISBURY KOP BATHOLITH, KAAPVAAL CRATON

This paper, first authored by Marcel Vinicius Santos Leandro, is in preparation for submission to *South African Journal of Geology.* The following aspects of the research were done independently by Marcel Vinicius Santos Leandro while receiving standard supervision by his supervisors Gary Stevens, Jean-François Moyen, and Alex F.M. Kisters: (i) sample preparation; (ii) petrographic description; (iii) SEM imaging; (iv) mineral picking; (v) generation of figures; (vi) writing of the manuscript. Riana Rossouw acquired U-Pb zircon by LA-ICP-MS.

Contribution Roles Taxonomy (CRediT) classification - **Marcel Vinicius Santos Leandro**: Data curation; Formal Analysis; Investigation; Methodology; Visualization; Writing – Original Draft Preparation. **Gary Stevens**: Conceptualization; Data Curation; Funding Acquisition; Project Administration; Resources; Supervision; Validation; Writing – Review & Editing. **Jean-François Moyen:** Data Curation; Funding Acquisition; Resources; Supervision; Validation; Writing – Review & Editing.

U-Pb zircon geochronology and chemical characterization of the Mesoarchean Salisbury Kop batholith, Kaapvaal Craton

Marcel V.S. Leandro [a]*, Gary Stevens [a], Jean-François Moyen [b]

[a] Department of Earth Sciences, Stellenbosch University, Private Bag X1, Matieland, 7602, Stellenbosch, South Africa

[b] Université Jean-Monnet, Laboratoire Magmas et Volcans, UCA-CNRS-IRD, Aubière F-63170, France

*Corresponding author: marcel.leandro@hotmail.com; https://orcid.org/0000-0002-5177-890X

Abstract

The Archean Salisbury Kop batholith (SB) intrudes the metavolcanic and metasedimentary rocks of the Barberton Greenstone Belt (BGB) and surrounding gneisses within the Eastern Kaapvaal Craton. The SB is predominantly composed of medium to coarse-grained leucogranites and minor granodiorites indicative of its felsic parental magma and crystallization under low-temperature and low-pressure conditions. Geochemical analyses reveal that the SB granodiorites align with the geochemical range of the GMS suite and are akin to the sodium-rich granodiorites of the Mpuluzi Batholith but are distinct from the granodiorites of the Nelspruit Batholith. The leucogranites are potassic and peraluminous and share similar trace elements and REE signatures with the granodiorites. The described zircon preserves the texture of igneous crystals with concentric zonation. New U-Pb zircon dating of a granodiorite sample yielded a crystallization age of 3094 ± 10 Ma (2s; MSWD = 0.79; n = 48) and 3100 ± 11 Ma (2s; MSWD = 1.03; n = 32) for the titanite, which constrains the crystallization age of the SB and provide a minimum age for the deposition and deformation of the metasedimentary sequences of the Moodies Group. The concordance of zircon and titanite ages, coupled with their preservation, indicates that the SB remained unaffected by subsequent magmatic events post-emplacement. The geochemical features of the granodiorites and granites suggest an origin derived from a felsic magma likely derived from the lower crust, while the mafic magma contributions are minimal.

Keywords: *In situ* U-Pb dating; Archean; Granodiorite;

4.1. Introduction

The investigation of the origin, nature, and stabilization of the first crustal segments during Earth's early stages demands meticulous studies, given the scarcity of Archean remnants which often are overprinted by later events (e.g., Moyen et al., 2006; Anhaeusser, 2014; Kröner et al., 2016). Additionally, the geodynamic conditions prevailing during the Archean may have differed significantly from modern plate-tectonic environments (e.g., Van Kranendonk et al., 2014; Robb et al., 2021), hindering its correlation with modern geological registers.

The Barberton Granite-Greenstone Terrane (BGGT), located in the Eastern Kaapvaal Craton within South Africa, is a famous example of Paleoarchean remnants due to its well-preserved and well-exposed outcrops (e.g., Anhaeusser and Robb 1983; de Ronde and de Wit, 1994; Anhaeusser, 2014). The BGGB consists of two main components, the Barberton Greenstone Belt (BGB) and numerous granitoid plutons (e.g., Anhaeusser and Robb 1983; de Ronde and de Wit, 1994; Robb et al., 2021). The polyphase-deformed BGB supracrustal belt is a keel of folded supracrustal rocks that are tectonically interleaved by complex granitoid-gneiss terrain encompassing sodic rocks of the tonalite-trondhjemite-granodiorite (TTG) suite, voluminous potassic rocks of the Granodiorite-Monzogranite-Syenogranite (GMS) suite, and a younger (< 2.95 Ga) and minor volume of post-Pongola granitoids (e.g., Anhaeusser and Robb 1983; Yearron, 2003; Robb et al., 2006; Clemens et al., 2010; Moyen et al., 2021; Robb et al., 2021).

The investigation of the GMS and TTG suites has provided important insights regarding the evolution of the early crust. The compositional shift from sodic to potassic magmatism recorded in the BGGB occurred between. 3.2 and 3.1 Ga which is broadly associated with the final stages of the Kaapvaal Craton stabilization (e.g., Anhaeusser and Robb, 1983; Kamo and Davis, 1994; Clemens et al., 2010; Gumsley et al., 2015; Wilson and Zeh, 2018). This crustal stabilization occurred earlier than in most cratons, a characteristic that makes these rocks essential to unravel the geological process acting on the early Earth. Some of the TTG and GMS suite plutons have been comprehensively studied with publications covering aspects ranging from field features and petrography to isotopic features (e.g., Anhaeusser and Robb, 1993; Westraat et al., 2005; Clemens et al., 2010; Moyen et al., 2021), while other plutons, such as the Salisbury Kop batholith (SB) received less attention.

The SB is intrusive into metavolcanic and metasedimentary rocks at the northern portion of the BGB (e.g., Heubeck et al., 1993). Thus, the geochronological investigation of the SB may help to constrain the depositional and deformational events related to the development of the BGB sequences and continental lithosphere. This research characterizes the petrography and whole-rock chemistry of representative rocks of the SB and reassesses their ages by U-Pb zircon and titanite, aiming to contribute to the understanding of the local tectono-thermal evolution.

4.2. Analytical Methods

4.2.1. Sample preparation

The preparation of the rock powder for whole-rock analysis, petrographic description, *in situ* TREE analysis, U-Pb, and bulk rock composition measurements were carried out at the Central Analytical Facilities (CAF) at Stellenbosch University in South Africa. Lab Crystals in Lucknow, Uttar Pradesh, India, prepared the thin sections.

4.2.2. Petrographic analysis and imagining

Petrographic investigation of the relevant accessory minerals was conducted using optical and scanning electron microscopy at the CAF. The backscattered electron (BSE) and cathodoluminescence detectors coupled in a Zeiss Merlin Field Emission Scanning Electron Microscope (SEM) were used for analysis. The mineral mounts and thin sections were coated with carbon. Electron images were captured with an accelerating voltage of 20 kV, a probe current of 11 nA, and a working distance of 9.5 mm. These images allowed for identifying and selecting pristine crystal areas for chemical and isotopic analysis while avoiding areas with cracks, inclusions, and post-magmatic modifications. The major mineral composition of feldspar and titanite was obtained using Energy Dispersive Spectroscopy coupled with the SEM.

4.2.3. Whole-rock compositions

The whole-rock major oxide compositions were analyzed using X-ray Fluorescence Spectrometry (XRF), following the method described by Eggins (2003). Standards used included basalt BE-N, JB-1, BHVO-1, granodiorite JG-1, granite WITS-G, and quality control material HUSG1, which were analyzed after every 15 samples.

The trace elements were analyzed using a 193 nm Excimer laser ablation system from Applied Spectra, coupled with an Agilent 7700 ICP-MS. The reference materials BCR-2, BCR-2G, BHVO-1, and BHVO-2G were used, and they were run at the beginning and end of each batch of samples, with sample bracketing conducted after every five samples. Drift corrections were applied, and all measurements were duplicated. The whole-rock compositions are given in Table 4-2. The standard average measurements and relative standard deviations are included in the supplementary material.

4.2.4. U-Pb dating

4.2.4.1. Zircon

In situ U–Pb zircon ages were determined for a granodiorite sample (sample SB02) at CAF using a ThermoScientific Element 2 sector field Inductively Coupled Plasma Mass Spectrometry (ICP-MS), paired with a Resolution 193 nm Excimer laser ablation system from

Applied Spectra. The laser spot sizes were 11 µm due to the small sizes of the picked zircon. The instrument conditions were a frequency of 7 Hz and a sample ablation time of 30 seconds. The analysis sequence was done in standard-sample bracketing mode. The masses measured included ^{202}Hg, ^{204}Pb, ^{206}Pb, ^{207}Pb, ^{208}Pb, ^{238}Th, and ^{238}U. The U-Pb isotopic composition of zircon was obtained using the GJ-1 zircon (Jackson et al., 2004, Horstwood et al., 2016) as primary reference material and the 91500 (Wiedenbeck et al., 1995) and Plešovice zircon (Sláma et al., 2008) as secondary reference materials. The data reduction was conducted using the U-Pb Saturn software (Silva et al., 2023). The 91500 zircon yielded concordia ages of 1063 ± 7/13 Ma (2s; MSWD = 0.86; n = 9 and the Plešovice zircon a 335 ± 5/6 Ma (2s; MSWD = 0.57; n = 6) age, consistent with the published reference values (Wiedenbeck et al., 1995; Sláma et al. 2008). The final age uncertainties are reported as 2 sigma (2s) and quoted as α/β (without/with systematic uncertainties; Horstwood et al., 2016).

4.2.4.2. Titanite

In situ U–Pb titanite ages were determined for the granodiorite sample SB02, at the CAF using a ThermoScientific Element 2 sector field ICP-MS, paired with a Resolution 193 nm Excimer laser ablation system from Applied Spectra. The laser spot sizes were 20 µm. The instrument conditions were a frequency of 7 Hz and a sample ablation time of 30 seconds. The analysis sequence was done in sample bracketing mode. The primary reference material was the NIST612 glass standard (Jochum et al., 2011). The BLR-1 titanite (e.g., Aleinikoff et al., 2007) and Khan River (Mazoz et al., 2022) were used as quality control. The data reduction was conducted using the U-Pb Saturn software (Silva et al., 2023) and the concordia diagram was plotted with the IsoplotR (Vermeesch, 2018). The BRL-1 yielded ^{206}Pb/^{238}U mean age of 1056 ± 1.1 Ma (MSWD = 0.1, n = 14) and the Khan River yielded ^{206}Pb/^{238}U mean age of 502 ± 0.7 Ma (MSWD = 3.2, n = 8).

4.3. Local Geology

4.3.1. The Barberton Granite-Greenstone Terrane

The BGGT registers a protracted evolution with fold-and-thrust structures formed during two main deformational events at ca. 3450 - 3440 Ma (D1) and 3230 – 3225 Ma (D2) (e.g., de Wit et al., 1992; de Ronde and de Wit, 1994; Lowe, 1994; de Ronde and Kamo, 2000). The D2 event is associated with a crustal shortening responsible for the predominantly NE-SW

oriented structures of the belt (e.g., Kamo and Davis, 1994; De Ronde and De Wit, 1994; Lowe, 1994; Lana et al., 2011).

The BGB comprises the ca. 3550 - 3280 Ma ultramafic to mafic volcanic succession and felsic volcanoclastic sequences of the Onverwacht Group (e.g., Kröner et al., 1996; Kröner et al., 2016), 3259 - 3225 Ma clastic and volcanoclastic sequences of the Fig Tree Group and sandstones and polymict conglomerate of the < 3220 Ma Moodies Group (e.g., Kröner et al., 1996; Lowe and Byerly, 1999). The emplacement of the TTG suite plutons is coeval with the D2 event, and emplaced during two main magmatic events, ca. 3550 to 3450 Ma and ca. 3250 Ma (e.g., de Ronde and de Wit, 1994; Dziggel et al., 2002; Kisters et al., 2003; Moyen et al., 2019).

4.3.2. The GMS suite

The TTG suite was followed by the emplacement of the GMS suite, between 3140 Ma and 3074 Ma (e.g., Maphalala and Kröner 1993; Schoene and Bowring, 2007; Kamo and Davis, 1994; Moyen et al., 2021). The GMS suite is characterized by wide and multi-compositional batholiths, often with tabular shape and synmagmatic shear zones along their margins (e.g., Anhaeusser and Robb, 1983; Kamo and Davis, 1994; Belcher and Kisters, 2006; Robb et al., 2021) and minor syenogranitic plutons of the Boesmanskop Alkaline Complex (e.g., Anhaeusser et al., 1983; Moyen et al., 2021). Internally, these plutons are texturally and compositionally diverse, a feature often attributed to the build-up of the plutons by multiple magma batches (e.g., Dziggel et al., 2002; Westraat et al., 2005; Belcher and Kisters, 2006).

4.3.3. The Salisbury Kop batholith

Two plutons display intrusive relationship with the Moodies group, the Mpuluzi batholith at the south of the BGB and the SB at the north of the BGB (e.g., Heubeck et al., 1993; Lana et al., 2011). The Salisbury Kop batholith covers an area of 115 km^2 and consists of coarse-grained homogeneous granodiorites and granites (e.g., Heubeck et al., 1993; Robb et al., 2006). The SB intrudes and truncates folded rocks of the northern BGB (Figure 4-1 A), including coarse-grained, well-sorted sandstone and conglomerates of the Moodies group; and massive actinolite-chlorite schists of the Onverwacht Group (Heubeck et al., 1993; Lowe and Byerly, 1999).

The SB is bordered by the Nelspruit Batholith to the north and the Pigg's Peak Batholith to the east (e.g., Anhaeusser and Robb, 1983; Heubeck et al., 1993; Robb et al., 2006). The ca. 3106 ± 3 Ma Nelspruit batholith is texturally variable, and its predominant rocks are granodiorites and quartz monzonites (e.g., Kamo and Davis, 1994; Robb et al., 2006). The

Nelspruit batholith can be further subdivided into smaller plutons (e.g., Berlin and Hebron pluton) and is intruded by post-Pongola granitoids (Kamo and Davis, 1994; Robb et al., 2006; Robb et al., 2021). The Pigg's Peak batholith is represented by medium to coarse-grained granites with a crystallization age ranging from 3140 ± 0.3 Ma to 3074 ± 4 Ma (e.g., Maphalala and Kröner, 1993; Schoene and Bowring, 2007).

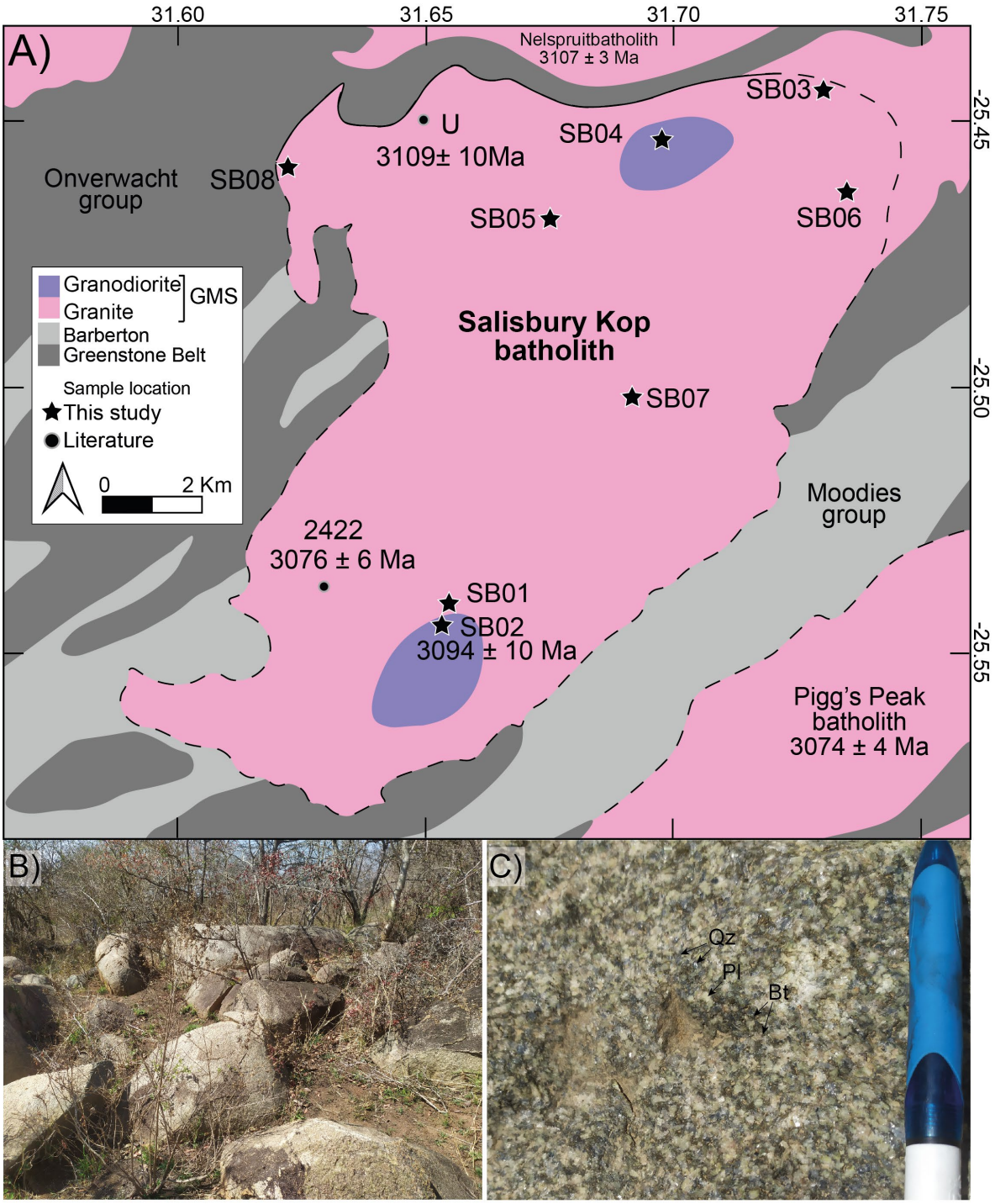

Figure 4-1. Geological map of the Salisbury Kop batholith displaying the sample locations and surrounding units. The dashed line represents the inferred limits of the pluton (after Kamo and Davis, 1994; Robb et al., 2006). B) Representation of rolled block outcrops of the SB. C) Representative texture of the coarse-grained granodiorite.

4.4. Results

The SB rocks form a terrain that is topographically lower than the BGB mountains. The SB outcrops are scarce and occur as rounded block clusters, stream beds and road cuts (Figure 4-1 B). Most outcrops are composed of homogeneous leucocratic granite with a fine- to medium-grained texture. Outcrops in the central portions of the batholith display homogeneous granodiorite with a medium- to coarse-grained, hypidiomorphic, and isotropic texture (Figure 4-1 C). The coordinates of the sampled rocks are reported in Table 4-1.

Table 4-1. Coordinates of the sampled rocks from the Salisbury Kop batholith and rock type.

Sample	Latitude (dec)	Longitude (dec)	Facies
SB01	-25.69072	31.17485	Granite
SB02	-25.54347	31.65262	Granodiorite
SB03	-25.44417	31.73028	Granite
SB04	-25.45398	31.69680	Granodiorite
SB05	-25.46880	31.67367	Granite
SB06A	-25.45915	31.65262	Granite
SB06B	-25.45915	31.65262	Granite
SB07	-25.50162	31.65262	Granite
SB08	-25.46047	31.65262	Granite

4.4.1. Petrography

The granodiorites and granites of the SB display a monotonous mineral assemblage composed of angular subhedral to euhedral white plagioclase phenocrysts, subhedral to anhedral K-feldspar phenocrysts (< 1.0 cm), and quartz in their interstices. The plagioclase (oligoclase and albite) contains very altered cores, and the K-feldspar occurs as interstitial microcline and scarce angular phenocrysts display perthite and microperthite exsolutions. Biotite is the ubiquitous mafic mineral and often displays zircon and apatite inclusions (Figure 4-2 A-B) and chloritization. The accessory mineral assemblage is euhedral diamond-shaped titanite, apatite, anhedral epidote, zircon, and Fe-Ti oxides (ilmenite and magnetite). Mica, chlorite, and sericite are the common secondary minerals.

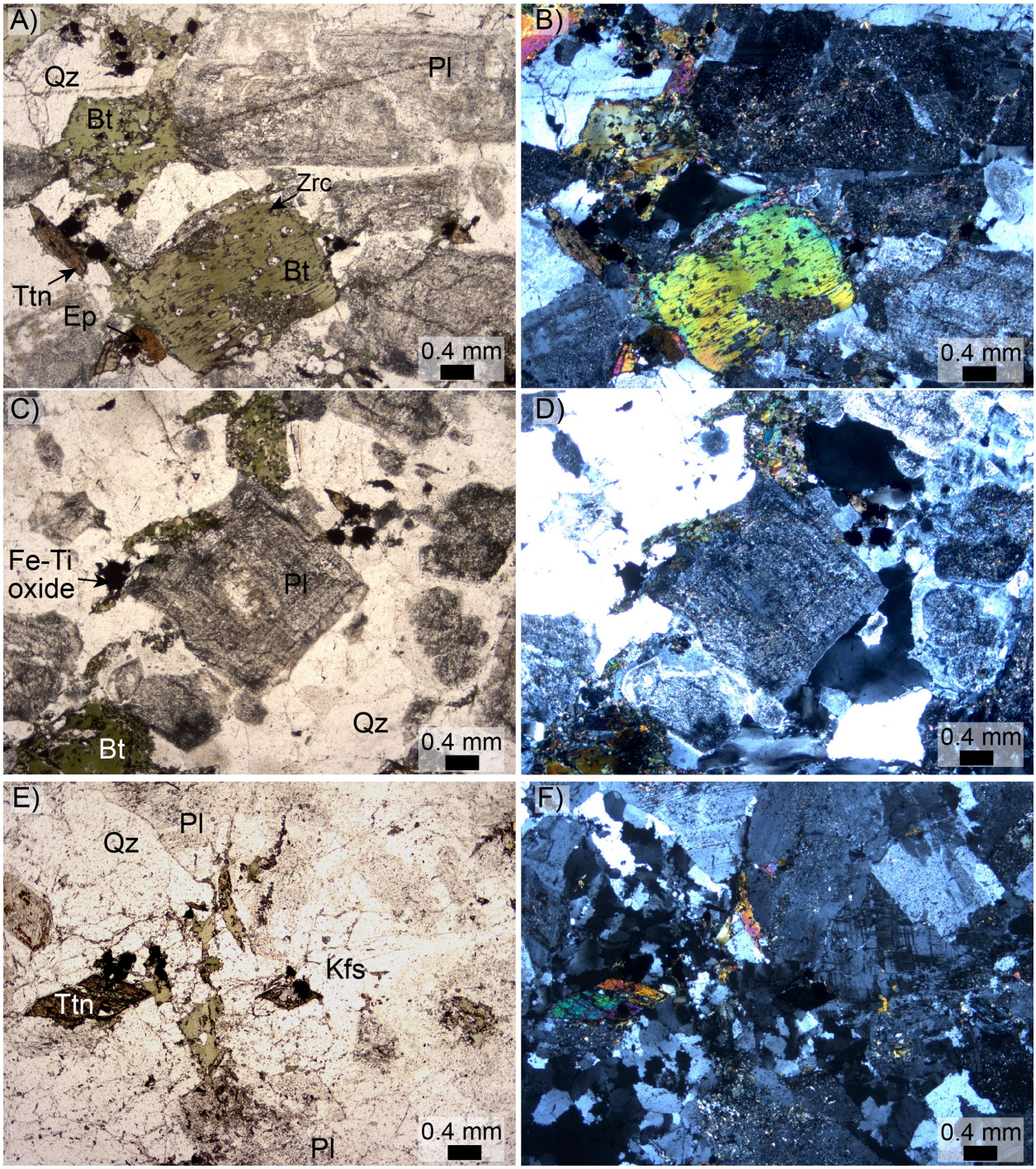

Figure 4-2. Photomicrographs illustrating representative textures of the SB granodiorites (A-D) and granites (E-F), displaying angulous plagioclase, K-feldspar (microcline), anhedral quartz (Qz) euhedral biotite (Bt), euhedral diamond-shaped titanite (Ttn). Images A, C, and E were captured under plane-polarized light, while B, D, and F were taken under cross-polarized light.

4.4.2. Whole-rock chemistry

The granodiorites exhibit SiO_2 contents of 66.7 and 68.7 wt% (Figure 4-3 A), Na_2O of 4.8 and 5.0 wt%, and K_2O of 2.6 and 1.9 wt%, classifying them within the sodic series (Figure 4-3 B). The SB granodiorites are metaluminous, with Alumina Saturation Index within the range reported for the GMS suite (Figure 4-3 C). They also display low concentrations of

ferromagnesian oxides, with MgO less than 1.4 wt% and FeO_T below 4.6 wt%, along with CaO concentrations ranging from 3.4 to 4.6 wt% (Figure 4-4).

The granodiorites of the SB are characterized by low Rb concentrations (<74 ppm), high Sr (<1504 ppm) and Y contents <26 ppm (Figure 4-4 I; Table 4-2). On the spider diagram the granodiorite exhibits negative Nb, Ta, and Ti anomalies, along with a positive Pb anomaly (Figure 4-5A) and LREE enrichment over HREE, without an Eu anomaly (Figure 4-5B).

The granite of the SB displays SiO_2 contents from 71.0 to 77.5 wt%, K_2O+Na_2O from 8.0 to 8.8 wt%. The granites plot in the potassic series and peraluminous field (Figure 4-3 B-C) and are classified as medium-K leucogranites, according to the division proposed by Moyen et al. (2021).

The granite shares similar chemical features with the granodiorites despite the higher SiO_2 contents (71.0 to 77.5 wt%) and K_2O+Na_2O (8.0 to 8.8 wt%). It also has lower concentrations of FeO_T (<1.9 wt%), MgO (<0.5 wt%), and CaO (<1.6 wt%). The granite display higher Rb contents, up to 297 ppm, while their Sr and Y contents are lower than those of the granodiorites (<432 ppm and <13 ppm, respectively). On the primitive mantle-normalized trace element diagram, the granites display similar trace element and REE signatures as the granodiorites, though with generally lower concentrations and more pronounced negative P and Ti anomalies.

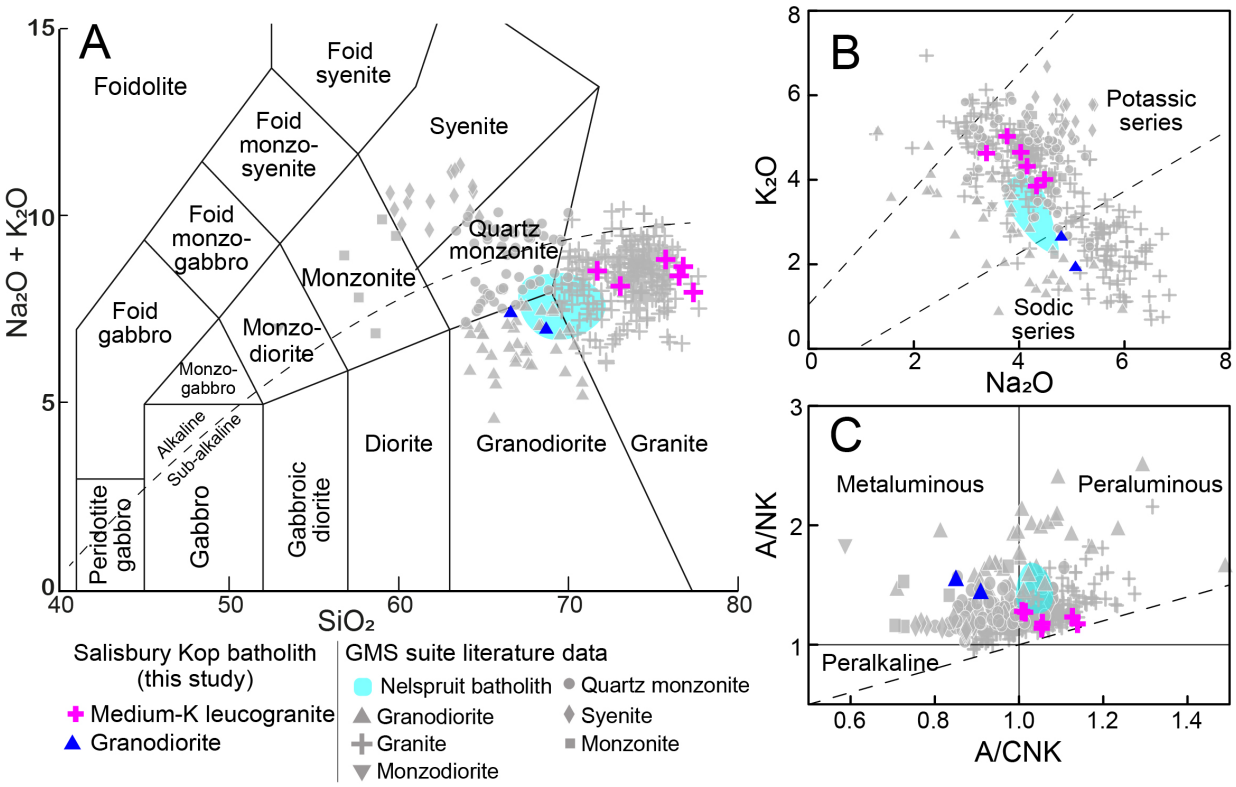

Figure 4-3. Classification diagrams with plot of rock compositions of the SB and GMS suite. A) Plot of total alkalis vs. silica (TAS) diagram (Middlemost, 1994). B) K_2O vs Na_2O (wt%) diagram with the potassic and sodic series fields

of Middlemost (1975). C) Peralkalinity vs Alumina Saturation Index diagram of Shand (1943), A/CNK: $Al_2O_3/(CaO+Na_2O+K_2O)$; A/NK: $Al_2O3/(Na_2O+K_2O)$ (molar ratio). The gray symbols represent the GMS suite samples according to their chemical classification. The GMS suite literature data were obtained from Anhaeusser and Robb, 1983; Westraat et al. (2005); Moyen et al. (2021) and Leandro et al. (2024).

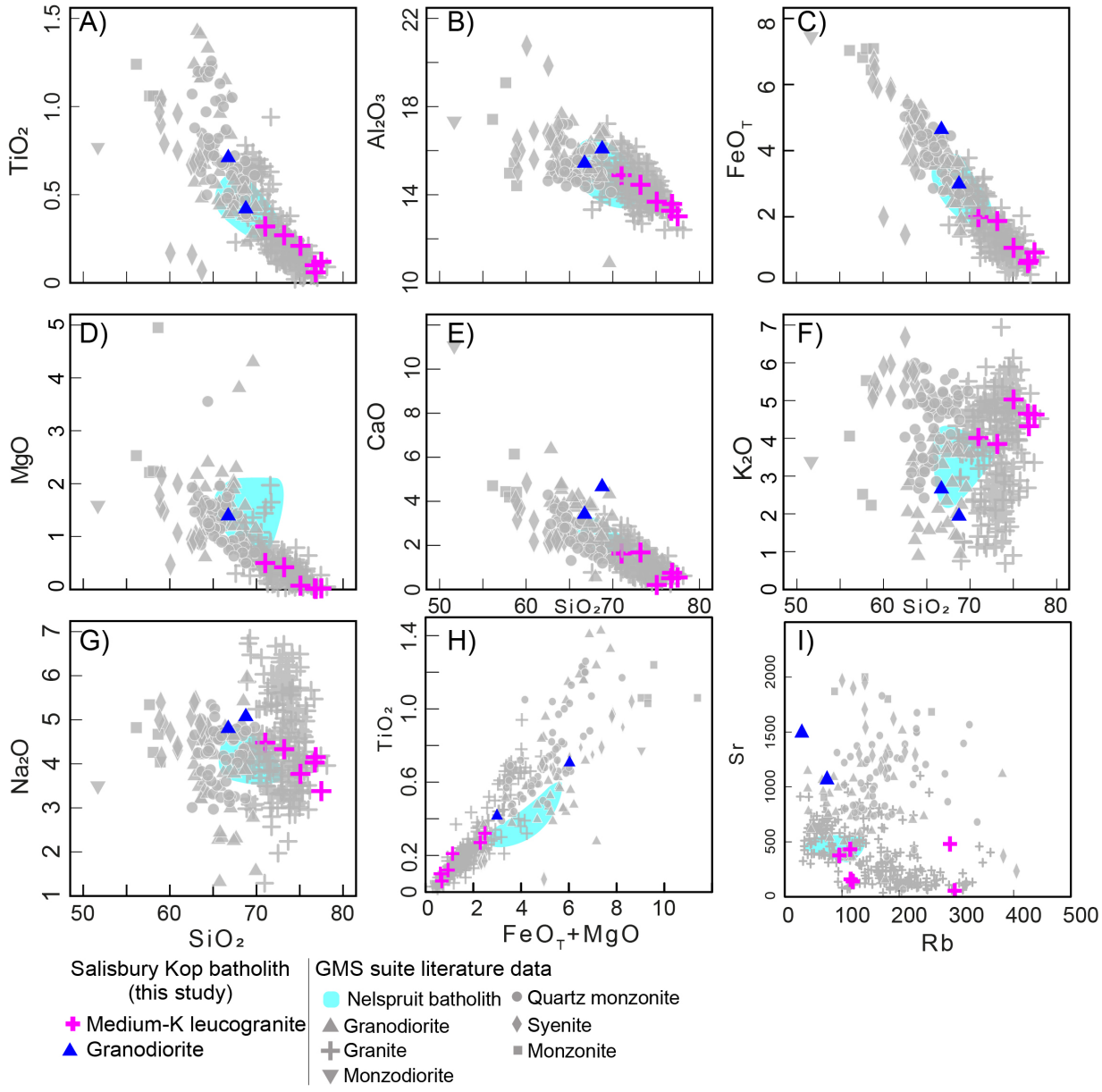

Figure 4-4. Binary diagrams for relevant major oxides (wt%) and trace elements (ppm). A) TiO_2 vs SiO_2; B) Al_2O_3 vs SiO_2; C) FeO_T vs SiO_2; D) MgO vs SiO_2; E) CaO vs SiO_2; F) K_2O vs SiO_2; G) Na_2O vs SiO_2; H) TiO_2 vs FeO_T +MgO vs SiO_2; I) Sr vs Rb (ppm). Symbols and references are the same as those used in Figure 4-3.

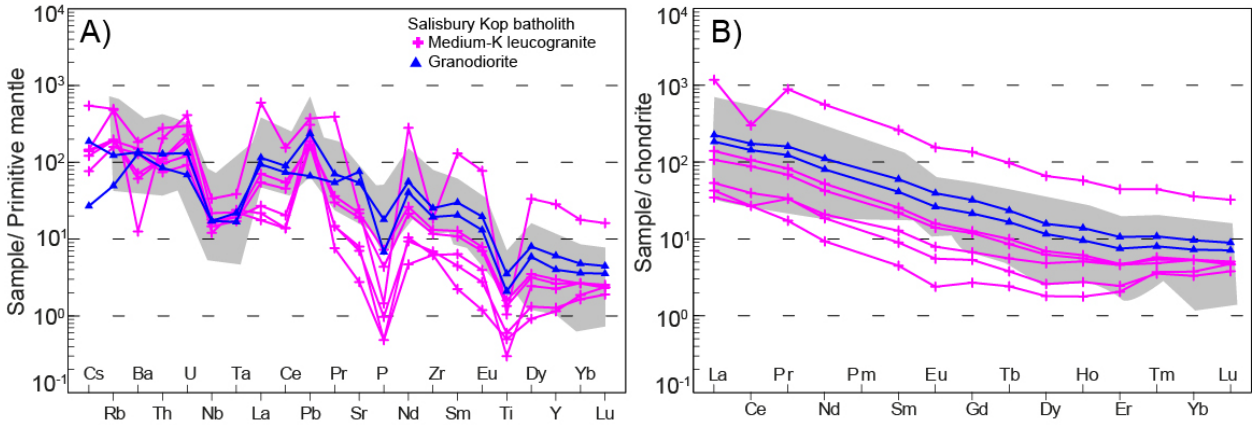

Figure 4-5. Spider diagram showing trace element and REE data for SB samples, normalized to the Primitive Mantle (McDonough and Sun, 1995) and chondrite (Nakamura, 1974), respectively. The gray area indicates the compositional range of granodiorites from the GMS suite reported by Westraat et al. (2005) and Moyen et al. (2021).

Table 4-2. Major oxides (wt%), trace elements and REE contents (ppm) of granites and granodiorites of the SB.

Facies	Medium-K leucogranite						Granodiorite	
Sample	**SB01**	**SB03**	**SB05**	**SB06B**	**SB07**	**SB08**	**SB02**	**SB04**
SiO_2	77.5	76.8	75.1	71.0	76.7	73.2	66.7	68.8
TiO_2	0.1	0.1	0.2	0.3	0.1	0.3	0.7	0.4
Al_2O_3	13.0	13.6	13.7	14.9	13.3	14.5	15.4	16.1
FeO_T	0.9	0.7	1.1	2.0	0.6	1.9	4.6	3.0
MnO	0.0	0.0	0.0	0.1	0.0	0.0	0.1	0.1
MgO	0.0	BD	0.1	0.5	0.0	0.4	1.4	BD
CaO	0.5	0.8	0.2	1.6	0.5	1.7	3.4	4.7
K_2O	4.6	4.3	5.0	4.0	4.7	3.9	2.7	1.9
Na_2O	3.4	4.2	3.8	4.5	4.0	4.3	4.8	5.1
P_2O_5	0.0	0.0	0.0	0.2	0.0	0.1	0.4	0.1
LOI	0.8	0.4	1.0	1.0	0.7	0.7	0.8	0.9
Mg#	3.7	-	10.5	30.9	5.6	28.6	34.8	-
Na_2O+K_2O	8.0	8.5	8.8	8.5	8.7	8.2	7.5	7.0
Sc	10	9.8	9.8	10.5	11.3	9.5	13.3	10.1
V	11	8	19	26	9	26	67	48
Cr	12	9	11	16	9	15	21	17
Ni	12	9	10	15	7	12	16	12
Cu	43	33	53	82	35	72	79	71
Zn	25	17	30	63	36	60	91	10
Rb	119	115	145	115	297	95	74	30
Sr	140	159	239	433	55	377	1079	1504
Y	6	10	60	13	5	11	26	17
Zr	73	65	95	139	65	123	266	204
Nb	11	8	11	12	14	10	11	11
Cs	3	3	2	3	12	2	4	1
Ba	474	405	604	994	83	848	893	857
La	18	14	193	46	11	35	74	61
Ce	34	23	128	92	23	76	150	124
Pr	4	4	50	9	2	8	18	14
Nd	12	13	174	33	6	27	70	51
Sm	2	3	26	5	1	4	12	8
Eu	0	1	6	1	0	1	3	2
Gd	2	2	19	4	1	3	9	6
Tb	0	0	2	1	0	0	1	1
Dy	1	2	11	2	1	2	5	4
Ho	0	0	2	0	0	0	1	1
Er	1	1	5	1	1	1	2	2
Tm	0	0	1	0	0	0	0	0
Yb	1	1	4	1	1	1	2	2
Lu	0	0	1	0	0	0	0	0
Hf	3	2	3	4	4	3	7	6
Ta	1	1	1	1	1	1	1	1
Pb	25	25	28	25	46	28	36	10
Th	9	9	11	8	16	6	10	7
U	5	4	3	2	8	2	3	1
Eu/Eu*	0.8	0.9	0.8	0.9	0.7	0.9	0.9	0.9

FeO_T = FeO + Fe_2O_3; LOI = Loss on ignition; Eu/Eu* = $Eu_{CN}/(Sm_{CN}+Gd_{CN})^{\wedge 0.5}$; CN = Chondrite Normalized

4.4.3. U-Pb dating

4.4.3.1. Zircon age

The zircon hosted in the granodiorite sample SB02 is euhedral and angular and presents oscillatory concentric zonation characteristic of igneous crystals. They range in length from 10 µm to 120 µm, but commonly are small (< 60 µm). The U-Pb analyses were conducted on varying sizes and morphologies of zircon crystals to minimize sampling bias. Cathodoluminescence electron images of representative crystals are shown in Figure 4-6 A. The zircon spots analyzed are characterized by Th/U from 2.1 to 0.8.

The analysis plot on a discordia line yielded an upper intercept age of 3094 ± 10 Ma (2s; n=48; MSWD = 0.79). This age is interpreted as the crystallization age of the host rocks. Their lower intercept age curve demonstrates the recent Pb loss (Figure 4-6 B). The U-Pb dataset produced is presented in Table 4-3. The small dimensions of crystals jeopardize the LA-ICP-MS analysis by limiting the laser spot size (11 µm) and the number of analyses done on a single grain.

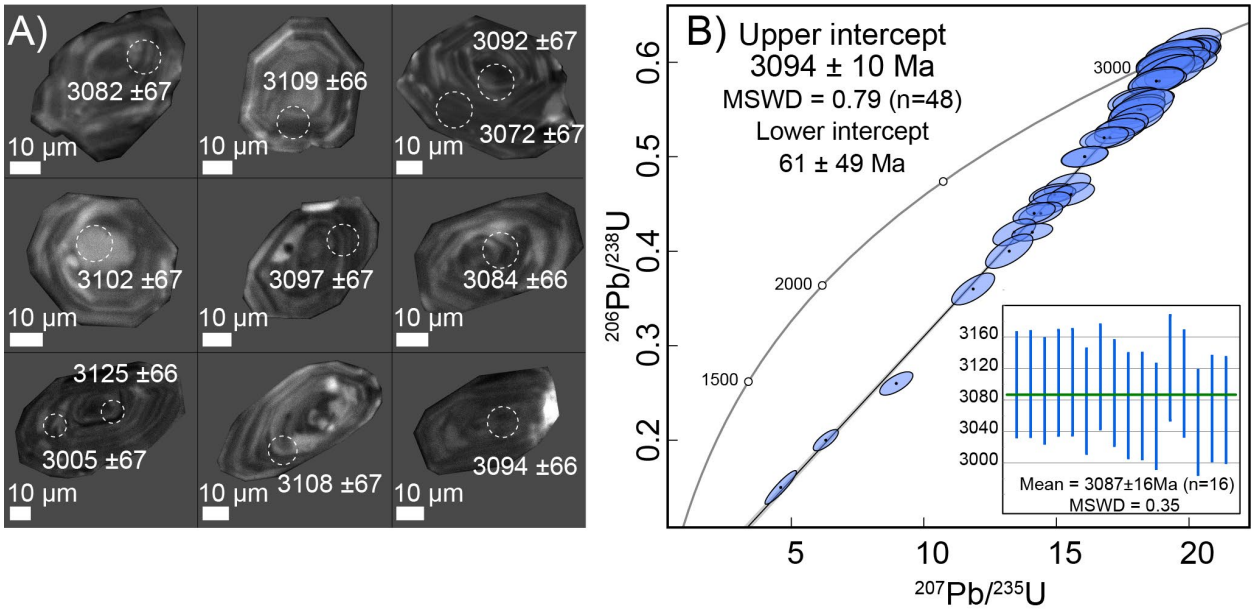

Figure 4-6. A) Representative cathodoluminescence images of zircon crystals from the coarse-grained granodiorite (sample SB02), with white circles marking analyzed areas along with their $^{207}Pb/^{206}Pb$ ages (Ma) and associated 2σ uncertainties. B) U-Pb concordia diagram for the coarse-grained granodiorite of the SB, not corrected for common Pb. The insert show the $^{207}Pb/^{206}Pb$ mean age of the concordant spots. MSWD: Mean Square Weighted Deviates.

Table 4-3. U-Pb isotopic data of zircon hosted in the coarse-grained granodiorite.

Sample SB02	Concentration (ppm)			Radiogenic ratios							Calculated ages (Ma)						Concordance	
Spot	**^{238}U**	**^{232}Th**	**Th/U**	**^{207}Pb/^{206}Pb**	2σ (%)	**^{207}Pb/^{235}U**	2σ (%)	**^{206}Pb/^{238}U**	2σ (%)	***ρ***	**^{206}Pb/^{238}U**	2σ (abs)	**^{207}Pb/^{235}U**	2σ (abs)	**^{207}Pb/^{206}Pb**	2σ (abs)	206/238 x 207/235	207/206 x 206/238
010	207.0	314.3	1.6	0.23	4.1	18.8	4.6	0.58	2.1	0.5	2951	51	3030	48	3082	67	97.4	95.8
011	139.0	229.8	1.7	0.24	4.1	20.0	4.6	0.61	2.1	0.5	3063	52	3091	48	3109	66	99.1	98.5
012	171.7	238.5	1.4	0.24	4.1	17.0	4.5	0.52	1.8	0.4	2705	39	2936	46	3099	67	92.1	87.3
013	112.4	124.4	1.1	0.24	4.1	19.9	4.6	0.61	2.1	0.5	3066	52	3088	48	3103	67	99.3	98.8
014	130.8	182.3	1.4	0.24	4.1	17.5	4.8	0.53	2.5	0.5	2753	55	2960	50	3104	67	93.0	88.7
015	196.1	221.3	1.1	0.24	4.1	18.1	4.8	0.55	2.4	0.5	2838	54	2992	49	3097	67	94.9	91.6
016	189.9	279.9	1.5	0.24	4.1	19.7	4.6	0.61	2.0	0.4	3062	49	3078	48	3089	67	99.5	99.1
017	197.9	258.2	1.3	0.24	4.1	13.2	5.5	0.40	3.7	0.7	2181	69	2696	56	3108	67	80.9	70.2
018	216.8	350.0	1.6	0.23	4.1	14.7	4.7	0.45	2.3	0.5	2414	47	2796	48	3084	66	86.3	78.3
024	231.7	363.8	1.6	0.24	4.1	19.5	4.7	0.59	2.4	0.5	2993	58	3064	49	3111	66	97.7	96.2
025	174.8	218.3	1.2	0.23	4.1	16.1	4.5	0.50	1.8	0.4	2618	39	2881	46	3070	67	90.9	85.3
026	132.4	167.1	1.3	0.24	4.1	18.8	4.6	0.58	2.0	0.4	2930	48	3030	48	3097	67	96.7	94.6
027	122.4	141.8	1.2	0.24	4.1	17.4	4.4	0.53	1.7	0.4	2732	37	2957	46	3114	67	92.4	87.7
028	296.7	375.7	1.3	0.25	4.1	15.6	4.7	0.46	2.2	0.5	2429	45	2849	48	3162	67	85.2	76.8
029	347.2	555.9	1.6	0.24	4.1	14.4	4.7	0.44	2.2	0.5	2355	44	2777	48	3100	67	84.8	76.0
030	175.6	280.3	1.6	0.23	4.1	19.2	4.5	0.60	2.0	0.4	3020	47	3050	47	3069	67	99.0	98.4
031	227.8	276.7	1.2	0.24	4.1	15.4	4.6	0.47	2.2	0.5	2486	45	2841	48	3104	67	87.5	80.1
032	280.6	305.5	1.1	0.24	4.1	11.9	5.6	0.36	3.8	0.7	1960	65	2594	56	3134	66	75.6	62.5
033	130.4	184.8	1.4	0.24	4.1	20.0	4.4	0.60	1.7	0.4	3043	42	3090	47	3121	67	98.5	97.5
034	159.8	244.2	1.5	0.24	4.1	19.9	4.5	0.61	1.9	0.4	3080	46	3087	47	3092	67	99.8	99.6
035	158.6	170.8	1.1	0.23	4.1	19.4	4.5	0.61	1.9	0.4	3051	47	3064	48	3072	67	99.6	99.3
041	176.6	293.8	1.7	0.24	4.1	18.9	4.5	0.58	1.8	0.4	2948	43	3036	47	3094	66	97.1	95.3
042	602.7	594.4	1.0	0.22	4.1	4.6	11.0	0.15	9.7	0.9	896	82	1749	94	3007	67	51.2	29.8
043	113.6	148.3	1.3	0.24	4.1	20.0	4.8	0.61	2.5	0.5	3076	60	3092	50	3102	67	99.5	99.2
044	177.6	248.5	1.4	0.24	4.1	18.5	4.4	0.56	1.6	0.4	2866	38	3014	46	3114	66	95.1	92.0

Table 4-3. U-Pb data of zircon hosted in the coarse-grained granodiorite (continued).

Spot	^{238}U	^{232}Th	Th/U	$^{207}Pb/^{206}Pb$	2σ (%)	$^{207}Pb/^{235}U$	2σ (%)	$^{206}Pb/^{238}U$	2σ (%)	ρ	$^{206}Pb/^{238}U$	2σ (abs)	$^{207}Pb/^{235}U$	2σ (abs)	$^{207}Pb/^{206}Pb$	2σ (abs)	206/238 x 207/235	207/206 x 206/238
045	671.5	1306.4	1.9	0.22	4.1	6.3	6.1	0.20	4.6	0.7	1200	50	2019	57	3005	67	59.4	39.9
046	158.2	211.6	1.3	0.24	4.1	18.0	4.7	0.54	2.3	0.5	2793	53	2990	49	3125	66	93.4	89.4
047	258.3	310.3	1.2	0.23	4.1	14.9	4.4	0.46	1.6	0.4	2446	33	2811	45	3084	67	87.0	79.3
048	232.5	353.0	1.5	0.23	4.1	16.8	4.5	0.52	1.8	0.4	2700	40	2924	46	3082	67	92.3	87.6
050	134.4	178.7	1.3	0.23	4.1	17.9	4.6	0.56	2.0	0.4	2879	46	2987	47	3060	67	96.4	94.1
051	154.3	216.4	1.4	0.24	4.1	19.7	4.7	0.60	2.2	0.5	3036	54	3075	49	3101	67	98.7	97.9
052	434.1	350.5	0.8	0.23	4.1	13.4	4.9	0.42	2.8	0.6	2253	53	2709	50	3069	67	83.2	73.4
059	389.5	795.2	2.1	0.23	4.1	18.1	4.4	0.56	1.8	0.4	2862	42	2995	46	3086	66	95.5	92.7
060	203.4	322.6	1.6	0.23	4.1	14.2	4.6	0.44	2.1	0.5	2346	42	2760	47	3079	67	85.0	76.2
061	187.3	272.1	1.5	0.23	4.1	19.3	4.3	0.6	1.5	0.4	3048	37	3055	46	3059	67	99.8	99.6
064	165.7	249.8	1.5	0.24	4.1	20.1	4.6	0.62	2.1	0.5	3090	52	3096	48	3099	66	99.8	99.7
065	144.2	182.6	1.3	0.23	4.1	19.1	4.8	0.59	2.5	0.5	2996	61	3047	50	3081	67	98.3	97.2
066	564.5	690.4	1.2	0.25	4.2	8.96	5.7	0.26	3.9	0.7	1504	52	2334	56	3167	68	64.4	47.5
067	197.4	238.4	1.2	0.23	4.1	16.1	4.4	0.50	1.8	0.4	2626	39	2881	46	3065	67	91.1	85.7
068	171.2	269.2	1.6	0.23	4.1	19.5	4.5	0.61	2.0	0.4	3057	48	3067	47	3073	67	99.7	99.5
075	307.2	603.9	2.0	0.24	4.1	14.1	4.5	0.42	1.8	0.4	2250	34	2756	46	3151	66	81.6	71.4
076	87.6	70.8	0.8	0.24	4.2	18.1	4.6	0.55	2.0	0.4	2837	45	2994	48	3101	68	94.8	91.5
078	144.0	226.5	1.6	0.23	4.1	19.1	4.7	0.60	2.2	0.5	3017	53	3047	49	3067	67	99.0	98.4
079	327.7	477.4	1.5	0.23	4.1	14.8	4.6	0.46	2.0	0.4	2450	41	2802	47	3066	67	87.4	79.9
080	146.1	188.8	1.3	0.23	4.1	19.6	4.4	0.61	1.7	0.4	3064	40	3073	46	3078	67	99.7	99.5
081	136.6	157.1	1.2	0.24	4.1	20.1	4.6	0.61	2.0	0.4	3088	49	3096	48	3100	67	99.8	99.6
084	190.1	291.7	1.5	0.23	4.1	19.0	4.4	0.6	1.8	0.4	3032	43	3044	46	3051	66	99.6	99.4
085	90.5	151.6	1.7	0.24	4.5	18.2	5.5	0.55	3.2	0.6	2809	73	3000	57	3130	74	93.7	89.8

ρ = Correlation coefficient between the isotopic ratios $^{206}Pb/^{238}U$ and $^{207}Pb/^{235}U$

4.4.3.2. Titanite age

Titanite crystals hosted in the granodiorite sample SB02 were analyzed from homogeneous zones with Th/U range from 13.6 to 0.8. The common Pb-corrected data of the SB titanite define a linear array, yielding a lower intercept crystallization age of 3100 ± 11 Ma (2s; MSWD = 1.03; n = 32) and $^{207}Pb/^{206}Pb$ intercept at 0.448 in the Terra-Wasserburg concordia diagram (Figure 4-7), which is within uncertainty concordant with the zircon age obtained.

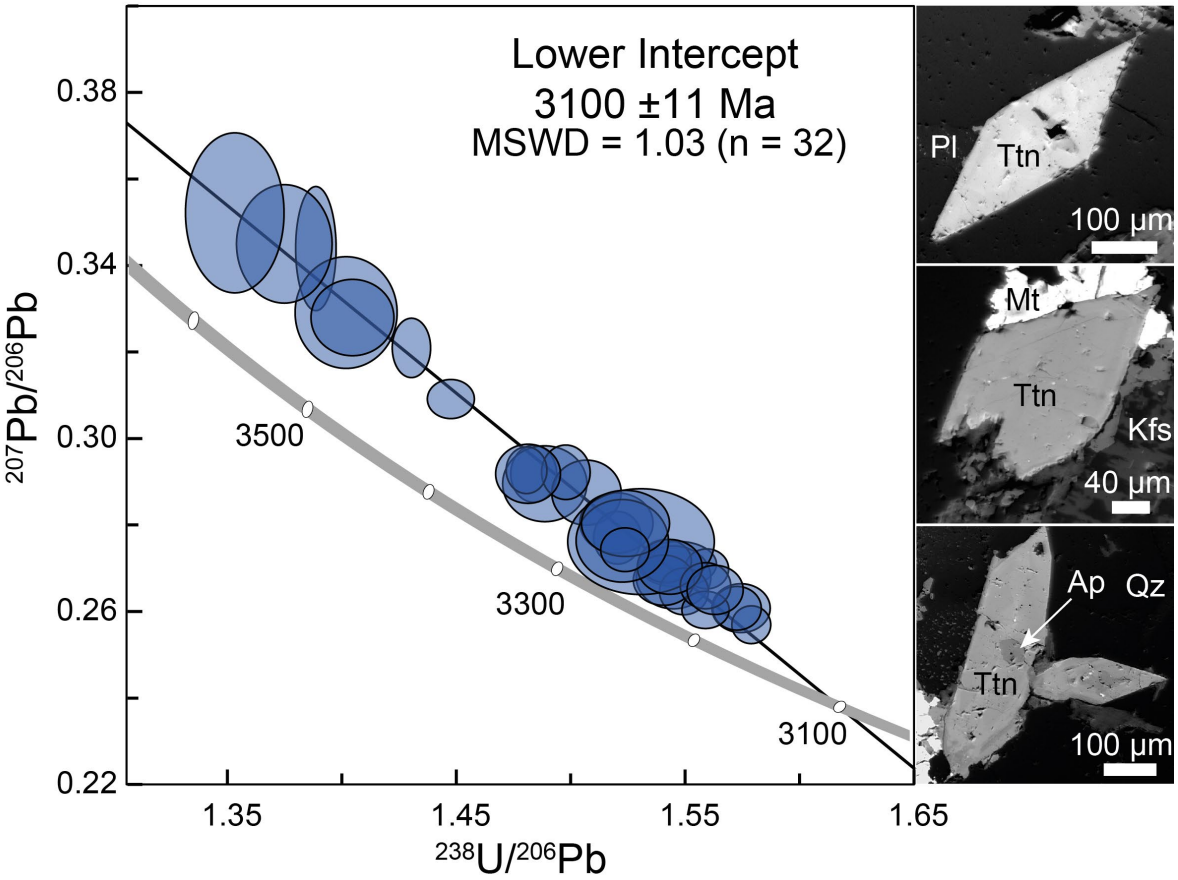

Figure 4-7. Tera-Wasserburg concordia diagram for titanite, showing a low intercept age of 3100 ± 11 Ma (uncorrected for ^{204}Pb). Insert: BSE image illustrating titanite crystals analyzed. Ap: apatite; Kfs: K-feldspar; Mt: magnetite; Pl: plagioclase; Qz: quartz; Ttn: titanite.

4.5. Discussion

The granite s.s. is the predominant rock type of the SB, while the granodiorites occur in constrained areas (Figure 4-1). The presence of oligoclase and albite as the main plagioclase and biotite as predominant mafic phase of the system reflect the felsic nature of the parental magma. Additionally, it may reflect low temperatures and pressures during crystallization, further supporting an origin from felsic magmas.

The SB granodiorites plot within the geochemical range reported for the GMS suite and are chemically akin to the granodiorites with higher Na_2O reported in the Mpuluzi batholith (e.g., Westraat et al., 2005; Moyen et al., 2021). On the other hand, the SB granodiorites are chemically distinct from the

potassic and peraluminous granodiorites of the Nelspruit Batholith (Robb, 1977). The SB and Nelspruit batholith contrast is also observed in the CaO, Na_2O, and Sr contents, suggesting even though they share similar textures and are spatially close, these two batholiths could have chemically distinct sources.

The SB granodiorites are characterized by low Rb concentrations and high Sr and Y contents. These features associated with the negative Nb, Ta, and Ti anomalies, along with the positive Pb anomaly (Figure 4-5 A) support an origin from a felsic magma derived from the lower crust, with minor contributions of mafic melts (e.g., Pearce et al., 1984; Harris and Tindle, 1986). Thus, the source might be chemically heterogeneous composed predominantly of supracrustal materials with meta-TTG and metasedimentary components, in agreement with what was proposed for the Heerenveen and Mpuluzi batholiths (e.g., Moyen et al., 2021).

The analysis of a large population of zircon and titanite crystals demonstrates the high precision and consistent repeatability of the ca. 3094 ± 10 Ma U-Pb zircon age (Figure 4-6 B) and 3100 ± 11 Ma obtained for the titanite (Figure 4-7) hosted in the granodiorite of the SB corroborates the 3109 ± 10 Ma (n = 5) age proposed by Kamo and Davis (1994) as crystallization age of the batholith and minimum deposition and deformation age of the Moodies group. On the other hand, the younger 3076 ± 6 Ma single-grain evaporation Pb-Pb obtained by Heubeck et al. (1993) might reflect late crystallized zircon zones. The titanite ages, which align with the zircon ages within the uncertainty, indicate the pristine nature of the analyzed rocks and suggest that these rocks remained unaffected by subsequent magmatic events following their emplacement.

4.6. Conclusion

The SB is predominantly composed of granite s.s., with granodiorites occurring in restricted areas, reflecting its felsic nature and crystallization under low-temperature conditions. The geochemical data indicate that the SB granodiorites align with the GMS suite and are chemically similar to those of the Mpuluzi batholith but distinct from the granodiorites of the Nelspruit Batholith, underscoring chemically heterogeneous sources, for these neighboring batholiths. The granodiorites likely originated from a felsic lower crust source.

The robust U-Pb ages of zircon (3094 ± 10 Ma) and titanite (3100 ± 11 Ma) represent the crystallization age of the SB and establish the minimum age for the deposition and deformation of the Moodies Group. The concordant titanite and zircon ages, along with the absence of evidence for later magmatic overprints, suggest that the rocks of the SB batholith remained pristine post-emplacement.

4.7. Acknowledgment

This research was supported by an RSA NRF grant to Gary Stevens via the SARChI program and by IRP BuCoMO, a collaborative research project funded by the CNRS and the NRF. This is BuCoMO contribution A15. We thank Riana Rossouw and Cris Lana for LA-ICP-MS analyses and Madelaine Frazenburg for assistance with SEM analyses.

4.8. References – Chapter 4

1. Aleinikoff, J.N., Wintsch, R.P., Tollo, R.P., Unruh, D.M., Fanning, C.M., and Schmitz, M.D., 2007. Ages and origins of rocks of the Killingworth dome, south-central Connecticut: Implications for the tectonic evolution of southern New England. *American Journal of Science*, *307*(1), 63-118. https://doi.org/10.2475/01.2007.04

1. Anhaeusser, C.R., 2014. Archaean greenstone belts and associated granitic rocks–a review. *Journal of African Earth Sciences*, *100*, 684-732. https://doi.org/10.1016/j.jafrearsci.2014.07.019

2. Anhaeusser, C.R., and Robb, L.J., 1983. Geological and geochemical characteristics of the Heerenveen and Mpuluzi batholiths south of the Barberton greenstone belt and preliminary thoughts on their petrogenesis. In: Anhaeusser, C.R. (Ed.), Contributions to the Geology of the Barberton Mountain Land. *Geological Society of South Africa Special Publication, 9*, 131-152.

3. Belcher, R.W., and Kisters, A.F.M., 2006. Syntectonic emplacement and deformation of the Heerenveen batholith: conjectures on the structural setting of the 3.1 Ga granite magmatism in the Barberton granite-greenstone terrain, South Africa. *Geological Society of America, Special Publication, 405,* 211–231. https://doi.org/10.1130/2006.2405(12)

4. Clemens, J.D., Belcher, R.W., Kisters, A.F., 2010. The Heerenveen batholith, Barberton Mountain Land, South Africa: Mesoarchaean, potassic, felsic magmas formed by melting of an ancient subduction complex. *Journal of Petrology, 51(5)*, 1099-1120. https://doi.org/10.1093/petrology/egq014

5. De Ronde, C.E., and de Wit, M.J., 1994. Tectonic history of the Barberton greenstone belt, South Africa: 490 million years of Archean crustal evolution. *Tectonics, 13(4)*, 983-1005. https://doi.org/10.1029/94TC00353

2. De Ronde, C.E.J., and Kamo, S., 2000. An Archaean arc-arc collisional event: a short-lived (ca. 3 Myr) episode, Weltevreden area, Barberton greenstone belt, South Africa. *Journal of African Earth Sciences, 30*, 219 - 248. https://doi.org/10.1016/S0899-5362(00)00017-8

6. De Wit, M.J., Roering, C., Hart, R.J., Armstrong, R.A., de Ronde, C.E.J., Green, R.W.E., Tredoux, M., Peberdy, E., and Hart, R.A., 1992, Formation of an Archean continent. *Nature, 357*, 553–562. https://doi.org/10.1038/357553a0

7. Dziggel, A., Stevens, G., Poujol, M., Anhaeusser, C.R., and Armstrong, R.A., 2002. Metamorphism of the granite–greenstone terrane south of the Barberton greenstone belt, South Africa: an insight into the tectono-thermal evolution of the 'lower' portions of the Onverwacht Group. *Precambrian Research*, *114*(3-4), 221-247. https://doi.org/10.1016/S0301-9268(01)00225-X

8. Eggins, S.M., 2003. Laser ablation ICP-MS analysis of geological materials prepared as lithium borate glasses. *Geostandards Newsletter, 27(2)*, 147-162. https://doi.org/10.1111/j.1751-908X.2003.tb00642.x

9. Gumsley, A., Olsson, J., Söderlund, U., de Kock, M., Hofmann, A., and Klausen, M., 2015. Precise U-Pb baddeleyite age dating of the Usushwana Complex, southern Africa–Implications for the Mesoarchaean magmatic and sedimentological evolution of the Pongola Supergroup, Kaapvaal Craton. *Precambrian Research, 267,* 174-185. https://doi.org/10.1016/j.precamres.2015.06.010

10. Harris, N.B., Pearce, J.A., and Tindle, A.G., 1986. Geochemical characteristics of collision-zone magmatism. *Geological Society, London, Special Publications*, *19*(1), 67-81. https://doi.org/10.1144/GSL.SP.1986.019.01.04

11. Heubeck, C., Wendt, J.I., Toulkeridis, T., Kroner, A., and Lowe, D., 1993. Timing of deformation of the Archaean Barberton greenstone belt, South Africa: constraints from zircon dating of the Salisbury Kop pluton. *South African Journal of Geology*, *96(1),* 1-8. https://hdl.handle.net/10520/AJA10120750_525

12. Horstwood, M.S., Košler, J., Gehrels, G., Jackson, S.E., McLean, N.M., Paton, C., Pearson, Sircombe, K., Sylvester, P., Vermeesch, P., Bowring, J.F., Condon, D.J., and Schoene, B., 2016. Community-derived standards for LA-ICP-MS U-(Th-) Pb geochronology–Uncertainty propagation, age interpretation and data reporting. *Geostandards and Geoanalytical Research, 40(3)*, 311-332. https://doi.org/10.1111/j.1751-908X.2016.00379.x

13. Jackson, S.E., Pearson, N.J., Griffin, W.L., and Belousova, E.A., 2004. The application of laser ablation-inductively coupled plasma-mass spectrometry to in situ U-Pb zircon geochronology. *Chemical Geology, 211*, 47-69. https://10.1016/j.chemgeo.2004.06.017

14. Jochum, K.P., Weis, U., Stoll, B., Kuzmin, D., Yang, Q., Raczek, I., Jacob, D.E., Stracke, A., Birbaum, A., Frick, D.A., Günther, D., and Enzweiler, J., 2011. Determination of reference values for NIST SRM 610–617 glasses following ISO guidelines. *Geostandards and Geoanalytical Research, 35(4)*, 397-429. https://doi.org/10.1111/j.1751-908X.2011.00120.x

15. Kamo, S.L., and Davis, D.W., 1994. Reassessment of Archaean crustal development in the Barberton mountain land, South Africa, based on U-Pb dating. *Tectonics, 13(1)*, 167-192. https://doi.org/10.1029/93TC02254

16. Kisters, A.F., Stevens, G., Dziggel, A., and Armstrong, R.A., 2003. Extensional detachment faulting and core-complex formation in the southern Barberton granite–greenstone terrain, South Africa: evidence for a 3.2 Ga orogenic collapse. *Precambrian Research*, *127*(4), 355-378. https://doi.org/10.1016/j.precamres.2003.08.002

17. Kröner, A., Anhaeusser, C.R., Hoffmann, J.E., Wong, J., Geng, H., Hegner, E., Xie, H., Yang, J. and Liu, D., 2016. Chronology of the oldest supracrustal sequences in the Palaeoarchaean Barberton Greenstone Belt, South Africa and Swaziland. *Precambrian Research, 279*, 123-143. https://doi.org/10.1016/j.precamres.2016.04.007

3. Kröner, A., Hegner, E., Wendt, J.I., and Byerly, G.R., 1996. The oldest part of the Barberton granitoid-greenstone terrain, South Africa: evidence for crust formation between 3.5 and 3.7 Ga. *Precambrian Research, 78(1-3)*, 105-124. https://doi.org/10.1016/0301-9268(95)00072-0

4. Lana, C., Buick, I., Stevens, G., Rossouw, R., and De Wet, W., 2011. 3230–3200 Ma post-orogenic extension and mid-crustal magmatism along the southeastern margin of the Barberton Greenstone Belt, South Africa. *Journal of Structural Geology, 33(5)*, 844-858. https://doi.org/10.1016/j.jsg.2011.03.007

18. Leandro, M.V.S., Stevens, G., Moyen, J.F., Kisters A.F.M., and Ferreira, A., 2024. Generating Archean syenites by intracrustal processes: A review of the Boesmanskop Alkaline Complex, Eastern Kaapvaal Craton. *Lithos, in press. http://dx.doi.org/10.2139/ssrn.4972697*

5. Lowe, D.R., 1994. Accretionary history of the Archaean Barberton greenstone belt (3.55 - 3.22 Ga), southern Africa. *Geology, 22*, 1099-1102.

6. Lowe, D.R., and Byerly, G.R., 1999. Stratigraphy of the west-central part of the Barberton greenstone belt, South Africa. In: Lowe, D.R., Byerly, G.R. (Eds.), Geologic Evolution of the Barberton Greenstone Belt, South Africa. *Geological Society of America Special Paper, 329*, 1–36.

19. Maphalala, R.M. and Kröner, A., 1993. Pb-Pb single zircon ages for the younger Archaean granitoids of Swaziland, southern Africa. Abstract In: 16th *International colloquium on Africa geology*, 201–206.

20. Mazoz, A., Gonçalves, G.O., Lana, C., Buick, I.S., Corfu, F., Kamo, S.L., Wang, H., Yang, Y., Scholz, R., Queiroga, G., Fu, B., Martins, L., Schannor, M., Abreu, A.T., Babinski, M., Peixoto, E., and Santos, R.V., 2022. Khan River and Bear Lake: two natural titanite reference materials for high-spatial resolution U-Pb microanalysis. *Geostandards and Geoanalytical Research*, *46*(4), 701-733. https://doi.org/10.1111/ggr.12444

21. McDonough, W.F., and Sun, S.S., 1995. The composition of the Earth. *Chemical Geology, 120*, 223-253. https://doi.org/10.1016/0009-2541(94)00140-4

22. Middlemost, E.A., 1975. The Basalt Clan. *Earth-Science Reviews, 11(4)*, 337-564. http://dx.doi.org/10.1016/0012-8252(75)90039-2

23. Middlemost, E.A., 1994. Naming materials in the magma/igneous rock system. *Earth-science reviews, 37(3-4)*, 215-224. https://doi.org/10.1016/0012-8252(94)90029-9

24. Moyen, J.F., Stevens, G., and Kisters, A., 2006. Record of mid-Archaean subduction from metamorphism in the Barberton terrain, South Africa. *Nature*, *442*(7102), 559-562. https://doi.org/10.1038/nature04972

25. Moyen, J.F., Stevens, G., Kisters, A.F.M., Belcher, R.W., and Lemirre, B., 2019. TTG Plutons of the Barberton Granitoid-Greenstone Terrain, South Africa. *Developments in Precambrian Geology, 15*, 607-667. https://doi.org/10.1016/S0166-2635(07)15056-8

26. Moyen, J.F., Zeh, A., Cuney, M., Dziggel, A., and Carrouée, S., 2021. The multiple ways of recycling Archaean crust: A case study from the ca. 3.1 Ga granitoids from the Barberton Greenstone Belt, South Africa. *Precambrian Research, 353,* 105998. https://doi.org/10.1016/j.precamres.2020.105998

27. Nakamura, N., 1974. Determination of REE, Ba, Fe, Mg, Na and K in carbonaceous and ordinary chondrites. Geochimica et cosmochimica acta, 38(5), 757-775. https://doi.org/10.1016/0016-7037(74)90149-5

28. Pearce, J.A., Harris, N.B., and Tindle, A.G., 1984. Trace element discrimination diagrams for the tectonic interpretation of granitic rocks. *Journal of petrology*, *25*(4), 956-983. https://doi.org/10.1093/petrology/25.4.956

29. Robb, L.J., 1977. *The geology and geochemistry of the Archaean granite-greenstone terrane between Nelspruit and Bushbuckridge, Eastern Transvaal*. Doctoral dissertation, University of the Witwatersrand.

30. Robb, L.J., Brandl, G., Anhaeusser, C.R., Poujol, M., Johnson, M.R., and Thomas, R.J., 2006. Archaean granitoid intrusions. *In*: Johnson, M.R., Anhaeusser, C.R., Thomas, R.J. (Eds.), *The Geology of South Africa*, 57-94.

31. Robb, L.J., Meyer, F.M., Hawkesworth, C.J., and Gardiner, N.J., 2021. Petrogenesis of Archaean granites in the Barberton region of South Africa as a guide to early crustal evolution. *South African Journal of Geology 2021*, *124*(1), 111-140. https://doi.org/10.25131/sajg.124.0021

7. Schoene, B., and Bowring, S.A., 2007. Determining accurate temperature–time paths from U–Pb thermochronology: An example from the Kaapvaal craton, southern Africa. *Geochimica et Cosmochimica Acta, 71(1)*, 165-185. https://doi.org/10.1016/j.gca.2006.08.029

32. Shand, S.J., 1943. Eruptive rocks: their genesis, composition, classification, and their relation to ore deposits, with a chapter on meteorites. *Journal of Geology, 56(6)*, 593-593. https://doi.org/10.1086/625564

33. Silva, J.P., Lana, C., Mazoz, A., Buick, I., and Scholz, R., 2023. U-Pb Saturn: New U-Pb/Pb-Pb Data Reduction Software for LA-ICP-MS. *Geostandards and Geoanalytical Research*, *47*(1), 49-66. https://doi.org/10.1111/ggr.12474

34. Sláma, J., Košler, J., Condon, D.J., Crowley, J.L., Gerdes, A., Hanchar, J.M., Horstwood, M.S.A., Morris, G.A., Nasdala, L., Norberg, N., Schaltegger, U., Schoene, B., Tubrett, M.N., and Whitehouse, M.J., 2008. Plešovice zircon - a new natural reference material for U-Pb and Hf isotopic microanalysis. *Chemical Geology, 249,* 1-35. https://10.1016/j.chemgeo.2007.11.005

35. Van Kranendonk, M.J., Kröner, A., Hoffmann, J.E., Nagel, T., and Anhaeusser, C.R., 2014. Just another drip: Re-analysis of a proposed Mesoarchean suture from the Barberton Mountain Land, South Africa. *Precambrian Research, 254*, 19-35. https://doi.org/10.1016/j.precamres.2014.07.022

36. Vermeesch, P., 2018. IsoplotR: A free and open toolbox for geochronology. *Geoscience Frontiers, 9(5)*, 1479-1493. https://doi.org/10.1016/j.gsf.2018.04.001

37. Westraat, J.D., Kisters, A.F.M., Poujol, M., and Stevens, G., 2005. Transcurrent shearing, granite sheeting and incremental construction of the tabular 3.1 Ga Mpuluzi batholith, Barberton granite-greenstone terrane, South Africa. *Journal of the Geological Society, 162(2)*, 373-388. https://doi.org/10.1144/0016-764904-026

38. Wiedenbeck, M., Allé, P., Corfu, F., Griffin, W.L., Meier, M., Oberli, F., Von Quadt, A., Roddick, J.C., and Spiegel, W., 1995. Three natural zircon standards for U-Th-Pb, Lu-Hf, trace element and REE analysis. *Geostandards and Geoanalytical Research, 19,* 1-23. https://10.1111/j.1751-908X.1995.tb00147.x

39. Wilson, A.H., and Zeh, A., 2018. U-Pb and Hf isotopes of detrital zircons from the Pongola Supergroup: Constraints on deposition ages, provenance and Archean evolution of the Kaapvaal craton. *Precambrian Research, 305*, 177-196. https://doi.org/10.1016/j.precamres.2017.12.020

40. Yearron, L.M., 2003. *Archaean granite petrogenesis and implications for the evolution of the Barberton Mountain Land, South Africa*. Doctoral dissertation, Kingston University

CHAPTER 5. CONCLUSION

5.1. U-Pb geochronology

The textural, mineralogical and geochemical features observed in the BAC and SB rocks underscore the well-documented heterogeneity of the GMS suite (e.g., Moyen et al., 2021a; Clemens et al., 2010) even though the magmatic event responsible for the formation of this suite being constrained to a relatively short timespan (Figure 5-1). U-Pb zircon analysis of the KZD quartz monzonite yielded a crystallization age of 3118 ± 9 Ma. The zircon crystals from the SB granodiorites produced an age of 3094 ± 10 Ma, while titanite yielded an age of 3100 ± 11 Ma. This range of ages likely reflects the incremental assembly of the plutons.

The higher crystallization temperatures recorded by zircon and titanite in the syenites compared to those in the quartz monzonites, suggests that the syenites crystallized prior to quartz monzonite. Therefore, the quartz monzonite age of 3118 ± 9 Ma can be interpreted as the minimum age of the syenites.

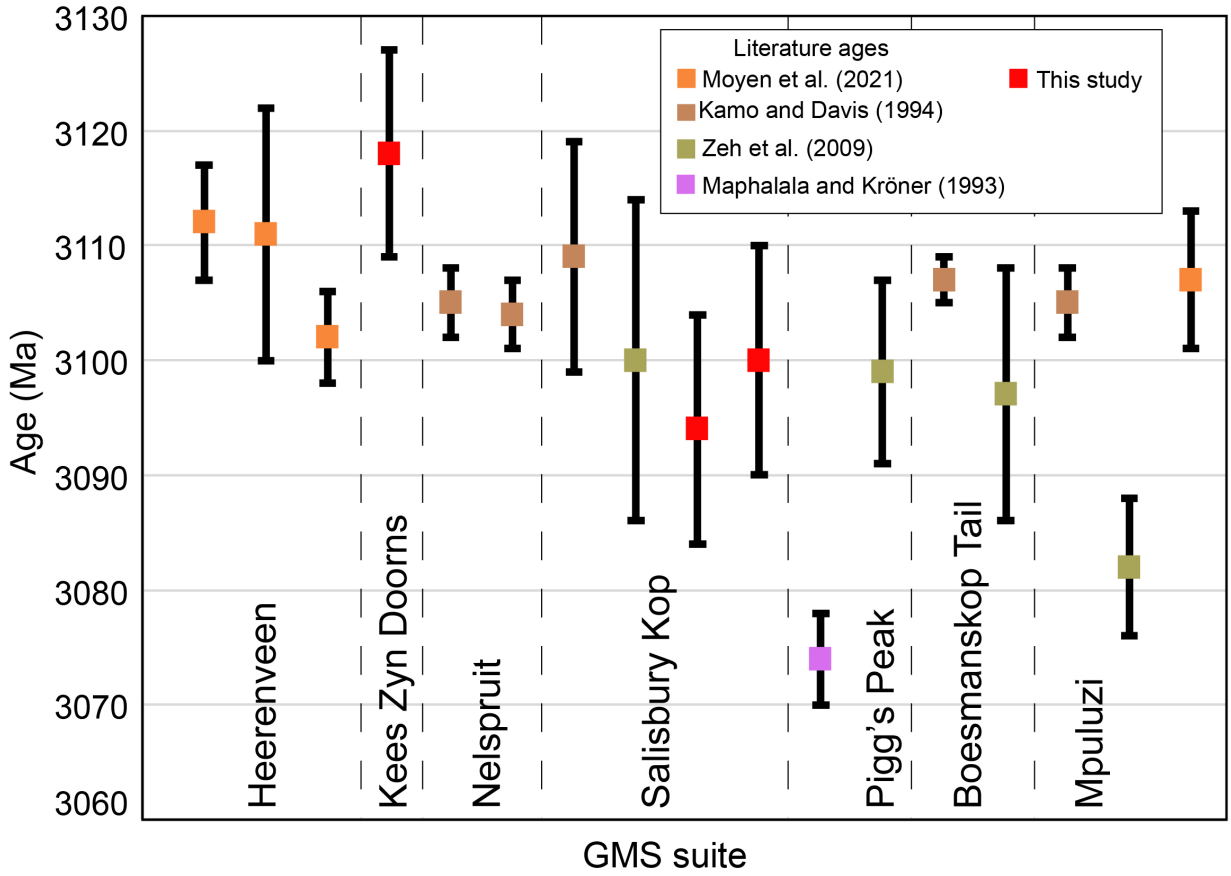

Figure 5-1. Representative U-Pb crystallization ages for the GMS suite delimitating the age range of the suite, shown with 2σ uncertainty bars. The literature ages are reported by Maphalala and Kröner (1993), Kamo and Davis (1994), Zeh et al. (2009), and Moyen et al. (2021).

5.2. Origins of Heterogeneity in the GMS suite

This research demonstrated the critical role of mineral accumulation in forming the cumulate rocks characterized by K-feldspar phenocrysts in the BAC. The mineral accumulation was associated with rhyolitic melt loss from the system. The syenites likely underwent greater rhyolitic melt loss compared to the quartz monzonites. Thus, the varying proportions of cumulate and intercumulate phases likely contributed to the significant heterogeneity observed in the granitoids of the GMS suite.

The BAC syenites and quartz monzonites are K-feldspar cumulus rocks representing the most potassic and REE-rich rocks of the GMS suite. These rocks exhibit high-temperature mineral assemblages, including high-Zr titanite and high-Ti zircon, alongside pyroxene, amphibole, pristine orthoclase and the notable absence of high-Ti biotite. These features reflect the hot (> 850 ^{o}C), REE-rich nature of the magmas from which the syenites and quartz monzonites crystallized. In contrast, the homogeneous leucogranites and granodiorites of the SB contain idiomorphic biotite crystals and lack cumulus textures, suggesting they are chilled magmas derived from more evolved and cooler magmas, likely produced from shallower sources than the syenites and quartz monzonites.

Consequently, fractional crystallization of magmas from a single compositional source is not capable of accounting for the petrographic and chemical diversity observed in the BAC and SB rocks. Instead, the partial melting of compositionally heterogeneous sources at varying depths, combined with multiple processes during melt ascent and emplacement - such as fractional crystallization and melt loss - is required to explain the internal heterogeneities within the GMS plutons (e.g., Clemens et al., 2009; Clemens et al., 2010; Moyen et al., 2021a; Robb et al., 2021; Leandro et al., 2024).

5.3. Source inference

Geochemical evidence, including negative $\varepsilon Nd_{(t)}$ and $\varepsilon Hf_{(t)}$ values (e.g., Moyen et al., 2021), low MgO, Cr, and Ni, as well as negative Nb, Ta, and Ti anomalies in the BAC, SB and other GMS suite plutons, along with the presence of ca. 3.2 Ga inherited zircon cores (Zeh et al., 2009) suggests a source predominantly composed of crustal materials isotopically similar to the TTG suite rocks. This evidence indicates limited contribution from mantle-derived materials (e.g., Robb et al., 2006; Moyen et al., 2021a,b; Leandro et al., 2024).

Although the main geodynamic settings acting during the Archean remain a topic of intense debate (e.g., Brey and Shu, 2018; de Wit et al., 2018; Chowdhury et al., 2020), it is widely accepted the ca. 3.4 Ga and ca 3.2 Ga compressional event resulted in the formation of major NE-SW trending folds and thrust faults in the BGB, as well as significant crustal thickening and the burial and heating of supracrustal rocks (e.g., de Ronde and de Wit, 1994; Lowe, 1994; De Ronde and Kamo, 2000).

The crustal thickening and recycling of the chemically complex local gray gneiss crust, including meta-TTG, meta-sediments, and metavolcanic rocks (likely similar to the lower sequences of the Onverwacht group) could have generated a heterogenous mid- to lower crust source with variable degrees of K-enrichment (e.g., Clemens et al., 2010; Moyen et al., 2021b; Robb et al., 2021). The heat produced by this thickened crust, along with possible mantle heat and input from mafic magmas during the waning periods of compression may have triggered anatexis of the composite lower crust (Figure 5-2). The high-temperature mineral assemblage of the syenites and quartz monzonites suggests that these rocks originated from high-temperature, anhydrous anatexis.

The zones of weakness and syn-magmatic shear zones created by compressional forces also served as pathways for the episodic ascent and emplacement of potassic crustal melt at shallow levels (e.g., Robb et al.,1986; Westraat et al., 2005; Belcher and Kisters, 2006), leaving behind a refractory lower crust.

The low-degree partial melting of the reworked gray gneiss crust, occurring outside the stability field of biotite, likely generated hot, incompatible element-enriched melts which were necessary for the formation of the volumetrically small syenites and quartz monzonites of the BAC. Therefore, their parental magmas likely represent the initial expression of the high-K magmatism that built up the GMS suite. The emplacement of the BAC parental magmas completely or partially submitted to shear zone dynamics facilitated the ascent of small melt batches through dyke-like structures, transporting incompatible elements (alongside radioactive elements) to shallower levels and contributing to craton stabilization (e.g., Clemens et al., 2009; Belcher and Kisters, 2006). This geodynamic setting, coupled with the assembly of the BAC through multiple melt batches, prompted structurally assisted K-feldspar accumulation and melt loss from the magma chambers via a filter-pressing-like mechanism. Additionally, it facilitated the NW-SE alignment and dyke-like disposition of the KZD, BT, and younger Usushwana mafic complex.

The upward propagation of heat triggered the partial melting of more fertile, shallower crustal layers, producing the voluminous, cooler parental magmas responsible for producing the the wide leucogranites and granodiorites of the GMS suite. These features underscore the importance of crustal reworking in the building up of the suite, crustal differentiation and stabilization of the early crust.

The extensive dataset produced in this research suggests that the syenites with remarkably high contents of incompatible elements can be produced by a simple anatexis process involving typical Archean lower crust compositions (meta-TTG + metasedimentary rocks), in combination with fractional crystallizations and rhyolitic melt loss. This indicates that classical mechanisms of syenite production (e.g., Fitton and Upton, 1987), involving low degrees of partial melting were applicable even during the Archean times, during the onset of the potassic magmatism production. Therefore, the scarcity of Archean syenites may be due to overprinting and destruction of these rocks, rather than an inherent impossibility in their formation.

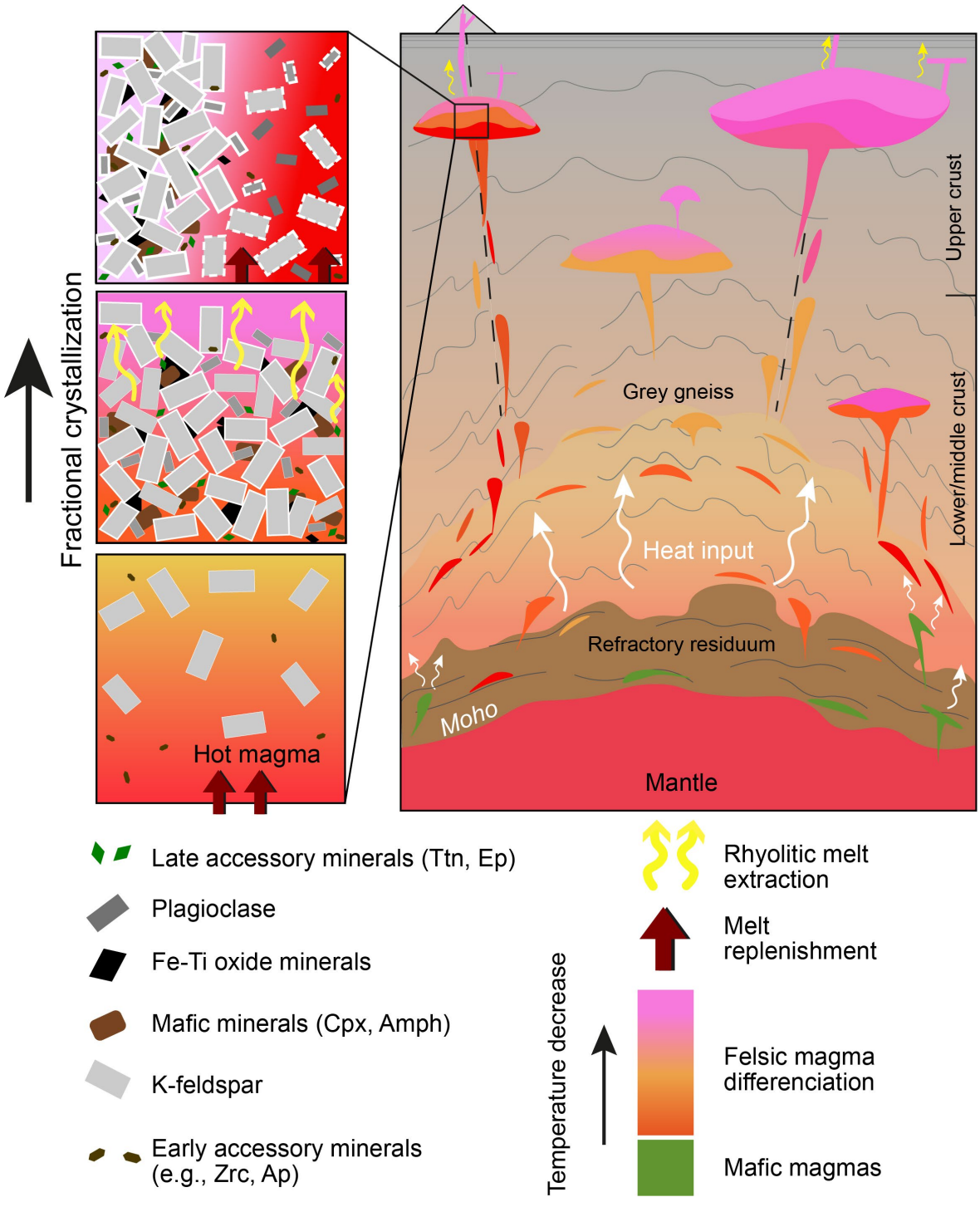

Figure 5-2. Schematic illustration of intra-crustal magma generation model during decompression of a previously thickened crust, based on Moyen et al. (2021b). Mantle upwelling and ascent of mafic magmas triggered localize crustal melting. The upward movement of magma to shallower levels was enabled by weak transcrustal structures.

5.4. References – Chapter 5

1. Belcher, R.W., and Kisters, A.F., 2006. Syntectonic emplacement and deformation of the Heerenveen batholith: Conjectures on the structural setting of the 3.1 Ga granite magmatism in the Barberton granite-greenstone terrain, South Africa. *Geological Society of America, 405*, 211-231. https://doi.org/10.1130/2006.2405(12)1

2. Brey, G.P., and Shu, Q., 2018. The birth, growth and ageing of the Kaapvaal subcratonic mantle. Mineralogy and Petrology, 112(Suppl 1), 23-41. https://doi.org/10.1007/s00710-018-0577-8

3. Chowdhury, P., Chakraborty, S., Gerya, T.V., Cawood, P.A., and Capitanio, F.A., 2020. Peel-back controlled lithospheric convergence explains the secular transitions in Archean metamorphism and magmatism. *Earth and Planetary Science Letters, 538*, 116224. https://doi.org/10.1016/j.epsl.2020.116224

4. Clemens, J.D., Belcher, R.W., and Kisters, A.F., 2010. The Heerenveen batholith, Barberton Mountain Land, South Africa: Mesoarchaean, potassic, felsic magmas formed by melting of an ancient subduction complex. *Journal of Petrology, 51(5)*, 1099-1120. https://doi.org/10.1093/petrology/egq014

5. Clemens, J.D., Helps, P.A., and Stevens, G., 2009). Chemical structure in granitic magmas–a signal from the source?. *Earth and Environmental Science Transactions of the Royal Society of Edinburgh, 100(1-2),* 159-172. https://doi.org/10.1130/2010.2472(11)

6. De Ronde, C.E., and de Wit, M.J., 1994. Tectonic history of the Barberton greenstone belt, South Africa: 490 million years of Archean crustal evolution. *Tectonics, 13(4)*, 983-1005. https://doi.org/10.1029/94TC00353

7. De Ronde, C.E.J., and Kamo, S., 2000. An Archaean arc-arc collisional event: a short-lived (ca. 3 Myr) episode, Weltevreden area, Barberton greenstone belt, South Africa. Journal of African Earth Sciences, 30, 219 - 248. https://doi.org/10.1016/S0899-5362(00)00017-8

8. de Wit, M., Furnes, H., MacLennan, S., Doucouré, M., Schoene, B., Weckmann, U., Martinez, U., and Bowring, S., 2018. Paleoarchean bedrock lithologies across the Makhonjwa Mountains of South Africa and Swaziland linked to geochemical, magnetic and tectonic data reveal early plate tectonic genes flanking subduction margins. *Geoscience Frontiers*, *9*(3), 603-665. https://doi.org/10.1016/j.gsf.2017.10.005

9. Kamo, S.L., and Davis, D.W., 1994. Reassessment of Archaean crustal development in the Barberton mountain land, South Africa, based on U-Pb dating. *Tectonics, 13(1)*, 167-192. https://doi.org/10.1029/93TC02254
10. Lowe, D.R., 1994. Accretionary history of the Archaean Barberton greenstone belt (3.55 - 3.22 Ga), southern Africa. *Geology, 22*, 1099-1102.

11. Maphalala, R.M. and Kröner, A., 1993. Pb-Pb single zircon ages for the younger Archaean granitoids of Swaziland, southern Africa. Abstr. 16th Colloq. *African Geology, Mbabane, Swaziland, 2*, 201–206.

12. Moyen, J.F., Zeh, A., Cuney, M., Dziggel, A., and Carrouée, S., 2021a. The multiple ways of recycling Archaean crust: A case study from the ca. 3.1 Ga granitoids from the Barberton Greenstone Belt, South Africa. *Precambrian Research, 353*, 105998. https://doi.org/10.1016/j.precamres.2020.105998

13. Moyen, J.F., Janoušek, V., Laurent, O., Bachmann, O., Jacob, J. B., Farina, F., Fiannacca, P., and Villaros, A., 2021b. Crustal melting vs. fractionation of basaltic magmas: Part 1, granites and paradigms. *Lithos, 402*, 106291. https://doi.org/10.1016/j.lithos.2021.106291

14. Robb, L.J., Barton Jr, J. M., Kable, E.J.D., and Wallace, R.C., 1986. Geology, geochemistry and isotopic characteristics of the Archaean Kaap Valley pluton, Barberton mountain land, South Africa. *Precambrian Research, 31(1)*, 1-36. https://doi.org/10.1016/0301-9268(86)90063-X

15. Robb, L.J., Meyer, F.M., Hawkesworth, C.J., and Gardiner, N.J., 2021. Petrogenesis of Archaean granites in the Barberton region of South Africa as a guide to early crustal evolution. *South African Journal of Geology 2021*, *124*(1), 111-140. https://doi.org/10.25131/sajg.124.0021

16. Zeh, A., Gerdes, A., and Barton Jr, J. M., 2009. Archean accretion and crustal evolution of the Kalahari Craton—the zircon age and Hf isotope record of granitic rocks from Barberton/Swaziland to the Francistown Arc. *Journal of Petrology, 50(5),* 933-966.https://doi.org/10.1093/petrology/egp027